Mechanism of action of a class of antibiotics from their entry to their target in bacteria : a real time visualization

Maho Okuda

▶ **To cite this version:**

Maho Okuda. Mechanism of action of a class of antibiotics from their entry to their target in bacteria : a real time visualization. Molecular biology. Université Paris Sud - Paris XI, 2015. English. NNT : 2015PA112239 . tel-01599239

HAL Id: tel-01599239
https://theses.hal.science/tel-01599239

Submitted on 2 Oct 2017

HAL is a multi-disciplinary open access archive for the deposit and dissemination of scientific research documents, whether they are published or not. The documents may come from teaching and research institutions in France or abroad, or from public or private research centers.

L'archive ouverte pluridisciplinaire **HAL**, est destinée au dépôt et à la diffusion de documents scientifiques de niveau recherche, publiés ou non, émanant des établissements d'enseignement et de recherche français ou étrangers, des laboratoires publics ou privés.

UNIVERSITÉ PARIS-SUD

ÉCOLE DOCTORALE 426 :
GÈNES GÉNOMES CELLULES

Laboratoire : Institut de Biologie Intégrative de la Cellule

THÈSE DE DOCTORAT

SCIENCES DE LA VIE ET DE LA SANTÉ

par

Mlle Maho OKUDA

Mécanisme d'action d'une classe d'antibiotiques depuis leur entrée jusqu'à leur cible chez la bactérie : visualisation en temps réel

Date de soutenance : 30/09/2015

Composition du jury :

Directeur de thèse :	**Dr.** Satoko YOSHIZAWA	Directeur de recherche (I2BC-CNRS)
Co-directeur de thèse :	Dr. Dominique FOURMY	Directeur de recherche (I2BC-CNRS)
Rapporteurs :	Dr. Carine TISNÉ	Directeur de recherche (CNRS-Université Paris Descartes)
	Dr. Gilles TRUAN	Directeur de recherche (INSA-Toulouse)
Examinateurs :	Pr. Jean-Luc PERNODET	Professeur (CNRS-Université Paris Sud)
	Dr. Mathias SPRINGER	Directeur de recherche émérite (IBPC-CNRS)

Acknowledgements

This phD study was performed in the team <Structure and dynamics of RNA> in I2BC, CNRS (Gif-sur-Yvette, France). For me it represents a very rewarding period, during which I learned a lot both professionally and personally.

I wish to express a sincere thank you to juries to have accepted to judge this thesis, the reporters Dr. Carine Tisné and Dr. Gilles Truan, and examiners Pr. Jean-Luc Pernodet and Dr. Mathias Springer. And I would like to thank my three tutors: Dr. Mathias Springer (he is also a member of the jury), Dr. Jean-Louis Fourrey, and Dr. Christophe Possoz, for their insightful comments and the hard question which incented me to widen my research from various perspectives.

Throughout my thesis work, I would like to express my sincere gratitude to the director of my thesis Dr. Satoko Yoshizawa and the director of laboratory Dr. Dominique Fourmy for the continuous support of my PhD study and related research, for their patience, motivation, and immense knowledge. Their guidance helped me in all the time of research and writing this thesis. I could not have imagined having better advisors and mentors for my PhD study. I am also grateful to them for providing me an opportunity to join their team and study in France. This four years study was one of the most enjoyable and rewarding experiences that I have ever had.

I would like to thank the members in the laboratory. My thesis would not have been possible without their helps. I thank Dr. Hélène Walbott and Dr. Sylvie Auxilien, for the stimulating discussions, for the guidance on life in France, and for all the fun we have had in this four years. I also thank Dr. Thomas Plénat for his many advices and assistance on microscope and the data analysis techniques. And many thanks to Dr. Chie Tomikawa for her encouragement.

I thank Laëtitia Besse (Imagif, CNRS) for her expertise in live cell imaging and her help on images acquisitions and analysis with N-STORM super-resolution microscope. I also thank Dr. Samie Jaffrey (Weill Medical College, Cornel University) for providing the Spinach1 Spinach1.2 and tSpinach1.2 sequences on plasmids, and Dr. Etienne Dervyn (INRA, Jouy en Josas) for providing *Bacillus subtilis* strain wt 168.

I want to thank to Japan Student Services Organization, French embassy in Japan and FRM (Fondation pour la recherché Médicale, FDT20140931068) for their financial support granted through my thesis work.

Last but not the least, I would like to thank my friends and my family in Japan. Without their encouragement, it would be much harder for me to continue studying for several years in France.

Abbreviation

BF : **B**right **F**ield
bME : **2**-**M**ercapto**E**thanol
CCCP : **C**arbonyl **C**yanide m-**C**hloro**P**henyl hydrazone
Cy5 : **Cy**anine**5**
DC : **D**uty **C**ycle
DFHBI : 3,5-**DiF**luoro-4-**H**ydroxy**B**enzylidene **I**midazolinone
DMSO : **DiM**ethyl **S**ulf**O**xide
DMS : **DiM**ethyl **S**ulfate
DNA : **D**eoxyribo**N**ucleic **A**cid
dSTORM : **d**irect **S**tochastic **O**ptical **R**econstruction **M**icroscopy
EDPI, II : **E**nergy-**D**ependent **P**hase **I**, **II**
EDTA : **E**thylene**D**iamine**T**etraacetic **A**cid
EmCCD : **E**lectron **m**ultiplying **C**harge-**C**oupled **D**evice
FRET : **F**luorescence **R**esonance **E**nergy **T**ransfer
GFP : **G**reen **F**luorescent **P**rotein
GTP/GDP : **G**uanosine **T**ri**P**hosphate/ **G**uanosine **Di**P**h**osphate
IPTG : **I**so**P**ropyl **T**hio**G**alactoside
LB : **L**uria-**B**ertani broth
LPS : **L**ipo**P**oly**S**accharide
MIC : **M**inimum **I**nhibitory **C**oncentration
Neo-Cy5 : **Neo**mycin-**Cy**anine5
OD : **O**ptical **D**ensity
PCR : **P**olymerase **C**hain **R**eaction
PI : **P**ropidium **I**odide
PMF : **P**roton **M**otrice **F**orce
PSF : **P**oint **S**pread **F**unction
RNA : **R**ibo**N**ucleic **A**cid
mRNA : **m**essenger RNA
rRNA : **r**ibosomal RNA
tRNA : **t**ransfer RNA
rrn : **rRN**A operon
SELEX : **S**ystematic **E**volution of **L**igands by **EX**ponential enrichment
TIRF : **T**otal **I**nternal **R**eflection **F**luorescence microscopy
TR : **T**exas **R**ed
3D-STORM : **3 D**imension-**S**tochastic **O**ptical **R**econstruction **M**icroscopy

Résumé : Des techniques variées de visualisation de molécules d'intérêt sur cellules vivantes ou fixées ont permis de suivre leur synthèse, localisation, dégradation et autres activités.

Dans cette étude, nous avons développé deux outils de fluorescence pour étudier la synthèse des protéines sur bactéries vivantes. Le premier décrit l'utilisation du système Spinach pour l'imagerie du ribosome. Cette approche diffère des méthodes conventionnelles qui utilisent des protéines fluorescentes puisque l'ARN ribosomal 16S contient un aptamère qui rend fluorescent un composé fluorogène. Une étude comparative de la performance de différents aptamères Spinach a été réalisée. Un deuxième outil se focalise sur l'accumulation d'un antibiotique de la famille des aminoglycosides (ligand du ribosome) conjugué à un fluorophore. Ce nouveau conjugué de la néomycine, qui a conservé son activité bactéricide permet pour la première fois de visualiser l'accumulation de l'antibiotique sur bactérie vivante. Cela permet une analyse au niveau de la cellule unique d'une population bactérienne exposée à l'antibiotique. Nous avons également obtenu des données sur la localisation de l'antibiotique une fois qu'il a pénétré dans la bactérie à une résolution inégalée par microscopie super-résolutive.

Nous espérons que ces deux méthodes vont maintenant permettre une meilleure compréhension de la synthèse des protéines et fournir une vue nouvelle de la pénétration des antibiotiques dans les bactéries pour y produire leur action bactéricide.

Mots-clés: microscopie de fluorescence, microscopie super-résolutive, traduction, ribosome, aminoglycosides, aptamère Spinach.

Abstract: Various visualizing techniques have previously enabled monitoring the fate of molecules of interest: their expression, localization, degradation and other activities in live or fixed cells.

In this study, we have developed two fluorescent tools to study protein synthesis in live bacterial cell. The first one describes the application of Spinach system to ribosomes imaging. This is different from conventional methods (that use fluorescent proteins) in that 16S rRNA contains an inserted RNA aptamer that elicits fluorescence of a fluorogenic compound. A comparative study of the performance of different Spinach aptamers was performed here. A second system focuses on the uptake of a fluorescently labeled ligand of the ribosome, neomycin an antibiotic of the class of aminoglycosides. This novel neomycin conjugate, which kept its bactericidal activity allows for the first time imaging of aminoglycoside uptake on live bacteria. This opened the door to a single cell analysis of bacterial cell populations. We also obtained data about the localization of the antibiotic once inside the bacteria to an unprecedented resolution using super resolution microscopy.

We hope that both of these methods will contribute to a better understanding of protein synthesis as well as provide a novel view on the way antibiotics penetrate cells and perform their bactericidal action.

Keywords: fluorescence microscopy, super-resolution microscopy, translation, ribosome, aminoglycosides, Spinach aptamer.

Index

Chapter I

Introduction

I. 1 Translation in bacterial cell

I. 1. 1 Ribosomal Structure and Function

Translation is the process whereby genetic information, in the form of messenger RNA, is used to synthesize the corresponding sequence of amino acids found in proteins. A molecular machine, the ribosome, which is a ribonucleoprotein complex of about 2.5 MDa, is responsible for the protein synthesis. Growing cells spend approximately 50 % of the energy they consume to make proteins (1). The rate of proper protein synthesis usually limits the rate of bacterial growth. Hence ribosome bears an enormous responsibility to carry out its function at a marvelous pace and with great fidelity. A ribosome consists of two unequally sized subunits. In bacteria, these two units are referred to as the 50S (large) subunit and 30S (small) subunits according to their sedimentation rates by centrifugation. The 30S subunit contains a strand of rRNA labeled 16S RNA with 1540 nucleotides and 21 proteins, whereas the 50S subunit houses 23S RNA with 2900 nucleotides, 5S RNA with 120 nucleotides and 34 proteins (Figure I-1-1). Association of the 50S and 30S subunits through a network of molecular interactions results in the fully functional 70S ribosome. X-ray crystallographic efforts have yielded extensive structural data for a ribonucleoprotein macromolecule (2-9). More recently, structures of ribosomes in various functional complexes, such as the complex containing tRNA (deacylated initiator $tRNA^{fMet}$ and $tRNA^{Phe}$), mRNA and 70S ribosome (10), were determined.

Transfer RNA (tRNA) serves as the physical link between the nucleotide sequence of nucleic acids (DNA and RNA) and the amino acid sequence of proteins. Every cell contains a population of tRNA that bind and deliver different amino acid to ribosome. Each tRNA has similar molecular mass (~ 25 kD) and the same L shaped tertiary structure (Figure I-1-2). At the end of the long arm of this L shape, they have a three base anticodon sequence that is complementary to an mRNA nucleoside base triplet (codon) and that decides the nature of amino acid to be delivered at a specific codon. The mRNA, which interacts with the ribosome near the subunit interface, uses this base triplet to recognize and gather appropriate tRNAs from the cytoplasm (11-13). At the CCA tail

at 3' end of tRNA molecule, the amino acid that is specific to an anticodon is attached by an aminoacyl-tRNA synthetase to form the aminoacyl-tRNA through formation of an ester bond between the carboxylate group of the amino acid and the terminal adenine residue of tRNA. Hence there is at least one tRNA molecule for every amino acid used in protein synthesis.

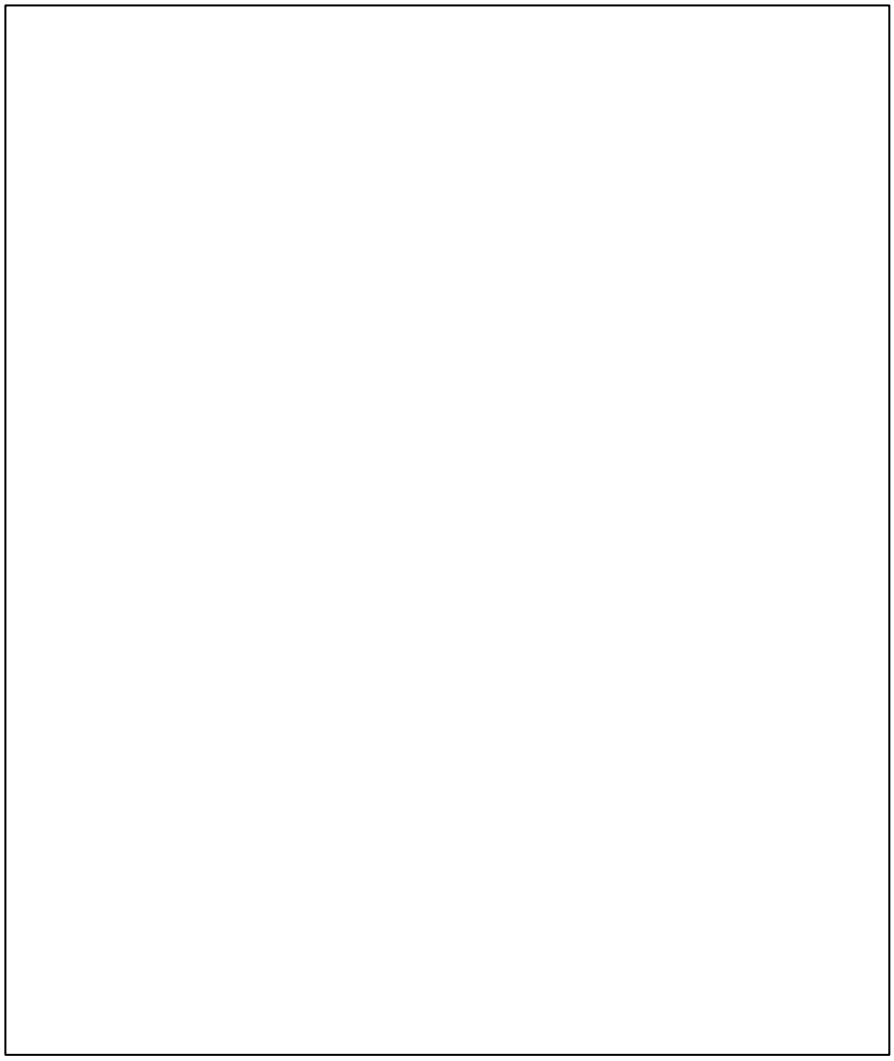

Figure I-1-1: Structure of the ribosome. (A) 'Top' view of the 70S ribosome with mRNA and A- P- and E-site tRNAs. B, C, Exploded views of the 30S subunit (B) and 50S subunit (C). Source (14) The structure of the L7/L12 arm was fitted onto the 70S ribosome (15) with mRNA elongated by modeling.

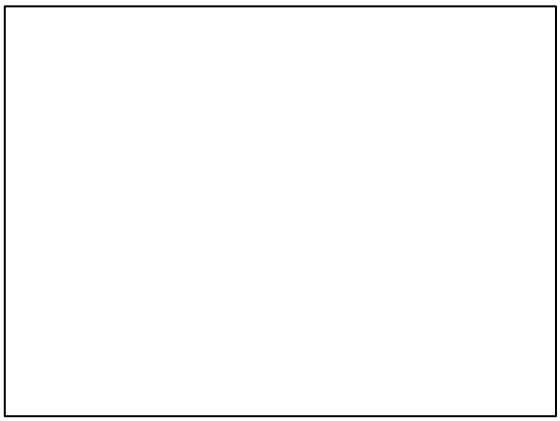

Figure I-1-2: Tertiary structure of tRNA
(LIFE SCIENCE web textbook Edited by: CSLS/The University of Tokyo
http://csls-text.c.u-tokyo.ac.jp/index_active.html).

Ribosome has three unique tRNA binding sites (Figure I-1-3) straddling both 30S and 50S subunits: A site (for "aminoacyl"; the site for binding aminoacyl-tRNA), P site (for "peptidyl"; the site for tRNA with the growing polypeptide chain) and E site (for "exit"; where deacylated tRNA resides prior to its release from the ribosome). An aminoacyl-tRNA that delivers an amino acid travels along these three sites within the ribosome by entering at the A site, moving from the A to the P site and finally exiting from the E site.

During translation, the 30S subunit holds mRNA and the anticodon stem loop of the correct (cognate) tRNA in place so that the codons of mRNA stay paired with the anticodons of tRNA. Meanwhile the aminoacylated end of tRNA is at the 50S subunit, where the peptide bond formation is catalyzed and transfer of an amino acid from the A-site tRNA to the nascent polypeptide chain within the P site takes place.

Once this elongation step is carried out and the correct amino acid has been added to the growing peptide chain, the newly deacylated-tRNA in the P site must be replaced by peptidyl-tRNA in the A site, subsequently a new aminoacyl-tRNA is delivered in the A site for addition of the next amino acid. Additionally, the tRNA within the E site is ejected in order to create the necessary vacancy for deacylated-tRNA in P site. This movement of tRNA from one site to the next is called "translocation", resulting in progress of ribosome along mRNA by one codon.

Figure I-1-3: Schematic of the steps for tRNA delivering, new peptide bond formation and translocation. The figure was modified using Figure 1 of (16).

I. 1. 2 Stages in protein synthesis and the specific components

Translation of mRNA encoded genetic information into the proper protein is often subdivided into four stages (Figure I-1-4). These stages are known as initiation, elongation, termination and ribosome recycling; each stage requiring a very specific set of components.

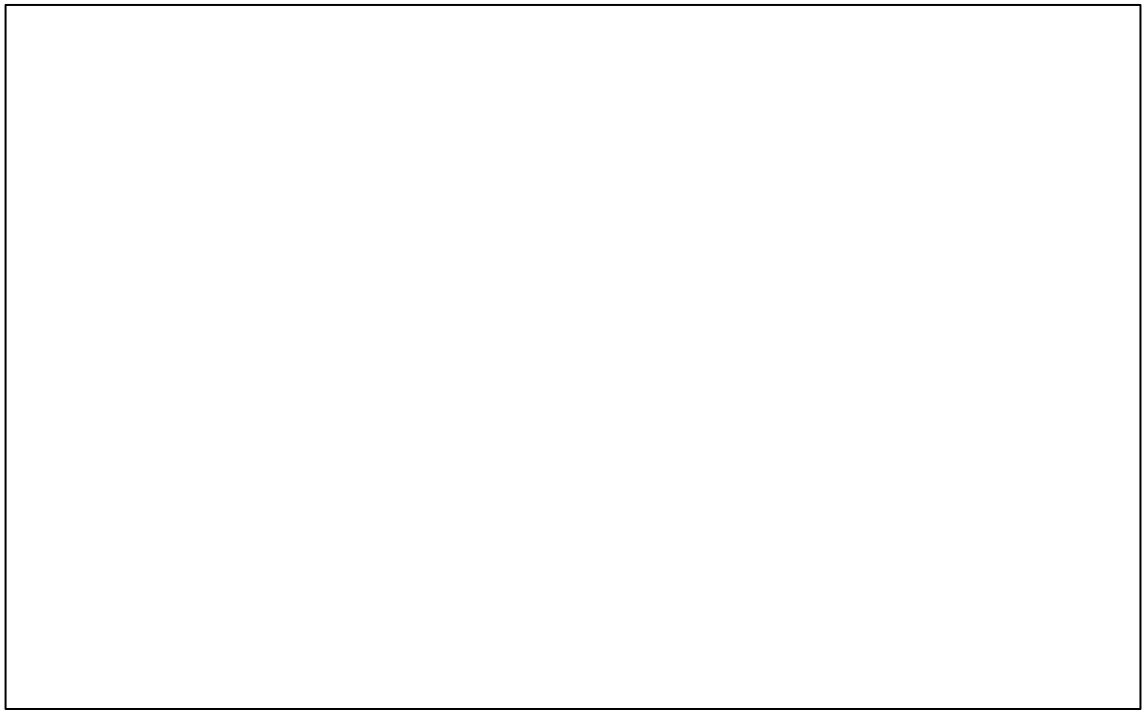

Figure I-1-4: Overview of bacterial translation. For simplicity, not all intermediate steps are shown (14).

I. 1. 2. 1 Initiation

Initiation in the bacterial ribosome begins with binding of Initiation Factor 3 (IF3) to the 30S ribosomal subunit to promote dissociation of the ribosome into subunits (17). Subsequent association of IF1 with A site of the 30S subunit is thought to guide the initiator tRNA to the ribosomal P site by blocking the A site (18,19). Then, the rest of molecules involved in translational initiation associate with the 30S subunit: IF2, mRNA and the initiator aminoacylated-tRNA (N-formylmethionyl-tRNA: fMet-tRNA^{fMet}). The Shine-Dalgarno (SD) sequence of mRNA interacts with a complementary sequence (anti-SD sequence) at the 3' end of the 16S rRNA, which helps positioning the AUG start codon within the P site. fMet-tRNA^{fMet} binds to P site due to the steric hindrance at the A site created by IF1. On complex formation of this initiator tRNA substrate to its anticodon, GTP bound IF2 joins the initiation complex. The combination of both, IF2 and fMet-tRNA^{fMet}, triggers binding of the 50S subunit. Finally, GTP bound to IF2 is hydrolyzed to GDP, resulting in a conformational change within the ribosome that releases all three initiation factors. A fully functional 70S ribosome is now ready for elongation.

I. 1. 2. 2 Elongation

A cycle of elongation corresponds to reading a codon on the mRNA and adding the correct amino acid to the polypeptide chain. The accuracy of the translation is based on selecting the correct aminoacyl-tRNA in response to each codon present in the A site. To begin, the appropriate aminoacyl-tRNA is brought in as a form of ternary complex with elongation factor-Tu (EF-Tu) and GTP. This complex of tRNA and EF-Tu is recognized by the 70S ribosome by base pairing of the codon-anticodon as well as by the interaction with the ribosome (20).

Structurally, the geometry of base pairs of this codon-anticodon pairing is controlled by three highly conserved nucleotides A1492, A1493 and G530 of 16S rRNA in 30S subunit(21). If Watson-Crick pairing between codon-anticodon is correct, the hydrolysis of GTP to GDP on the G domain of EF-Tu is strongly stimulated by the ribosome to release the EF-Tu-GDP complex from the ribosome, leaving only the aminoacyl-tRNA behind. Thus, ribosome receives the correct amino acid to add to a growing polypeptide with the very low error rate of 10^{-4} (22,23).

The central chemical event in elongation is the peptidyl-transferase reaction (Figure I-1-5), in which a nucleophillic attack of the a-amino group of the aminoacyl-tRNA onto the ester carbon of the peptidyl-tRNA forms a new peptide bond. The catalytic site is in domain 5 of the 23S rRNA in 50S subunit, which binds to the CCA ends of aminoacyl- and peptidyl-tRNAs.

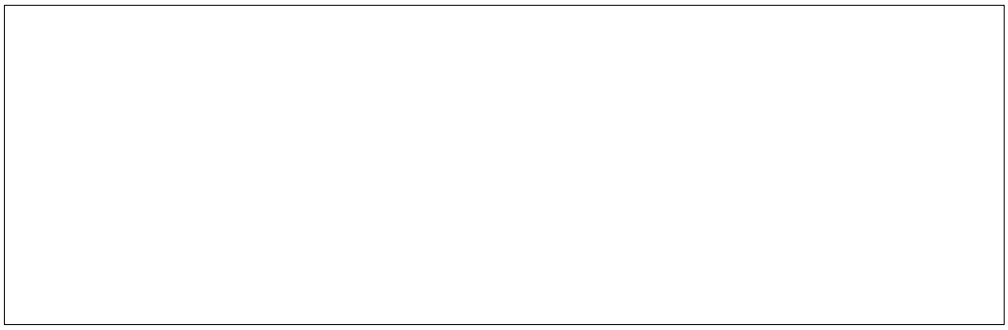

Figure I-1-5: A schematic of peptide-bond formation (14).

The final step of elongation is known as translocation. As the ribosome prepares for the next aminoacyl-tRNA, it must shift one codon towards the 3' end of mRNA. A protein called elongation factor G (EF-G) helps facilitating the translocation process by coupling the energy of GTP hydrolysis to conformational changes within the ribosome (24). After translocation, ribosome empties the A site for the next aminoacyl-tRNA by the transition of both peptidyl-tRNA from A site to P site and deacylated-tRNA from P site into E site. EF-G, bound near the A site, provides the energy needed for these movements through hydrolysis of GTP.

I. 1. 2. 3 Termination

Termination and release of a polypeptide represent the last step of protein synthesis for which the ribosome is responsible. To signal the end of the coding sequence to ribosome, one of the three termination codons in mRNA (UAA, UAG, UGA) occupies the A site. Once this happens, a series of three release factors consisting of class I (RF1 and RF2) and class II (RF3) starts functioning for properly dismantling the ribosome. RF1 and RF2 first recognize the stop codon in the A site (25). This recognition event induces the hydrolysis of the completed polypeptide chain from the P site tRNA to release the newly synthesized protein from the ribosome (26,27). RF3 is thought to accelerate the dissociation of RF1/2 from the ribosome after peptide release by inducing conformational change of ribosome through the exchange of GDP for GTP bound to RF3.

I. 1. 2. 4 Ribosome recycling

After the function of RF3, ribosome is left with mRNA and the deacylated tRNA in the P site (post-termination complex). The ribosome must be recycled into subunits for a new round of protein synthesis to begin. In bacteria, an essential protein called ribosome recycling factor (RRF) works together with EF-G to carry out this process (28). Structural analysis of the post terminated complex bound to RRF and EF-G using cryo-electron microscopy (29) and X-ray crystallography

(30) provided a model of sequence of events in binding of RRF and EF-G to the ribosome (Figure I-1-6) (30). RRF binds to ribosome at A/P site and locks the ribosome in the ratcheted state (ratcheting mechanism concerns movements of the head platform and body domains of 30S subunit). Subsequently, EF-G binds ribosome to interact with RRF unlike in translocation where EF-G interacts with tRNA. EF-G binding changes the binding position and conformation of RRF resulting in the shift of anticodon loop of the deacylated-tRNA in P to E site. As EF-G binding to the ribosome favors the unratcheted state, the head of 30S subunit is rotated back to its original position, which causes further conformational change of the complex for dissociating 30S and 50S subunits. The precise sequence of events that leads to release of all bound components is still unknown. IF3 is also suggested to be involved in the release of mRNA and deacylated-tRNA from the 30S subunit (31,32) and to keep the split subunits separated (33).

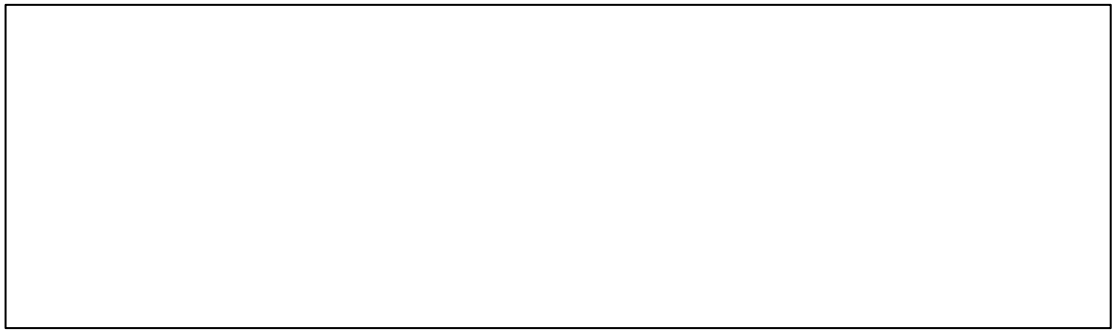

Figure I-1-6: Schematic diagram showing steps of the recycling process (30).

I. 1. 3 Translation cycle and antibiotics

As described above, translation is central to the cellular activity. Also, as illustrated in the previous section, translation cycle is constituted by multiple steps in which various interplay between the ribosome and the translation factors enables rapid protein synthesis and assures accuracy in translation. Due to its importance, translation is a functional target for many antibiotics. Indeed, for every step of translation, antibiotics that inhibit the reaction to proceed have been discovered (Figure I-1-7). Among these, in the following section 3, I will discuss in detail on aminoglycoside antibiotics that inhibit the decoding process.

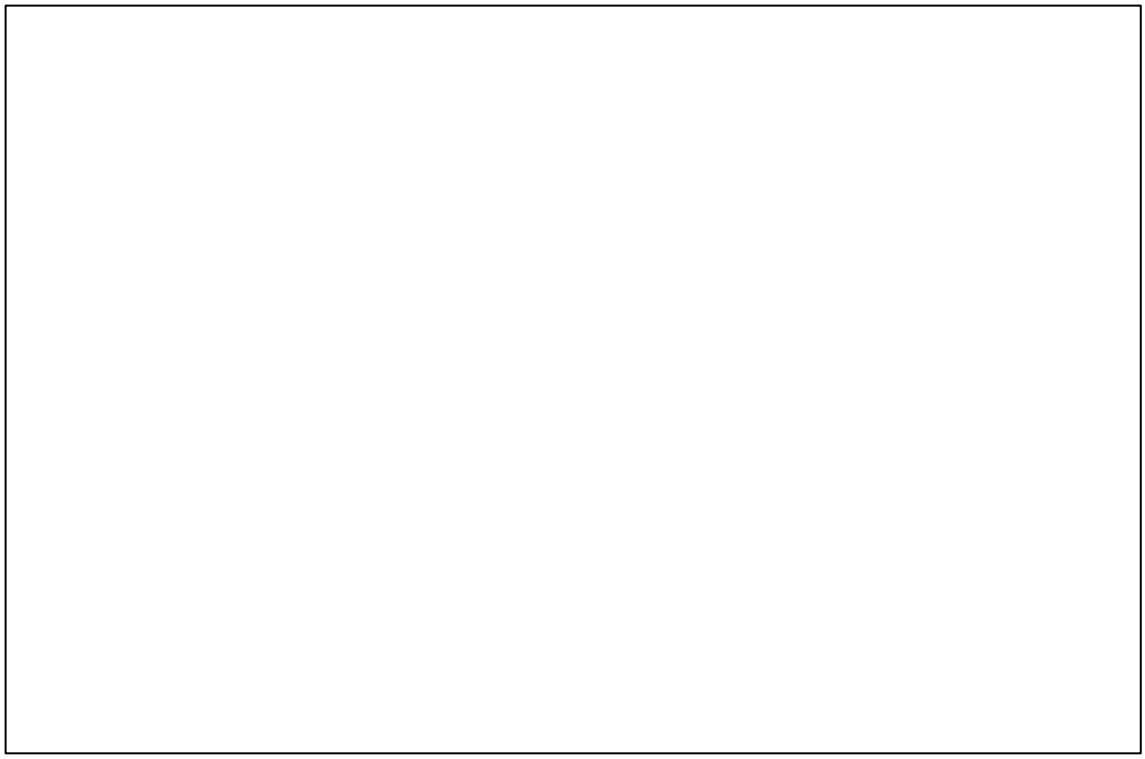

Figure I-1-7: Antibiotics known to inhibit every step of translation. Taken from reference (34).

I. 2 Live cell imaging of bacterial cells (using GFP and the derivative method)

The discovery and the use of Green Fluorescent Protein (GFP) have made strong contribution to cell imaging. The fusion of GFP gene to the gene of a target protein leads to the expression of a GFP fused protein of interest in living cell, which makes it possible to track the protein dynamics: expression, localization and degradation.

I. 2. 1 GFP

Green Fluorescent Protein (GFP) from the jellyfish *Aequorea victoria* is the best-characterized fluorescent protein. GFP forms a chromophore spontaneously and emits light without any cofactor after excitation at appropriate wavelength. When the gene for GFP is fused to the gene of a protein of interest, the fate of the target protein can be followed by monitoring of the GFP fluorescence with microscopy: expression, localization, degradation and other activities. Mutagenesis efforts in GFP have resulted in new GFP variants with stronger fluorescence, more protein stability or emission color variation range from blue to yellow (35). Now the GFP family has become a commonly used tool in molecular biology and cell biology. Martin Chalfie, Osamu Shimomura, and Roger Y. Tsien were awarded the 2008 Nobel Prize in Chemistry for their discovery and development of the GFP.

GFP first appeared in a report that *Aequorea aequorea* emits green fluorescence in response to the irradiation of ultraviolet light in 1955. Shimomura *et al*. identified GFP (36) as one of the proteins involved in the luminescence reaction together with aequorin. Osamu Shimomura also proposed that the structure of the chromophore is p-hydroxybenzylideneimidazolinone (Fig I-2-1 A), which was validated using NMR spectroscopy (37). Three residues (Ser65-Tyr66-Gly67) form the chromophore spontaneously (38,39) (Fig I-2-1 B).

A

B

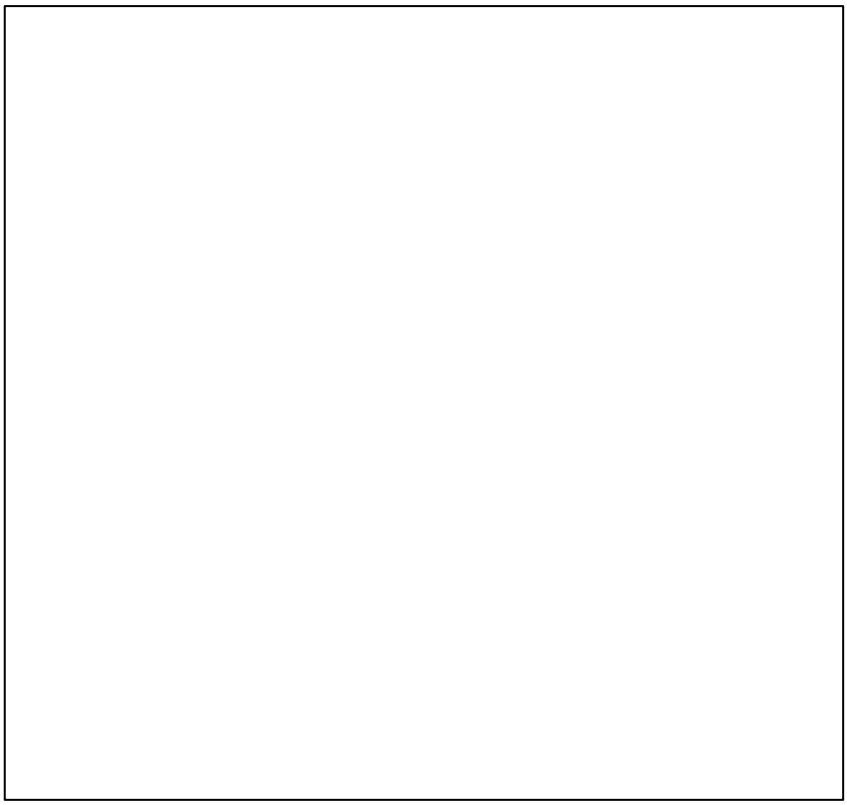

Figure I-2-1: The fluorescence chromophore formed by amino acid residues 65-67 (Ser65-Tyr66-Gly67)**.** (A) 4-(*p*-Hydroxybenzylidene)-imidazolin-5-one structure of the chromophore. The O*y*, O*x*, and N atoms shown in bold are possible protonation sites. The ϕ and τ dihedral angles can rotate in the excited state. (B) Mechanism of intramolecular biosynthesis of the wild type GFP chromophore and improved mutant S65T (40).

Cloning and sequencing of GFP gene showed that GFP is a small protein with a molecular weight of approximately 27 kDa composed of 238 amino acids (41). Publications that describe the expression of GFP displaying a bright green fluorescence in organisms other than *Aequorea victoria* were published successively: *E. coli* and *C. elegans* (42), *Sacharomyces cerevisiae* (43) and Dorosophila oogenesis (44). It was confirmed that formation of a fluorescent

chromophore in GFP does not require an unknown enzyme system, idiosyncratic to *Aequorea victoria*. The first structure of wild-type GFP was determined in 1996 (45). The majority of the sequence of GFP forms a barrel structure composed of 11 b-sheets to surround a single helix that is located inside. The central helix carries the chromophore in the middle, which is derived from three residues, Ser65, Tyr66 and Gly67 in wild type GFP. There are other short helices located at the top and the bottom of the barrel to function as lids to help burying the chromophore into the protein structure (Figure I-2-2).

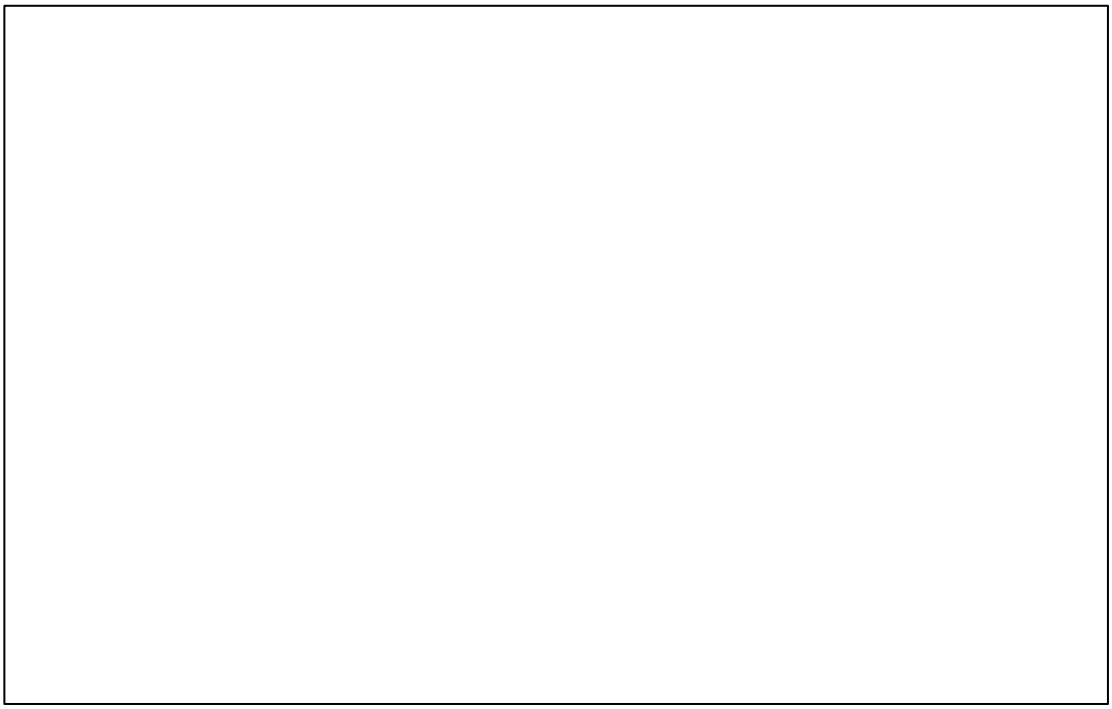

Figure I-2-2: Tertiary structure of wild-type GFP (1GFL (45)). (A) End-on view. (B) Side view. Eleven strands of β-sheet form an antiparallel β-barrel with short α-helices forming lids on each end. The fluorophore is inside the can, as a part of a distorted α-helix, which runs along the axis of the cylinder (46).

Neither denatured GFP (47), the chromophore-containing hexapeptide fragment (37,38), nor synthetic model compounds (48-50) are significantly fluorescent. They, however, become highly fluorescent at 77 K, indicating that inhibition of vibration or rotation around the exo-methylene double bond of the chromophore prevents reduction in fluorescence due to fast internal conversion (46,51,52).

In GFP, surrounding residues such as Arg96, Tyr145, His148, Phe165, Ser205 and Glu222 hold the structure of the chromophore rigidly using a combination of hydrogen bonds and

hydrophobic side chains (Figure I-2-3). As the chromophore is not allowed for conformational change, it radiates energy as light rather than through a thermal process.

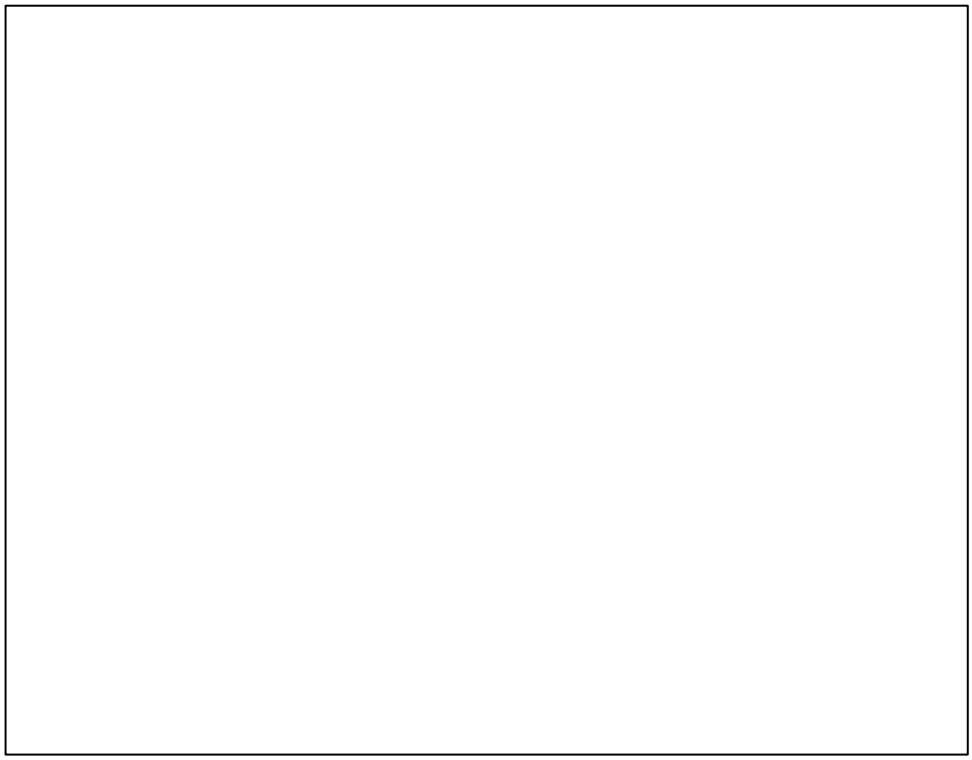

Figure I-2-3: Amino acid side chains, main chain carbonyls and amides, and solvent waters in the immediate vicinity of the chromophore of S65T GFP (mentioned later). Probable hydrogen bonds are shown as dotted lines labeled with the distance between the heteroatoms in angstroms.

The excitation spectrum of GFP fluorescence has two peaks. First peak of a dominant curve is at 395 nm and the other peak is at 475 nm. On the other hand, the emission spectrum has a sharp maximum at about 505 nm (35) (Figure I-2-4 A). Change in protonation is responsible for the different absorption. The 395 nm absorption is normally attributed to a neutral form (phenol) of the chromophore, and the absorption at 475 nm to an anionic form (phenolate) (48) (Figure I-2-4 B). The anion and neutral species are connected by a ground-state equilibrium.

Mutations of residues forming the chromophore or surrounding chromophore make a large impact on photophysical characteristics of GFP. When Ser65 is substituted with Thr, Ala or Gly, the chromophore forms the phenolate anion form and does not have 395 nm excitation peak. It was shown that in GFP S65T, the main peak of the excitation spectrum of wild type GFP was shifted from the UV to 488 nm with the emission peak kept at 509nm (40) (Figure I-2-5).

A

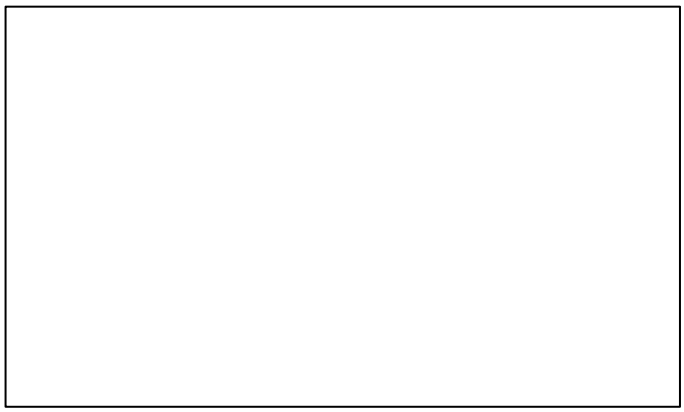

B

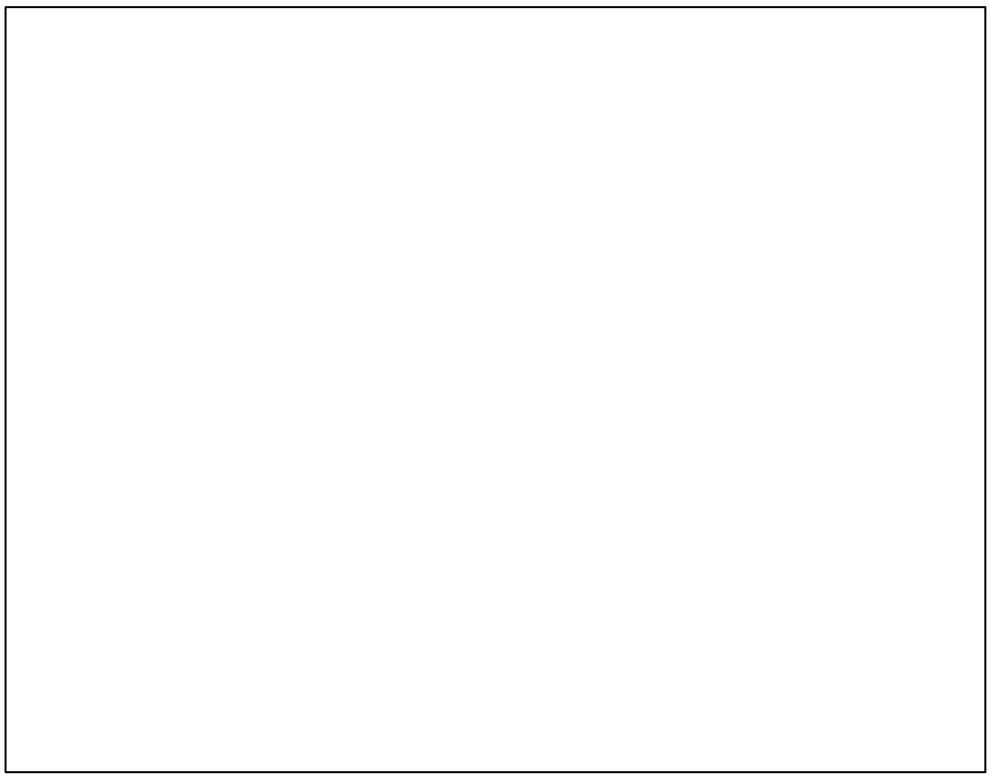

Figure I-2-4: (A) Fluorescence excitation and emission spectra of wild-type GFP (solid and dashed lines, respectively) (B) GFP chromophore in two forms (neutral and anionic) with nearby basic amino acids His148, Gln94, and Arg96, and the acid, Glu222 (46).

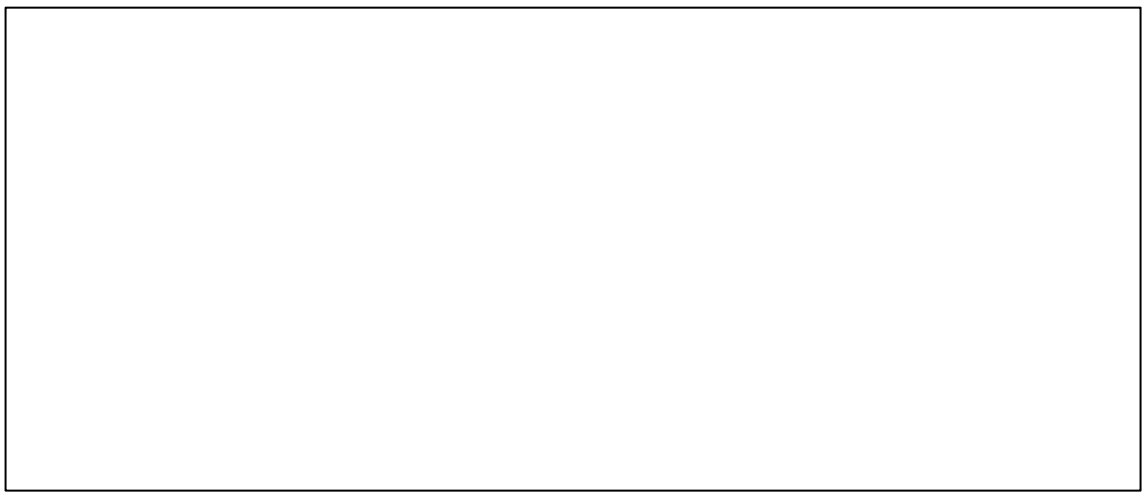

Figure I-2-5: Excitation spectra of wild-type GFP (a) and the S65T mutant (b). Excitation spectra were recorded at the emission peak wavelengths (508 nm for wild-type and 510 nm for S65T)(40).

Further mutation F64L was added to GFP S65T to acquire more efficient folding ability at 37 ˚C (53), which is now called enhanced GFP (EGFP) and widely used as a marker molecule.

I. 2. 2 RNA imaging in live cell

Now it is a well-known fact that RNA, with its various functional and structural characteristics, makes a strong contribution to the cellular biological activity. Monitoring where a specific RNA is synthesized, whether it is transported and how it is degraded, greatly helps full understanding of the function of the RNA molecule. FISH (Fluorescence In Situ Hybridization) gives images of the cell containing precious information of the RNA localization at a specific moment. However, the method requires cell fixation to wash away the excess of fluorescent probes used for hybridization, and thus is not adapted for real time imaging. Methods to visualize RNA in a cellular environment developed to date are summarized below.

I. 2. 2. 1 Oligonucleotide probe system

There is a method for visualizing cellular endogenous RNA where a molecular beacon is introduced into a cell. Molecular beacon (MB) that is mainly used for mRNA detection is a hairpin-shaped single stranded oligonucleotide probe with a quencher on one side and a fluorescent molecule on the other. The loop, which is usually 15-25 bases, is designed to have complementary

sequence to the RNA of interest. The stem portion consists of 4-6 complementary base pair regardless of the target mRNA. Usually, the fluorescence is lost due to the short distance between the fluorophore and the quencher. Binding to the target RNA opens the structure, activating the fluorescent signal of the probe thereby enabling visualization of cellular endogenous RNAs. However, the stem within the molecular beacon sometimes breathes spontaneously, which results in a mixture of the fluorescence from two kinds of the same probe, with and without binding to the target mRNA. To solve this problem, dual FRET (Fluorescence Resonance Energy Transfer) MBs have been developed where FRET signal occurs between the fluorescent molecules of the two MBs that are designed to bind to RNA sequence in series (Figure I-2-6). The technique allows eliminating the false positive fluorescent signal due to the spontaneous opening of the MBs since this form would not give FRET. Shortcoming of this technique is that it requires microinjection to introduce the probes into the cell, which possibly can cause some damage. Also it is necessary to introduce the probes into the cell one by one, and thus for a large scale analysis the introduction step can be too much time consuming. Another drawback of MBs is that once introduced into the cytoplasm they are transferred into the nucleus. Therefore, it is necessary to connect MBs to proteins that localize in the cytoplasm or to quantum dots to prevent sequestration in the nucleus (54,55). However, combining large molecules with MBs probes is likely to interfere with the dynamics of the RNA.

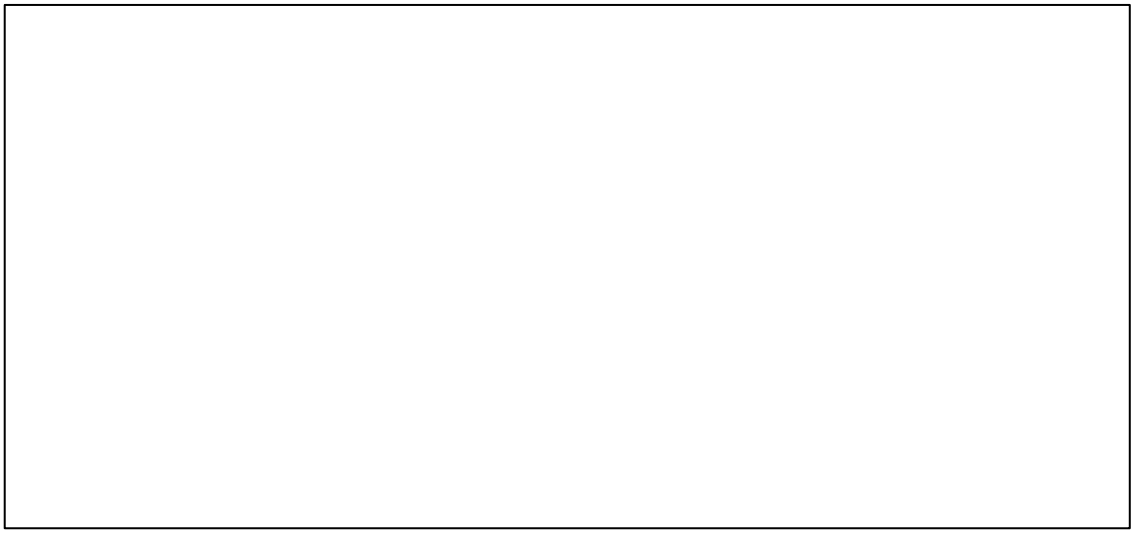

Figure I-2-6: concept of dual FRET molecular beacons. Hybridization of donor and acceptor MBs to adjacent regions on the same mRNA target results in FRET between donor and acceptor fluorophores upon donor excitation. By detecting FRET signal, fluorescence signals due to probe/target binding can be readily distinguished from that due to MB degradation and non-specific interactions (source (56)).

I. 2. 2. 2 RNA aptamer-protein/ fluorescent ligand system

Here, an RNA aptamer sequence that has been selected to bind a protein is fused to a target RNA. Fusion of the aptamer sequence into a particular gene of interest generates its corresponding transcript containing the functional aptamer. At the same time, the fluorescent ligand for the RNA aptamer is introduced into the cells to visualize the target RNA (Figure I-2-7).

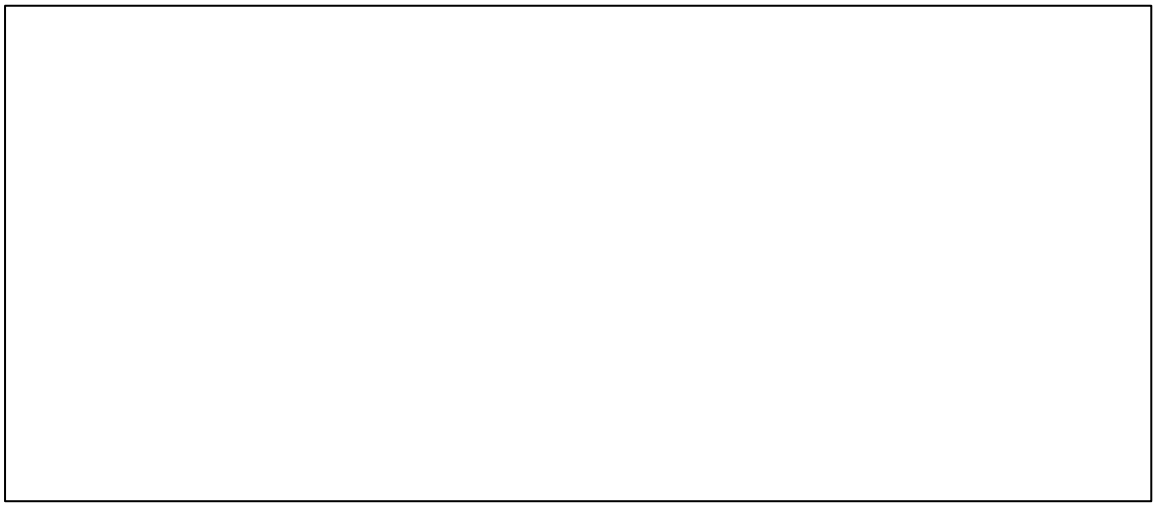

Figure I-2-7: Aptamer-based strategies for RNA labeling. (A) An aptamer tag binds to an RNA-binding protein (RBP) genetically fused to GFP, resulting in fluorescent labeling of the RNA. (B) The aptamer tag binds to a low molecular weight fluorogenic dye, inducing fluorescence from the dye. (Source (57))

I. 2. 2. 2-A RNA aptamer-protein system

In the first system, the ligand is a fluorescently labeled protein that is fused to an RNA binding protein. The RNA aptamer-protein system is often based on naturally occurring high-affinity interactions between specific RNA structural motifs and their binding proteins. This system requires co-expression of transcripts of interest fused to an aptamer sequence and the protein partner fused to a fluorescent protein such as GFP. Fluorescent protein allows visualizing the localization of the target RNA under fluorescence microscopy when the additional domain of RNA binding peptide is coupled with an aptamer. Currently, this system that expresses both the RNA and a fluorescent protein using plasmid is the method most frequently used for RNA imaging in a living cell. Various sets of RNA-protein complexes have been devised to date for RNA imaging in living bacterial, fungal, plant and animal cells. Here I give some examples.

MS2-GFP is a prototype and the most frequently used among RNA aptamer-protein system for RNA imaging. MS2 is a phage coat protein that binds specifically to a 19-nt RNA stem-loop forming sequence (58,59). There are some problems: one is that GFP sometimes is cleaved from the RNA recognition peptide. Such free GFP and unbound ligands cause an increase of the background. Another is the need for multiple insertions of MS2-GFP binding domains into the target RNA. Single mRNA detection was achieved when 24 binding sites were inserted (59).

There are many other RNA aptamer-protein interactions in this category including λN22 system, which is the second most frequently implemented system after MS2. It is also worthwhile to mention BglG system and PP7, etc. These interactions can be found in the review by Urbanek et al., 2014 (60).

I. 2. 2. 2-B Aptamer-fluorescent ligand system

Recently another RNA detecting system has been developed based on the interaction of a fluorescent molecule and a specific RNA structural motif. In the RNA Aptamer-dye system, an organic dye that exhibits fluorescence only in the state bound to an aptamer is used. This is important because it reduces the background caused by the free dye. The RNA aptamer sequence for the fluorophore was selected using SELEX, while an RNA aptamer-protein system is normally based on a naturally occurring protein-RNA interaction. This system has several advantages comparing to the two conventional methods mentioned above, for example: i) the dye has better cell permeability than MBs; ii) the RNA aptamer-dye complex that is smaller than an aptamer-protein complex so that it is expected to have less perturbation on the original function of RNA of interest.

i) Sulforhodamine B

An RNA aptamer for a fluorescent dye Sulforhodamine B (Figure I-2-8 A) was identified and named as SRB-2 (61) (Figure I-2-8 B). Afterwards, the use of Sulforhodamine B with quencher anchored was reported. Sulforhodamine B, whose fluorescence is quenched in free state, becomes fluorescent in complex with RNA aptamer because it leads to dissociation of the quencher (62) (Figure I-2-8 C).

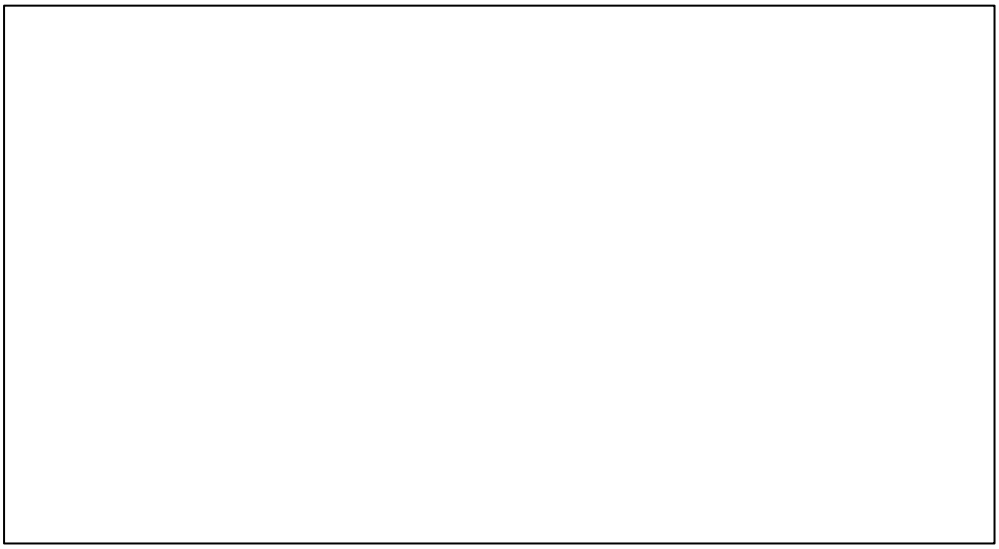

Figure I-2-8: (A) Structure of Sulforhodamine B. (B) Secondary structure model of the RNA aptamer, SRB-2. (C) Concept of fluorescence system using Sulforhodamine B and the aptamer RNA sequence SRB-2. F and Q in the figure indicate Sulforhodamine B and a quencher respectively (62).

ii) DFHBI

3,5-difluoro-4-hydroxybenzylidine imidazolinone (DFHBI) is a conditionally fluorescent dye developed in a completely different way. DFHBI was designed as mimic of EGFP that is not fluorescent in itself, but exhibits fluorescence when it forms a complex with its selected aptamer RNA called Spinach (63). The details about DFHBI-Spinach complex are described in the next section.

I. 2. 2. 3 New RNA detecting method based on GFP fluorophore

GFP like chromophore-RNA aptamer system was proposed by Jaffrey and colleagues (63). The concept was to create a mimic of EGFP using a synthetic compound that is analogous to the chromophore of GFP S65T (Figure I-2-9 A) and a specific RNA structure motif that plays the role corresponding to the GFP polypeptide except for the three residues to form the chromophore (Figure I-2-9 B). RNA aptamers that specifically bind DFHBI were identified using SELEX. The aptamers were found to strongly activate fluorescence of the chromophores due to steric constrains of the chromophore isomerization upon binding to the aptamer. The brightest RNA consisted of a 98-nucleotide aptamer named Spinach. The chromophore DFHBI was designed to have similar spectral characteristics to EGFP, whose absorbance spectrum has a major peak at blue light rather than UV light like wild type GFP (Figure I-2-9 C).

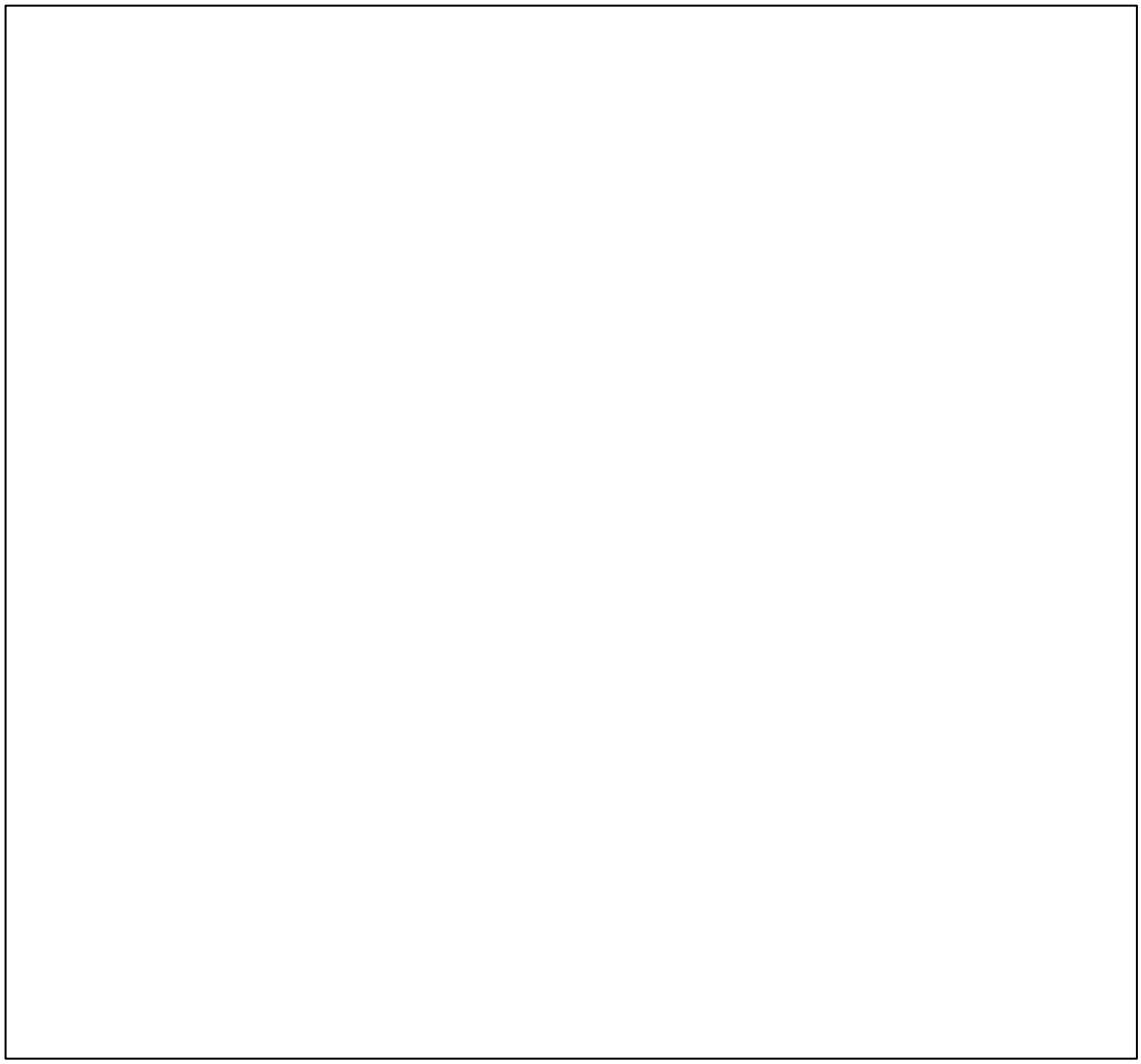

Figure I-2-9: (A) Structures of HBI (green) in the context of wild-type GFP, DMHBI: analogue of chromophore of wild-type GFP and DFHBI: analogue of chromophore of GFP S65T. (B) Scheme of fluorescence from Spinach-DFHBI complex. The binding of DFHBI to the RNA aptamer Spinach activates green fluorescence upon 473 nm illumination (Blue light). (C) Absorbance spectra of GFP-like fluorophores. DFHBI shows one peak at blue light while DMHBI has two at UV and blue light. Sources for figures (63,64).

Since the first paper on DFHBI-Spinach system (63), mutation study of the RNA has been pursued to obtain new Spinach molecules performing with better structural stability, higher affinity to DFHBI and brighter fluorescence (63,65,66) (Figure I-2-10). This resulted in the generation of Spinach1.1, Spinach1.2 and Spinach2 (65). Spinach2, especially, is introduced as the best Spinach sequence. At the same time, miniaturization of Spinach was pushed forward. Spinach

was subjected to the truncation of 30 bases to generate spinach-mini with 90 % signal intensity of original Spinach, which was called as 24-2 mini (24-2 stands for the serial number of Spinach through SELEX) (63) (Figure I-2-10). Furthermore, recent crystal structure analysis on Spinach1.2 in complex with DFHBI revealed the core bases for eliciting fluorescence, which allowed generating a minimized Spinach (51 bases), named Baby Spinach (66) (Figure I-2-12 D).

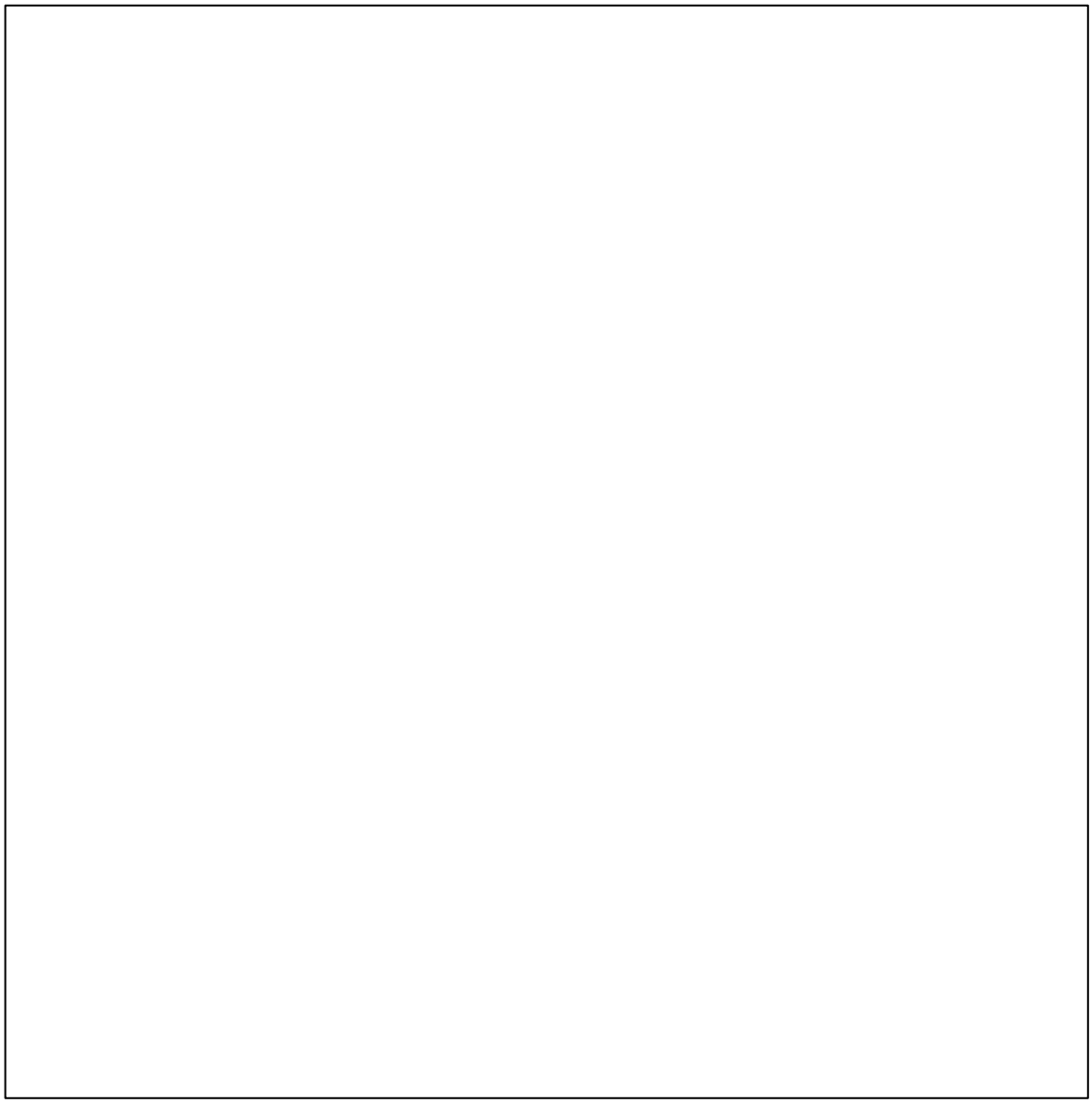

Figure I-2-10: Secondary structure of Spinach and its variants. Spinach, Spinach1.1, Spinach1.2, Spinach2 and Spinach-mini. Sequence shown in red are unique for Spinach1.1, Spinach1.2 and Spinach-mini. Residues in blue are unique for Spinach2. Shaded part in Spinach was truncated in Spinach-mini. 24-2 is the serial number for Spinach used in (63). Baby Spinach is shown in next Figure I-2-12.

Several groups study on the photophysics of Spinach. Spinach-DFHBI upon illumination loses the fluorescence faster than GFP, but it recovers the signal after a certain delay. On the other hand, once GFP is bleached, the fluorescence does not come back. To explain this difference, one model was proposed that DFHBI suffers from cis-trans isomerization upon illumination resulting in loss of fluorescence (Figure I-2-11) (64). In GFP, from the crystallographic structural point of view, it is said that such isomerization cannot occur (67). In the model, the isomer of DFHBI is ejected from spinach because it is not suited for the shape of cavity in Spinach. Subsequently a new free DFHBI molecule arrives and binds to Spinach letting the complex recover the fluorescence.

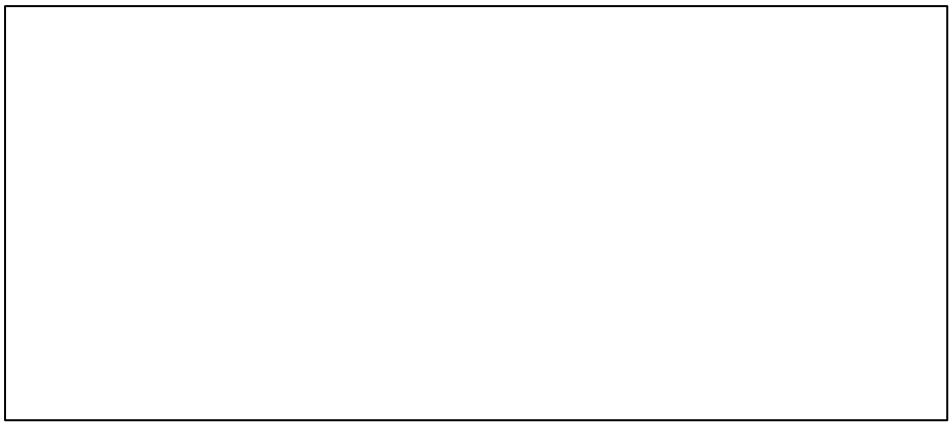

Figure I-2-11: Proposed model of the fluorescence behavior of the Spinach-DFHBI complex upon illumination (64).

Crystallographic studies on Spinach with and without DFHBI (66,68) revealed the unique structure of Spinach and the molecular interactions inside the complex (Figure I-2-12 A,B). Spinach forms a bent 11 nm long stick-like structure. In the center, three tandem quadruplexes, two G-quadruplexes and one GUUC-quadruplex were found. The DFHBI binding pocket was found above the quadruplexes surrounded by the first G-quadruplex (G26-G30-G65-G70), a base triple (U32-A64-U61) and an unpaired G31. Structural analysis prompted understanding on the mechanism of Spinach fluorescence. Cis-DFHBI was found in the crystal structure of Spinach-DFHBI complex. In addition, in ligand-free Spinach, the binding cavity seems ready to accommodate cis-DFHBI rather than trans-DFHBI (Figure I-2-12 D, E and F). Cis-DFHBI seems to be able to form more hydrogen bonds between the nucleotides surrounding the fluorophore binding site. Furthermore, DFHBI-Spinach complex structure showed that DFHBI is partially accessible and residue A69, which is located near the entrance of DFHBI binding pocket, can move flexibly (Figure I-2-12 C). These observations support the above-mentioned model on an exchange mechanism of photoconverted DFHBI (64) where the structure prompts release of the resulting trans-DFHBI after illumination.

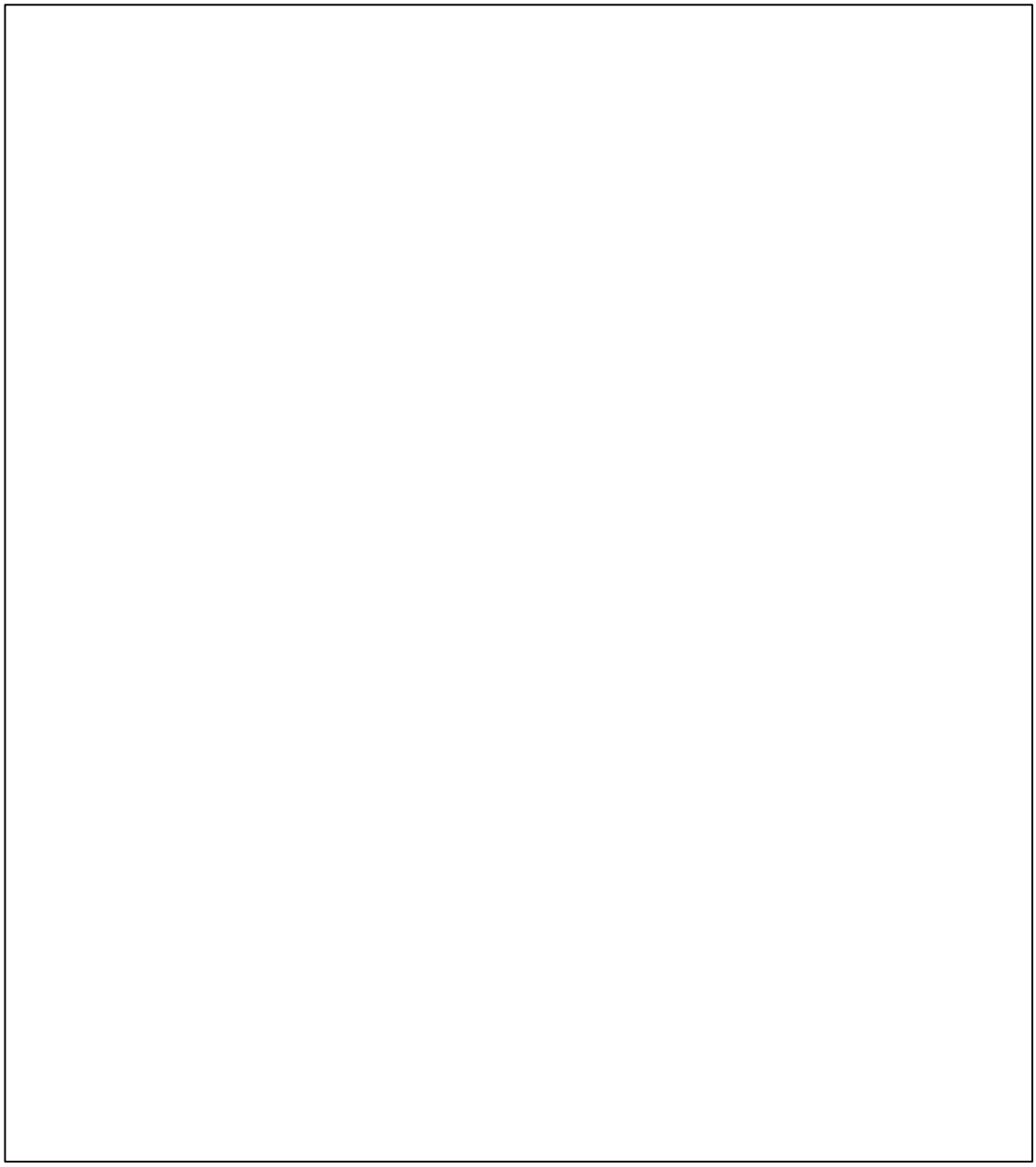

Figure I-2-12: Structure of the Spinach–DFHBI complex. (**A**) Sequence and secondary structure of Spinach–DFHBI. Thin lines denote chain connectivity and Leontis-Westhof symbols denote noncanonical base pairs. Numbering scheme for Spinach1.2 (65) is used. (B) Overall structure of Spinach-DFHBI complex. (C) Molecular surface of Spinach–DFHBI binding site showing the accessibility of external environment to DFHBI and A69 at the entrance. (D) Secondary structure of Baby Spinach. (D) View of the DFHBI binding site with *cis*-DFHBI bound (**E**) View of the DFHBI binding site modeled with *trans*-DFHBI in comparison with **(D)**. The *trans*-DFHBI exhibits steric clashes and fewer hydrogen bonds than *cis*-DFHBI. (**F**) Alternate orientation of *trans*-DFHBI modeled for comparison, also showing fewer favorable interactions than **(D)**. Source (66).

I. 2. 3 STORM

I. 2. 3. 1 Super-resolved fluorescence microscopy

For high-precision imaging inside cells, fluorescence microscopy with high performance is essential as well as development of the appropriate fluorescent probes. Due to the nature of light as a wave, the image of a point is spread on the detector by half of the wavelength, which makes the spatial resolution of 200-300 nm in conventional fluorescence microscopy. In order to overcome the diffraction limit, super-resolution optical microscopy has been developed. So far several super resolution techniques have emerged based on different strategies to achieve the spatial resolution of sub 100 nm: Saturated excitation (SAX) microscopy, Stimulated emission depletion (STED) microscopy and the microscopy using super localization method, which is commonly referred to as either Stochastic Optical Reconstruction Microscopy (STORM) (69) or (fluorescence) PhotoActivated Localization Microscopy ((F)PALM) (70). Erik Betzig, Stefan W. Hell and W. E. Moerner were awarded the Nobel Prize in Chemistry in 2014 for the development of these super-resolution fluorescence microscopy techniques. STORM used in this study is described in detail below.

I. 2. 3. 2 Principle of STORM

Photons from a point source will hit the microscope detector with spatial probability density determined by their point spread function (PSF) (Figure I-2-13 A). Neglecting background and pixelation, the probability density of photon detection in the lateral plane is approximately Gaussian (71) (Figure I-2-13 B). From the knowledge that the photon distribution on the detector stems from a point source, the center of the point spread function can be estimated with nanometer precision (72-74) (Figure I-2-13 C). This technique to obtain the position of a point source of photons is termed “super localization method”.

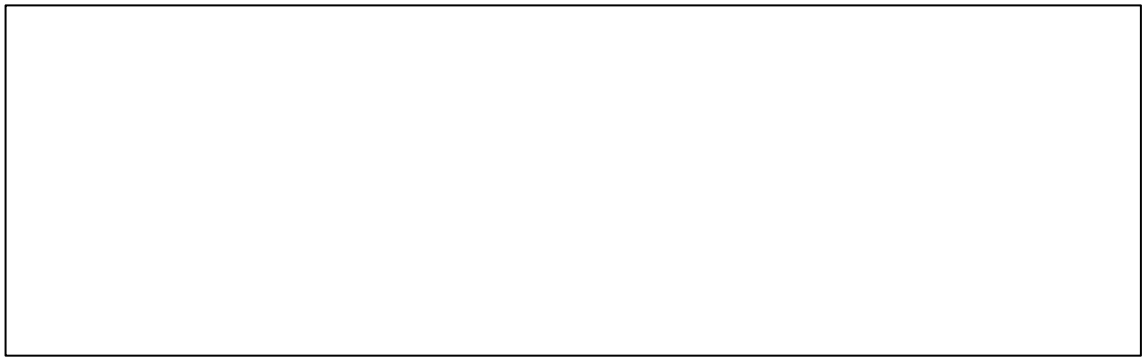

Figure I-2-13: (A) Pixelated fluorescence intensity from single fluorophore in x- and y-directions of the detector. (B) Fluorescence intensity in x-direction (grey bars) fitted to a Normal distribution

(red line). (C) Probability density of the center (x=0) of the Normal distribution in (B). The knowledge that there is a single emitter allows the position of the point source to be estimated much more precisely (C) than the width of the PSF (B). Source (71).

However if several fluorescent molecules are localized within an area corresponding to the diffraction limit and emit light at the same time, it is impossible to obtain the PSF from a single point fluorescent probe. Therefore super-resolved single-fluorophore microscopy using the localization method requires the active control of the concentration of the fluorescence emitter so as to have each emitter separated by larger distance than a diffraction limit. In order to respond to this requirement, photoswitchable probes that can be converted between fluorescent (on) and dark (off) states are used. The sequentially acquired images give positions of randomly activated fluorescent point source with an accuracy exceeding the diffraction limit of light. Eventually the positional information about theoretically all molecules in the structure of interest is combined to assemble a reconstruction of the fluorescent structure in one image (Figure I-2-14).

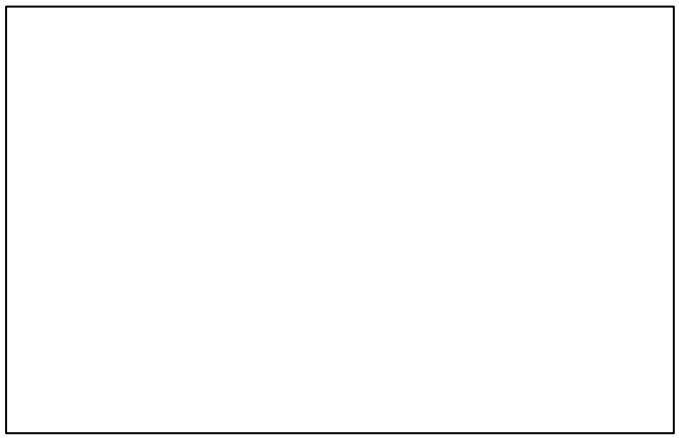

Figure I-2-14: Principle of STORM. A circular, sub-diffraction-limit-sized object is densely labeled with fluorophores. Exciting these fluorophores (shown as a solid circles) simultaneously results in the diffraction-limited case, where the circular feature is obscured. However, by turning on a single fluorophore, the position of that fluorophore (shown as a "+") can be determined by Gaussian fitting. The molecule is turned off and a different molecule is turned on. The process is repeated until sufficient localizations map the object structure (75).

I. 2. 3. 3 Photoswitchable fluorescent probe

This method depends on photoswitchable probes that can be converted between fluorescent (on) and dark (off) states. The photoswichable probes include both organic fluorescent dyes and fluorescent proteins.

Cy5 is one of the recommended probes for single color imaging together with Alexa 647. They are the highest performing reversible photoswitches to date (75). These dyes share the expected characteristics for use in STORM (Figure I-2-15): high photons, a low-Duty Cycle (<0.001) (Duty Cycle: fraction of time a molecule spends in the fluorescent state), high photostability, and a high number of switching cycles (75). Photoswitching to a dark state occurs upon illumination with red laser light, in the presence of specific chemical components: an oxygen scavenging system to reduce photobleaching, a primary thiol to induce photoswitching (76-78), and a buffer to maintain a stable pH (79). Different thiols derivatives and their concentrations can change the photoswitching properties of dyes (75). Activation from the dark state is either spontaneous or can be promoted by illumination with violet light.

I. 2. 3. 4 3D-STORM

The standard fluorescence microscopy's PSF contains little information about the axial (z) position of a single emitter. For extension to three-dimensional (3D) imaging, a variety of methods have been developed (Figure I-2-16 A): optical astigmatism (80) (ii), double-helix PSF (81) (iii), multifocal plane imaging (82) (iv) and interferometry (83) (v). For astigmatism-based 3D STORM used in this study, a cylindrical lens is inserted into the detection pathway to change the PSF shape in the x and y directions depending on the position of the fluorophore relative to the focal plane (Figure 2-3-4-B). The fluorescence image can then be fitted to an elliptical Gaussian function, where the centroid is used to determine the x–y position and the shape used to determine the z-position. Here, the achievable axial resolution for a single objective is 50–60 nm (80).

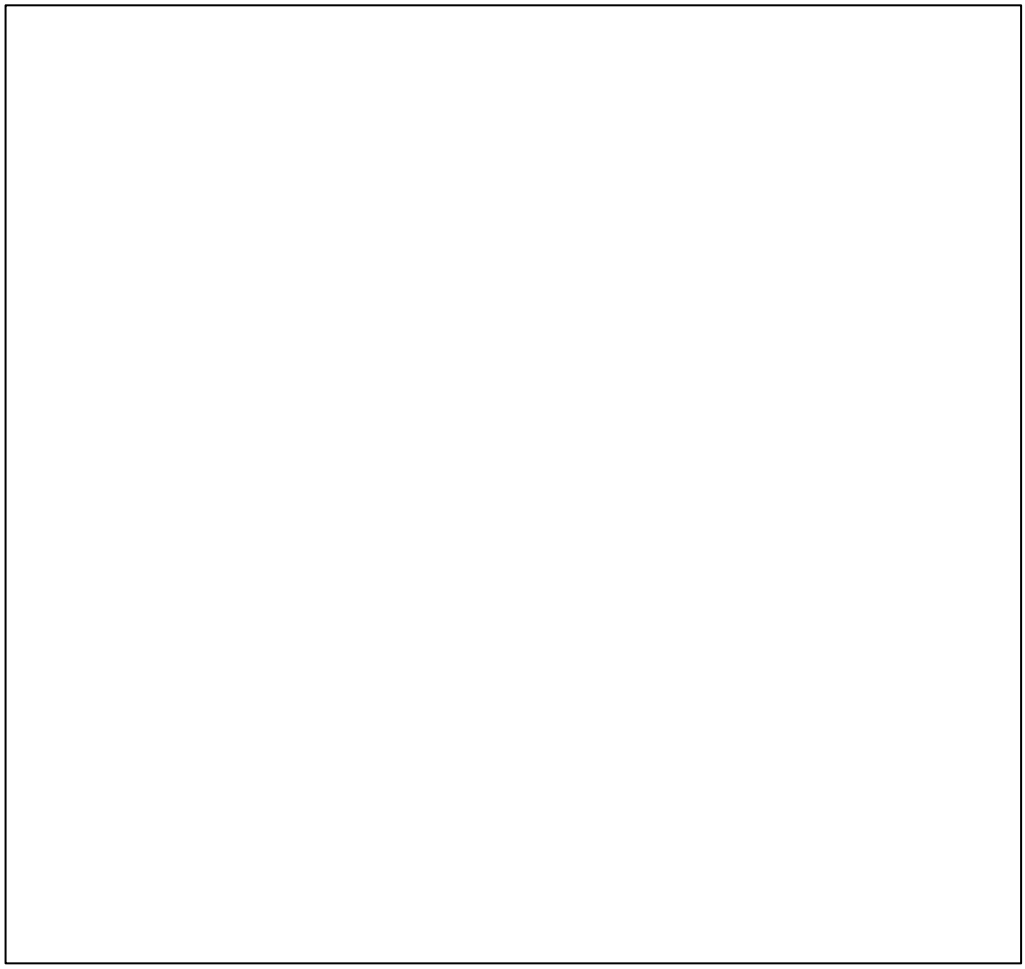

Figure I-2-15: Photoswitchable probe properties and their impact on STORM images. (A–D) A subdiffraction-sized circle is labeled with probes, whose positions are shown as stars. The fluorescence image is shown as a solid circle and the determined centroid as "+". (A) A probe with high photon number, low DC, and high photostability can resolve the circular feature of the object. (B) If the photon number is too low, the increased error in localizing each molecule will give the appearance of a filled rather than open circle. (C) If the DC is too high, the overlapping fluorescence images from having multiple molecules emitting per diffraction-limited spot will preclude the identification of any one probe. Achieving single-molecule density requires either reducing the labeling density or bleaching the sample, and a sufficient number of localizations can no longer be identified to resolve the circle. (D) Similarly, if the photostability is too low, a significant number of molecules will photobleach before being localized, leading to a sparse localization density (79).

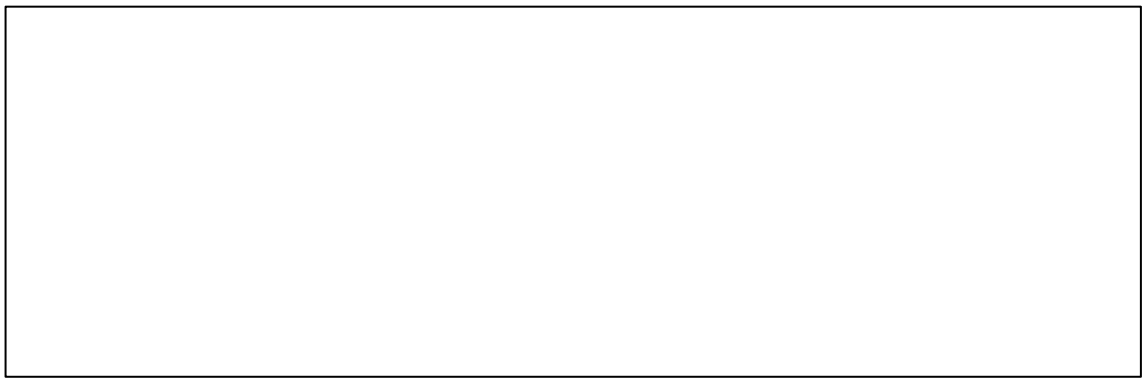

Figure I-2-16: 3D super-resolution fluorescence imaging. (A) To extract the location of individual single-molecule emitters with high precision in all three spatial dimensions, the symmetry of the standard microscope PSF (i) must be broken and the PSF re-designed to encode information in the z (axial) direction by a well-defined shape change. Widely adopted schemes include: (ii) an astigmatic PSF, where the slowly changing ellipticity of the single- molecule image can be calibrated to provide a z estimate. (iii) the double-helix (DH) PSF features two well-defined spots revolving around a common center as a function of z., (iv) bi-plane methods assess the relative detected brightness of images formed in two shifted image planes. (v) 4Pi axial localization methods rely on interferometric detection and two matched objective lenses to collect fluorescence from both sides of the sample (73). (B) Practical single-bead image taken at different z-positions with astigmatism-based 3D STORM. At z=0, the image is symmetric. At positions above and below the focal plane, the image becomes elliptical in the x and y directions, respectively. The image shape can be used to assign a z-position to each molecule.

I. 3 The ribosome: a major target for antibiotics

More than half of the antibiotics used in medicine target the ribosome. They bind to the functional sites of ribosomal RNA (Figure I-3-1) and either block or alter the translational machinery. These drugs have been very useful to dissect the mechanism of protein synthesis since a specific drug can affect each step. Here, in this work, I will focus on aminoglycosides.

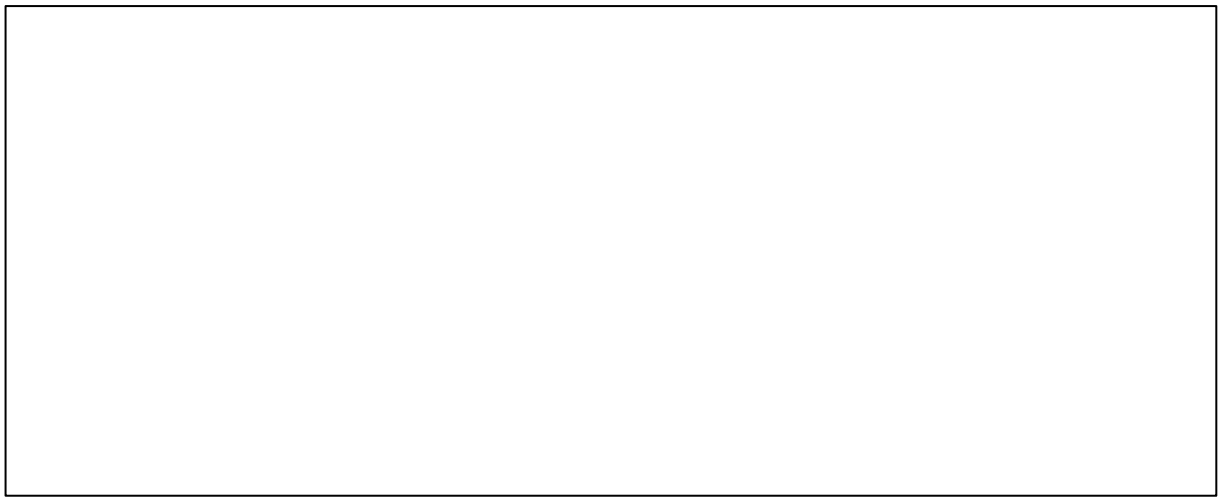

Figure I-3-1: Antibiotics target the functionally important regions of the ribosome. Figure is according to Poehlsgaard *et al*., (84).

I. 3. 1 Discovery, structure and the family

I. 3. 1. 1 Discovery of streptomycin

Aminoglycosides are a family of antibiotics that are composed of aminomodified sugars with large structural diversity (Figure I-3-2). The first aminoglycoside to be discovered as early as in 1943 by Selman Waksman and his student Albert Schatz is streptomycin that is produced by *Streptomyces griseus*. It is also the first antibiotic that was found to be active against *Mycobacterium tuberculosis*. This discovery was of strong importance and Selman Waksman received the Nobel Price of Medicine in 1952. This was the beginning of a new field of research but also initiated the use of aminoglycosides in medicine. These drugs have toxicity to kidneys and auditory hair cells but nevertheless, they represent an important part of the antibiotic arsenal and are largely used to treat bacterial infection worldwide (85,86).

I. 3. 1. 2 Structural characteristics

Later on, many other aminoglycosides were discovered and among them is the class of

neomycin. The neomycin family shares a common core of rings I and II that are conserved. On the contrary streptomycin lacks a common 2-deoxystreptamine moiety (conserved ring II) that is present in many other class members.

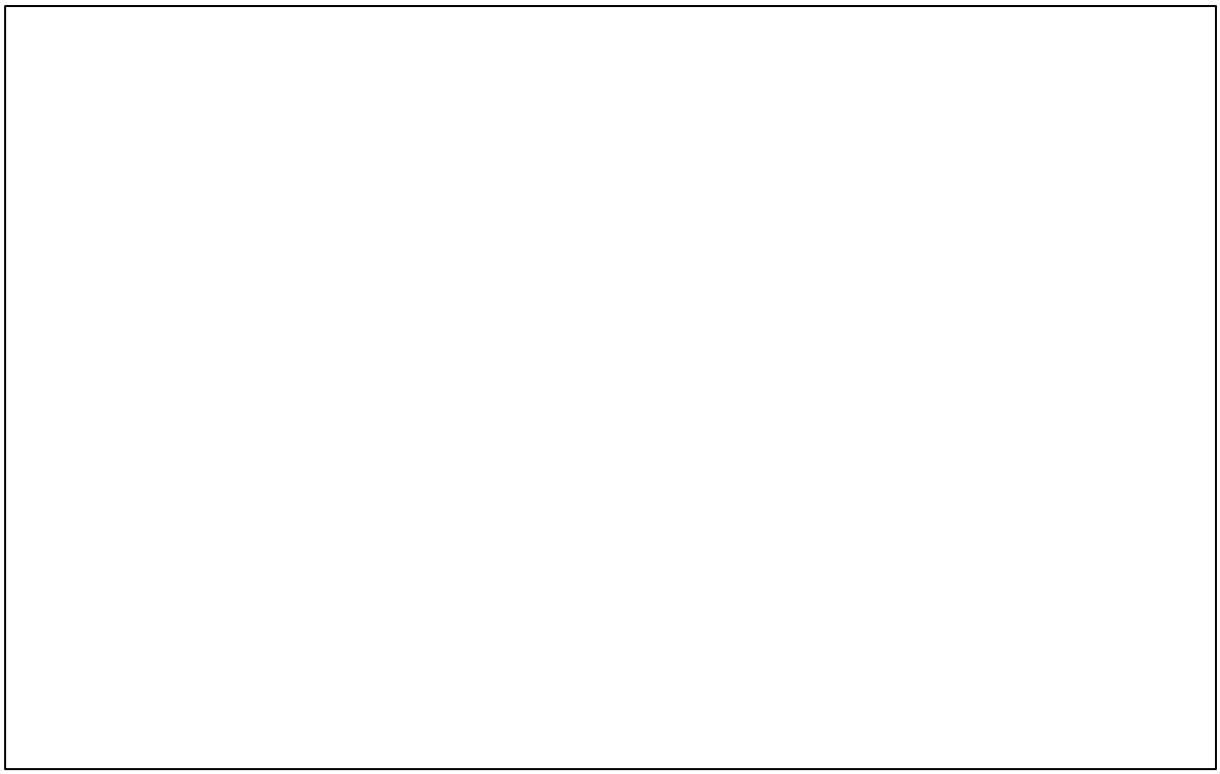

Figure I-3-2: Structure of aminoglycoside family. Top panel displays some aminoglycosides of the neomycin family. Rings are numbered and the chemical structure of variable positions indicated. Ring II is made of deoxystreptamine and is very conserved. The panel at the bottom shows the structure of streptomycin, the first aminoglycoside to be discovered.

I. 3. 2 Mechanism of the antibiotic action

I. 3. 2. 1 Aminoglycosides and their mode of action

They are one of the most characterized antibiotics and bind both subunits of the ribosome causing miscoding or inhibiting translocation and recycling (34,87,88). The well-characterized neomycin aminoglycosides have been shown to accelerate both forward reaction rates (GTPase activation and accommodation) in tRNA selection and to reduce the rate of cognate and near-cognate tRNA dissociation from A site (87,89). These drugs are translocation inhibitors (88,90), and also promote back-translocation (91-93).

Majority of aminoglycosides bind within an internal loop in helix 44 (h44) of the 30S subunit that mainly forms the decoding site (94). This interaction has been characterized biochemically by chemical probing (95,96) and also structurally in complexes of aminoglycosides bound to small RNA fragments mimicking h44 (97-101). Also, the mechanism of decoding and the action of aminoglycosides at the decoding center have been the subject of very intense studies by ribosomal X-ray crystallography (7,12,94,102-104). The binding of aminoglycosides stabilizes nucleotides A1408, A1492, and A1493 in a conformation that is distinct from that observed in the absence of the drug (Figure I-3-4). Moreover, the antibiotic favors the destacking of A1492 and A1493 (nucleotides critical for A-site tRNA binding (105)) from h44 into a position where they interact with the codon-anticodon helix. An X-ray study of the *Escherichia coli* ribosome revealed that paromomycin has a second binding site in helix 69 (H69) of 23S rRNA (106) (Figure I-3-3). A recent work shed light on the action of aminoglycosides at the decoding center and H69 however the interplay between these two proximal sites remains unknown (107). Based on some recent and unexpected results on the 70S crystal structures in complex with mRNA and tRNAs, a new model was proposed for the recognition of the codon-anticodon helix by the decoding center with new insights into the interaction of paromomycin (108,109). In this model the antibiotic partially induces a conformation of rRNA around the decoding center similar to that observed for cognate tRNA.

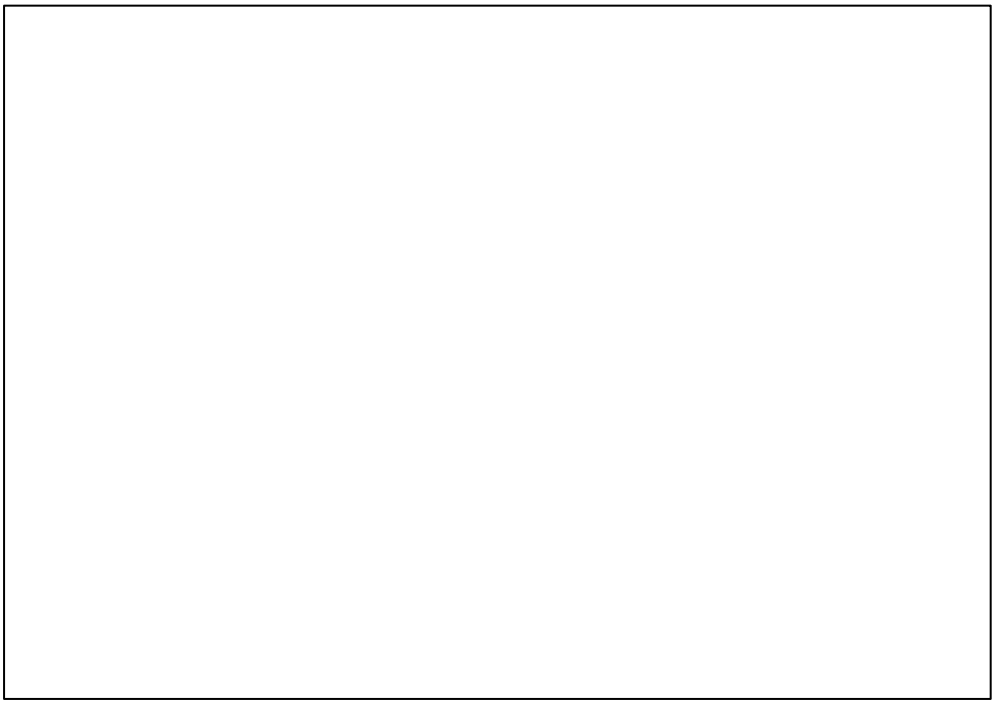

Figure I-3-3: Panel from figure 2 of the manuscript by Demeshkina *et al*., (108). Paromomycin (green) is bound into the decoding site on 16S rRNA. The tRNA is displayed in red and mRNA in yellow. The differences between complexes formed with near-cognated tRNA in presence and absence of paromomycin are highlighted.

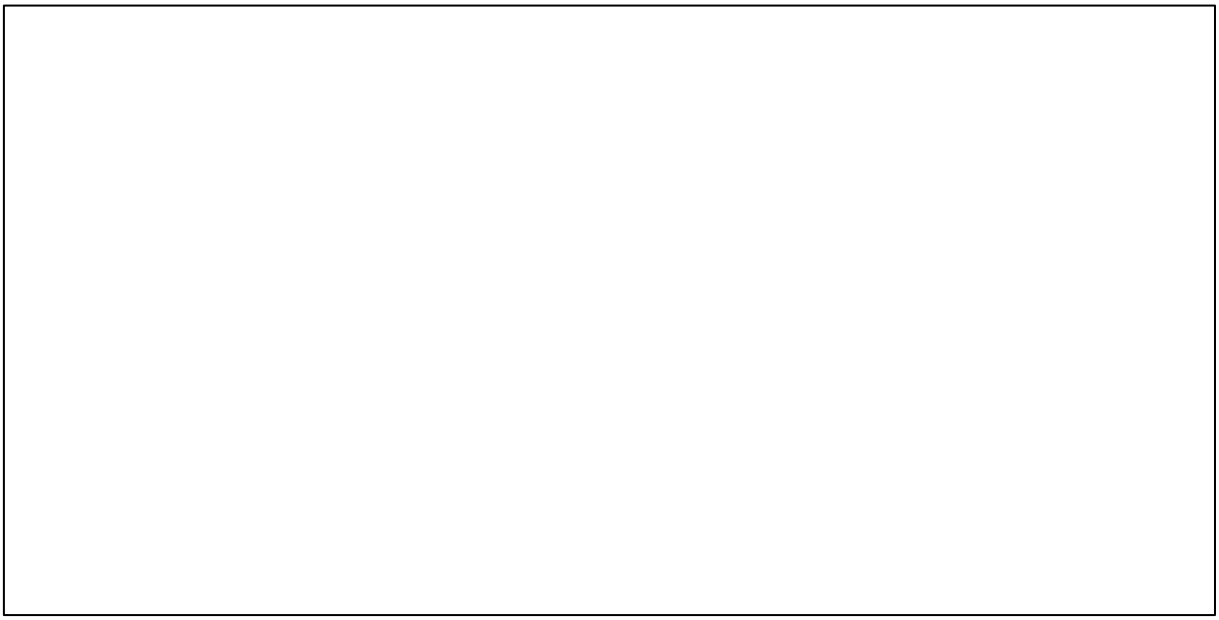

Figure I-3-4: Panel from figure 3 of the manuscript by Wang *et al*., (107). (A) Bound neomycin (Neo) molecules are displayed. One molecule is bound to the decoding site (h44) in the 16S rRNA and a second molecule interacts with H69 of 23S rRNA on the 50S subunit. (B) Details of the

binding pocket in H69 are highlighted.

Once in the cytoplasm, the bactericidal effect of aminoglycosides is thought to result from misreading of mRNA and misfolding of membrane proteins (110,111). Aminoglycosides cause misreading on only a subset of near-cognate codons and therefore their effect may be less general than previously thought (112). It was proposed that this process leads to oxidative stress and cell death (110,113,114). However, it should be reminded that ram (ribosome ambiguity mutations) *E. coli* strains that have single amino-acid mutations of the ribosomal proteins S4 and S5, which cause comparable levels of misreading as aminoglycosides, are viable (115). It is therefore unclear whether miscoding leads to cell death via oxidative stress or not. In line with this observation, it was shown that Fe-S proteins promote aminoglycosides induced cell death without the involvement of the reactive oxygen species (ROS) response (116). Keren *et al.,* also proposed that ROS is not involved in antibiotic mediated cell death (117). More recently, a study with more robust assays that supports the ROS response was reported (118). This illustrates the difficulties in characterizing the responses induced by antibiotics and in fact much remains unclear.

Genome wide studies about aminoglycoside action are emerging. For instance, the laboratory of Colin Manoil used a deep-sequencing procedure (transposon sequencing Tn-seq (119)) for monitoring large numbers of transposon mutants of *Pseudomonas aeruginosa* (120). This method allowed screening for mutations reducing intrinsic resistance of *P. aeruginosa* to the aminoglycoside tobramycin. The authors identified several genes including genes involved in envelope stress response pathways, which may help protect cells from aminoglycoside-induced mistranslated proteins that would disrupt the membrane (121). A more recent study by the laboratories of Kim Lewis and Andrew Camilli advanced our understanding of the genetic basis of antibiotic tolerance by applying Tn-seq to identify several pathways involved in gentamicin tolerance (122). In particular, their findings suggest that in stationary phase, the activation of flagellar motility and biosynthetic pathways decrease the cellular energy state and thus highly diminish gentamicin sensitivity.

I. 3. 3 Mechanism of the uptake

I. 3. 3. 1 Three steps in aminoglycoside uptake

It is thought that accumulation of aminoglycosides by bacteria growing in aerobic conditions occurs in three consecutive phases (123,124) (Figure I-3-5).

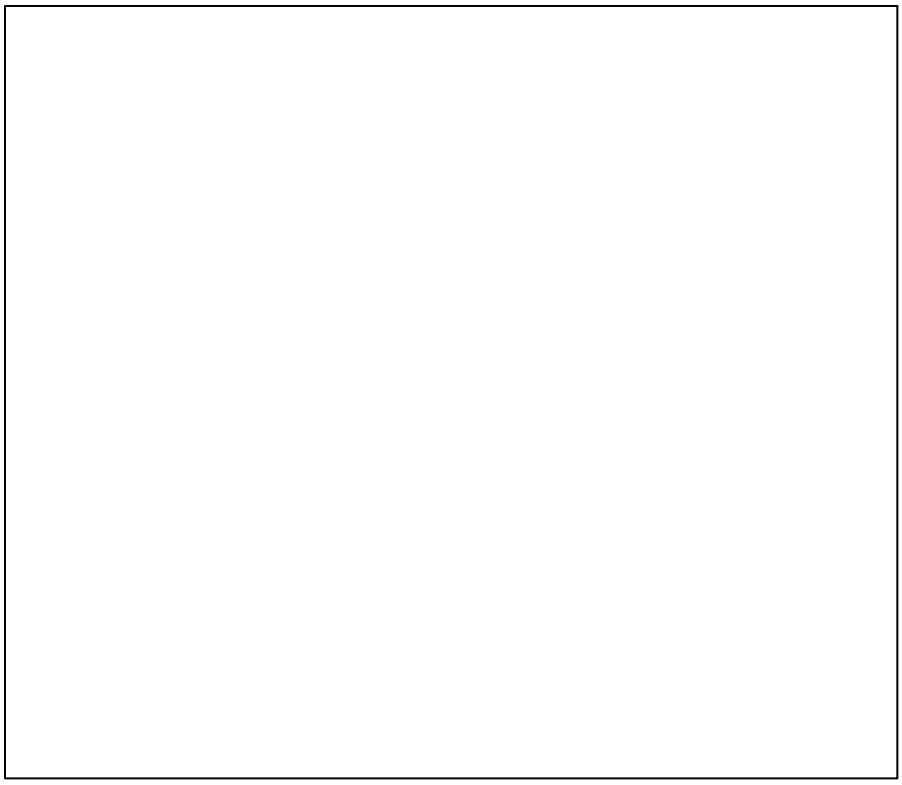

Figure I-3-5: This panel is adapted from Anand et al., (125). Cells were incubated with radiolabeled streptomycin (SM) and filtrated to measure the accumulation (or adsorption) of the aminoglycoside in *E. coli* cells. Our current understanding of aminoglycoside uptake is represented in color with step 1, the energy-dependent phase I (EDPI) and energy-dependent phase II (EDPII). EDPI (blue) in the original data was hidden by step 1 where aminoglycosides (AG) bind to the bacterial cell wall. The addition of chloramphenicol (indicated by "+CE") two minutes before adding streptomycin inhibits EDPII (orange). This phase is again active if toluene, that triggers membrane permeabilization, is added. This shows that active protein synthesis is necessary for EDPII.

i) Electrostatic binding:

First the drugs would bind to anionic sites at the membrane instantaneously and in a reversible way. It was also proposed that lipopolysaccharide (LPS) would directly interact with the polycationic aminoglycosides thereby facilitating their uptake (126). Therefore, a self-promoted uptake mechanism for aminoglycosides was favored in terms of hypothesis rather than a mechanism involving porin channels (127) (Figure I-3-6). In this mechanism, the antibiotic interacts with the outer cell wall and this interaction increases the permeability of this cell wall to the antibiotic. This step would be followed by two irreversible energy dependent phases termed energy-dependent phase I and II (EDPI and EDPII, respectively) (Figure I-3-5).

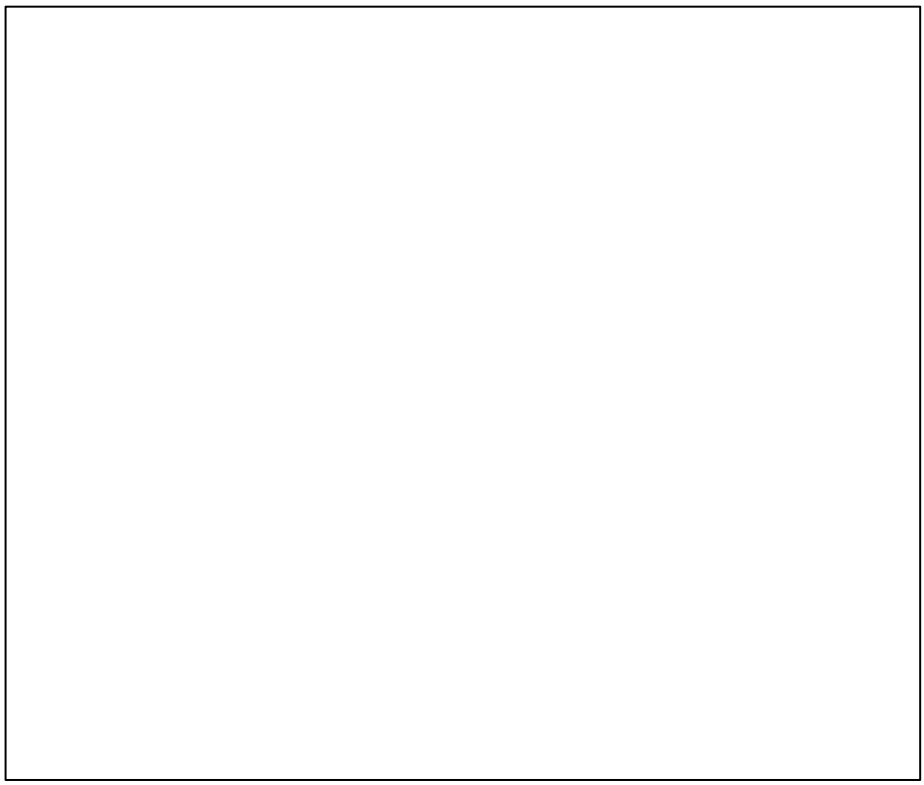

Figure I-3-6: This panel is adapted from Hancock and Bell (128). The two possible routes are indicated: porins or the polycationic path. Binding of divalent cations (Ca^{2+}, Mg^{2+}) interferes with aminoglycoside accumulation possibly by blocking the polycationic route. Lipopolysaccharides are labeled LPS.

ii) Energy-dependent phase I :

The first step is followed by EDPI that varies in its duration and rate depending on the antibiotic concentration used. It was also noticed a relation between the growth rate of bacteria prior to the addition of the antibiotic (129). Bacteria that are in exponential phase were found to be very efficient in antibiotic accumulation. On the contrary, cells that are in the stationary phase are poorly sensitive to aminoglycosides. EDPI occurs very early, before inhibition of protein synthesis and death. EDPI can be blocked by inhibitors of electron transport such as carbonyl cyanide-m-chlorophenyl-hydrazone (CCCP). The mechanism of transport of aminoglycosides across the cytoplasmic membrane is poorly characterized and may involve quinone-linked redox energy or other components of the electron transport chain or both. Aminoglycosides may also initially enter by nonspecific membrane channels created by low-level intrinsic misreading or some imperfections in the cytoplasmic membrane in particular in the area of growth where the membrane is being made (130). Finally, in 1987, it was still unclear if the phase EDPI was not the result of progressive binding of aminoglycosides to the external cytoplasmic membrane (124,131). In fact, to

date much remains unknown about the phase EDPI.

iii) Energy-dependent phase II :

The third phase remains also unclear. It requires energy from the electron transport chain and ATP hydrolysis however has diffusion kinetics (132). The phase EDPII requires aminoglycoside sensitive ribosomes, and inhibitors of protein synthesis such as chloramphenicol can abolish EDPII (125) (Figure I-3-5). It is thought that miscoding by aminoglyclosides that entered the cytoplasm during EDPI produces membrane proteins that are misfolded and lead to membrane permeabilization. Addition of chloramphenicol before incubating with streptomycin blocks protein synthesis and therefore would prevent permeabilization of the membrane abolishing EDPII (Figure I-3-5). This permeabilization has been observed by the leakage of amino acids, nucleotides or K^+ (133-136) and bacteria observed after treatment with streptomycin (137) had a collapsed appearance in scanning electron images.

I. 3. 4 Fluorescent derivatives of aminoglycosides: state of the art

As described above, most of our knowledge on aminoglycoside accumulation in bacteria comes from early studies that used radiolabeled aminoglycosides (124,125,138). However, bacteria grow and divide asynchronously. Therefore, in order to follow the dynamics of aminoglycosides action, a fully active fluorescent derivative with conserved uptake and bactericidal activities would allow real time monitoring of their action at the single cell level.

I. 3. 4. 1 Texas-Red gentamicin

A Texas Red conjugate of gentamicin (Gent-TR) has been described (139) that is often used on eukaryotic cells. The laboratory of James Collins used this compound to nicely identify specific metabolites that stimulate the proton-motive force and enable killing of dormant bacteria or persisters (140). However this conjugate may suffer some drawbacks for studying the effect of aminoglycosides on bacteria for the following reasons that will also be discussed in chapter III:

1) Gent-TR is prepared by mixing an excess of gentamicin to Texas Red (TR) without any subsequent purification of the gentamicin-TR compound. Among the different amine groups, the primary amine at position 5' of ring I is the most reactive placing the dye at this position. However, ring I (in particular position 5') establishes critical contacts with the ribosomal decoding site (7,97,98). In addition, single and di-methylation at this position decrease affinity for the decoding site (98). If placed in the structure of the ribosome bound to gentamicin, the Texas Red probe would protrude out of the minor groove of rRNA helix 44,

in the site of the codon-anticodon interaction, thereby directly preventing the reading of the genetic code (Figure I-3-2). Therefore, gentamicin-TR might not be an active aminoglycoside causing miscoding and was used as a tracer for monitoring uptake.

2) In the work by Allison *et al*., FACS was used to measure the level of uptake of Gent-TR (140). Authors also checked the uptake of the Texas Red probe (see supplementary figure 11 in (140)). However it is important to notice, in the work, that Texas Red presents a high level of uptake. This does not influence the conclusions of the work by Allison and co-workers since they were based on relative changes. The laboratories of Kim Lewis and Andrew Camilli also used very recently Gent-TR for a FACS analysis of persisters (122). Thus, for studying localization and effects of aminoglycosides at the single cell level, the Gent-TR cannot be used.

Chapter II

A strategy for identifying a robust Spinach aptamer for live-cell imaging

II. 1 Design of Spinach-ribosome for ribosome visualization

Our goal was to develop a robust system for imaging ribosomes in bacteria. The strategy differs from what is performed usually for ribosome visualization where either a ribosomal protein is fused to a fluorescent protein (141,142) or the technique of fluorescence *in situ* hybridization (FISH) is used on fixed cells (143). These approaches do not allow observing for instance a specific population of ribosomes translating an mRNA in real time. For reaching such a goal, one needs to label the ribosomal RNA and apply it to specialized ribosomes that only translate specific mRNAs (144). The advantage of specifically tagging specialized ribosomes would be to only observe the localization of these ribosomes and not to be disturbed by the bulk ribosomes contained in the cell (which in this case are not fluorescent). Unlike mRNA that has untranslated regions, rRNA forms the structure of the ribosome and needs to interact with many proteins and RNA. Therefore, fluorescent tagging of the ribosome should be performed carefully so as not to interfere with its structure and its function. We have chosen the first aptamer-fluorogen complexe that has been developed that elicits fluorescence at different wavelengths: Spinach (63,145). Here, Spinach RNA sequences were introduced into helix 33a of 16S rRNA (Figure II-1A) where we substituted the UUCG tetraloop by Spinach RNAs. The helix is not involved in any tertiary interaction and protrudes outside the ribosome structure (Figure II-1B). This region of 16S rRNA is not phylogenetically conserved (146) and extension of the helix does not perturb *E. coli* ribosomal function (147).

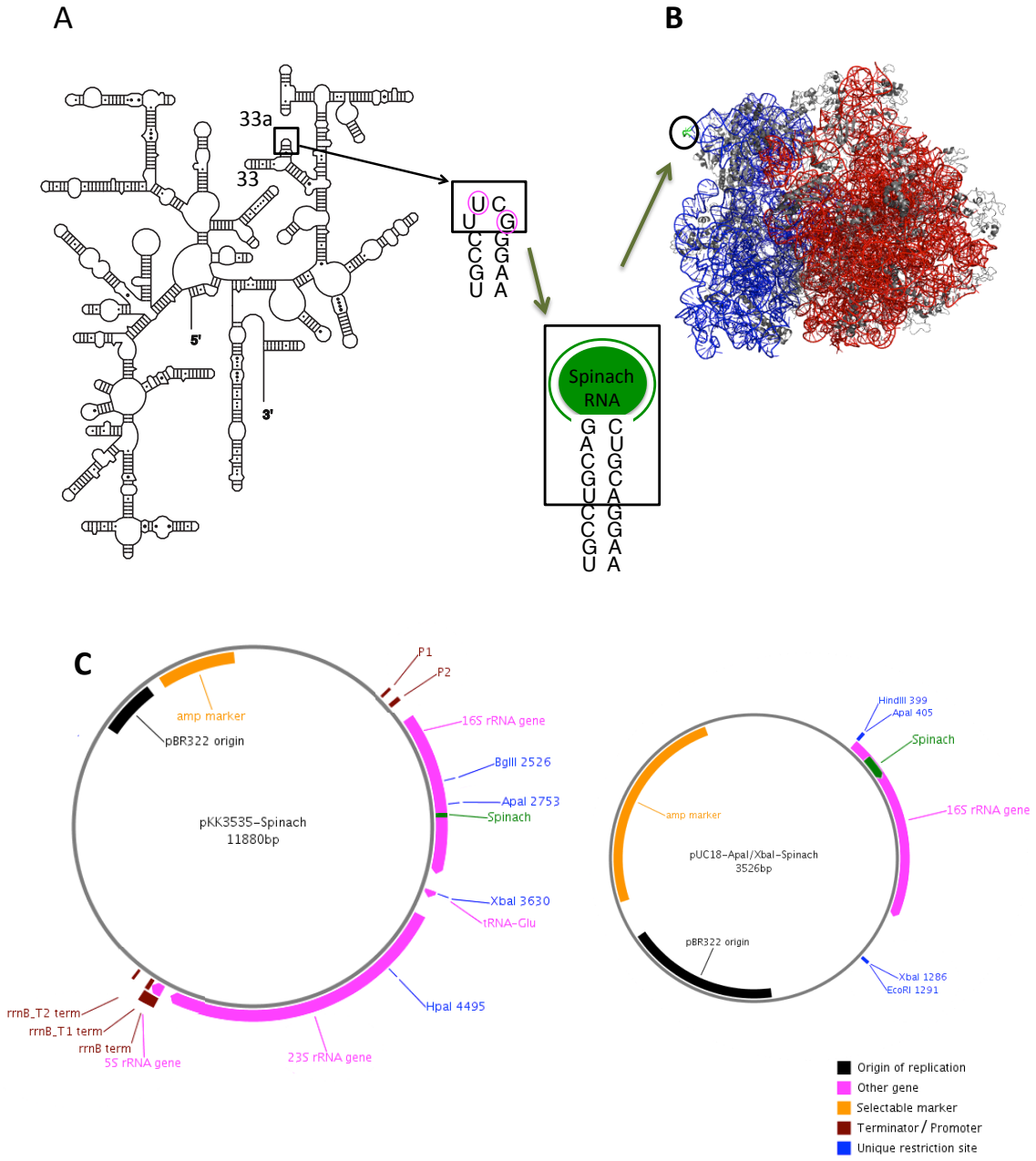

Figure II-1: (A) Insertion site of Spinach sequences into 16S rRNA. Secondary structure of 16S rRNA. The site of insertion is boxed. Ribosomal helices 33 are labeled. (B) Side view of 70S ribosome where the tip of h33a has been highlighted. 16S and 23S rRNA molecules are respectively in blue and red. Bases T1030G and G1032A that were modified to introduce the PstI site are circled. (C) Maps of pUC and pKK3535 vectors designed in this study.

II. 1. 1 Plasmid construction

We developed our version of vector pKK3535 for expressing fluorescently labeled ribosome (Figure II-1C). pKK3535 plasmid carries the wild-type rrnB rRNA operon under the control of the native constitutive promoter P1P2 (148). The *ApaI/XbaI reg*ion of in 16S rRNA gene was subcloned from pKK3535 into Hind III/ EcoR I site of pUC18 (pUC18-ApaI/XbaI). Pst I site was created in the loop of h33a by substitution of two base, T1030G and G1032A (Figure II-1A), using site-directed mutagenesis kit (pUC18-ApaI/XbaI-PstI). Spinach sequences were amplified with PCR using primers designed to possess extra 15 bases in the 5' end that are homologous to the host vector and were inserted into PstI site of pUC18-ApaI/XbaI-PstI (pUC18-ApaI/XbaI-Spinach, Figure II-1C left). The ApaI/XbaI fragment with an insertion of Spinach was put back into pKK3535 that is a vector for ribosome expression (pKK3535-Spinach, Figure II-1C right).

II. 2 Spinach family

Since the first publication (63) that introduced DFHBI and RNA aptamer24-2, which is now termed Spinach, the improvement of Spinach sequence has continued by mutagenesis and from a structural point of view. In this study, we tested eight sequences, including the original Spinach, for their properties as a fluorescent tag in a structured cellular RNA, the ribosomal RNA. The goal was to compare their performances in terms of fluorescence and resistance to degradation and identify a robust system.

II. 2. 1 RNA aptamer (Spinach) sequence

The sequences and secondary structures of Spinach used in this study are summarized in table II-1 and Figure II-2. Spinach1 is the first sequence found as an RNA aptamer able to activate DFHBI fluorescence. Spinach was modified to generate Spinach1.2 with more structural stability by removing some bases and substituting G-C pairs for some A-U or G-U pairs (Figure II-2). In addition, generation of spinach2 was reported (65), which showed the best fluorescence properties when in complex with DFHBI among all Spinach. In the process of improvement for structural stability, a longer version of Spinach1.2 was designed to contain a chimera of the human $tRNA^{Lys3}$ scaffold (tSpinach1.2) (63,149) (Figure II-2). On the opposite, a miniaturized version of Spinach has been developed. 18 bases in P3 stem and J1-2 junction were truncated from Spinach to create Spinach-mini, which still maintains 90 % of original Spinach fluorescence (63). I designed spinach2-mini as a truncated version of Spinach2 to harbor the same structural characteristics as

Spinach-mini. Recent crystal structure analysis of Spinach1.2 in complex with DFHBI revealed the structural bases for fluorescence, which allowed to generate a minimized version of Spinach, named Baby Spinach. In my study, as a trial model of further smaller Spinach miniaturization, mBaby Spinach was designed by removing 4 base pairs from P3 stem of Baby Spinach (Figure II-2).

Table II-1: Spinach sequence

Name	**Sequence**
Spinach (98-nts)	GACGCAACUGAAUGAAAUGGUGAAGGACGGGUCCAGGUGU GGCUGCUUCGGCAGUGCAGCUUGUUGAGUAGAGUGUGAGC UCCGUAACUAGUCGCGUC
Spinach-mini (80-nts)	GACGCGACCGAAAUGGUGAAGGACGGGUCCAGUGCUUCGG CACUGUUGAGUAGAGUGUGAGCUCCGUAACUGGUCGCGUC
Spinach1.2 (95-nts)	GACGCGACCGAAUGAAAUGGUGAAGGACGGGUCCAGCCGG CUGCUUCGGCAGCCGGCUUGUUGAGUAGAGUGUGAGCUCC GUAACUGGUCGCGUC
tSpinach1.2 (153-nts)	GCCCGGAUAGCUCAGUCGGUAGAGCAGGACGCGACCGAAU GAAAUGGUGAAGGACGGGUCCAGCCGGCUGCUUCGGCAGC CGGCUUGUUGAGUAGAGUGUGAGCUCCGUAACUGGUCGCG UCGUCCAGGGUUCAAGUCCCUGUUCGGGCGCCA
Spinach2 (95-nts)	GAUGUAACUGAAUGAAAUGGUGAAGGACGGGUCCAGUAG GCUGCUUCGGCAGCCUACUUGUUGAGUAGAGUGUGAGCUC CGUAACUAGUUACAUC
Spinach2-mini (80-nts)	GAUGUAACUGAAAUGGUGAAGGACGGGUCCAGUGCUUCGG CACUGUUGAGUAGAGUGUGAGCUCCGUAACUAGUUACAUC
mBabySpinach (35-nts)	AAGGACGGGUCCGUUCGCGUUGAGUAGAGUGUGAG
Baby Spinach (43-nts)	AAGGACGGGUCCAGUAGUUCGCUACUGUUGAGUAGAGUGU GAG

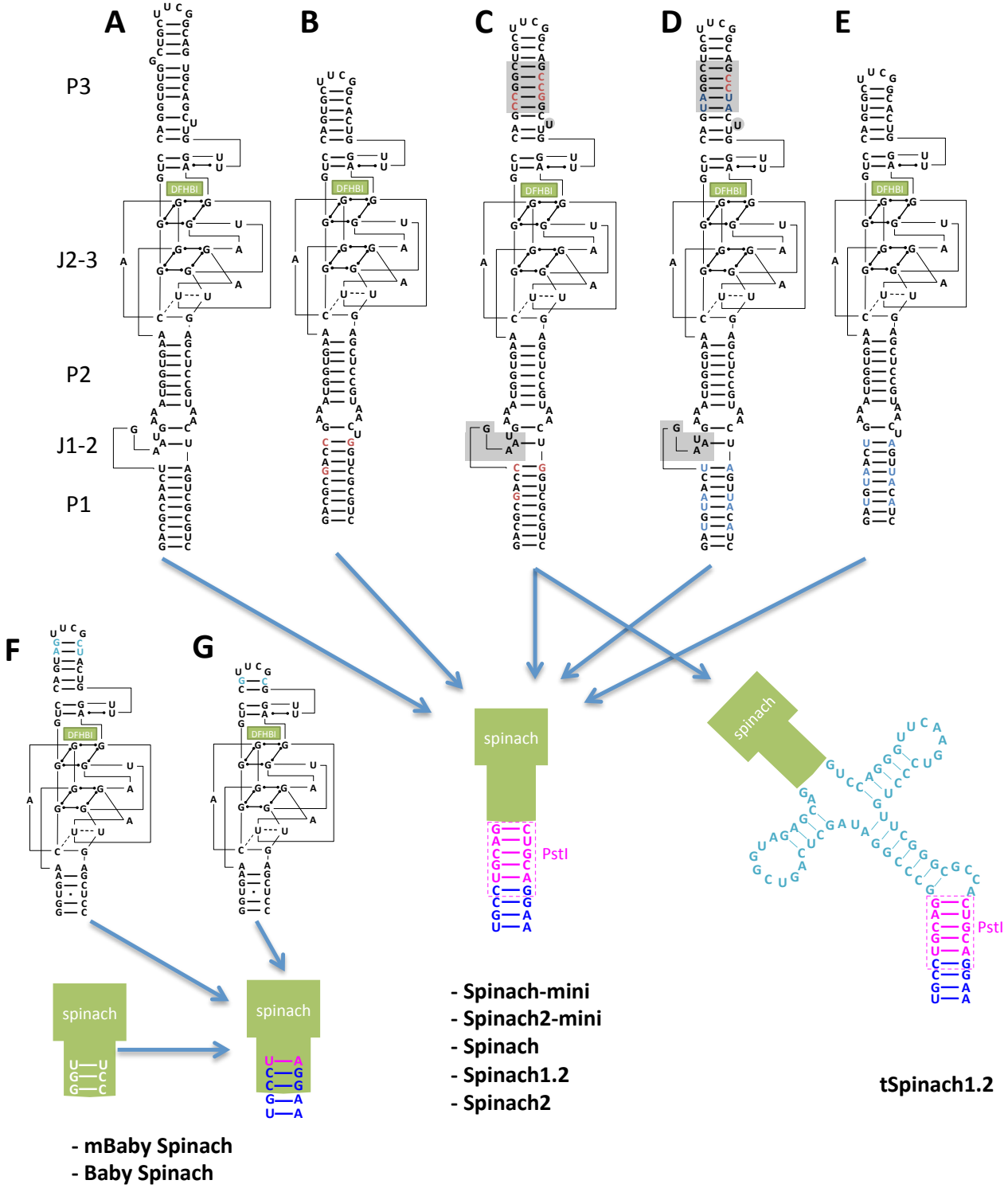

Figure II-2: Spinach secondary structures (A) Spinach (B) Spinach-mini (C) Spinach1.2 (D) Spinach2 (E) Spinach2-mini (F) Baby Spinach (G) mBaby Spinach. Spinach sequences are classified according to the type of constructs. DFHBI is highlighted in green. Grey boxes are the bases deleted in the "mini" versions of Spinach and Spinach2. Red bases are the mutation done to transform Spinach as Spinach1.2. Blue base pairs are specific bases of Spinach2.

II. 3 Fluorescence test of Spinach RNA transcripts

Before to study the Spinach sequences in the context of the ribosome we first investigated the level of fluorescence for each aptamer constructs in previously used buffers (65,66) and in the ribosome buffer (20 mM Tris-HCl (pH7.5), 100 mM NH_4Cl, 10 mM $MgCl_2$, 0.5 mM EDTA, 6 mM 2-mercaptoethanol) supplemented by 0.125 M KCl. Transcripts included helices 33a and 33 of 16S rRNA and thereby closely resemble the ribosomal context. Transcripts were generated by *in vitro* T7 transcription and purified by Dr. Satoko YOSHIZAWA. The RNAs were folded by a snap cool step. The crystal structure of Spinach revealed that K^+ and Mg^{2+} are part of the structure of folded DFHBI-Spinach complex (66,68). For this reason, buffers used for Spinach fluorescence assays contained these cations.

In the HEPES-KOH buffer used to describe the Spinach2 construct (65), at a ratio DFHBI/RNA of 2:1, three constructs, Spinach, Spinach-mini and Spinach2-mini performed 3 times better than other constructs (Figure II-3A). At a ratio of 100:1, differences narrowed down except for tSpinach1.2 that remained at 20% of the level measured for most of the other constructs. In a ribosome buffer supplemented by KCl, the same distribution was observed with also a leveling of the values in presence of a 100x excess of DFHBI (Figure II-3B). Levels of fluorescence were almost identical to the one measured in the HEPES buffer indicating that the ribosome buffer is also suitable for performing fluorescence assays of Spinach. Comparison of the effect of excess of DFHBI on the fluorescence levels for all constructs (Figure II-3C) shows that the differences are strong in the HEPES buffer whereas in the ribosome buffer excess of 2x or 100x of DFHBI poorly improved fluorescence. This suggests that Spinach constructs fold best in ribosome buffer supplemented with KCl.

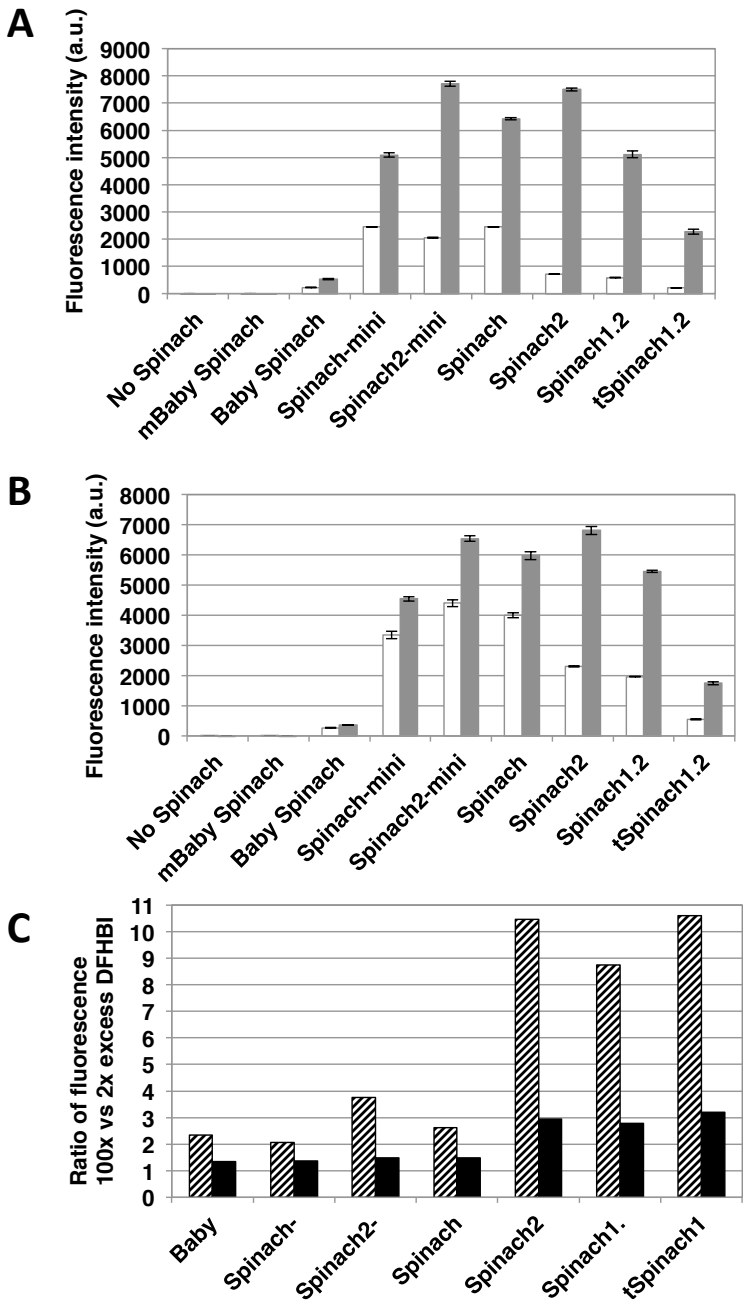

Figure II-3: Comparative analysis of the different Spinach transcripts. Levels of fluorescence of Spinach-DFHBI complexes were measured at 25°C from purified RNAs (0.1µM) with an excess of DFHBI (white bars 2x fold or grey bars 100x fold). A large excess of DFHBI ensures that the fluorescence is strongly dependent on the amount of RNA that is folded and can bind the fluorogen. A: HEPES buffer B: ribosome buffer. C: Comparison of fluorescence levels with 100x and 2x excess of DFHBI in HEPES buffer (grey bars) or ribosome buffer (black bars). Error bars are s. e. m. for three independent experiments.

We noticed that in the case of Baby, signals were surprisingly low. Therefore the RNA was refolded by a snap cool step followed by a slow decrease in temperature to improve refolding (66). Fluorescence levels were markedly improved and best in the Tris-HCl and ribosome buffer both containing Tris-HCl (Figure II-4A). The results indicate that baby Spinach needs a step of slow cooling for efficient folding. Since the 2-steps refolding improved the fluorescence levels for Baby Spinach, the other constructs were also subjected to this folding protocol (Figure II-4B). For all transcripts, the levels of fluorescence increased by at least 30% except for tSpinach1.2 sequence for which a large increase of 4 fold was observed. Finally tSpinach1.2 achieved fluorescence as high as Spinach1.2. It is reasonable as they share the same sequence of whole spinach except for existence of scaffold tRNA-like structure. It suggests one possibility that improper folding of the scaffold structure in tSpinach1.2 reduced its fluorescence in the other conditions. The efficiency of Baby Spinach folding remained inferior to all other Spinach aptamers.

The original ribosome buffer used for preparation of ribosome does not contain KCl. The importance of KCl was already reported using Spinach2 sequence (65). So here, we examined the extent to which the absence of KCl reduced fluorescence levels for all Spinach transcripts. We were expecting a substantial reduction of fluorescence because of the absence of KCl, so higher concentration of transcript (0.5 μM) was mixed with 1 μM (2x) DFHBI for measurement. Fluorescence levels were measured in ribosome buffer with (Figure II-5A) or without KCl (Figure II-5B), and then the ratio was calculated (Figure II-5 C). Spinach-mini, Spinach2-mini and Spinach were increased by 20-30 fold, while the others (Baby, Spinach2 and Spinach1.2 and tSpinach1.2) were increased by 40-60 fold. The rate of increase of Spinach2 agrees with the published data that the fluorescence in buffer containing 0.125 KCl and 5 mM $MgCl_2$ was 65 times higher than that in buffer containing 46 mM $MgCl_2$ (65). These results suggest that the best three (Spinach-mini, Spinach2-mini and Spinach) can fold to some extent independently from K^+ compared to the other Spinach sequences.

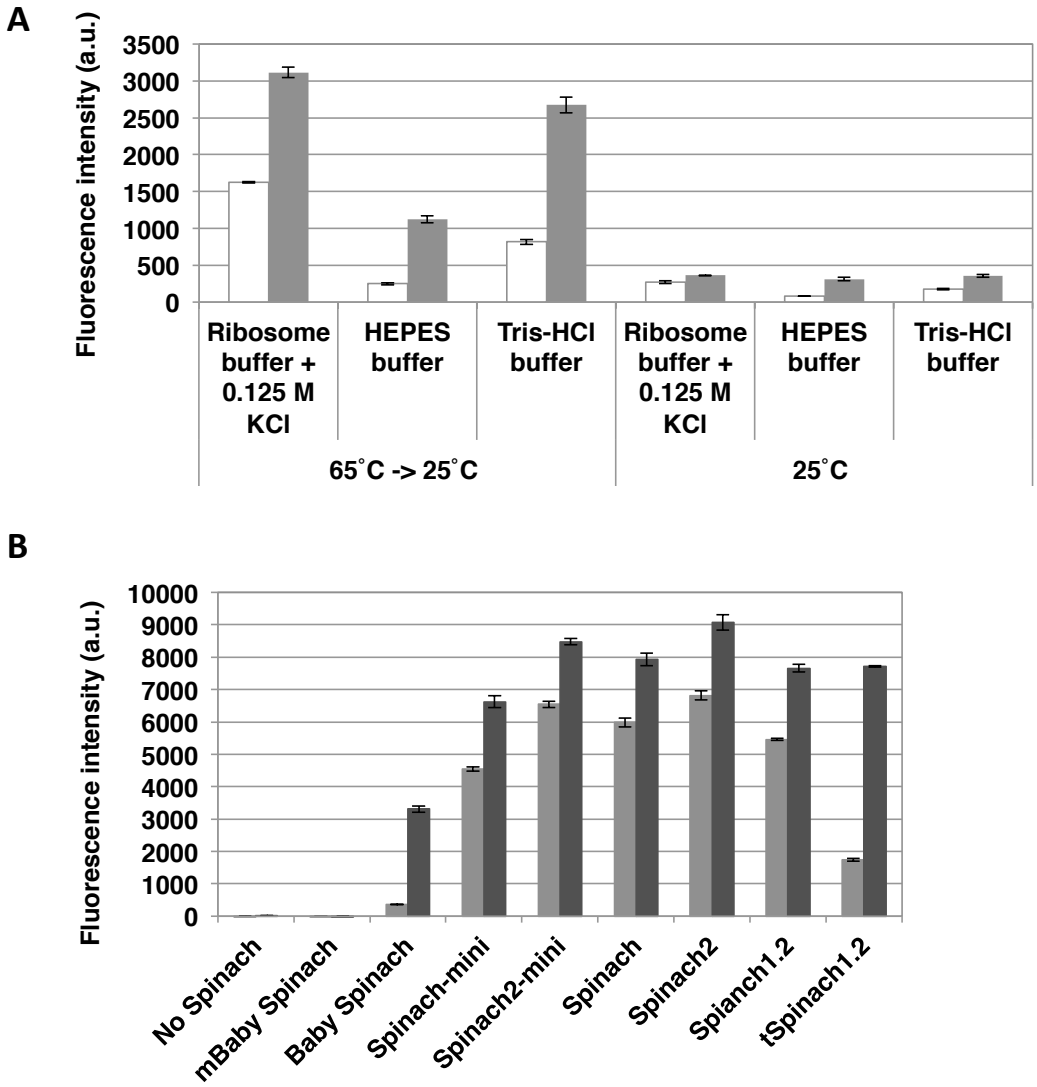

Figure II-4: Fluorescence of Baby Spinach strictly requires a slow cooling step for efficient folding. (A) Prior to fluorescence measurements, a folding step in water was included before evaluation of the yield of complex formation with DFHBI in different buffer conditions and excess of fluorophore (2x white bars; 100x grey bars). (B) Fluorescence levels of the different Spinach sequences in ribosome buffer supplemented with 125 mM KCl. The excess of DFHBI is 100 fold. Grey bars: snap cool folding protocol, dark grey bars snap cool and slow cooling protocol. Error bars are s. e. m. for three independent experiments.

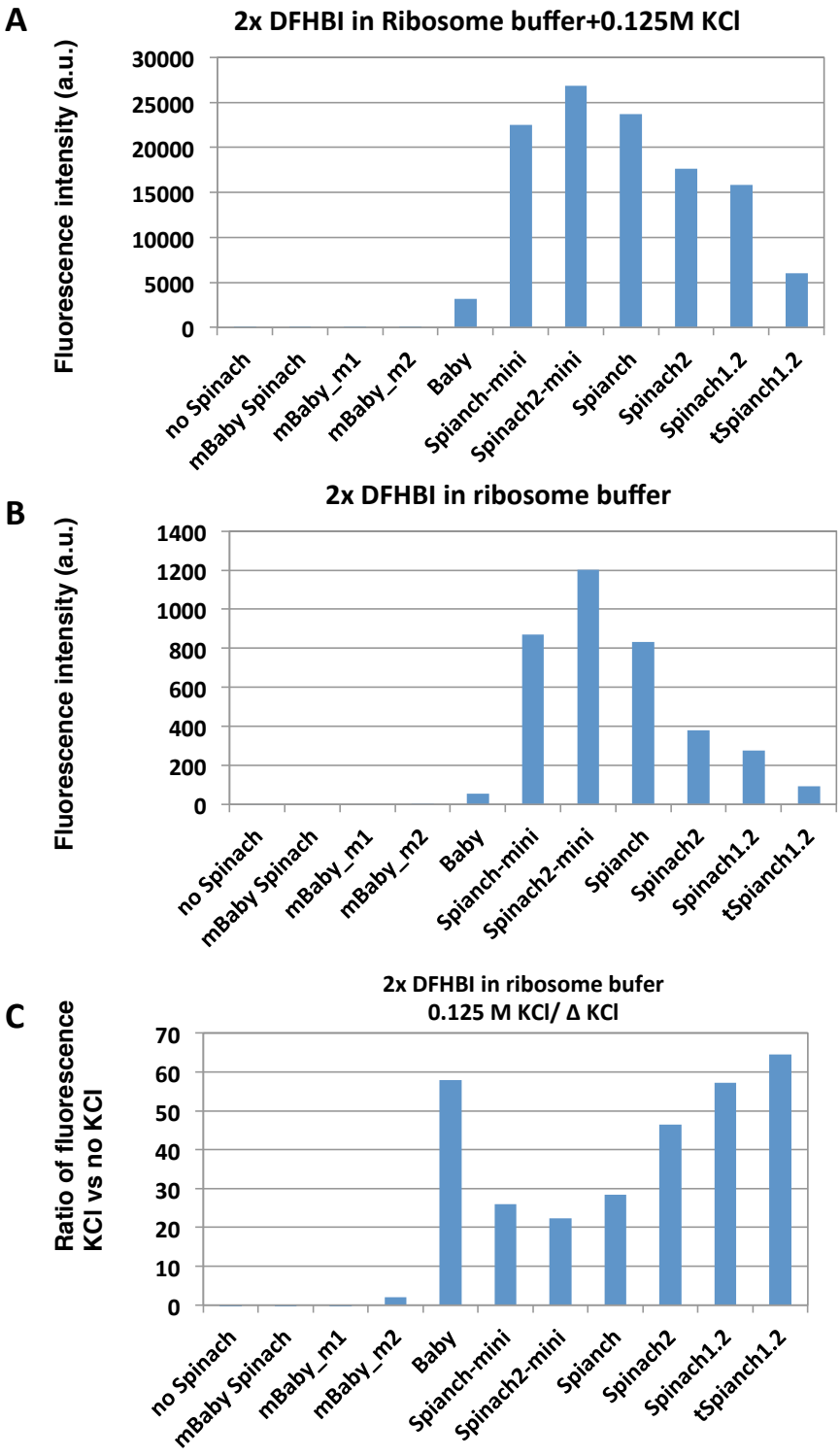

Figure II-5: Effect of K^+ on the fluorescence levels of Spinach transcripts. (A) Ribosome buffer with 2x excess of DFHBI. (B) Same ribosome buffer supplemented with 125 mM of KCl. (C) Effect of KCl on the different Spinach transcripts.

II. 4 Expression of spinach-ribosome in *E. coli* strain TA531

II. 4. 1 TA531 plasmid exchange

E. coli strain TA531 is the deletion mutant of all seven copies of chromosomal rRNA genes. TA531 harbors the plasmid pHC-rrnC carrying a single copy of rrnC operon and a kanamycin resistant gene. To obtain TA531 expressing only Spinach-ribosome instead of wild-type ribosome, pHC-rrnC was replaced with pKK3535-Spinach. First, TA531 was transformed with pKK3535-Spinach and inoculated into LB medium (amp). During at least 2 days incubation at stationary phase, some cells started to release the original pHC-rrC vector for whose kanamycin resistant gene is no longer required. The culture was spread on LB plates and incubated overnight. Each single colony was inoculated on two LB plates containing ampicillin or kanamycin respectively. The colonies that survived only on an ampicillin plate were selected. Achievement of the plasmid replacement with all pKK3535-Spinach in TA531 meant that each Spinach-ribosome can serve as a unique source of ribosome inside the cell and that they do not have lethal effect on either 16S rRNA maturation, subsequent ribosome biogenesis or function. The percentage of the successful colonies in plasmid replacement among total cells varied from 0.7 % to 10 % depending on the Spinach sequence inserted. Expressing homogenous population of ribosomes will facilitate the evaluation of the effect of Spinach insertion on cell growth and allow for the purification of pure Spinach-tagged ribosomes.

II. 4. 2 Effect of Spinach insertion on ribosome function

Insertion of Spinach into the ribosome might alter ribosome properties. To assess the extent to which Spinach insertion affects ribosomal function, growth rates of TA531 expressing only Spinach-ribosomes were measured. The comparison of growth rates for each TA531-Spinach strain are shown in Figure II-6A and table II-2.

Among the same type of Spinach, the shorter sequence is less likely to restrict ribosome function. Indeed, insertion of Baby Spinach turned out to have least effect on doubling time of TA531. On the other hand, difference in growth was seen among cells expressing ribosomes with the same size of Spinach insertion. Spinach and spinach2 (95 bases) and Spinach-mini and Spinach2-mini (80 bases) have different G-C pair contents, suggesting different folding abilities that might affect ribosome formation or function. In addition to that, results on mBaby Spinach laid out another possible factor to impair the function of ribosome.

mBaby Spinach was shown to be the most deleterious for *E. coli* growth despite the smallest size among all Spinach constructs. During cloning and plasmid replacement in TA531, I obtained 2 mutants of mBaby Spinach that suffered one point mutation: inside the loop (mBaby

m-1) and in P3 stem (mBaby m-2) (Figure II-6B). mBaby m-1 has the substitution U to C and mBaby m-2 corresponds to G to A mutation. Surprisingly, these two variants recovered wild-type cell growth rate (as no Spinach). In the case of mBaby Spinach, the slower growth rate could be due to a sequence around the loop. This sequence unique for mBaby Spinach probably affects ribosome formation. We noticed that these mutations disrupt a possible complementarity of sequence with another region of 16S rRNA. This possible base pairing between mBaby Spinach loop and 16S rRNA might affect ribosomal folding and/or assembly.

It is worth to note that Spinach1.2 containing the stabilizing tRNA scaffold (tSpinach1.2) altered the physiology of *E. coli* TA531 with the formation of cell aggregates (Figure II-6C). All other constructs tested here (Spinach, Spinach-mini, Spinach2, Spinach2-mini, Baby Spinach and mBaby Spinach did not modify the physiology of cells from liquid culture.

Table II-2: Doubling time

Spinach type	**Doubling time (min)**	
No spinach	49.8	± 3.4
mBaby	103.5	Measured only once
mBaby mutation 1	52.2	Measured only once
mBaby mutation 2	48.8	Measured only once
Baby	50.9	± 1.5
Mini 24-2	79.1	± 3.8
Mini 2	58.1	± 4.2
Long 24-2	85.6	± 4.7
Long 2	64.5	± 3.7
Long 1-1	84.5	± 5.7
Full 1-1	74.6	± 7.9

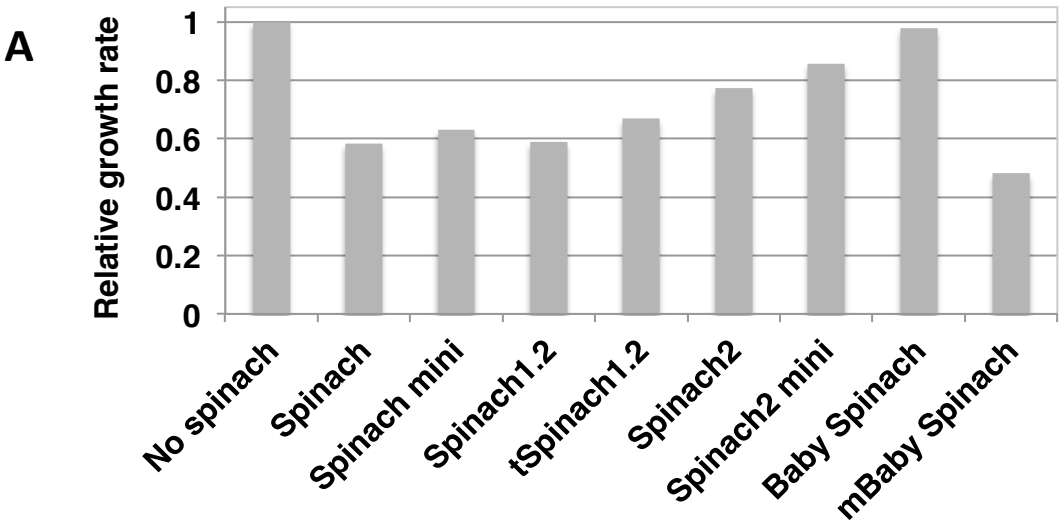

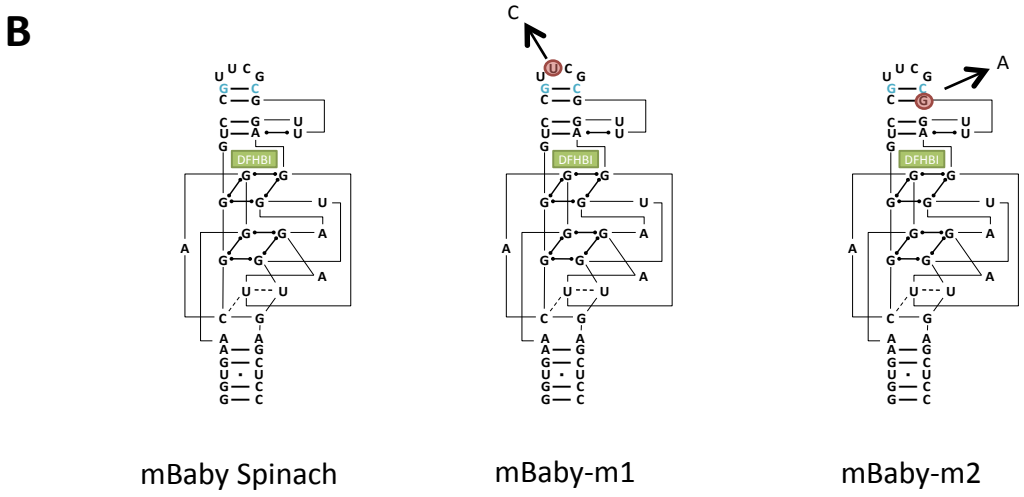

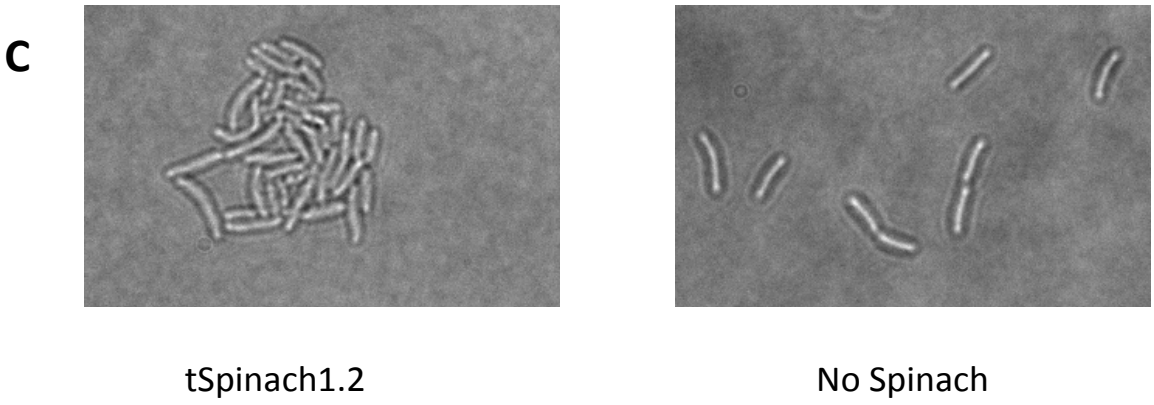

Figure II-6: (A) Growth-rate levels of *E. coli* for Spinach-containing ribosomes. Rates were measured in liquid culture at 37°C in rich media (LB). Values were normalized to *E. coli* strain TA531 containing unmodified ribosomes (no Spinach). (B) Secondary structures of the mBaby Spinach mutants. Mutations are indicated in red. (C) brightfield images of *E. coli* TA531 observed from fresh liquid culture in rich media (LB). Cells expressing 16S rRNA tagged with tSpinach1.2 formed aggregates (left panel).

II. 4. 3 In vitro measurement: Baby spinach is the best version of Spinach to activate DFHBI in the ribosome.

We then investigated the fluorescence levels of these Spinach aptamers in the context of the ribosome. Spinach containing ribosomes were purified from *E. coli* strain TA531 that has a single copy of rrnB operon with the Spinach insertion. This ensures homogeneity of Spinach-tagged ribosomes with absence of non-tagged ribosomes. Fluorescence levels for each construct are displayed on Figure II-7A. We first performed experiments in the following conditions: 1 μM RNA and 2 μM DHFBI using the ribosome buffer (20 mM Tris-HCl (pH7.5), 100 mM NH_4Cl, 10 mM $MgCl_2$, 0.5 mM EDTA, 6 mM 2-mercaptoethanol). Spectra were the same for all constructs (Figure II-8). On the contrary, signal intensities were found to be quite different among the constructs and K^+ strongly stimulated the amount of folded RNA between 40 to 100 fold (Figure II-7B). Previous versions of Spinach (i.e. Spinach, Spinach1.2 and tSpinach1.2) were not strongly fluorescent in the context of the 30S ribosomal RNA. Surprisingly the fluorescence signal measured for the recent 'superfolder' Spinach2 construct was only slightly higher. Instead, the best three constructs fell into the category of the miniaturized Spinach generation. Spinach-mini (80-nts) first described in the original work that revealed the Spinach RNA aptamer (63) contains a first deletion in the J1-2 junction and a second deletion in the paired region P3. We introduced the same deletions into Spinach-2 to generate Spinach2 mini (80-nts). Finally Baby Spinach, which is the smallest of all constructs (51-nts) and behaved poorly as a RNA transcript displayed the highest yield of folding and fluorescence. Fluorescent increase was also seen on mBaby Spinach, which was undetectable in transcript state. In context of ribosome, mBaby Spinach showed fluorescence though it was much weaker than the other Spinach constructs. These results demonstrate that ribosomal RNA serves as a powerful natural scaffold able to promote Baby and mBaby Spinach folding.

Fluorescence increase by addition of KCl was measured for mBaby Spinach, Baby Spinach, Spinach-mini, Spinach2-mini and Spinach2 (Figure II-7B). Similarly to the measurement in transcript, Spinach-mini and Spinach2-mini showed an increase at almost same rate (40 %), which was smaller than that of Spinach2 (85 %), though the general increase of rate of the these Spinach-ribosome were higher than that of transcript. Baby spinach was increased as much as Spinach2 in the form of transcript, while it was same for Spinach-mini and Spinach2-mini in context of ribosome. Interestingly addition of K^+ did not stimulate mBaby Spinach in transcript but it did in the ribosome context.

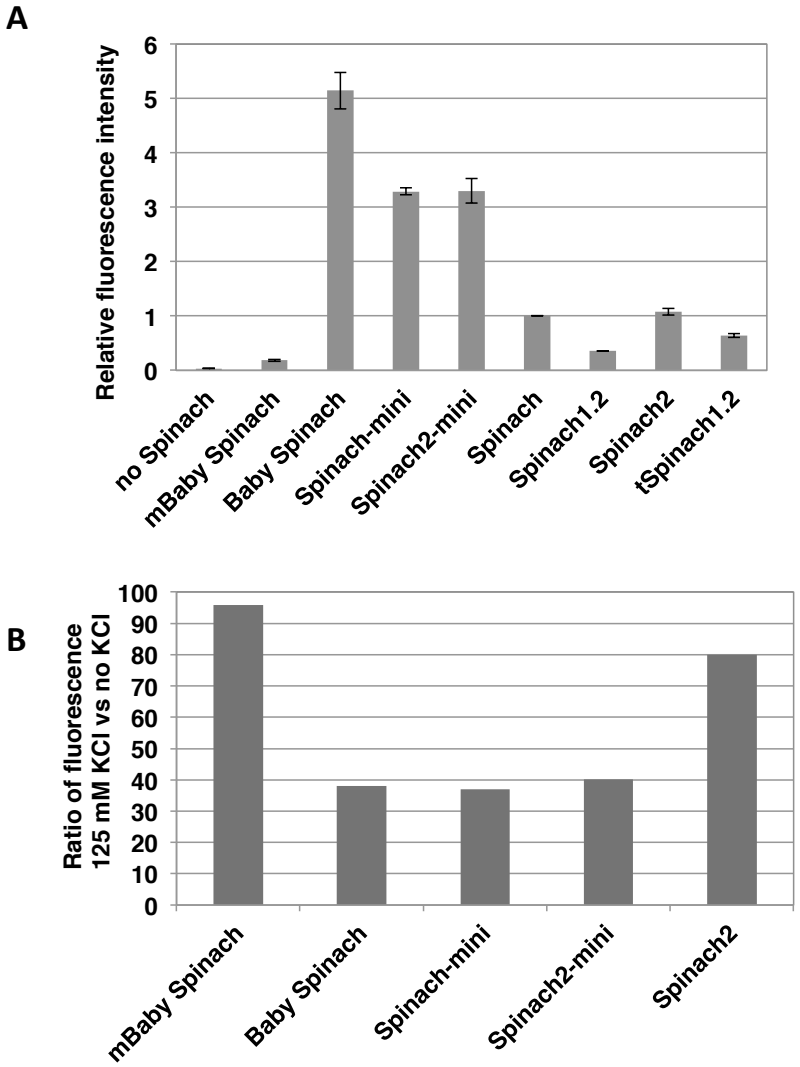

Figure II-7: Fluorescence levels for the different Spinach ribosome constructs. (A) Levels were measured at 25°C from purified 70S ribosomes (1μM) on a plate reader with the addition of 2 μM DFHBI. Values are normalized according to Spinach. (B) Addition of 125 mM KCl increased fluorescence levels. Error bars are s. e. m. for three independent experiments.

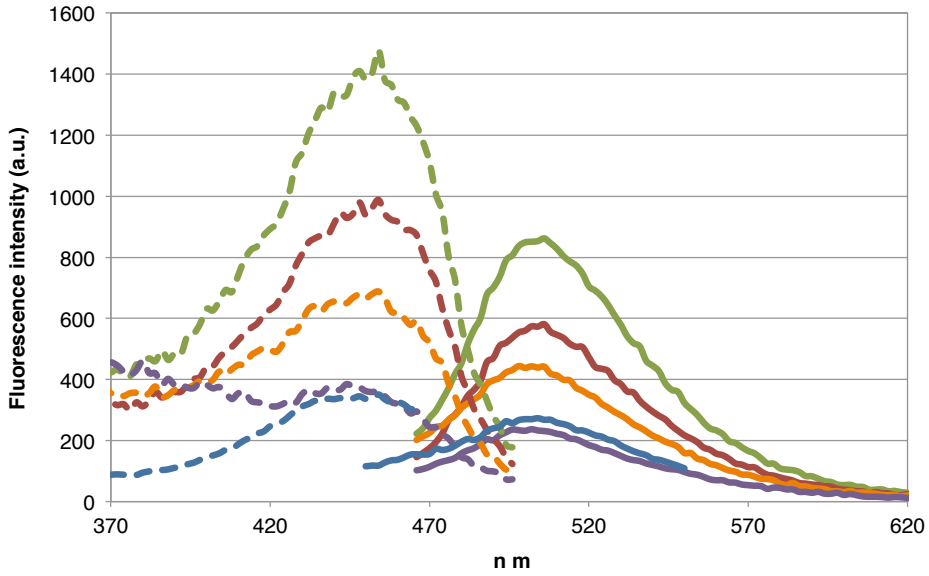

Figure II-8: We confirmed that emission spectra of DFHBI were the same for all constructs. Green: Baby; Red: spinach-mini; orange: Spinach2-mini; Blue: Spinach; Purple: Spinach2. Dotted lines: Excitation spectra; solid lines: Emission spectra

II. 4. 4 Addition of DFHBI does not affect cell growth

To confirm that DFHBI is non-toxic for cell growth, we measured the rate of growth of TA531 in presence of high concentration (200 μM) of DFHBI. During all the period of growth, there was no detectable effect of the presence of DFHBI in the culture (Figure II-9).

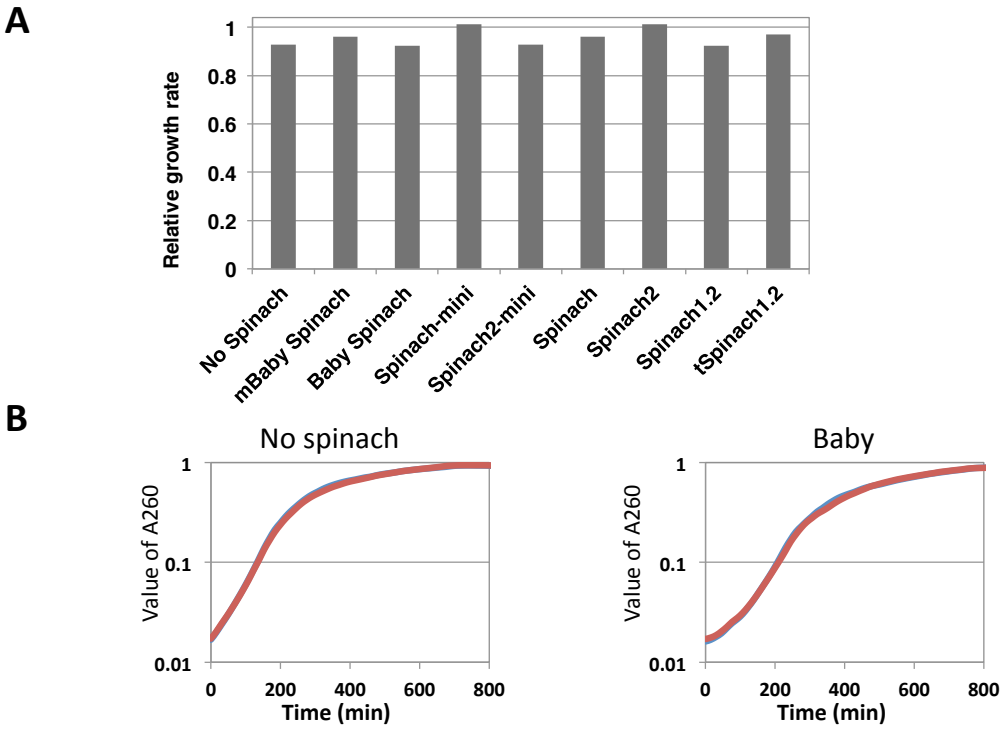

Figure II-9: generation time of *E. coli* cells TA531 expressing Spinach-tagged ribosomes is unaffected by the presence of 200 μM DFHBI in culture media (LB). Values are normalized to the growth rate of TA531 in absence of DFHBI (not represented). (B) Representative growth curve for cells expressing native 16S rRNA (left) or Baby Spinach-tagged 16S rRNA (right). Red curves: 200 μM DFHBI; Blue curves: no DFHBI.

II. 4. 5 Fluorescence measurement in liquid culture and live-cell imaging

Spinach-tagged ribosomes were then expressed in strain TA531 and levels of fluorescence were measured on a plate reader (Figure II-10). Values were normalized to the 16S rRNA expression levels obtained from RT-PCR on purified total RNA and were found to be quite homogenous among the samples (By Dr. Satoko Yoshizawa). Cells were grown in rich media and the culture media was exchanged for M9-Glucose media before addition of 20 mM DFHBI and incubation at 37°C. M9 media contains magnesium and potassium cations ensuring high levels of fluorescence for Spinach derivatives during measurements. Spinach 2, was found to be more fluorescent than Spinach in eukaryotic cells (65). In *E. coli* both aptamers generated similar signals (Figure II-10A). As observed *in vitro*, short Spinach constructs inserted in helix 33a of 16S ribosomal RNA clearly showed highest fluorescence signals. The minimized version of Spinach2 (2mini), 80-nts long was found to generate a signal 6 fold stronger than Spinach2. Similarly, the fluorescence emitted by the short version of Spinach was 6 fold stronger than its long counterpart.

But more importantly, Baby Spinach showed the highest yield of folding and was found to be 7-fold brighter than the 'superfolder' Spinach2. Therefore, the *in vivo* results mirror the *in vitro* data showing that there is a good agreement between both conditions.

Here, TA531 cells expressing ribosomes with insertion of Baby Spinach, Spinach2-mini (representative of mini version) and Spinach2 (representative of standard size) were incubated with 200 μM DFHBI and imaged (Figure II-10 B). Indeed Baby Spinach and Spinach2-mini behaved the best.

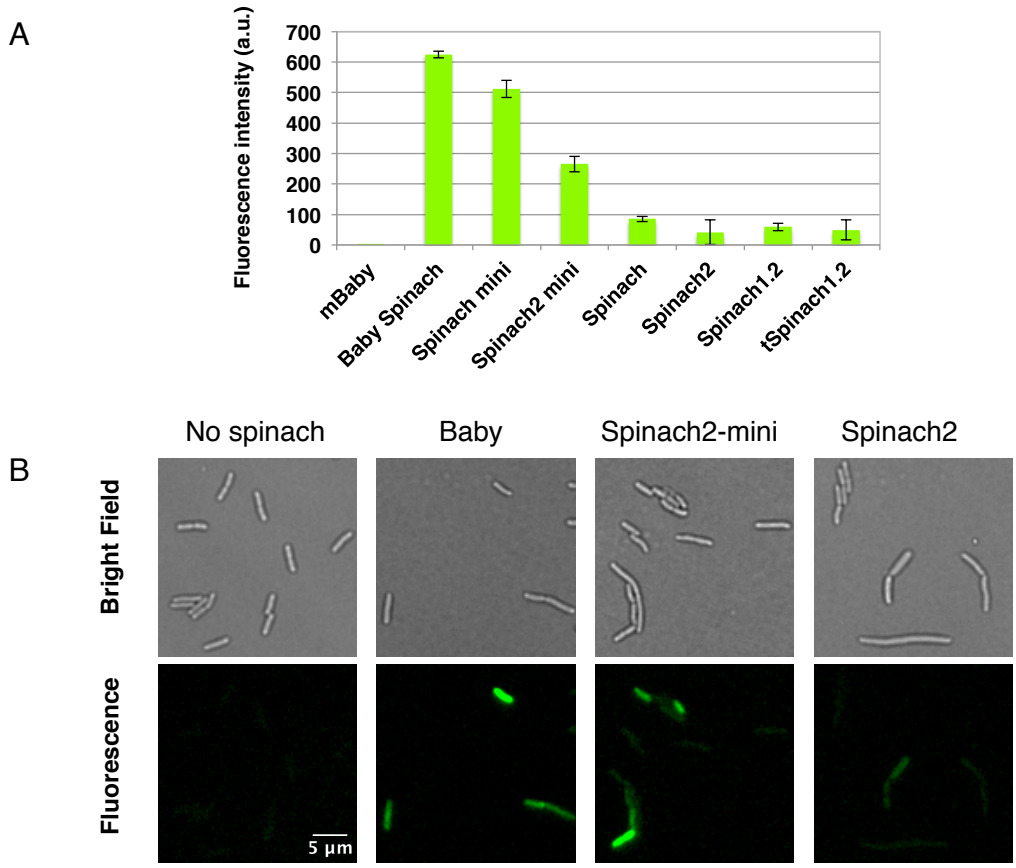

Figure II-10: *In vivo* fluorescent assay of ribosomal Spinach sequences. (A) Fluorescence signal from *E. coli* cells TA531 incubated with 20 mM DFHBI in M9-Glucose (2 mM magnesium) media at 37°C for 30 minutes. Samples were excited at 455 nm in a plate reader and fluorescence was recorded at 506 nm. Values were corrected for DFHBI background and normalized to the level of expression of 16S rRNA. Error bars are s. e. m. for three independent experiments. (B) Imaging of *E. coli* cells TA531expressing different Spinach-tagged ribosomes. Cells we incubated with 200 mM DFHBI-1T (a brighter analog of DFHBI) for 90 min at 37°C, mounted on agar pad and imaged at room temperature under the microscope. The signal is the sum of 5 cycles of excitation/acquisition (50 ms) spaced by 20 seconds necessary for fluorescence recovery (64). Brightness of the images was adjusted according to the signal of Baby Spinach. We note heterogeneity in the levels of fluorescence at the single cell level.

II. 5 RNA degradation *in vivo*

We then asked whether degradation could account for low fluorescence signals as the aptamer could be cleaved or degraded leading to reduced DFHBI binding. Therefore we tested if the RNA aptamers as well as the construct containing the tRNA scaffold are subjected to endo or exonucleotidic degradation during constitutive expression *in E. coli*. The following experiments have been performed by Dr. Satoko Yoshizawa. To visualize degradation products, total cellular RNA was extracted from cells TA531 expressing Spinach-tagged 16S rRNA. Analysis on 6% polyacrylamide denaturating gel followed by DFHBI-1T or SYBR Gold staining revealed the pattern of degradation products (Figure II-11A). mBaby Spinach that displayed very poor folding capabilities was undetectable on urea-PAGE stained with DFHBI-1T. Other constructs showed a major band corresponding to 16S rRNA. Lower molecular weight bands were detected for all constructs but were less intense for Baby Spinach (Figure II-11A). As expected, a control of total cellular RNA from a strain expressing non-tagged ribosome showed no identification of RNA products that would generate fluorescence with DFHBI-1T. The degradation bands observed with other constructs are therefore the results of cleavage of 16S rRNA molecules. Spinach-mini and Spinach 1.2 reproducibly produced a band of higher molecular weight that remains uncharacterized. A similar experiment was performed on purified Spinach ribosomes (Figure II-10B). Except for Baby Spinach that displayed a single band, all other constructs gave lower molecular weight bands indicating that cleavages within 16S rRNA occurred generating large fragments of rRNA containing the Spinach tag.

We next identified possible cleavage sites in the vicinity or within the Spinach tags on purified rRNA for three constructs (Figure II-11C). Purified ribosomes were phenol extracted to obtain rRNA samples that were subjected to fluorescent primer extension (150) (Figure II-11C). Endonucleotidic cleavage would result in a stop of primer extension by reverse transcriptase. In the case of tSpinach1.2, multiple bands were detected in the region of the aptamer and few bands within tRNA scaffold. Recently a model for degradation was proposed for Spinach with tRNA-scaffold sequences. Endonucleases, which normally process tRNAs in vivo, cleave the tRNA-scaffold of tBrocoli and tSpinach sequences step followed by a removal of the remaining flanking regions by trimming at the 3' terminus by exo- nucleases RNase T and RNase PH (151). In the context of the ribosome, the situation seems quite different as we did not observe strong primer extension stop at the 3' processing site of tRNA. Instead, multiple stops were observed rather in the aptamer sequence suggesting random endonucleotidic cleavages within this region but only few in the tRNA scaffold. The difference may be due to the context of tRNA scaffold. In our study the tRNA scaffold is inserted into h33a of rRNA, thus, 3' and 5' regions of the tRNA are embedded in

an RNA stem whereas they are flanked by single stranded regions in the construct used by Filonov et al., (151). In addition, the scaffold is close to the surface of the ribosome and the steric hindrance may also contribute to protect the tRNA sequence from attacks of RNases. The cleavages that we observed within the aptamer sequence are likely a consequence of strong accessibility and partial unfolding in the absence of DFHBI *in vivo*. The small size of Baby Spinach aptamer and its enhanced folding propensities likely prevents this non-specific degradation (Figure II-11C).

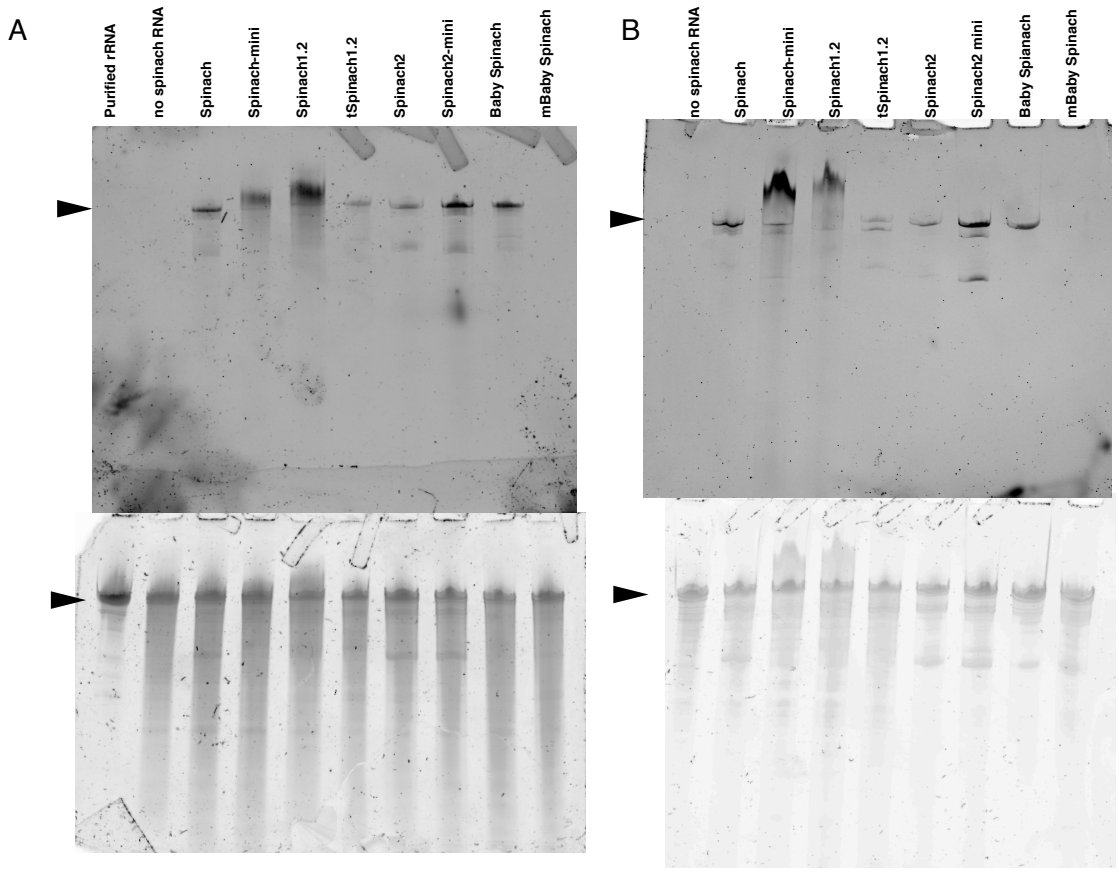

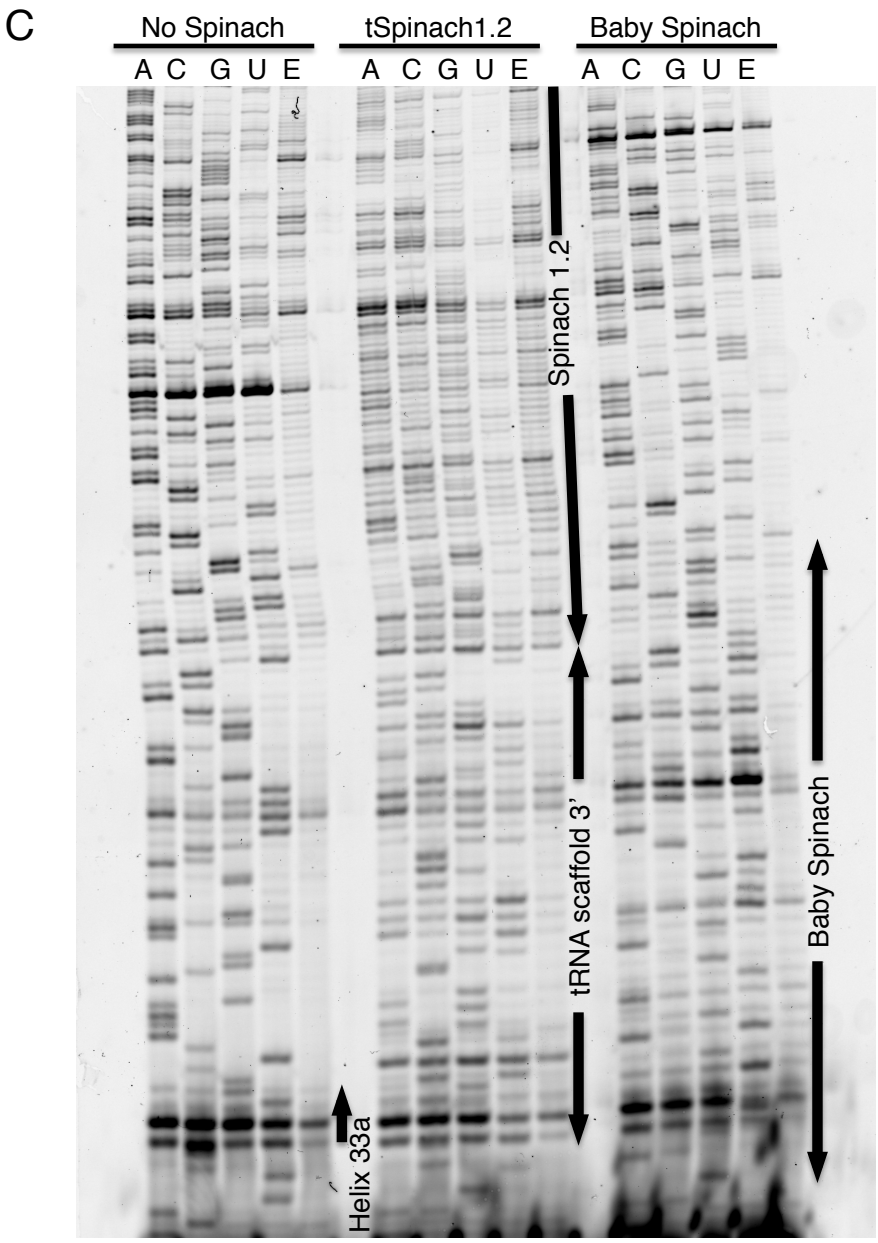

Figure II-11: Degradation of Spinach-tagged ribosomes. (A) Fractionation of total RNA from TA531 cells expressing Spinach-tagged ribosomes on urea-PAGE and stained with DFHBI-1T (top) and SYBR Gold (bottom). 16S rRNA bands are indicated by arrows. (B) Same experiment performed on corresponding purified ribosomes. (C) Fluorescent primer extension analysis of cleavage sites. FPE products were generated using Cy5 labeled DNA primer and analyzed on urea-PAGE. Regions corresponding to h33a, tRNA scaffold, Spinach and Baby Spinach are indicated by arrows.

II. 6 Conclusion

We have used a strategy that allowed the identification, among several Spinach constructs, of one aptamer (Baby Spinach) that presents robust stability and high performance in terms of fluorescence for live-cell imaging. The choice of location to insert the aptamer within the 16S rRNA was done in order not to affect the function of the ribosome. We found that the insert should be kept to an acceptable length since large sequences affect the growth rate of *E. coli* cells. More importantly we found that the natural scaffold provided by h33a promotes the folding of Baby Spinach aptamer, which by its small size was also found more resistant to enzymatic degradation in living cells. This indicates that Baby Spinach is an excellent system to visualize structured RNAs in live-cell imaging.

Chapter III

Aminoglycoside uptake by bacteria

III. 1 Introduction

Neomycin defines a class of aminoglycosides to which gentamicin is also belonging (see figure I-1). This class binds to the decoding site of the ribosome and cause miscoding and inhibit translation. Streptomycin, the first aminoglycoside to be discovered belongs to another class of aminoglycosides and does not bind to the same region of the small ribosomal subunit. Many investigators have studied on the mechanism of aminoglycoside uptake by bacteria as well as their mode of antibiotic action. The use of radioactively labeled streptomycin contributed to the estimation of the levels of accumulation in cells for each period of the uptake process (125,152). Recently flow cell cytometers were used to measure accumulation of a fluorescently labeled aminoglycoside (Gent-TR, see introduction section I-3.4) in a population of bacteria (122,140). These data can provide a qualitative view of aminoglycoside absorption within a cell population. However they cannot reveal the spatial and temporal variation of aminoglycoside transport at the single cell level.

Towards this goal, having an aminoglycoside that could be visualized by fluorescence microscopy would be very useful. As described in the introduction section I-3.4, Gent-TR suffers some drawbacks. By reading the publications that used the Gent-TR conjugate, we suspect that bacteria present a basal level of accumulation of the dye Texas Red (TR) in itself, which would represent a major obstacle for imaging the uptake of aminoglycosides by fluorescence microscopy. I confirmed this idea and the data are illustrated Figure III-1.

Considering the above remarks, the team used its previous expertise on the synthesis of active derivatives of neomycin to produce a new conjugate with preserved antibiotic activity. The dye is chemically incorporated at a unique reactive position within neomycin placing the probe in the major groove of helix 44 of 16S rRNA at a position that is not interfering with the binding and action of the drug. It was verified in the crystal structure of *E. coli* ribosomes bound to neomycin that this position can accommodate the fluorescent probe. Finally, we have chosen Cy5, a dye appropriate for super-resolution microscopy (75).

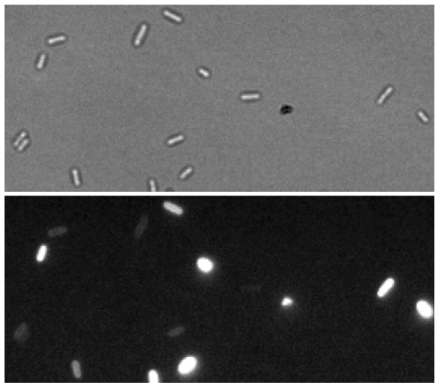

Figure III-1: *E. coli* cells accumulate the Texas Red dye. (Top) Brightfield image of MG 1655 live cells in exponential growth phase and incubated with Texas Red. (Bottom) Same field imaged for fluorescence. All cells incorporated the dye with some heterogeneity.

III. 2 Results

III. 2. 1 Neo-Cy5 synthesis and structure

The team of D Fourmy and S Yoshizawa previously developed in collaboration with Dr JL Fourrey, a derivative of neomycin that can be use to attach any additional chemical group. Here, this derivative was used to conjugate the fluorophore Cy5 to neomycin. Here after, this compound is called Neo-Cy5 (Figure III-2). After the coupling reaction, the conjugate was purified to remove the excess of reagents. We voluntary wish not to give experimental details of the synthesis as well as the details of the chemical structure of the conjugate until publication.

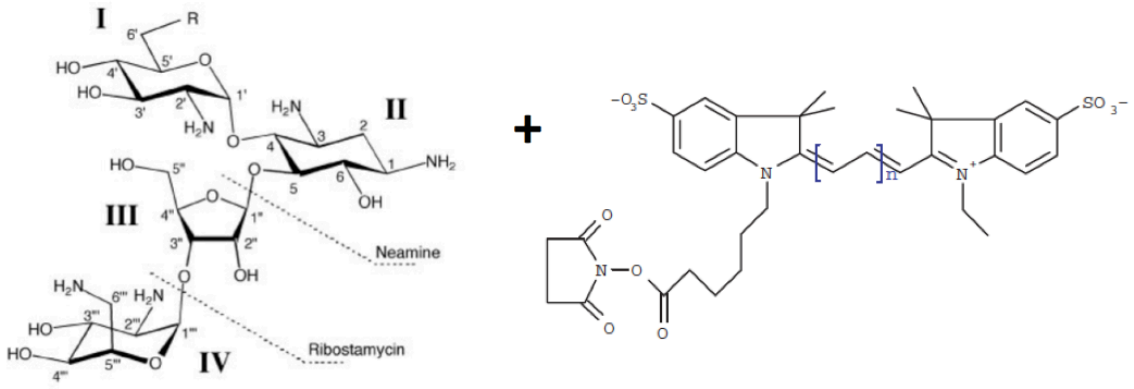

Figure III-2: The dye Cy5 was connected to a position of neomycin. This reaction was done using a neomycin derivative that allows the specifically conjugate the fluorophore to a single position of neomycin.

III. 2. 2 Binding of Neo-Cy5 to the decoding site

After purification, Neo-Cy5 binding to the decoding site of 16S rRNA in 70S ribosomes was tested. It was found that Neo-Cy5 binds to the decoding site albeit with an affinity slightly decreased compared to neomycin (Figure III-3). This result indicates that Neo-Cy5 has likely the typical aminoglycoside miscoding activity.

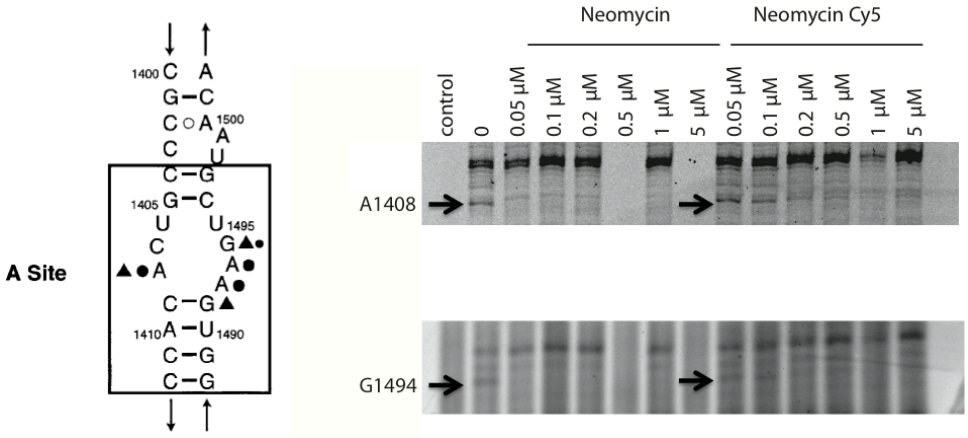

Figure III-3: Neo-Cy5 binds the decoding site of 16S rRNA in 70S ribosomes. (Left) Secondary structure of *E. coli* 16S RNA in the region of the A site (boxed). Nucleotides protected from chemical probes by A-site tRNA bound to 30S subunits are marked (circle). Nucleotides protected from chemical probes by aminoglycoside antibiotics bound to 30S subunits are marked with a triangle. (Right) Fluorescence scan of DMS probing reactions on 70S ribosomes. Protected bases are marked with an arrow.

III. 2. 3 Neo-Cy5 is an active antibiotic

Since the conjugate is likely to have the miscoding activity it should act as the parental antibiotic. Therefore, I measured the minimum inhibitory concentration (MIC) of normal neomycin and synthesized Neo-Cy5 for *E. coli* strain MG1655 in two minimal media, M9 and MOPS. These transparent media (low background in fluorescence) are suitable for the final aim of this study to follow time-dependent dynamic change of Neo-cy5 uptake in living cell. Cultivation for 15 hours in presence of several concentrations of neomycin or Neo-Cy5 gave a value of the MIC (table III-1). Higher concentrations of neomycin and Neo-Cy5 were required to inhibit the growth of MG1655 completely in M9 minimal medium, compared to MOPS medium. The MIC value of Neo-Cy5 turned out to be 4 or 5 times higher than neomycin. This MIC value is similar to the one of paromomycin, a closely related aminoglycoside that has a hydroxyl group instead of an amino group at the 6' position of ring I (labeled R in Figure III-2).

Table III-1

	Neomycin	Neo-Cy5
M9 medium	2.4 μM	9.6 μM
MOPS medium	0.8 μM	4 μM
LB medium	3.2 μM	Not determined

III. 2. 4 Neo-Cy5 uptake by Gram-negative bacteria

III. 2. 4. 1 Control experiments: testing uptake of Cy5 fluorophores by *E. coli*

Before to observe the uptake of Neo-Cy5 by bacteria, it was essential to evaluate a possible uptake of Cy5 by bacteria. I incubated cells with the dye Cy5 to check for its cytotoxicity, permeability across cell membrane and its eventual localization. As opposed to TR, I found that the fluorophore Cy5 alone does not accumulate in cells that are alive (Figure III-4). Among cells incubated with 0.4 μM Cy5, rare cells showed to have Cy5 signal, though it was very low, while the majority had no signal. However, this level of accumulation remains lower than the lowest active uptake of Neo-Cy5 by live cells that we will see in the following section. This result is very important and allowed me to observe active uptake of Neo-Cy5 by bacteria. Unlike in the case of active uptake of Neo-Cy5 (see below figure III-6), the low accumulation of Cy5 enabled us to use LIVE/DEAD kit, which showed that the cell with accumulation of Cy5 turned out to be dead cells. There is no Cy5 permeability across the membrane of living *E. coli* and little across the membrane of dead *E. coli* cells. Cells that are dead and reactive to propidium iodide (PI) accumulated Cy5 (Figure III-4). Localization of Cy5 to certain parts inside the cell was not detected.

To identify live and dead cell using microscopy, the Live/Dead Bac kit (Molecular Probes) was used. This kit contains two kinds of dyes: SYTO9 (green) that can enter both alive and dead cells, while the red dye propidium iodide (PI) can cross the cell membrane when it has damages, a situation for which the cell is declared dead. When the two dyes coexist inside cells on rare occasions, only the red fluorescence is detected because the green fluorescence is quenched by fluorescent energy transfer to the red dye.

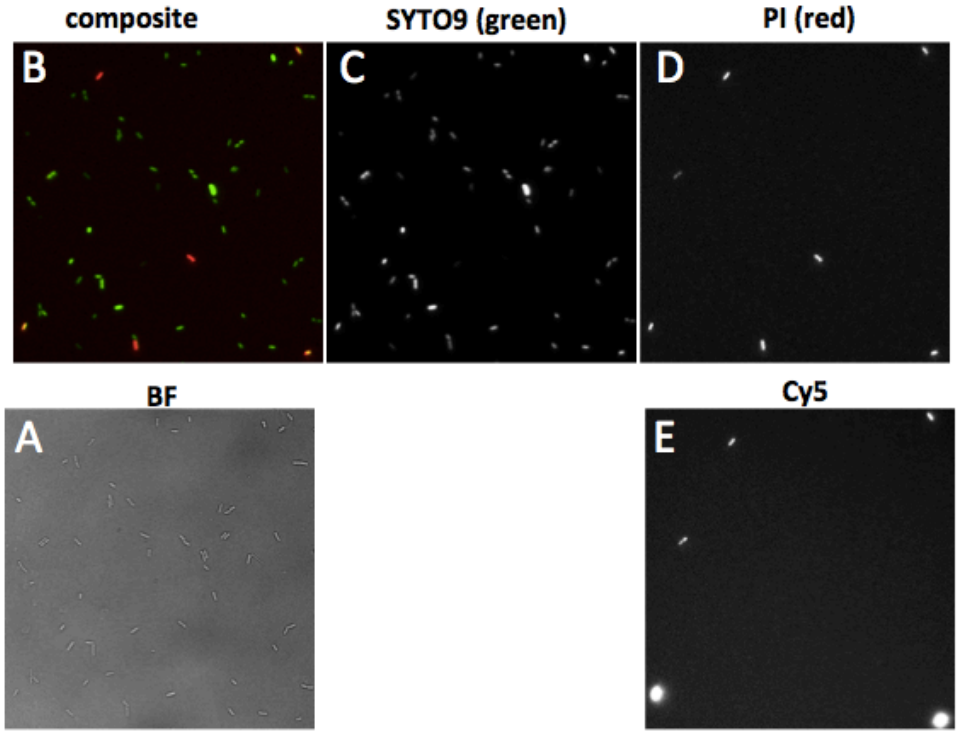

Figure III-4: Only rare dead *E. coli* cells very weakly accumulate Cy5 probe. (A) Brightfield image of MG 1655 live cells. (B) Composite image of cells imaged for SYTO9 (green) and propidium iodide (PI) (red). (C) SYTO9 uptake by live cells. (D) Cells with damaged membrane imaged by PI fluorescence. A weak fraction of the fluorescence comes from Cy5 emission. (E) Cy5 probe accumulates in dead cells. Only on very rare occasions, a green cell incorporates Cy5 probe.

III. 2. 4. 2 Imaging *E. coli* cells treated with Neo-Cy5

Having demonstrated that *E. coli* cells alive do not accumulate Cy5 dye, I then tested the properties of Neo-Cy5 for intracellular uptake properties. I visualized the accumulation of Neo-Cy5 in single live bacteria. Observation of *E. coli* strain MG1655 after the treatment with Neo-Cy5 was performed with the following protocol. A culture of *E. coli* MG1655 was stopped at an OD_{600} of 0.3 (in exponential phase) and incubated with 0.4 μM Neo-Cy5. Followed by washing of the cells to remove the excess of Neo-Cy5, Cy5 fluorescence signal inside the cells was observed using Total Internal Reflection Fluorescence (TIRF) Microscopy.

III. 2. 4. 3 Accumulation pattern and their characteristics

All cells accumulated Neo-Cy5 however several patterns were observed (Figure III-5). Since Cy5 itself failed to cross the bacterial membrane I can conclude that it is the property of Neomycin rather than that of Cy5 that leads to high-level accumulation or localization around the cell

membrane. Levels of fluorescence remained constant over several hours indicating that the uptake is irreversible as previously observed for aminoglycosides (125). In a first pattern, Neo-Cy5 accumulated to a relatively low amount in the periphery of the cell, presumably in the periplasm (Figure III-5). This peripheral accumulation is irreversible and persists in high-salt conditions suggesting that it does not correspond to the salt-sensitive binding to the membrane outside the cell (152). In a second pattern cells accumulated, also irreversibly, very high levels of antibiotic in the cytoplasm (Figure III-5). This uptake is fast as strong cytoplasmic uptake occurred for a fraction of cells within 2 minutes of exposure. As a third pattern, we observed that dividing cells show, in addition to the peripheral localization, a Neo-Cy5 accumulation at the septum where the membrane is newly synthesized (Figure III-5).

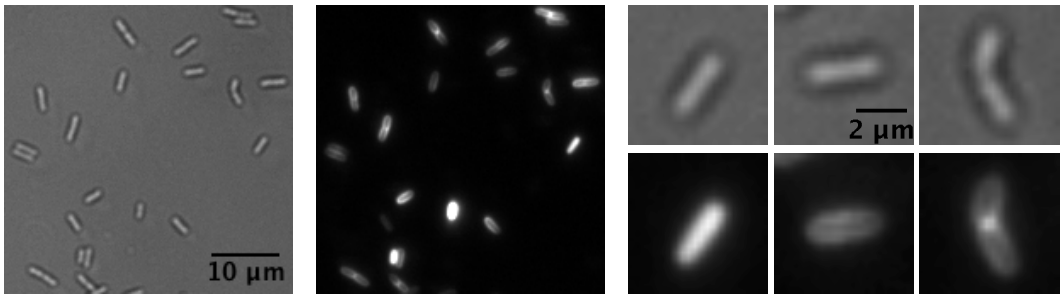

Figure III-5: Patterns of Neo-Cy5 localization in live *E. coli* cells. Left panels: Brightfield and fluorescence images. Excitation is at 642 nm and emission at 695 nm. Right panels (from left to right): Cell with cytoplasmic uptake (bright signal), peripheral localization and dividing cells showing accumulation at the periphery and at the septum.

1) "Coquillage" cell

We named the cells with peripheral accumulation as the "coquillage" pattern because they resemble the shape of a shell. In this type of cell, Cy5 signal was detected around the cell membrane (Figure III-5 middle right panel). This pattern was found for the majority of cells after a treatment of 5 min with 0.4 μM Neo-Cy5, which is ten times lower than the MIC (4 μM in MOPS). Some of these cells have stronger signal on poles in addition to the peripheral fluorescence. A sub-class in this category is represented by cells, which are dividing with always a strong concentration of the fluorescence at the septum (Figure III-5 right panels).

2) Cytoplasmic accumulation

Other cells were found to have a uniform distribution of Neo-Cy5 (Figure III-5 right panels). These cells with strong cytoplasmic Neo-Cy5 accumulation were rare in these conditions.

Most of them showed very strong signal suggesting that, in this state, Neo-Cy5 uptake proceeded in a more advanced state than the coquillage cells. On rare occasions, dividing cells show cytoplasmic uptake for both daughter cells.

Some cells, which were not categorized, had much lower signal that the cellular distribution of Neo-Cy5 was unclear. In any case, it is certain that all cells showed some signal after incubation with Neo-cy5 when compared to cells in absence of the drug (control).

III. 2. 4. 4 The fate of cells with cytoplasmic and "coquillage" patterns

With the LIVE/DEAD Baclight kit, I checked whether "coquillage" and cytoplasmic cells are alive or dead. As shown in Figure III-6, "coquillage" cells showed green fluorescence, while cells with cytoplasmic accumulation of Neo-Cy5 emitted red fluorescence. There is, however, one problem with the Neo-Cy5 cytoplasmic cells to evaluate if they are dead. Cy5 signal can slightly leak through the RFP filter set that is used for PI dye detection resulting in a contribution of Neo-Cy5 to the red fluorescence levels. In fact Neo-Cy5 cytoplasmic cells have so high Cy5 signal intensity that leakage of this signal is not negligible. So in this case, it was impossible to prove that the Neo-Cy5 cytoplasmic cells are dead using this kit. One possibility would have been to increase the concentration of PI in the range where Neo-Cy5 and PI can be discriminated (Figure III-7) however we did not consider this result since the cytotoxicity of PI (incubated first) might trigger Neo-Cy5 accumulation. The proof that cytoplasmic Neo-Cy5 accumulation triggers cell death came from following experiment (see below).

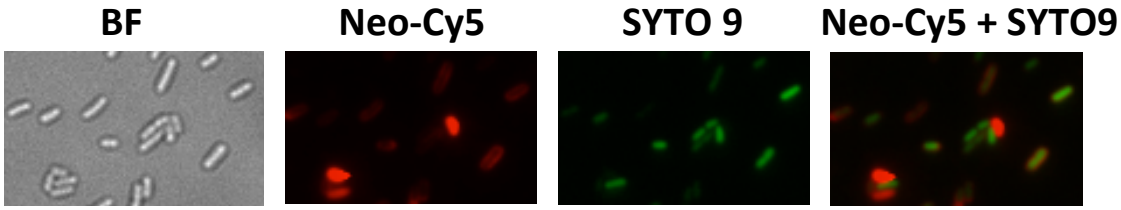

Figure III-6: *E. coli* cells were incubated with Neo-Cy5 and LIVE/DEAD kit (first with the kit as the incubation time is longer and then with Neo-Cy5). Note that the Neo-Cy5 that accumulated at the periphery in the coquillage pattern did not co-localize with the SYTO9 cytoplasmic dye. In this experiment, the PI concentration was diluted because we noticed that at the concentration recommended by the fabricant of reagents induce a high percentage of cell death (20%).

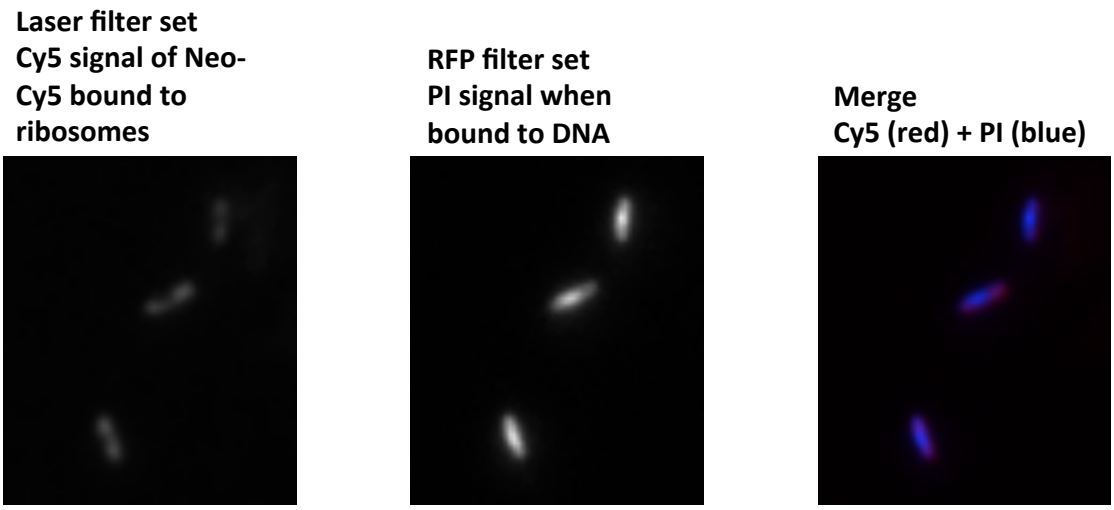

Figure III-7: At high concentration of PI, Neo-Cy5 and PI fluorescent signals can be discriminated.

Cells were left on agarose pad overnight under the microscope. Indeed, division of cells with cytoplasmic uptake was not detected any longer, suggesting that cells with absorption of Neo-Cy5 inside the cytoplasm were dead. On the contrary, cells with the "coquillage" pattern continued to divide (Figure III-8 and top panel Figure III-10).

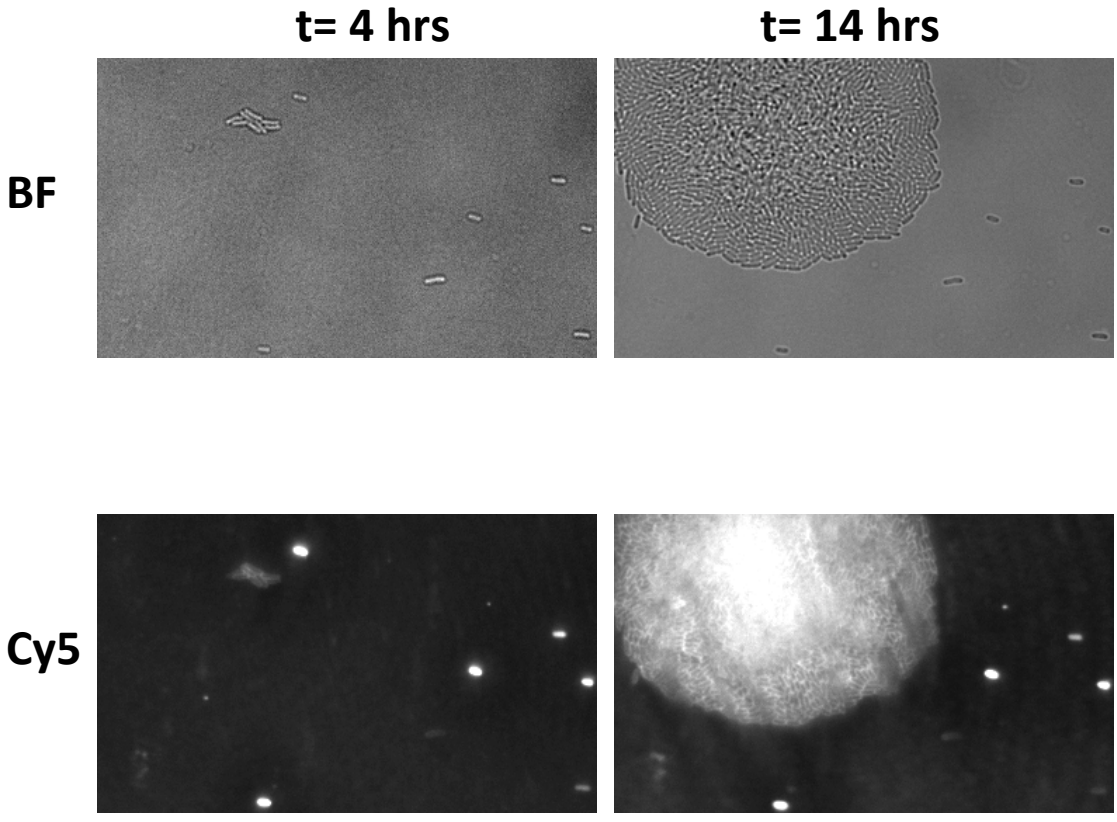

Figure III-8: Cells with cytoplasmic Neo-Cy5 accumulation are dead. *E. coli* cells MG1655 were exposed to Neo-Cy5 (8 μM). One cell with the "coquillage" pattern divided to form a colony after over night growth. None of the cells with cytoplasmic uptake could divide. Note that a low residual concentration of Neo-Cy5 tends to always remain even after several wash steps, which explains the accumulation in the bacteria forming the colony.

III. 2. 4. 5 Neo-Cy5 localization at the septum during cell division

Time-lapse imaging of *E. coli* strain SQ171 transformed with a plasmid carrying kanamycin resistant gene after treatment of Neo-Cy5 gave more information on the formation of the septum (Figure III-9). High accumulation of Neo-Cy5 appeared just before and after the cell division. The same observation was made with the strain MG1655 but unfortunately the imaging was of lower quality.

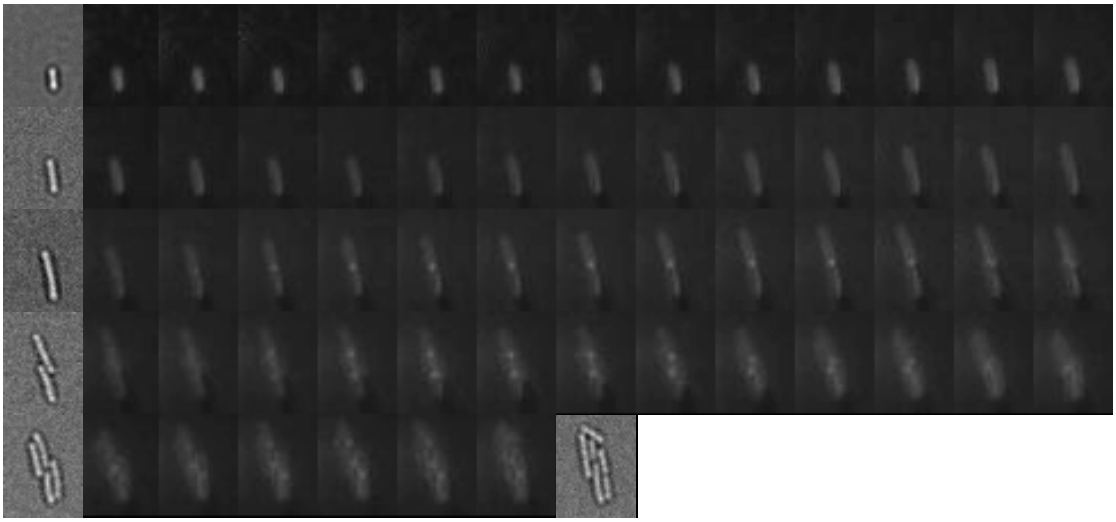

Figure III-9: Time-lapse imaging of *E. coli* SQ transformed with a plasmid carrying a neomycin resistant gene after 30 min treatment with 8 μM Neo-Cy5. Strong signal accumulation at the septum is detectable for each division. This accumulation is clearly visible in third and fourth rows. Images were taken every 5 min. Bright field images for each rows are given as well as the one at the end of the experiment.

III. 2. 4. 6 Fate of bacteria with cytoplasmic accumulation

The final action of cells treated with a lethal doze of neomycin is a loss of membrane integrity. This was shown in 1960 in the laboratory of B. Davis by detecting nucleotides or amino acid leakage in the medium (133). Here, I incubated cells with 8 μM Neo-Cy5 in M9 minimal medium, which is near the MIC value, for 50 minutes and followed the intracellular fluorescence signal of cell that accumulated high levels of Neo-Cy5. Before mounting cells on the agarose pad, excess of Neo-Cy5 was removed by washing with M9 medium. Cells that were strongly fluorescent at first lost the fluorescence one after another during the acquisition (Figure III-10). We interpreted this as leakage of Neo-Cy5 in M9 medium. We noted that in MOPS that has a low content in phosphate this leakage of Neo-Cy5 was not observed even after over night incubation under the microscope (Figure III-8).

III. 2. 4. 7 Where Neo-Cy5 accumulates exactly in "coquillage" pattern?

MG1655 was transformed with pGex-Spinach-mini plasmid where rRNA gene with Spinach-mini that was constructed in the previous chapter is inserted downstream of *tac* promoter. MG1655 expressing Spinach-mini tagged ribosome, which was induced by IPTG, was incubated with DFHBI prior to be treated with Neo-Cy5. Then cells were observed with both GFP filter and the Cy5 laser filter set (Figure III-11). The superposed images of GFP and Cy5 showed that in the "coquillage" pattern, the Cy5 signal was located slightly outside Spinach ribosome localization, which provides a demarcation of the cytoplasmic area. This observation supports the hypothesis that Neo-Cy5 is distributed in the periplasm in the "coquillage" pattern. However with the poor resolution we cannot rule out the possibility that Neo-Cy5 locates in the inner part of the cytoplasmic membrane. Note that this result is similar to the imaging of *E. coli* cell by SYTO9 and Neo-Cy5 on Figure III-6.

Next I focused on cells with cytoplasmic Neo-Cy5 accumulation. Selection of the strongest signals with both Spinach and Cy5 revealed a co-localization (Figure III-10; middle panel). It is reasonable because the main binding target of neomycin is the ribosome inside bacteria.

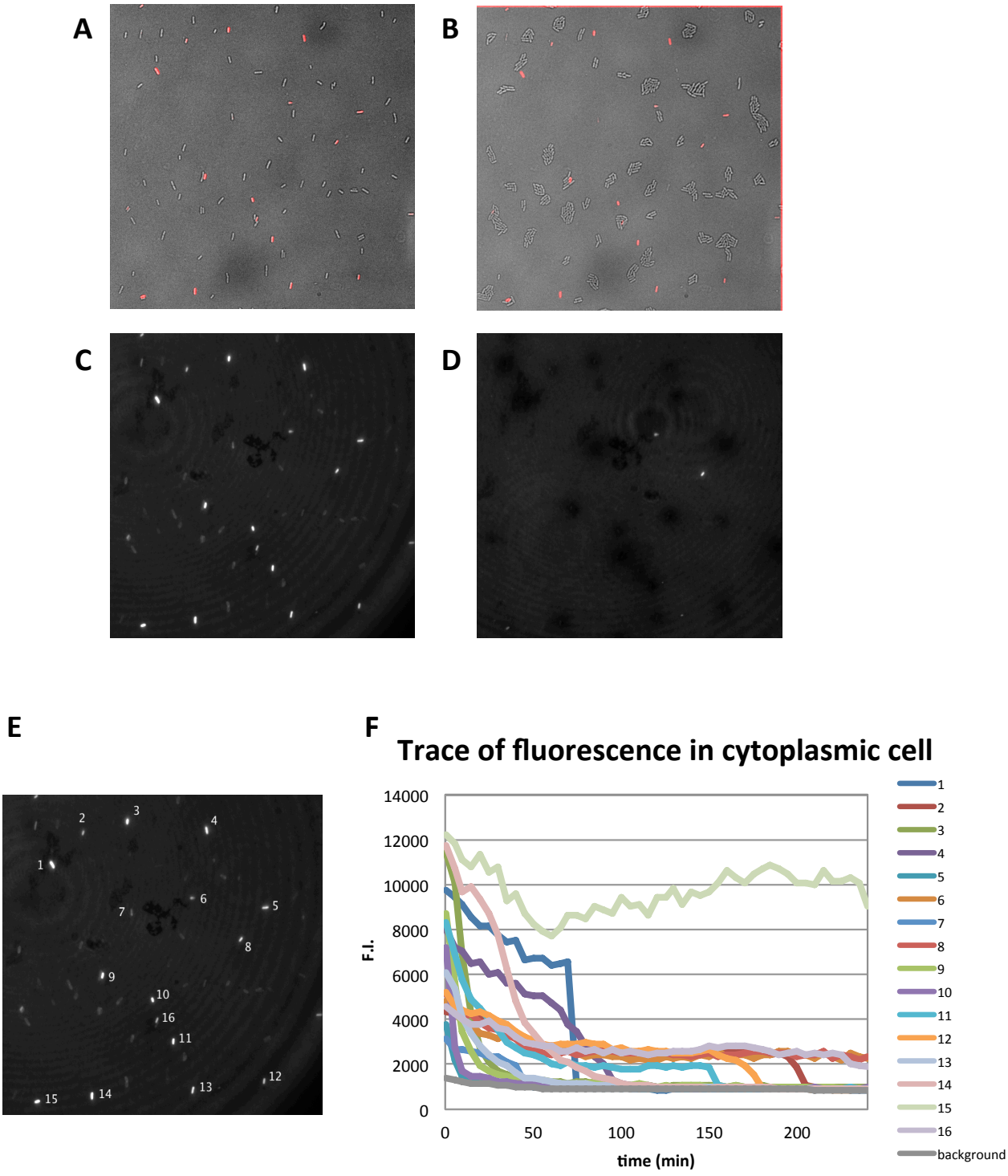

Figure III-10: Time-lapse observation of *E. coli* cells exposed to Neo-Cy5. (A) Brightfield and fluorescence image (red) overlaid recorded at the beginning of the experiment. (B) Same representation except for the brightfield image recorded at the end of the experiment. (C) Neo-Cy5 fluorescence signal at t=0 hr. (D) Neo-Cy5 fluorescence signal at t=4.5 hrs. (E) Cells were numbered and their levels of fluorescence monitored. (F) The measured fluorescence of each cell is plotted versus time. The decrease of fluorescence corresponds to Neo-Cy5 leakage in M9 medium due to membrane permeability.

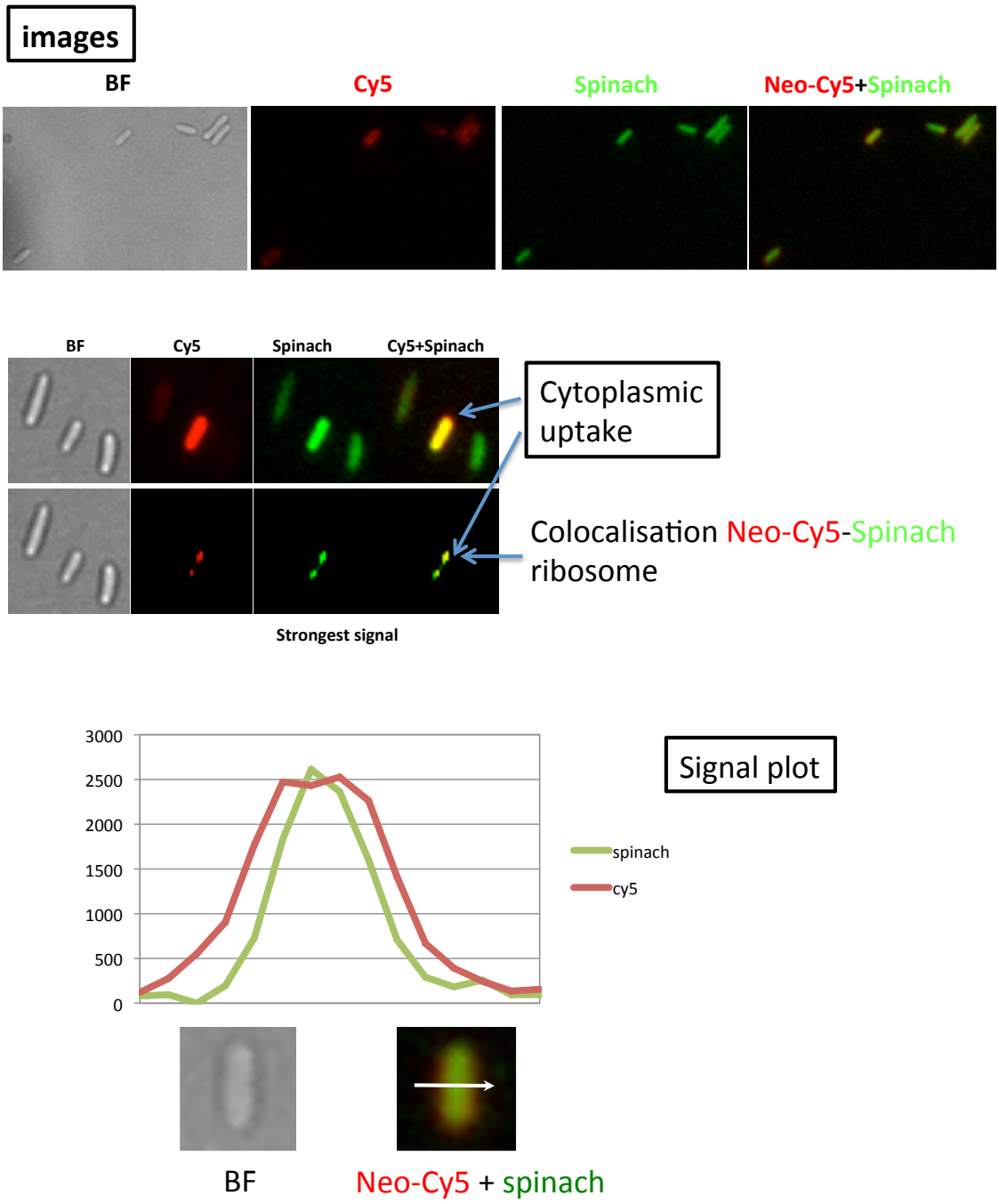

Figure III-11: *E. coli* cells expressing Spinach-mini ribosomes were exposed to Neo-Cy5 and imaged after a washing step. Top panels: imaging of cells for Spinach or Neo-Cy5 fluorescence. Middle panels: selection of the brightest signals for Spinach and Neo-Cy5. Bottom panels: plot of a cross section fluorescence signal for a representative cell harboring the "coquillage" pattern.

III. 2. 5 Going further with super-resolution microscopy

For improving our understanding of Neo-Cy5 localization, we worked out conditions to collect data using 2D and 3D dSTORM on live *E. coli* cells at the IMAGIF platform. Cells were immobilized for imaging either on agarose pad or on glass slides treated with poly-lysine. Reagents for depleting oxygen and assisting the transition of Cy5 into the dark state were added to cells. Oxygen depletion in the periplasm would be immediate as molecules of oxygen freely diffuse in and out by porins and more slowly through the membrane (153). It is usually considered that molecules with a molecular mass of less than 500 Da freely diffuse *via* porins (154). On the contrary, O_2 depletion in the cytoplasm might be slower and to occur only following the Neo-Cy5 treatment as the inner membrane integrity will be lost. In this case, information about the localization of cytoplasmic Neo-Cy5 molecules would only be accessible in the final stage of the action of the antibiotic.

After acquisition, images were reconstituted at the IMAGIF platform and analyzed. Three cells with each typical Neo-Cy5 accumulation pattern are shown in Figure III-12. Every dot in the images indicates a single molecule of Neo-Cy5. Dots are colored depending on the depth from the observation surface. In 2D image of "coquillage" cell, some Neo-Cy5 molecules were detected in the center (data not shown). However, in the 3D images, we confirmed that these molecules are actually located around the cell membrane therefore in this pattern there is no molecule of antibiotic present in the cytoplasm. In contrast, uniform distribution of Neo-Cy5 inside the cell was shown in the case of cytoplasmic accumulation (Figure III-11, A). For dividing cells, we clearly see strong signal at the septum. Two reasons could explain such a strong signal i) Neo-Cy5 binds molecules at the septum that present slow diffusion, therefore the fluorescence signal appears stronger with a better resolution in 3D STORM, ii) Neo-Cy5 binds to target(s) at the septum and strongly accumulate locally generating this strong signal. At this moment, the target of Neo-Cy5 at the septum is unknown. However, cells with "coquillage" pattern divide normally concentrating the drug at the septum at the moment of the division and this does not affect the bacteria, which continues to divide. Therefore it is likely that the binding of Neo-Cy5 at the septum has no effect on cell viability.

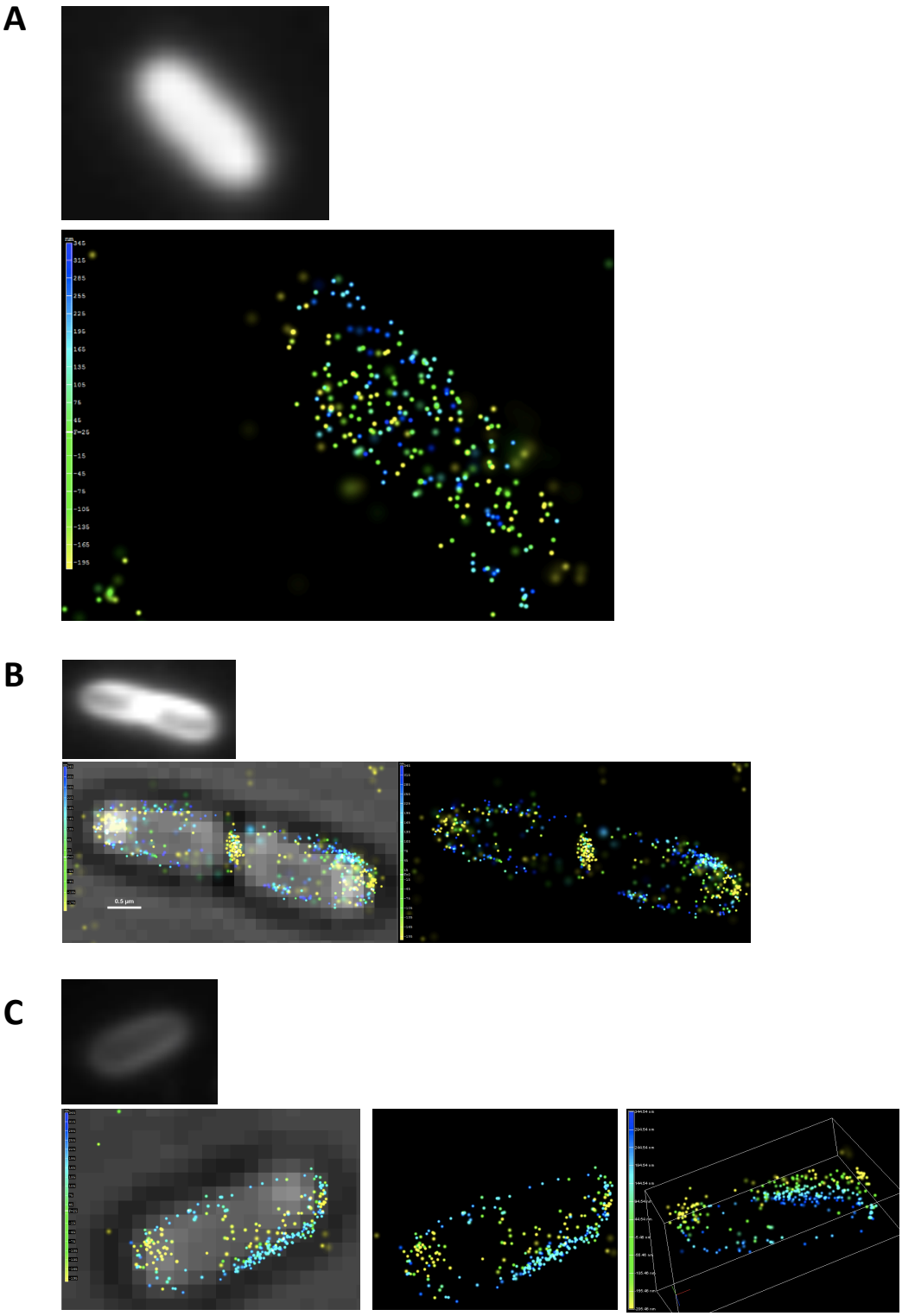

Figure III-12: Patterns of Neo-Cy5 localization in live *E. coli* cells. Images were obtained on the super-resolution microscope at the platform IMAGIF. (A) Cell with cytoplasmic uptake (bright signal). (A bottom) Same cell as in A imaged by 3D super-resolution dSTORM (molecules are color coded according to their position in z axis). (B) Representative image of the pattern observed for dividing cells showing accumulation at the periphery and at the septum. (C) Peripheral localization of Neo-Cy5 in MG 1655 cells.

III. 2. 6 Single cell analysis of Neo-Cy5 uptake

Since we can visualize the accumulation of Neo-Cy5 and classify cells according to their pattern of accumulation, this is an opportunity to perform a single cell analysis and evaluate the effects of experimental conditions on the uptake by a cell population.

III. 2. 6. 1 Strategy for single cell analysis histogram

Here from the laser image of Cy5 fluorescent signal, I made a histogram for visualizing the effects of several parameters on Neo-Cy5 uptake. This analysis is performed at the single cell level. To quantify the Neo-Cy5 accumulation levels, I built the strategy shown in figure III-13. The average fluorescence intensity of Cy5 signal within each cell region was measured (contours of cells are determined based on brightfield image). This value is therefore independent of the cell dimension. An average background value (usually 500 arbitrary units) was subtracted from the average fluorescence value measured. The percentage of the cell that accumulated the Neo-Cy5 in cytoplasm is shown in white bars in each histogram. In a reproducible way, a transition occurs between the “coquillage” and “cytoplasmic” patterns, which corresponds to a value of fluorescence intensity of 1000 arbitrary units. It should also be mentioned that the graphical representation of this data is difficult because the fluorescence signal of the cellular cytoplasmic uptake occurs on a wide range compared to the distribution of the “coquillage” pattern which is much more restricted. Therefore, up to 1000 arbitrary units, cells are classified by intervals of 100 units (or 50 units in some histograms below) whereas above 1000 units each interval contains 1000 units. This creates a distortion in the graph at 1000 but allows visualizing the full set of data on a single graph.

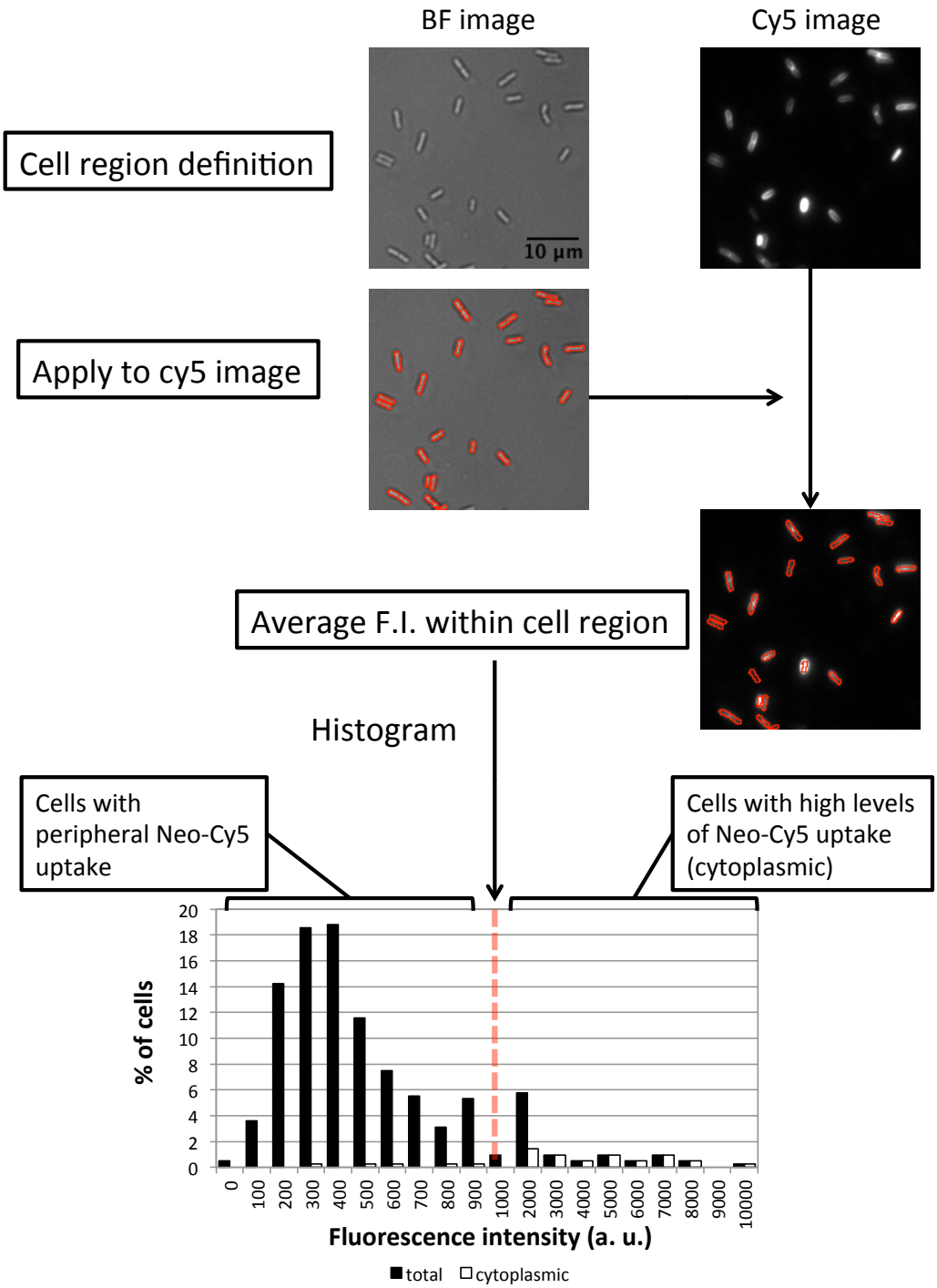

Figure III-13: Strategy of performing a single cell analysis. Brightfield and fluorescence images are taken on the same area. Bacterial cell contours are automatically identified and the average fluorescence signal within each bacterium is determined. Assignment of localization pattern was done by visual cell-by-cell. An example of such a histogram is shown at the bottom. The number of cells exhibiting certain range of fluorescence are counted and shown in histogram. Information on localization is also included in the histogram. Reproducibly, the transition from "coquillage" pattern to cytoplasmic occurs around a value of 1000 (a. u.) of fluorescence indicated here by a red line.

III. 2. 6. 2 MOPS and M9 medium

As mentioned above, the MIC values of neomycin and Neo-Cy5 for *E. coli* strain MG1655 were different in M9 and MOPS minimal media. In M9 medium, higher concentration of neomycin is required to kill *E. coli*. Medium can affect the neomycin uptake by *E. coli* (152) and here M9 minimal medium reduces the efficiency. MG1655 was incubated for 2 minutes with Neo-Cy5 (0.4 μM) in M9 or MOPS minimal medium respectively to compare the Neo-Cy5 uptake levels with a histogram. The histograms of uptake of Neo-Cy5 in MG1655 showed an increase in the percentage of cells with strong signal intensity (cells with cytoplasmic accumulation) in MOPS compared to M9. In MOPS, these cells with cytoplasmic uptake represented about 10% of the total number of cells (Figure III-14). Thus in the following sections, all observations were performed using MOPS minimal medium instead of M9.

Possible factor that caused such a difference in efficiency is the concentration of phosphate in each media. M9 contains higher concentration of phosphate than MOPS. Neomycin binds phosphate groups of target RNA site. High concentration of environmental phosphate might reduce the availability of the antibiotic for bacterial uptake.

III. 2. 6. 3 Uptake and time of exposure

It was previously observed that the accumulation of neomycin is dependent on the time and concentration of exposure (124). We wanted to test how these parameters affect the distribution of the patterns at the single cell level. Here I changed the incubation time: 2, 5, 10 and 30 min for a concentration of Neo-Cy5 at 0.4 μM. It is clear that the accumulation level increases as time proceeds (Figure III-15). After 2 min incubation, about 50 % of the cells had very low Cy5 signal as shown in the left two bars of the histogram. The percentage of these cells diminished in the 5 and 10 minutes incubation results, and finally disappeared after 30 min incubation.

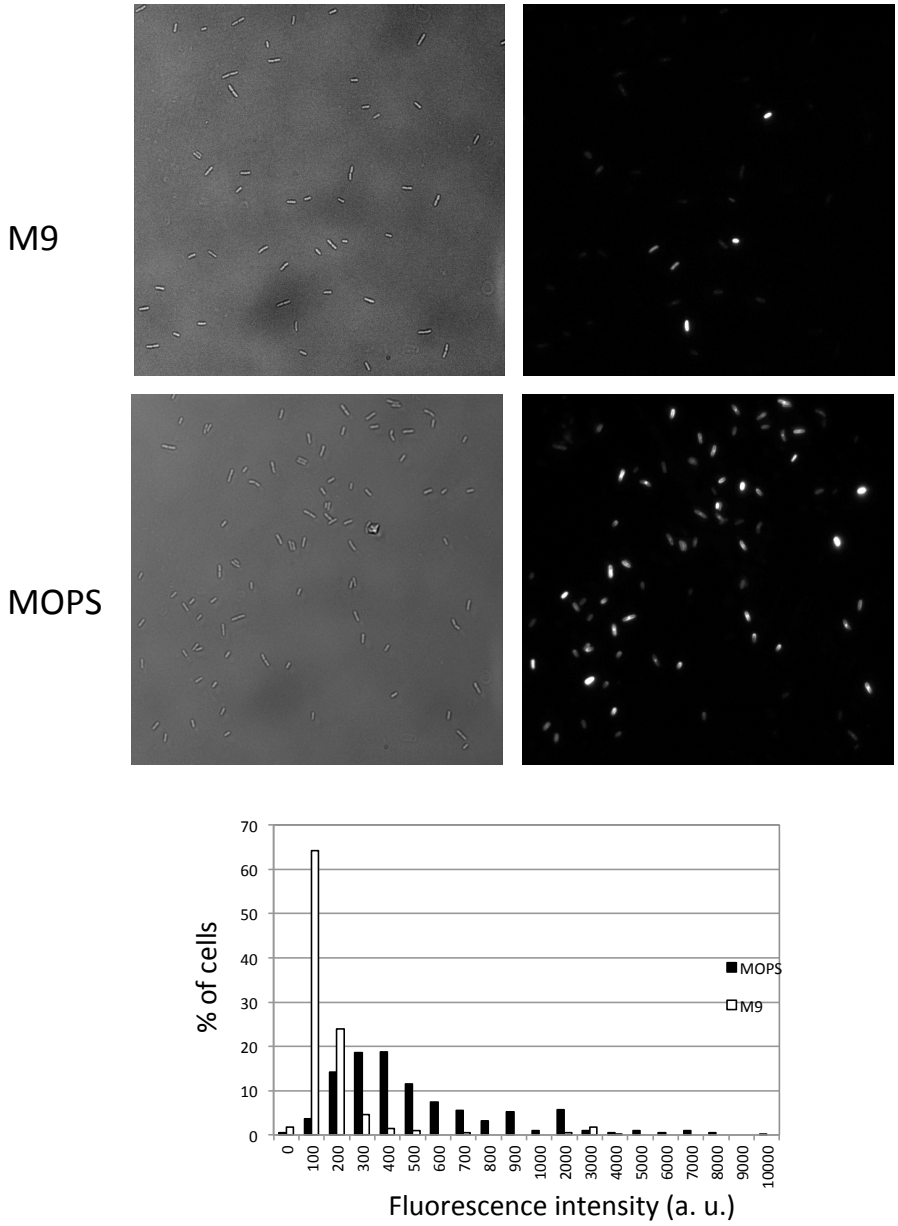

Figure III-14: Choice of the minimum media for observation of Neo-Cy5 uptake. Cells were exposed to the same concentration of drug (0.4 μM) and for the same incubation time (2 minutes). Levels of uptake were analyzed by fluorescence microscopy and are represented as a histogram for a direct comparison of M9 and MOPS media.

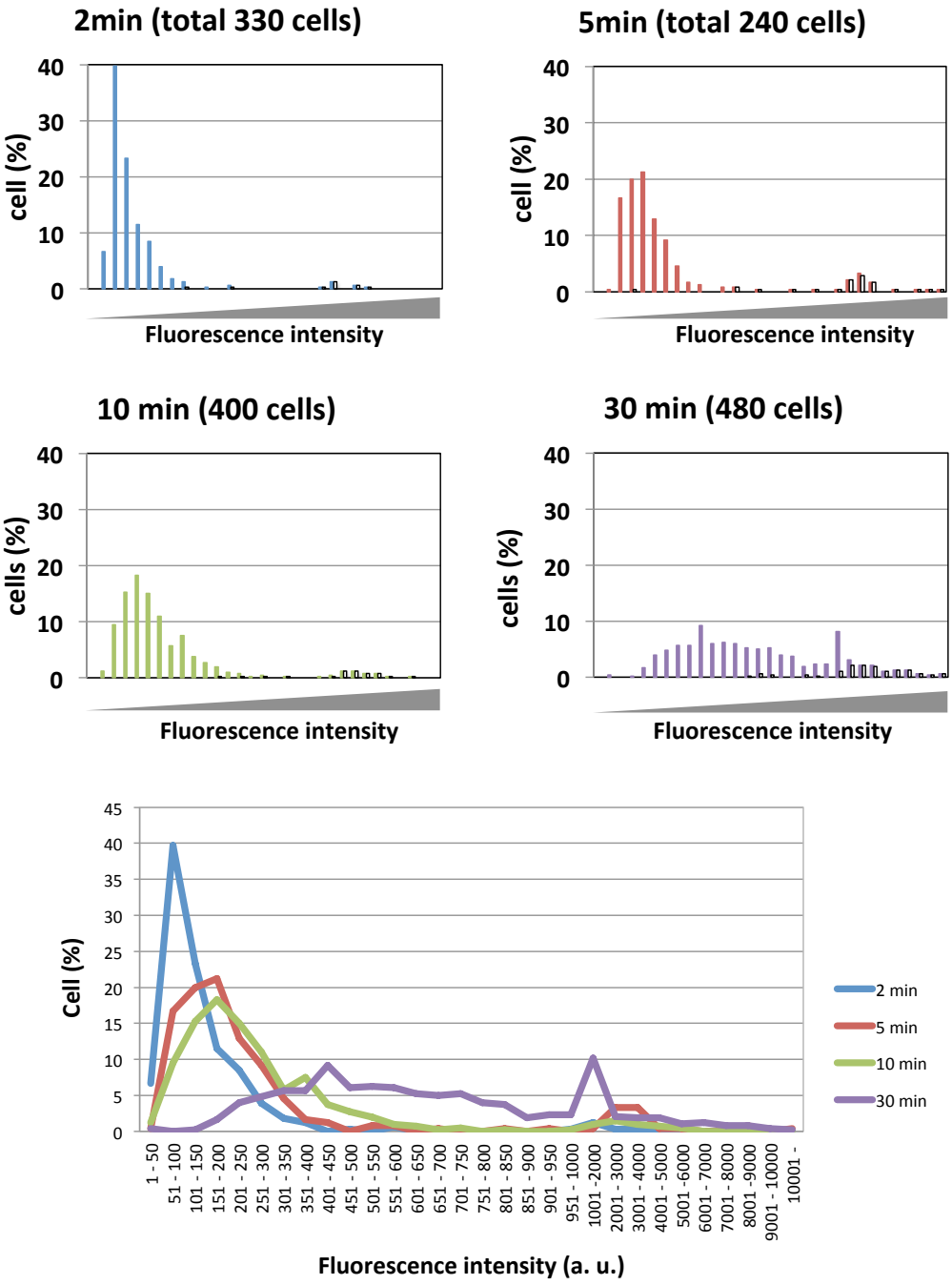

Figure III-15: Time dependence of the accumulation of Neo-Cy5. *E. coli* cells from a culture at 0.3 OD_{600} were incubated for different time with the antibiotic and imaged under the microscope. Data are presented in the form of histograms (scale of fluorescence intensities are the same) and summarized in the plot at the bottom. Note that cells were classified by fluorescence intensities every 50 units up to 1000 (left part of the graph) and then every 1000 units (right part of the graph).

III. 2. 6. 4 High concentration of Neo-Cy5: 2μM, 4μM and 8μM with short incubation

I then investigated the effect of concentration of the antibiotic. I added 2, 4 and 8 μM of Neo-Cy5 into the cell culture for 2 minutes, then collected cells, washed them to remove the excess of Neo-Cy5 and imaged them for Cy5 fluorescence. Increasing the concentration of Neo-Cy5 enlarged the percentage of cells with very strong signal. At a concentration of 2 μM, the majority of cells were found in the "coquillage" pattern and about 19% of cells accumulated Neo-Cy5 in the cytoplasm and these cells represent all of the bright cells (see Figure III-16, white bars top panel). At 4 μM, the fluorescence of the "coquillage" pattern increased. This is detected as a shift of the fluorescence on the histogram whereas the intensity of the cytoplasmic uptake was not strongly affected. Only the percentage of cells with "cytoplasmic" uptake slightly increased. For a concentration of 8 μM, (twice above the MIC value), the trends observed for the "coquillage" patterns at 2 and 4 μM continues as the "coquillage" cells became brighter with now fluorescence signals above 1000 arbitrary units (Figure III-16, difference between the green bars (total cells) and the white bars (cytoplasmic)). Again, the percentage of cells with cytoplasmic uptake increased from 22 to 29%.

Overall, the data clearly show that accumulation at the periphery is directly dependent on the external concentration of antibiotic at the same time of exposure. This could suggest a diffusive mechanism through the outer membrane *via* a route that remains to be characterized (see introduction). To obtain a clear answer, the data of only "coquillage" cells was further analyzed where the average signal per cell was plotted against the concentration of drug (Figure III-17). This experiment needs to be redone as for the moment samples were analyzed in a row and unfortunately imaging of points at 4 μM and 8 μM were delayed (it can be as much as one hour). This may have introduced a bias in the analysis due to very slow Neo-Cy5 leakage outside the bacteria resulting in a decrease of fluorescence. The same analysis will be performed for the cytoplasmic cells.

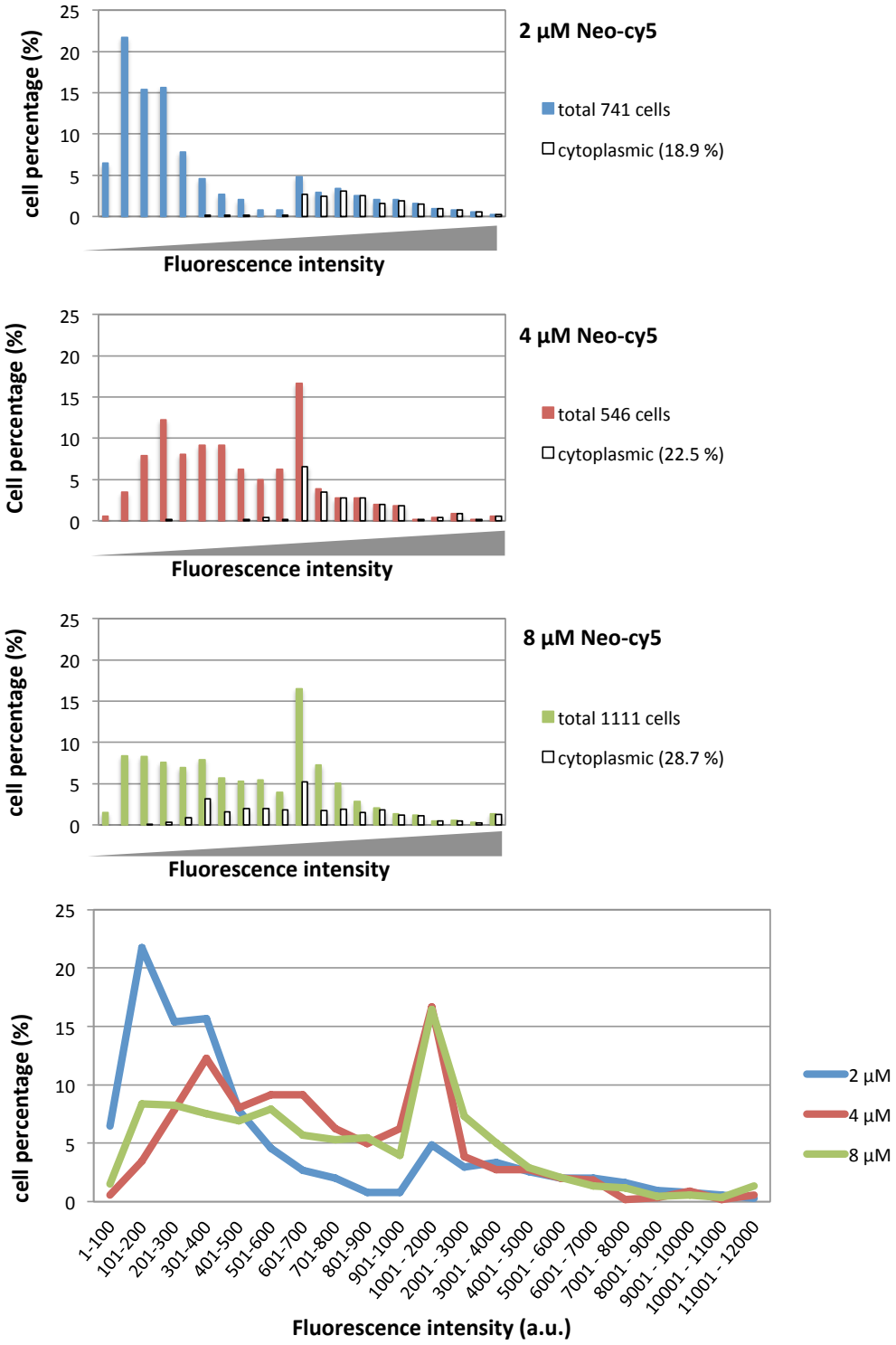

Figure III-16: Effect of the concentration of Neo-Cy5 on the uptake by *E. coli* MG1655 (culture at 0.3 OD_{600}. Time of exposure to the drug was 2 minutes. At the bottom, for clarity, the data are presented as plots rather than with a histogram.

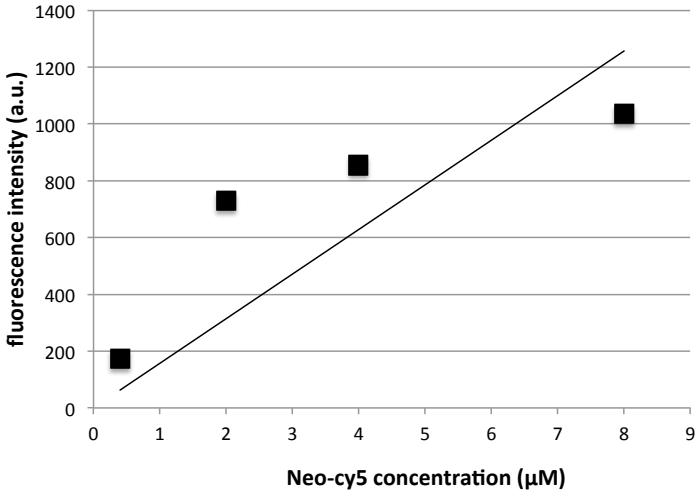

Figure III-17: Irreversible accumulation of the cell periphery as a function of the external concentration of Neo-Cy5. Cells were exposed to the drug for 2 minutes.

III. 2. 6. 5 Cell concentration

It was previously observed that diluting cells in water prior to antibiotic exposure increased the level of accumulation (152). However in this experiment two parameters were changed: the cell density and the concentration of salts in the media. Here we could clearly visualize the effect of cell density by performing our single cell analysis with the usual condition (cell culture of 0.3 OD_{600}) and then with a 10 and 100 fold dilutions in MOPS. The fraction of cells with cytoplasmic accumulation drastically increased close to 90% for cells exposed at an OD_{600} of 0.003 (Figure III-18). We tested if the medium of culture was responsible for such a result. A cell culture was collected at an OD_{600} of 0.3 and centrifuged to remove all bacteria. The supernatant was used for a dilution to an OD_{600} of 0.003. We obtained similar results indicating that dilution of bacteria in fresh media is not the cause of this strong efficiency of cytoplasmic uptake. This still remains difficult to explain especially considering that even with an OD_{600} of 0.3, an external concentration of Neo-Cy5 of 0.4 μM represents a huge reservoir for uptake.

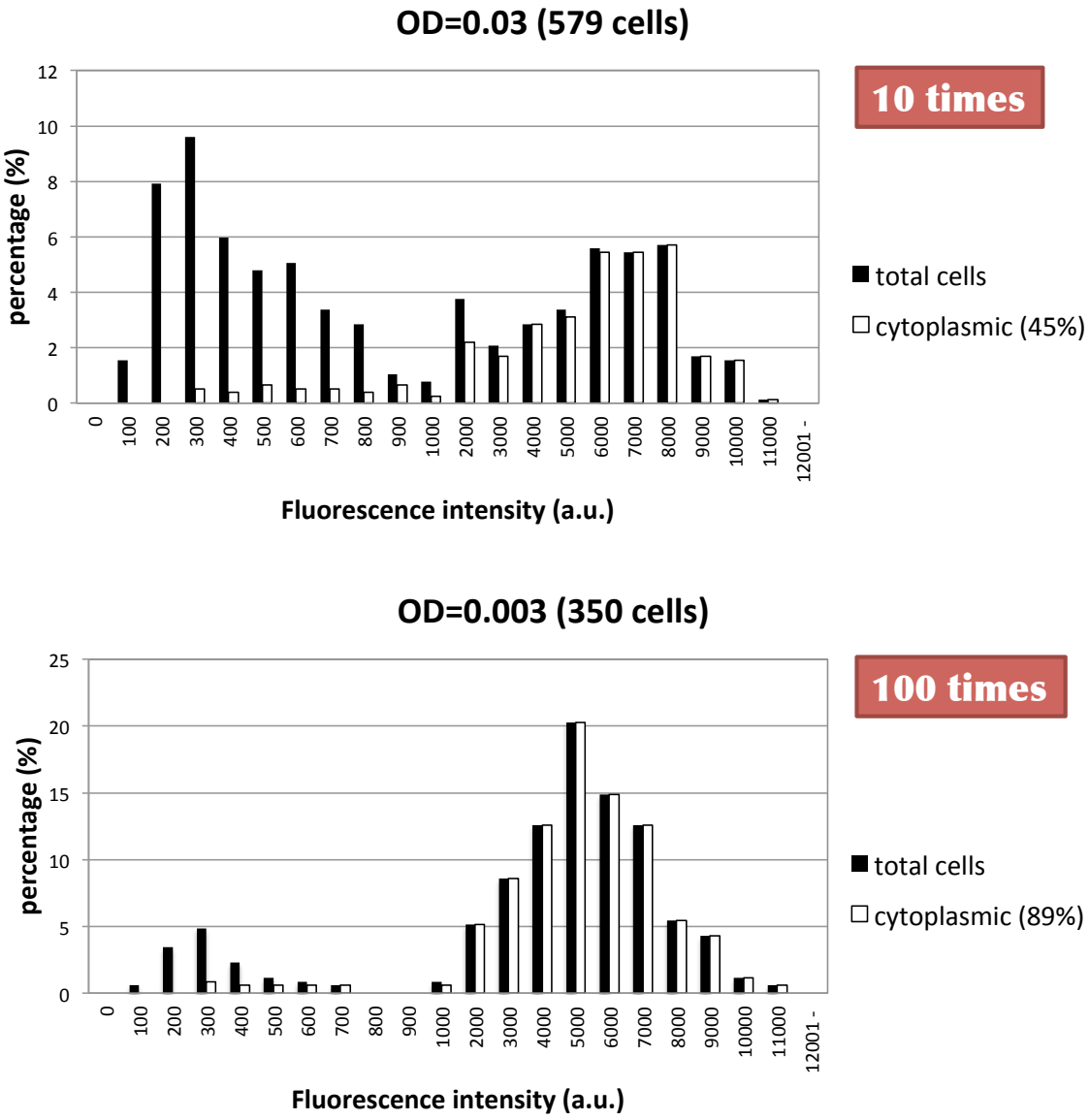

Figure III-18: Representative distributions of fluorescence levels in *E. coli* for cell densities of 0.03 or 0.003 for exposure to Neo-Cy5 at 0.4 μM. In these experimental conditions, 45% and 89% of cells have cytoplasmic uptake respectively.

III. 2. 6. 6 Effect of CCCP on Neo-Cy5 uptake

Aminoglycoside that crossed through the outer membrane of *E. coli* accumulates probably in the periplasm. Next step is crossing the inner membrane for the entry into the cytoplasm, which depends on the proton motrice force (PMF). The PMF results from the proton gradient that is established during the normal activity of electron carriers in the electron transport chain. To validate this transport model, Carbonyl cyanide *m*-chlorophenyl hydrazone (CCCP) has been previously used. CCCP is one of protonophore that allows protons to cross lipid bilayers leading to a decrease

of the proton gradient. It means that cells treated with CCCP do not uptake neomycin. This mechanism is still not understood in detail. The aim of this experiment was to check how the effect of CCCP impacts our results of Neo-Cy5 uptake. Here CCCP was added to cell cultures to concentrations of 40 μM or 100 μM before incubation with Neo-Cy5 (0.4 μM). As shown on the histograms (Figure III-19), addition of 40 μM CCCP reduced the amount of uptake of the drug (absence of cells with very strong uptake). This gave little change in the accumulation level for the majority of cells in the culture, which are in the "coquillage" state. At 100 μM of CCCP the effect is more pronounced with a complete inhibition of cytoplasmic uptake. What CCCP inhibits is Neo-Cy5 accumulation only in the cytoplasm and not in the cell periphery.

The effect of CCCP is also toxic for living cells. As illustrated for MG1655 growth in presence 10 – 200 μM CCCP (Figure III-20), at a concentration of 100 μM, CCCP was not lethal but it affected significantly cell growth. For our single cell analysis experiments we would like to be in conditions where CCCP is not at a lethal dose. Indeed, it is said in the literature that 20 μM CCCP, which does not affect MG1655 growth at all, is enough to decrease the proton gradient. And in most of publications showing a relationship between CCCP, PMF and aminoglycoside uptake (drug concentration of usually 5 to 10 μM), concentration around 10 to 25 μM CCCP are used to measure the effect (116,140,155). In my experiments, however, at a concentration of Neo-Cy5 of 0.4 μM (which is 1/10 of the MIC), only a small fraction of cells, usually a few percent, uptake the drug in the cytoplasm. This makes the evaluation of CCCP effect difficult and indeed at a concentration of 20 μM CCCP, I was not able to detect a change in Neo-Cy5 uptake (data not shown). Therefore I increased the concentration of the drug to a lethal level by using a mixture of 4 μM neomycin combined with 0.4 μM Neo-Cy5 (5 fold the MIC of neomycin). In these conditions I could detect the inhibition of cytoplasmic uptake with 20 μM of CCCP (Figure III-21). The effect of CCCP was also confirmed with the survival assay in combination with a visual inspection of the cells (Figure III-22).

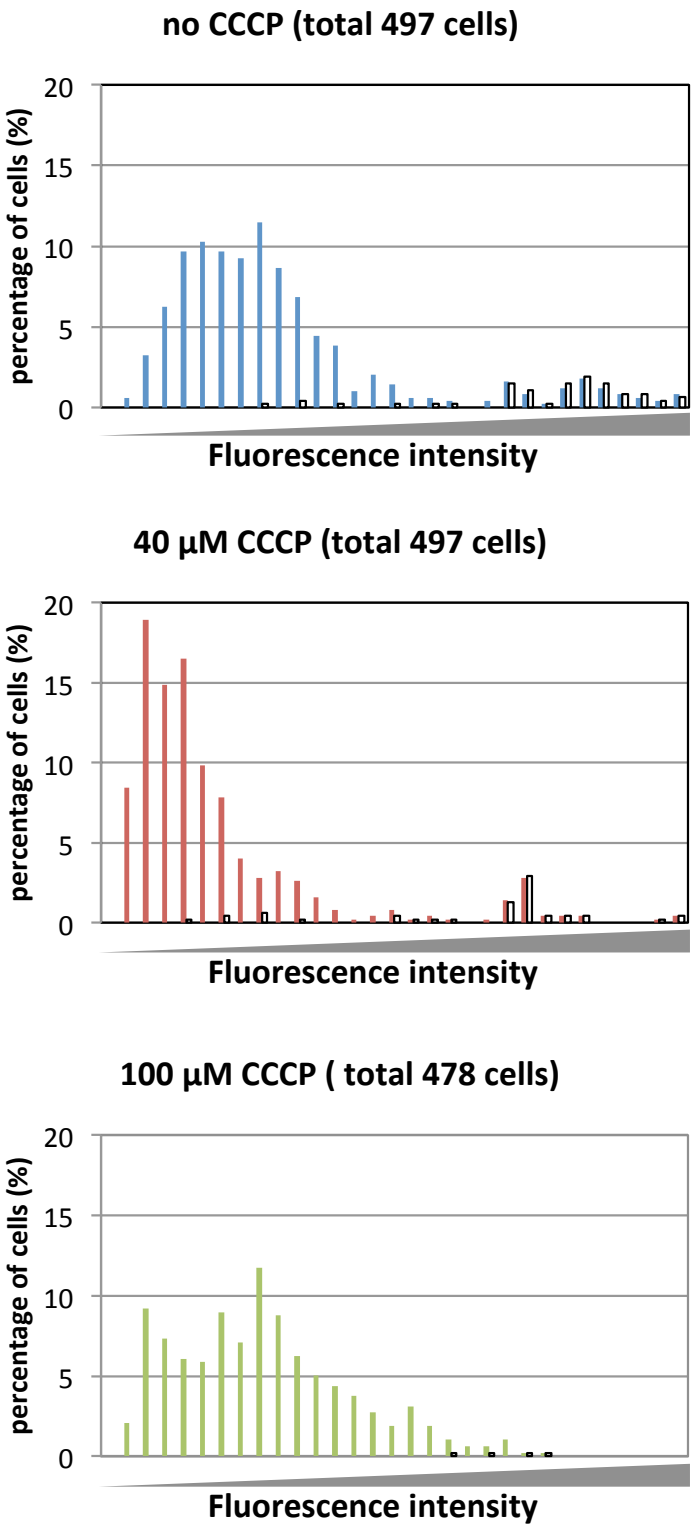

Figure III-19: Effect of CCCP on the Neo-Cy5 (0.4 μM) uptake by *E. coli* cells. CCCP inhibits cytoplasmic uptake and not the formation of "coquillage" pattern.

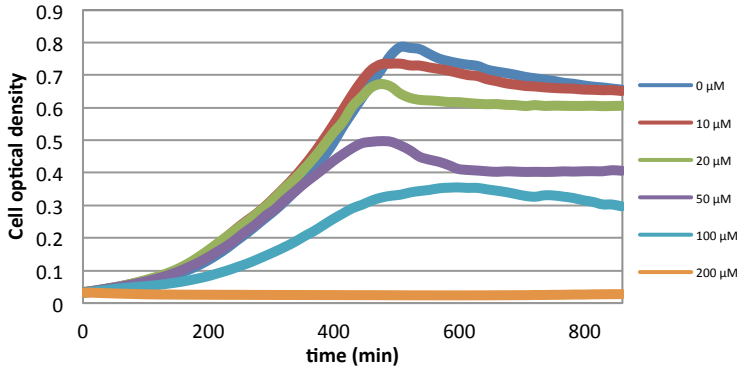

Figure III-20: Effect of CCCP concentration on the growth rate of *E. coli* MG 1655.

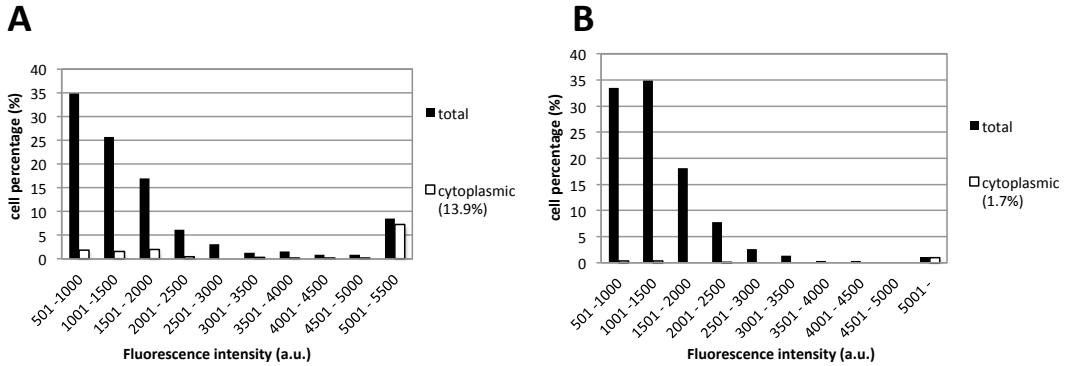

Figure III-21: Inhibition of cytoplasmic uptake with a non-toxic concentration of CCCP. (A) In absence of CCCP. (B) In presence of CCCP (20 μM).

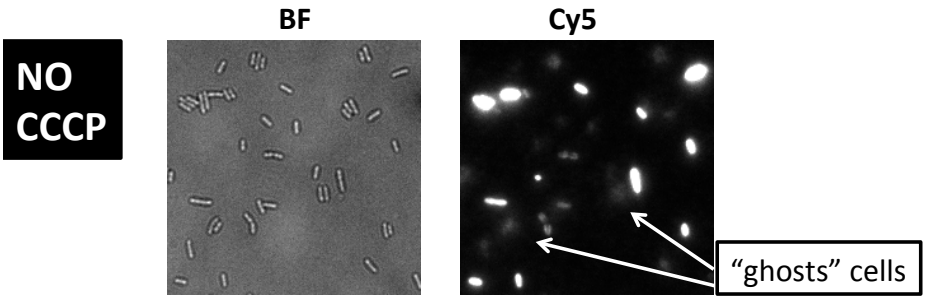

After 5 min incubation: Cytoplasmic = 98 %

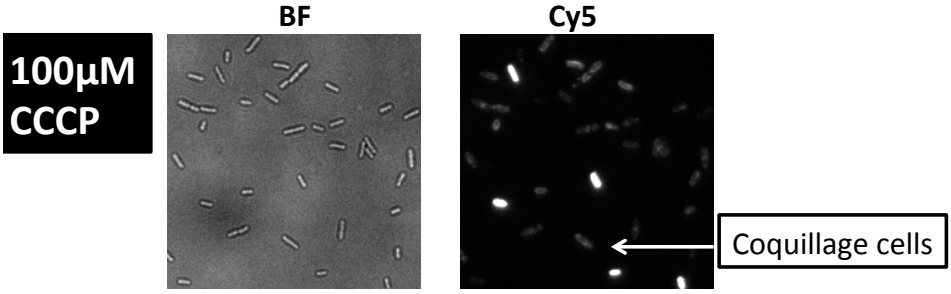

After 5 min incubation: Cytoplasmic = 8.7 %

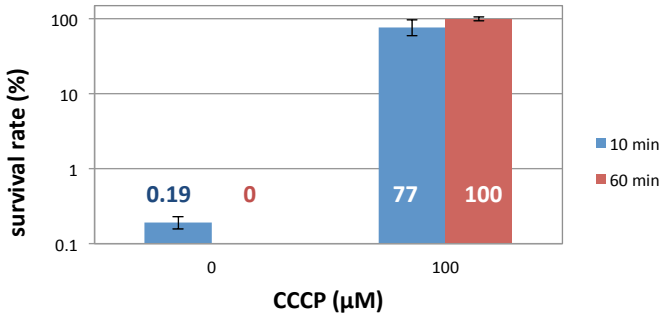

Figure III-22: Survival assay to measure the effect of CCCP. Cells at an OD_{600} of 0.3 were exposed to a mixture of 4 μM neomycin with 0.8 μM Neo-Cy5 for 5 minutes. However, the sample without CCCP was observed with a delay of 30 minutes. Without CCCP the drug acts strongly and almost all cells have cytoplasmic uptake with rapid permeabilization of the membrane leading to leakage of Neo-Cy5. In presence of 100 μM CCCP, the cytoplasmic uptake is blocked with a large population of "coquillage" cells. This correlates with the survival assay performed on the same cells where CCCP protects bacteria form the bactericidal action of the drug. Each dilution of the exposed culture was distributed in 4 different spots on a single LB plate. Error bars are standard deviation.

III. 2. 7 Is cell division a key of Neo-Cy5 uptake inside the cytoplasm?

What induces cells to change from periplasmic accumulation to cytoplasmic state? During the discussion on my annual thesis committee it was proposed that cell division opens the door for Neomycin uptake. Therefore I performed an experiment using cephalexin, an inhibitor of FtsI involved in the cell division (156). In presence of the drug, filamentation and rapid lysis of the cell occurs. Cephalexin was added to a cell culture (0.3 OD_{600}) 30 min before the incubation with Neo-Cy5 (0.4 μM). It resulted in the appearance of longer cells. Even in these longer cells, accumulation of Neo-Cy5 was detected in the middle part that corresponds to a septum (Figure III-23). On certain areas of the microscope slide, most of cells were having a septum. The single cell analysis revealed that the percentage of cells with cytoplasmic uptake was 7.2 % and 4.4 % in absence and in presence of cephalexin, respectively. At least at this concentration of the cephalexin, the change was too small to be recognized as an effect.

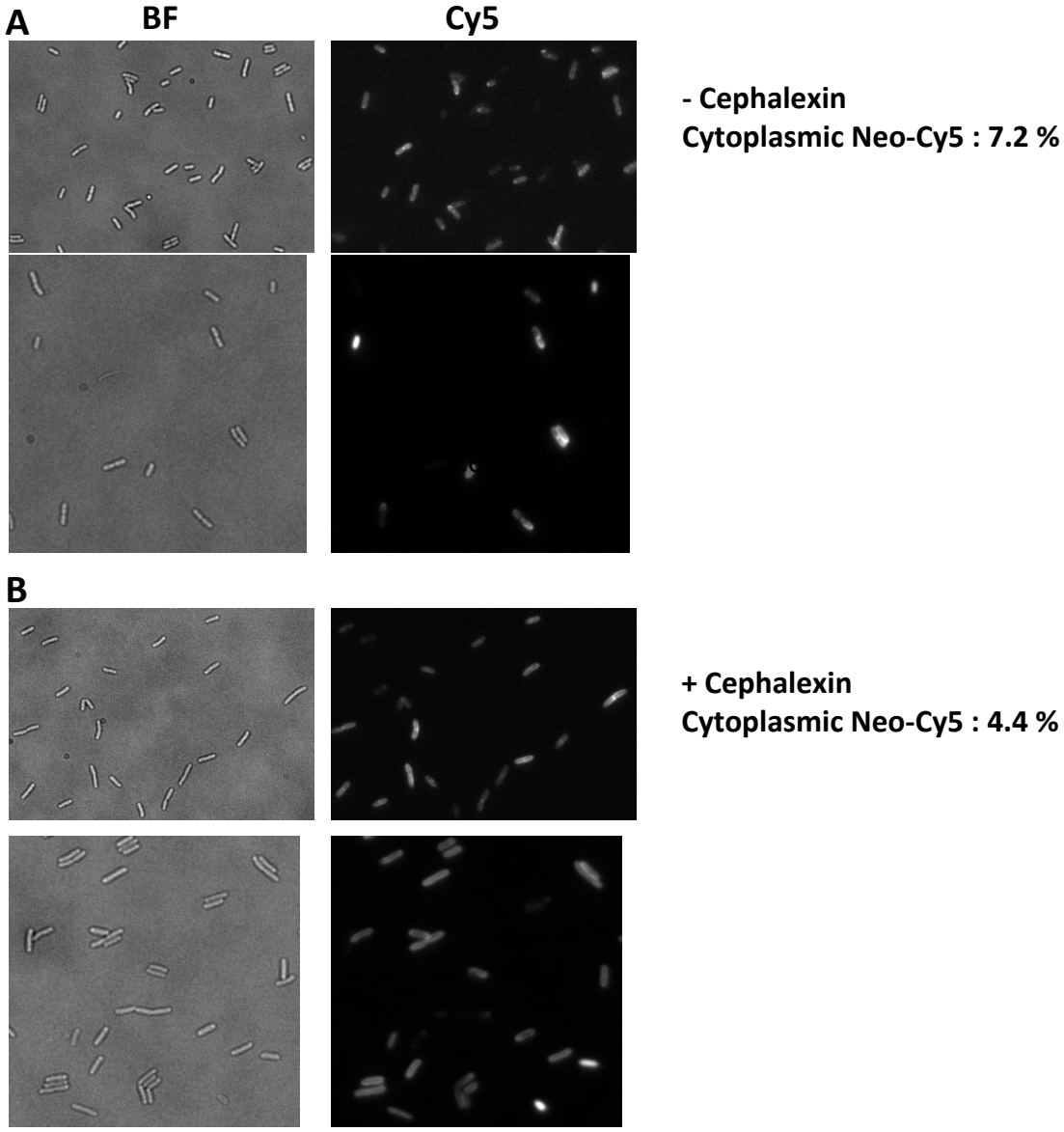

Figure III-23: Effect of Cephalexin on the Neo-Cy5 uptake. (A) Cells MG1655 in not treated with Cephalexin. (B) Cells were exposed to 10 μM of Cephalexin (MIC is 11 μM; (157)) for 30 minutes before the addition of 0.4 μM of Neo-Cy5.

III. 2. 8 Uptake by Gram-positive bacteria

After monitoring neomycin uptake by Gram-negative bacteria (*E. coli*), I characterized the Neo-Cy5 uptake by Gram-positive bacteria. Gram-positive bacteria have a thick, multilayered cell wall consisting mainly of peptidoglycan outside its inner membrane instead of the outer membrane of the Gram-negative bacteria. This peptidoglycan layer protects well Gram-positive

bacteria from physical stress but not from chemical stress because the permeability of drugs to peptidoglycan is higher compared to the barrier that represents the outer membrane of Gram-negative bacteria (158). Actually, the MIC of neomycin for *Bacillus subtilis* is reported to be 0.12 μg/mL (about 0.19 μM, which is about ten times lower than that for *E. coli*).

B. subtilis, which is a model organism for gram-positive bacteria, was used for the observation of Neo-Cy5 uptake. *B. subtilis* strain wt 168 is a single tryptophan-requiring auxotroph strain, whose derivative strains are used in virtually all academic research and many industries. Cultivation of *B. subtilis* strain wt 168 in MOPS minimal medium supplemented with tryptophan was stopped at an OD_{600} of around 0.3. The culture was incubated with 0.4 μM Neo-Cy5 for 10 and 30 minutes. After cell wash, observation was performed as done for *E. coli*.

The Cy5 image and histogram made from the recorded images are shown in Figure III-24 and 25. The "coquillage" pattern, which is the most frequent pattern in *E. coli*, in these conditions (culture at 0.3 OD_{600}), was surprisingly also seen for *B. subtilis* however it seemed to disappear quite fast (the observation needs to be confirmed and quantified). An accumulation at the septum occurs although at a much earlier stage of cell division compared to *E. coli* (Figure III-24). The histogram showed that Neo-Cy5 accumulation levels strengthened with increasing the incubation time from 10 min to 30 min (Figure III-25).

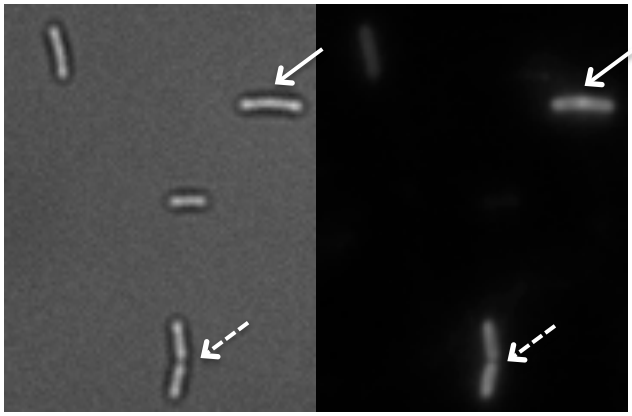

Figure III-24: Left panel is the imaging in brightfield of *B. subtilis* cells. Right panel is the same region in fluorescence after treatment with 0.4 μM Neo-Cy5 for 30 min. Note the early appearance of the accumulation of Neo-Cy5 at the septum (white arrows), which disappears at the final stage of division (white arrows with broken line).

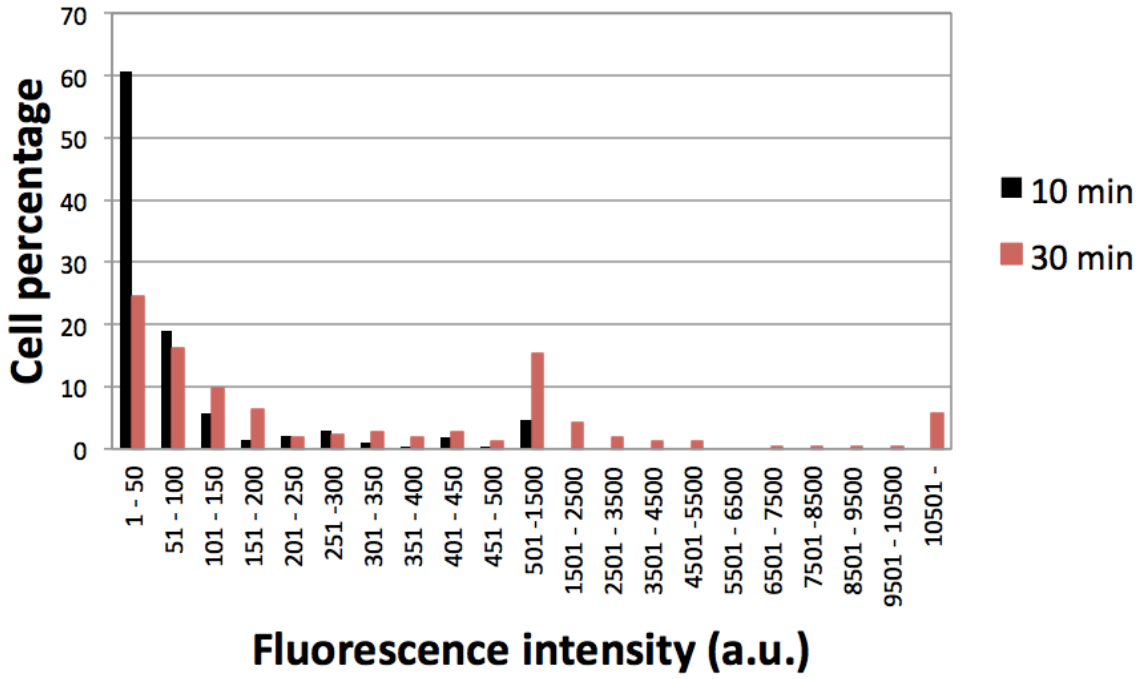

Figure III-25: Single cell analysis of Neo-Cy5 uptake by *B. subtilis* cells. Cell at an OD_{600} of 0.3 were exposed to Neo-Cy5 at 0.4 μM for the indicated time.

Surprisingly, on very rare occasions, a few cells seemed to have a "coquillage" pattern (Figure III-26). Strictly speaking, Gram-positive bacteria do not have periplasm because of the absence of outer membrane. There is, however, space between the peptidoglycan and the inner membrane, which is sometimes regarded as a periplasm and called the wall space (159).

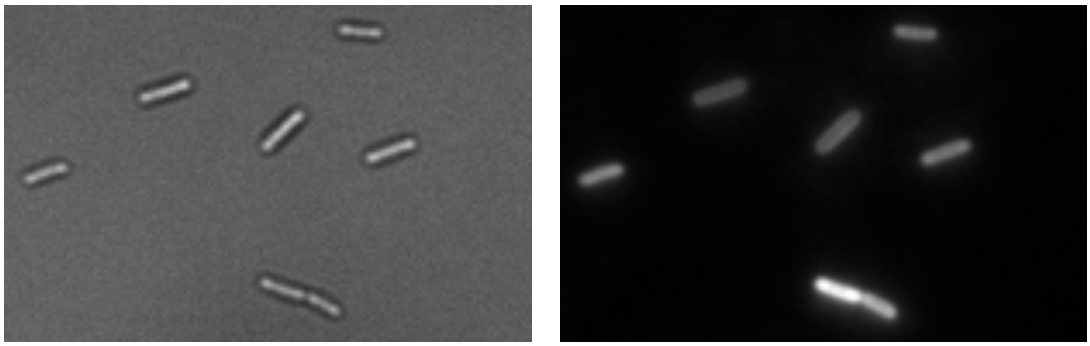

Figure III-26: Left panel brightfield imaging of *B. subtilis* cells. Right panel is the same field imaged in fluorescence.

Gram-positive bacteria also have a proton gradient that forms a PMF by accumulating proton in the gap space mentioned above. We wanted to investigate if the PMF is also strictly required for aminoglycoside uptake in *B. subtilis* as is in *E. coli*. The effect of CCCP was validated using Neo-Cy5. Since it is expected that CCCP might have larger effect on *B. subtilis*, a lower concentration of CCCP was used (10 μM). Addition of CCCP resulted in an overall decrease of Neo-Cy5 accumulation levels, while CCCP addition in MG1655 affected only part of the cell population, the one with cytoplasmic accumulation. In *B. subtilis*, CCCP addition had a drastic effect on Neo-Cy5 uptake on all cells as shown in the histogram in Figure III-27. Actually it was difficult to detect the Cy5 signal in presence of CCCP (Figure III-28).

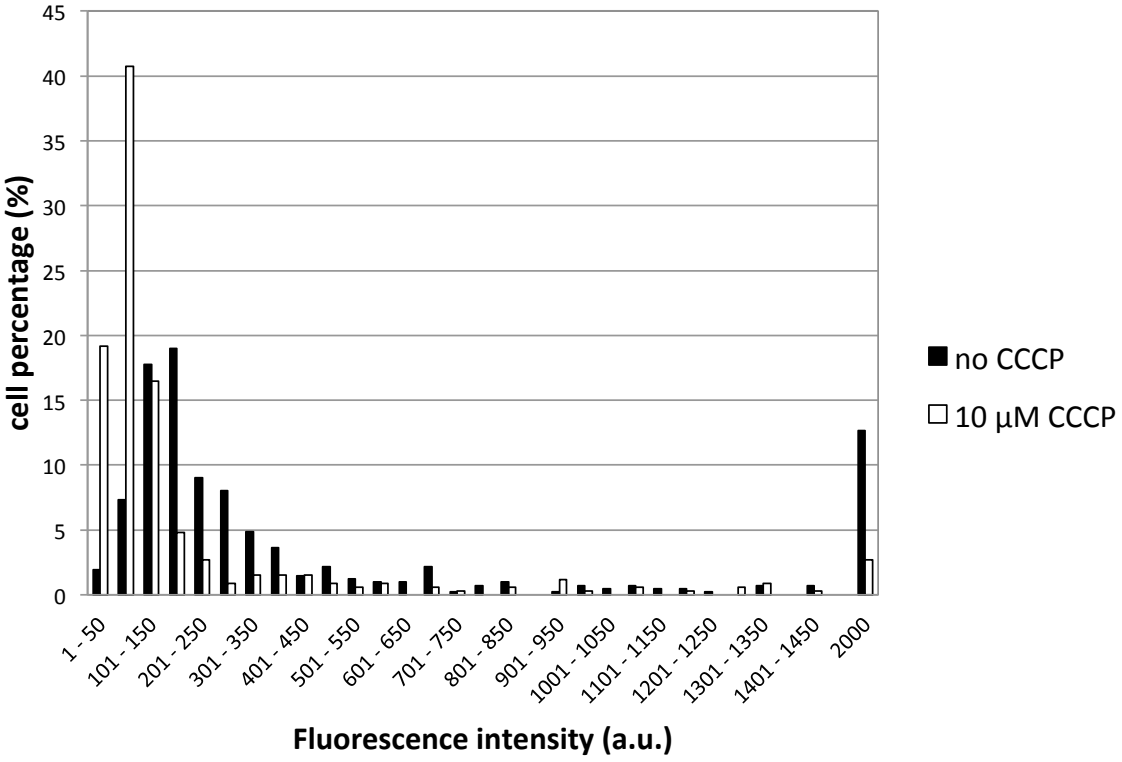

Figure III-27: Effect of CCCP on Neo-Cy5 uptake by Gram-positive bacteria.

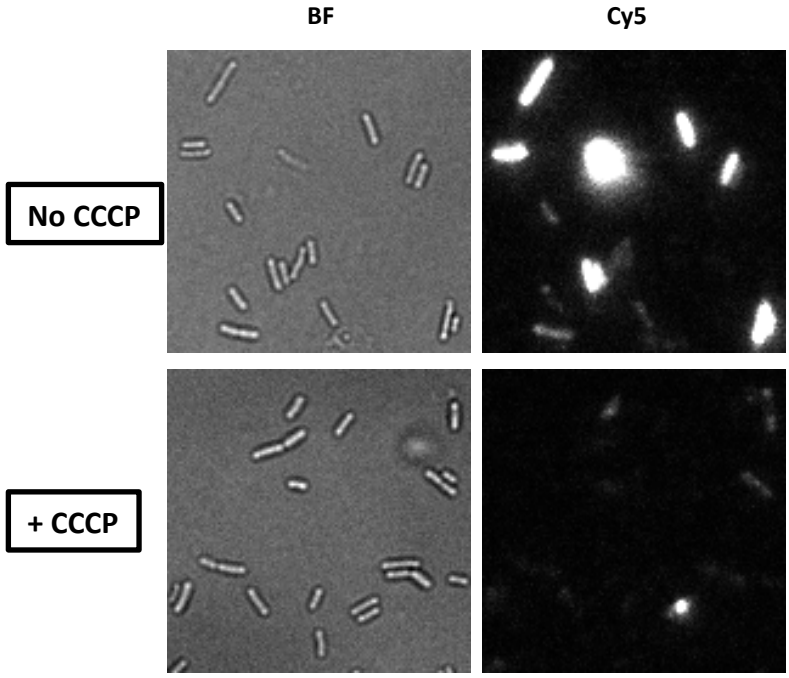

Figure III-28: Imaging of CCCP inhibition of Neo-Cy5 accumulation in *B. subtilis*. *B. subtilis* cells treated with Neo-Cy5 without (top) and with (bottom) are compared. Left panels are brightfield images. Right panels are fluorescence images of the same fields in the same conditions.

Chapter IV
Discussion

IV. 1 Spinach aptamer for live cell imaging of ribosome

IV. 1. 1 Size of Spinach insert is important

We performed a comparative study of the performance of different Spinach aptamers when inserted at a single position of a large structured cellular RNA, 16S rRNA. The site of insertion, helix 33a, was chosen because previous studies showed that this stem-loop protruding outside the ribosome is tolerant to receiving extra RNA sequences (147).

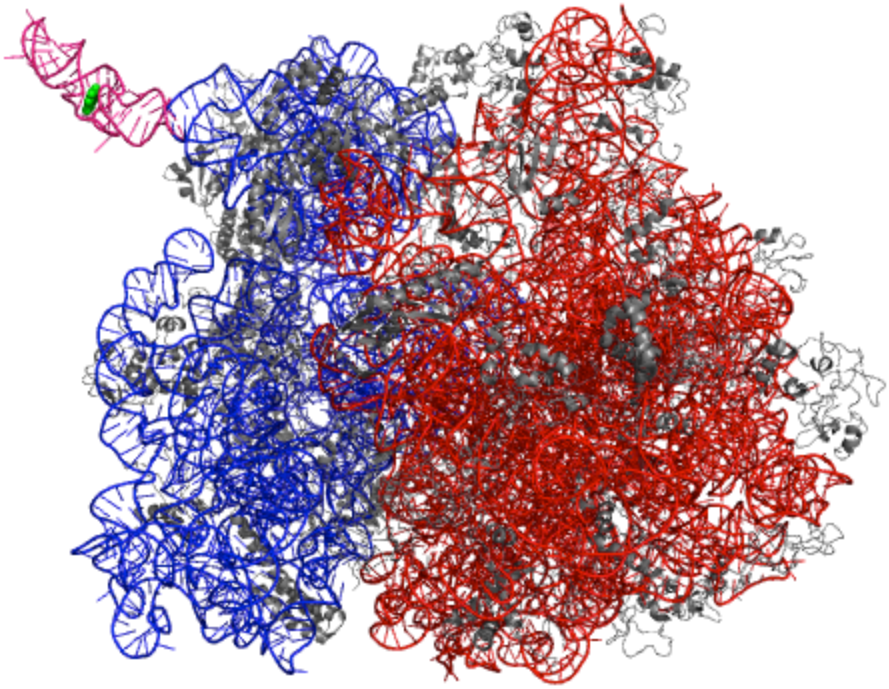

Figure IV-1-1: Model of the ribosome with insertion of Baby Spinach by superimposing the structure of Baby Spinach to base pairs of h33a of *E. coli* ribosome (PDB codes: 2AW4 and 2AVY) in PyMOL. Baby Spinach (pink) bound to DFHBI (green) was created based on the structure of Spinach with DFHBI (4KZD (68)) by truncation. 16S rRNA is shown in blue and 5S and 23 S rRNA are shown in red. All ribosomal proteins contained in 30S and 50S subunits are colored gray.

Here we show that the number of inserted nucleotides should be kept to a reasonable size since for the larger constructs, the growth rate of cells was altered. To better visualize this, I created

a model structure of Baby Spinach in PyMOL from the crystal structure of Spinach (68) by truncating the whole P1 stem, keeping part of P2 stem. This Baby Spinach model was superimposed on helix 33a of the ribosome structure (Figure IV-1-1). Baby Spinach insertion was shown in this study not to affect the ribosomal function. We can visually confirm the compact size of Baby Spinach in the whole ribosome compared to Spinach1.2 that has a very elongated structure (Figure IV-1-2). Even though h33a is located on the back side of the 30S ribosomal subunit, in addition to the strong susceptibility of long Spinach inserts to RNAse degradation, it is also possible that such elongated structures affect protein synthesis in polysomes where ribosomes are tightly packed (160).

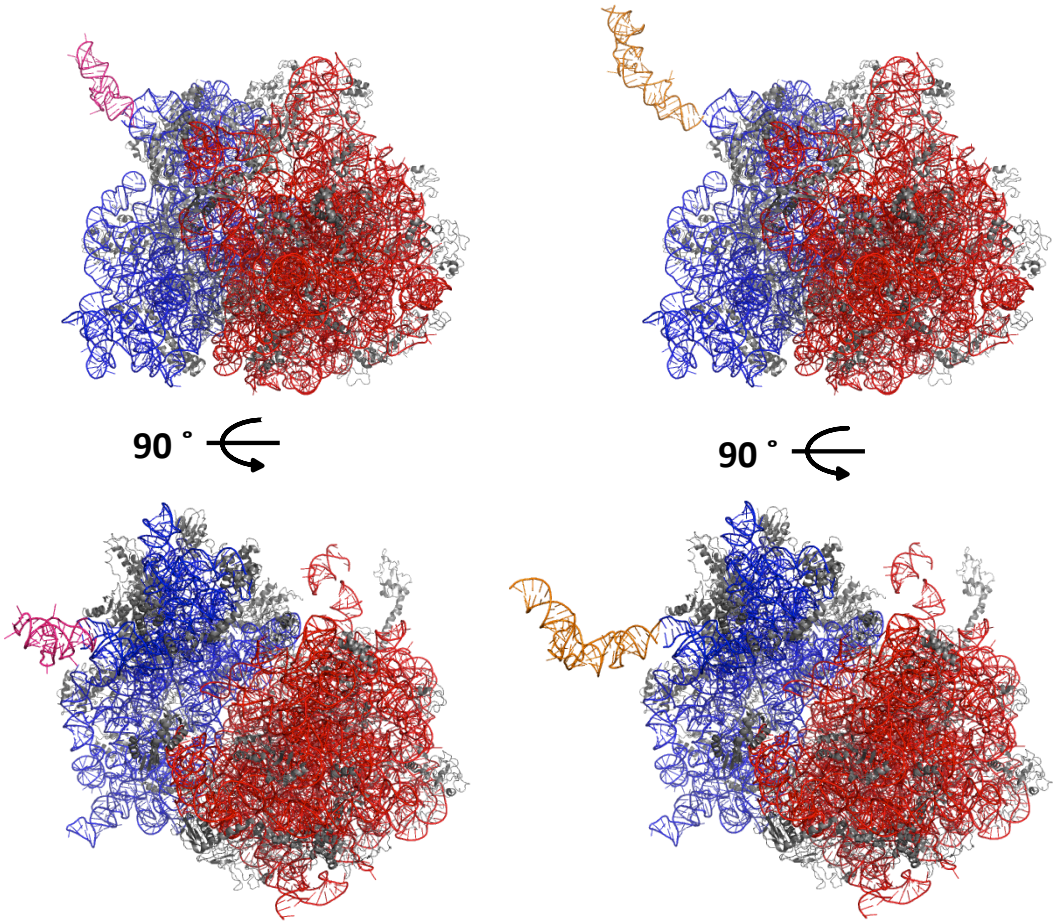

Figure IV-1-2: Model of ribosome with insertion of Baby Spinach (left) and Spinach1.2 (right) by superimposing structures of Baby Spinach or Spinach1.2 (PDB code: 4TS0 (66)) to *E. coli* ribosome (PDB codes: 2AW4 and 2AVY) in PyMOL. Colors are like in Figure IV-1. The lower structures are the result of 90° rotation to view ribosomes from the top.

IV. 1. 2 Effect of the sequence of Spinach inserts

Insertion of mBaby Spinach and its two variants showed that sequence can be an

important factor and impact the physiology of the cell. mBaby Spinach is smaller than Baby Spinach by 8 nucleotides. Two variants with different point mutations had altered cell growth in *E. coli* strain TA531, while mBaby itself was found to give the worst effect among all Spinach series. I focused on 5'- UUCGCGUU -3' sequence in mBaby Spinach that is a unique sequence among all Spinach constructs. mBaby Spinach variant (M1) has 5'- UC*CGCGUU -3' and the other (M2) has 5'- UUCGCA*UU -3' instead of the original sequence. There is a complementary sequence, 5'- AACGCGAA -3', found in helix 31 of 16S rRNA (Figure IV-1-3). Insertion of mBaby Spinach containing 5'- UUCGCGUU -3' might interact with this sequence, which might prevent proper ribosome folding.

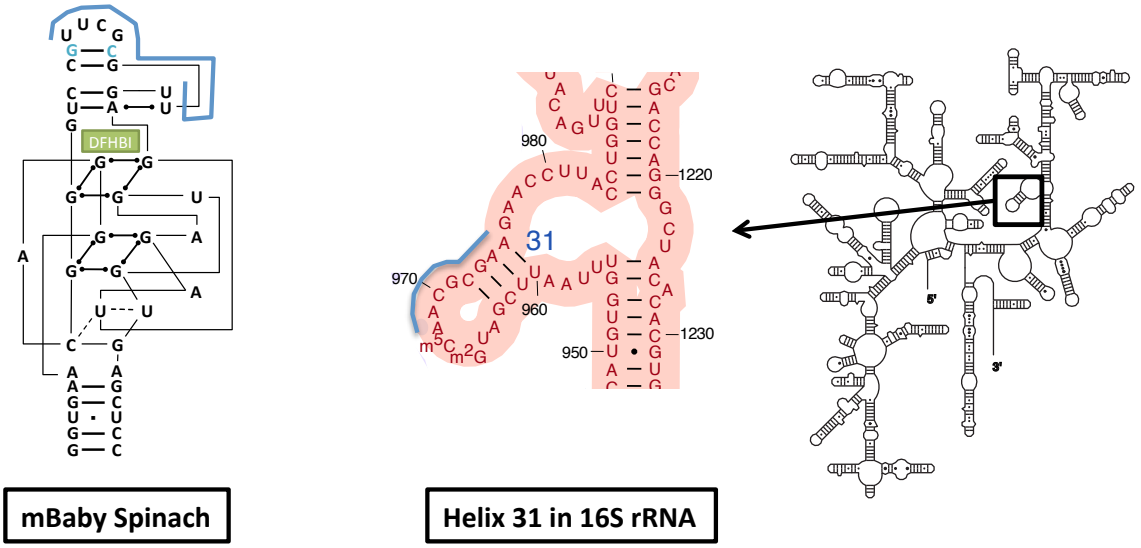

Figure IV-1-3: 5'-UUCGCGUU-3' sequence in mBaby Spinach and 5'-AACGCGAA-3' sequence in helix 31 in 16S rRNA.

IV. 1. 3 A strategy to identify the best Spinach tag for ribosome live cell imaging

Folding properties of the different aptamers were first evaluated comparatively *in vitro* using T7 RNA transcripts that emcompassed the full h33 domain of 16S rRNA. Surprisingly, Baby Spinach, which requires a specific folding protocol that includes slow thermal cooling did not perform well comparatively to the other Spinach aptamers. On the contrary, when the aptamers were expressed *in vivo* and purified in native form as Spinach tagged ribosomes, the results were drastically different. Clearly, shorter aptamers, Spinach-mini, Spinach2-mini and Baby Spinach were found superior to the other constructs in terms of fluorescence. The best construct is Baby Spinach, which is also the shortest one with 43 nucleotides inserted into the 16S rRNA. Similar results were obtained when fluorescence of the aptamers was assayed directly *in vivo* from cells

expressing the different Spinach-tagged ribosomes. These results indicate that the structured environment of ribosomal RNA helix 33a provides a natural scaffold that promotes folding of Baby Spinach for efficient fluorescent detection. The small size of Baby Spinach also prevents cleavage of 16S rRNA. This shows that Baby Spinach is appropriate to perform experiments on large structured cellular RNAs that will stay intact during the time of the experiment.

IV. 1. 4 Conclusion

We have used a strategy to identify the best performing Spinach tag for ribosome cell imaging. This approach can surely be applied to other structured cellular RNAs. This will enlarge our capacity to image ribosomes in live cells as to date it has only been achieved by labeling ribosomal proteins with members of the GFP family. For instance, the fluorescently labeled ribosome S2 protein was fused to YFP and allowed an estimation of the number of ribosomes in living *E. coli* cells using super-resolution microscopy (142). Ribosomal proteins L9 and L1 were also used for fusion with fluorescent proteins (141,161).The conventional methods have the benefit of fluorescence property of attached GFP family that can be applied to various experiments including the use in PALM. These methods, however, also have a weak point that they allow no choice but to label ribosomes uniformly or randomly in the cell. The amount of ribosomes in the cell represents a major obstacle for specific studies of translation. On the other hand, 16S rRNA contains catalytic sites of ribosomal action and other characteristics. Therefore one can use for instance specialized ribosomes where the anti-Shine-Dalgarno sequence has been engineered to bind to a specific mRNA of interest whose Shine-Dalgarno has also been modified (144). If both of such modifications are introduced in Baby Spinach tagged ribosomes, this method would allow visualizing a specific mRNA-ribosome complex (if the amount of fluorescent ribosomes is controlled to avoid any excess that would impaired observation). We expect these techniques to bring new information on the dynamics of ribosomes in living cell.

IV. 2 Aminoglycoside uptake in bacteria

IV. 2. 1 Neo-Cy5: a novel powerful tool

Since several decades, many laboratories have pushed forward the field of aminoglycoside transport across bacterial membranes. The literature is very abundant and nicely summarized in two reviews from 1987 (123,124). However there is still not a clear understanding of the molecular mechanisms by which aminoglycosides enter bacteria to perform their bactericidal action. Here, the goal was to provide a novel view of this mechanism using modern tools. A novel fluorescent aminoglycosides derivative was developed. The molecule retained antibiotic activity and its capacity to be accumulated in bacteria. In this study, it was demonstrated that the drug conjugate has retained its binding activity to the decoding center of the ribosome and therefore has a miscoding action. The MIC value of Neo-Cy5 remains comparable to that of the neomycin class antibiotics even though there is a 4-fold decrease compared to the parental molecule. The fluorophore used (Cy5) is an excellent dye for super-resolution microscopy therefore we could monitor the localization of the Neo-Cy5 conjugate to an unprecedented resolution. Our technique is still under development and improving (Figure IV-2-1).

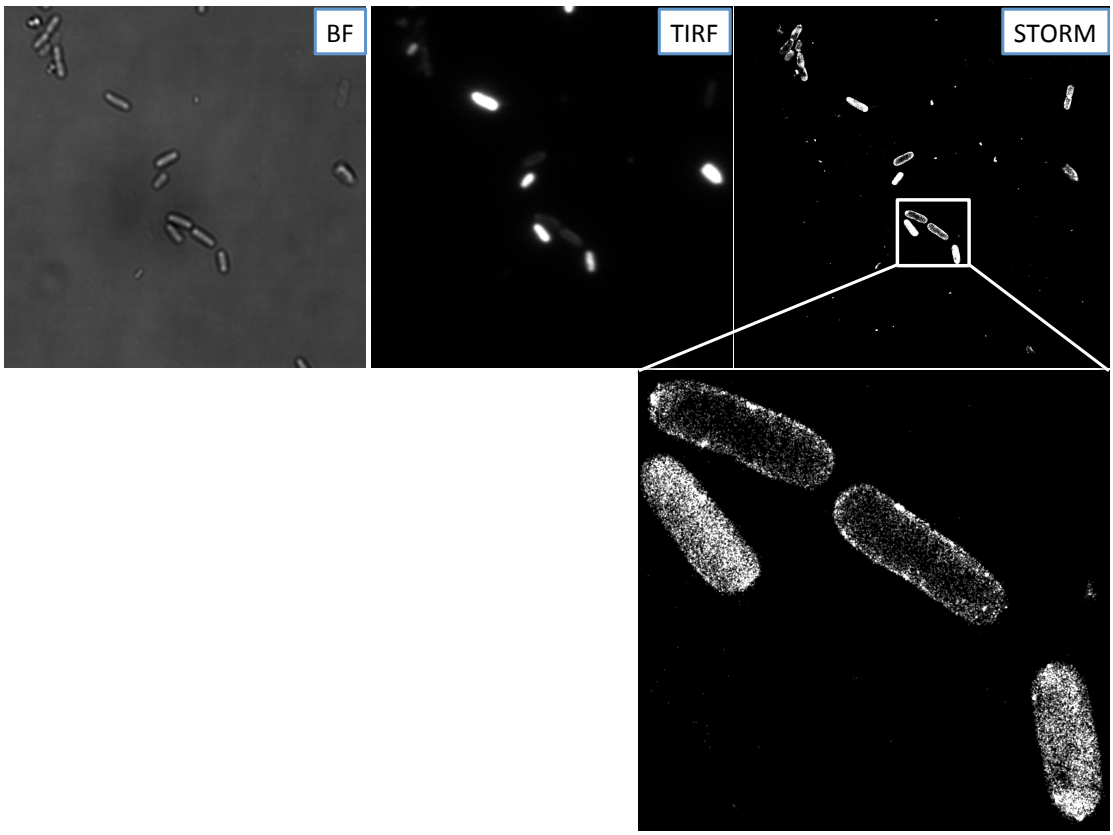

Figure IV-2-1: super-resolution imaging of Neo-Cy5 uptake on live cells.

IV. 2. 2 New insights at the single cell level

In Neo-Cy5 uptake experiments, several patterns were observed. All bacteria that are exposed to the drug irreversibly accumulate low levels in the periphery of the cell (possibly the periplasm). A fraction of the cells, which the extent depends on the medium utilized as well as the cell concentration, has for unknown reasons the capacity to uptake (also irreversibly) very strong concentration of aminoglycosides in the cytoplasm (10 times the levels found in the periphery of the cell). This uptake leads to membrane permeability and cell death, which we could monitor as the eventual leakage of the fluorescent aminoglycoside. A third pattern was observed for all dividing cells where Neo-Cy5 accumulates at the septum of division. This binding at the septum is not lethal since these cells continued to divide under the microscope. Nevertheless, this phenomenon was unexpected and would require further investigation to eventually identify a novel potential target for future aminoglycosides. It is worth to note that this septal localization looks very similar to the site of synthesis of the peptidoglycan identified by pulse labeling with fluorescent D-amino acids (162). Peptidoglycan synthesis is the target of many important antibiotics like vancomycin (in Gram positive bacteria) or beta-lactams acting on both Gram positive and negative.

Being able to classify under the microscope a cell population in different categories such as periplasmic or cytoplasmic uptake allows now performing a single cell analysis of a population of bacteria exposed to an aminoglycoside. We investigated the effect of time of exposure and the concentration of the drug in the media. As expected from the literature, increasing time allowed higher uptakes both at the periphery of the cell as well as in the cytoplasm. Increasing the concentration demonstrated that there is a direct link between the external concentration of the drug and the amount accumulating at the periphery of the cell. These results need to be confirmed but it would suggest a diffusive mechanism for going through the first membrane. It also raises intriguing question, how this diffusive mechanism can be one way since the accumulation is irreversible (on a reasonable time scale). This could result from the presence of LPS that strictly locate in the outer leaflet of the outer membrane and are involved in the self-induced mechanism. Once in the periplasm, the rate of efflux would be very low resulting in accumulation in the periplasm. More precise analyses will be performed on the cytoplasmic fraction of the cell population. This might be the first opportunity to de-convolute the overall uptake of aminoglycosides by bacteria for its two membranes outer and inner, which until now remained impossible.

Besides, time-lapse imaging on individual cell treated with fluorescently labeled aminoglycoside was performed for the first time here. These observations captured several

characteristic behavior of cells: the transient accumulation of neomycin at the septum during cell division; the sudden or graduate lost of fluorescence in cell indicating leakage of cell content including the accumulated Neo-Cy5. One of the future goal of this time-lapse imaging is to capture the moment of transition from periplasmic accumulation to cytoplasmic accumulation, which will prompt understanding aminoglycoside uptake mechanism that is now thought to consist with three phase: a first energy independent phase followed by two energy dependent phases.

We also demonstrated that the prontonophore Carbonyl cyanide *m*-chlorophenyl hydrazone (CCCP) that decreases the proton motrice force that is essential to aminoglycoside uptake only blocks the cytoplasmic uptake and not the peripheral accumulation. This again suggests that the crossing of the outer membrane would be diffusive whereas the movement across the inner membrane is an active process.

IV. 2. 3 Gram-negative versus Gram-positive

Finally, we investigated the active accumulation of aminoglycosides in a Gram-positive model bacteria: *B. subtilis* wt168 (Figure IV-2-2). Like Gram-negative bacteria, *B. subtilis* accumulates high cytoplasmic levels. Surprisingly we observe the "coquillage" pattern, which seemed to be very transient as removal of the excess of Neo-Cy5 from the medium lead to a disappearance of the peripheral fluorescence. If this pattern was stable in *E. coli* with the presence of the inner and outer membrane that clearly define the periplasm, the more permeable outer wall zone of *B. subtilis* (159) may not be able to retain Neo-Cy5 that leaks out.

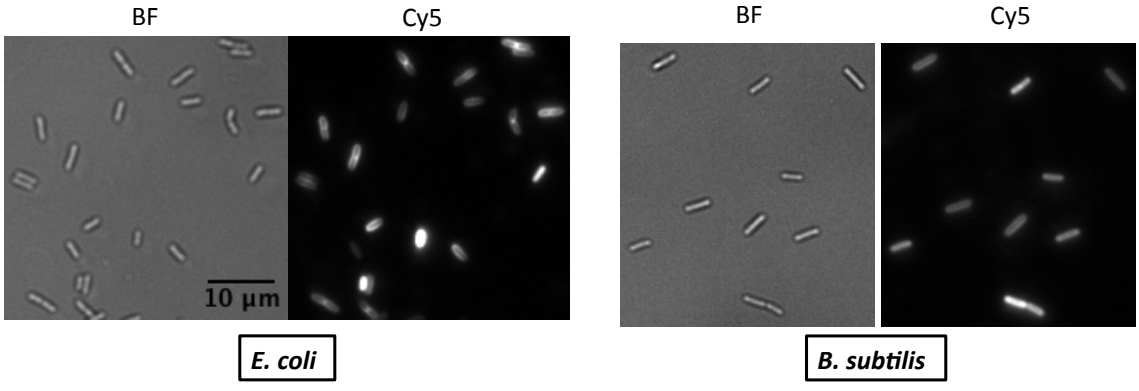

Figure IV-2-2: Images of *E. coli* (gram-negative bacterial: left) and *B. subtilis* (gram-positive bacteria: right) exposed to Neo-Cy5. *E. coli* population consists of cells with several characteristic patterns of accumulation: at the cell periphery, in the cytoplasm and at the septum. In *B. subtilis* Neo-Cy5 distributes in different patterns: uniformly even in dividing cell, in the periphery of cell.

We devoted most of our above work to the characterization of aminoglycoside uptake by *E. coli*, a gram-negative bacteria. Now, the uptake of Neo-Cy5 was also tested in Gram-positive bacteria using *B. subtilis* that is known to be more sensitive to aminoglycoside than *E. coli*. Very interesting differences were observed compared to the model bacteria *E. coli* with a possible "periplasmic-like" accumulation in the wall space which seems to be not irreversible and a concentration at the septum of cells at a very early stage of division, when the morphological signs of division are still not visible. The entry of Neo-Cy5 into the cytoplasm of *B. subtilis* and *E. coli* shares common characteristics with a dependence of the uptake to the PMF (blocked by CCCP) and the irreversibility of the uptake. It demonstrates that gram-positive and gram-negative bacteria, both utilize the proton motrice force for strong cytoplasmic uptake.

IV. 2. 4 Conclusion

We have now a better understanding of aminoglycoside uptake by Gram-positive and Gram-negative bacteria. There is still much to discover but progress has been made since the first experiment of Bernard Davis performed in 1960 (Figure IV-2-3). We now have the possibility to monitor the uptake in live but also at the single cell level. This may give us clues in the near future of what are the physiological differences between cells that give them the capacity or not to uptake very strong concentrations of neomycin. This will have implications in the understanding of the bactericidal activity of aminoglycosides and how they penetrate inside bacteria. This may allow the development of new strategies to favor uptake or develop new antibiotics for better antibiotherapy.

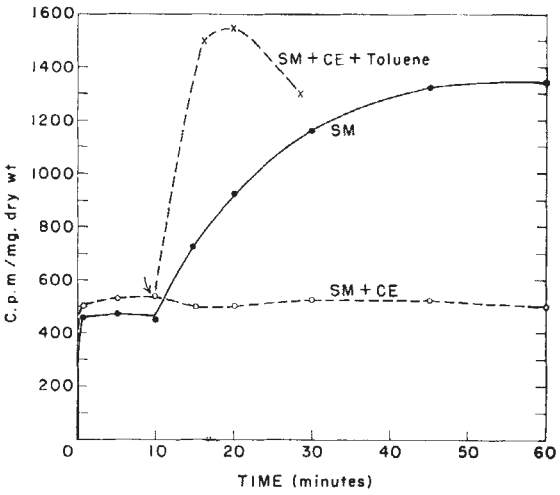

Fig. 1. Uptake of streptomycin labelled with carbon-14. 40 μgm./ml. of labelled streptomycin (formed from uniformly labelled glucose) was added to an exponentially growing shaking culture in minimal medium, and to two similar cultures (labelled *CE*) to which chloramphenicol (20 μgm./ml.) had been added 2 min. earlier. At the time indicated by the arrow, one *CE* culture received 0·02 ml. of toluene per ml. of culture

Figure IV-2-3: Figure 1 of the publication from the B. Davis laboratory "Uptake of Streptomycin by *Escherichia coli*" (125).

IV. 3 Conclusion and perspective

In this study, I have developed two fluorescent tools to study on protein synthesis in live gram-negative and gram-positive bacteria. The first one describes the application of Spinach system to ribosomes imaging. This is different from conventional methods (that use fluorescent proteins) in that 16S rRNA contains an inserted RNA aptamer that elicits fluorescence of a fluorogenic compound. A second system focuses on the uptake of a fluorescently labeled ligand of the ribosome, neomycin an antibiotic of the class of aminoglycosides. This novel neomycin conjugate, which kept its bactericidal activity allows for the first time imaging of aminoglycoside uptake on live bacteria. We also obtained data about the localization of the antibiotic once inside the bacteria to an unprecedented resolution using super resolution microscopy.

We hope that both of these methods will contribute to a better understanding of protein synthesis as well as providing a novel view on the way antibiotics penetrate into cells and perform their bactericidal action.

Chapter V

Materials and Methods

V. 1 Reagents and equipment

Chemicals used in this study were purchased from Sigma, PROLABO, MERCK or Invitrogen. DFHBI were purchased from Lucerna Technologies. A list of all primers used is provided as Table V-1. Bacterial strains were grown in LB or two minimal media; M9 minimal medium and MOPS minimal medium, at 37˚C, 200 rpm or on LB agar plates at 37˚C throughout this study. For the preparation of competent cell, SOB medium was used to grow *E. coli* strain XL-1 Blue, and 2x YT medium was used to grow the other *E. coli* strains. The composition of media and *E. coli* strains used in my study is written below. In some cases, media contained 100 μg/mL ampicillin or 50 μg/mL kanamycin. Cell imaging experiments were performed using an inverted microscope Zeiss (Axio-observer Z1). Fluorescence excitation, emission spectra and fluorescence intensity measurements were performed using a Tecan Infinite 200 PRO plate reader.

Medium compositions

LB: 1% (w/v) tryptone, 0.5% (w/v) yeast extract, 1% (w/v) NaCl

2xYT: 1.6% (w/v) tryptone, 1% (w/v) yeast extract, 0.5% (w/v) NaCl

SOB: 2% (w/v) tryptone, 0.5% (w/v) yeast extract, 0.05% (w/v) NaCl, 0.0186% (w/v) KCl, 10 mM $MgCl_2$, 20 mM glucose

Minimal media

M9: 47.75 mM Na_2HPO_4•$2H_2O$, 22.04 mM KH_2PO_4, 8.56 mM NaCl, 18.70 mM NH_4Cl, 2 mM $MgSO_4$, 0.1 mM $CaCl_2$

MOPS: 1.32 mM K_2HPO_4, 9.52 mM NH_4Cl, 0.523 mM $MgCl_2$, 0.276 mM K_2SO_4, 0.01 mM $FeSO_4$•$7H_2O$, 5 μM $CaCl_2$, 50 mM NaCl, 40 mM MOPS, 4 mM Tricine, 0.003 μM $(NH_4)_6(MO_7)_{24}$•$4H_2O$, 0.4 μM H_3BO_3, 0.03 μM $CoCl_2$(II)•$6H_2O$, 0.01 μM $CuSO_4$(II)•$5H_2O$, 0.08 μM $MnCl_2$•$4H_2O$, 0.01 μM $ZnSO_4$•$7H_2O$

***Escherichia coli* strains used in this study and the genotype and remarks**

MG1655: Wild type strain

F-, lambda-, ilvG-, rfb-50, rph-1

TA531: rrn deletants

F-, ara-600, Δ(rrsH-rrlH)770, Δ(codB-lacI)3, Δ(rrlG-rrsG)772::lacZ, Δ(recA-srl)306, srlR301::Tn10, Δ(rrlD-rrsD)773::cat, Δ(rrsC-rrlC)774::cat , Δ(rrsA-rrlA)771, Δ(rrsB-rrlB)769, thiE1?, Δ(purD-metA)768, ptRNA66, pHK-rrnC

SQ171: rrn deletants based on MG1655

ΔrrnGADEHBC (with pKK3535 and ptRNA67)

XL-1 Blue: Strain used for cloning

Δ(mcrA)183 Δ(mcrCB-hsdSMR-mrr)173 endA1 supE44 thi-1 recA1 gyrA96 relA1 lac [F′ proAB $lacI^qZ\Delta M15$ Tn10 (Tet^r)]

V. 2 Spinach aptamer for live cell imaging of ribosome

Plasmids construction

Spinach sequences used in this study are summarized in Table 1. Spinach2-mini is a truncated version of Spinach2 designed in this study to harbor the same structural characteristics as Spinach1-mini. The ApaI/XbaI region of rrnB operon was subcloned between HindIII and EcoRI sites of pUC18 in order to facilitate the generation of Spinach ribosome constructs (pUC18-AX). A PstI site was created in the helix 33a region by mutating T1030G and G1032A to facilitate insertion of Spinach sequences (pUC18-AXP). The different Spinach sequences were introduced at the PstI site. Each Spinach sequence was amplified by PCR and cloned into pUC18-AXP using either an In-Fusion HD Cloning Kit (Clontech) or a Quick Ligation Kit (NEB). The ApaI/XbaI fragments harboring Spinach sequences were then placed into pKK3535, which carries the entire rrnB rRNA operon under the control of the native constitutive promoter P1P2 (148). These constructs were named pKK3535-h33a-Spinach vectors. All oligonucleotides used are listed in Table 2.

Preparation of E. coli TA531 expressing Spinach-modified ribosomes

E. coli strain TA531 from which the seven copies of the chromosomal rRNA operon have been deleted harbours the plasmid pHC-rrnC carrying a single copy of rrnC operon as the sole source of rRNA genes and a kanamycin resistance gene (163). Replacement of pHC-rrnC in TA531

by pKK3535-h33a-Spinach plasmid was achieved by transformation of the *E. coli* followed by growth in liquid LB medium containing ampicillin for at least two days after reaching the stationary phase. The saturated culture was diluted and inoculated onto LB plates containing ampicillin, and single colonies were isolated. Plasmid substitution was tested by evaluating resistance of colonies to ampicillin and sensitivity to kanamycin. Colonies that survived only on ampicillin LB plates were selected.

Growth of *E. coli* expressing Spinach ribosomes

E. coli TA531 harbouring pKK3535-h33a-Spinach series plasmids were inoculated into liquid LB in Erlenmeyer flasks from glycerol stocks. The overnight cultures were diluted with 50 ml of fresh LB medium to an OD of 0.05 – 0.07. ODs at 600 nm were measured every 30 min until cell growth reached early stationary phase.

To confirm that DFHBI was not toxic to *E. coli* that express Spinach-modified ribosomal RNA, cell growth was measured in presence of DFHBI with an Infinite 200 PRO microplate reader. Wells of a 96-well microtiter plate containing 190 μL of LB were inoculated with 5 μL of an overnight culture (OD_{600} = 2) of *E. coli* strain TA531. The growth was followed by measuring the absorbance at 600 nm every 15 min at 37 °C with constant shaking at 218 rpm except during measurement.

Expression and purification of Spinach ribosomes

LB (1 L) was inoculated with 10 mL of a saturated overnight culture of *E. coli* TA531 harbouring pKK3535-h33a-Spinach plasmid and grown to an OD_{600} of 0.4. Cells were harvested by centrifugation (8000 g, 4 °C for 10 min) and washed with buffer A [20 mM Tris-HCl (pH 7.5), 100 mM NH_4Cl, 10 mM $MgCl_2$, 0.5 mM EDTA, 6 mM 2-mercaptoethanol]. Cells were frozen in liquid nitrogen and stored at -80 °C until use. All subsequent steps were performed at 4 °C or on ice. Cells were resuspended in buffer A and lysed using a bench-top press (Carver). Lysates were diluted with buffer A and centrifuged (15000 g). Crude ribosomes were then prepared by sedimentation (131000 g, 16 h) through sucrose cushions. The resulting ribosome pellet was washed twice with 1 mL of buffer A and resuspended in 250 μL of buffer A. Crude ribosomes were frozen in liquid nitrogen and stored at -80 °C.

Further purification of ribosomes were performed using a cysteine-charged sulfolink resin (164). A 100-μL aliquot of crude ribosome solution was diluted with the same volume of buffer B [20 mM Tris-HCl (pH 7.5), 10 mM $MgCl_2$, 0.5 mM EDTA, 2-mercaptoethanol] to adjust the concentration of NH_4Cl to be 50 mM and was then loaded to 2 mL of charged resin. The column

was washed with 10 mL of buffer B containing 60 mM NH_4Cl, and ribosomes were eluted with buffer B containing 500 mM NH_4Cl. Ribosomes in the eluted fractions were collected by ultracentrifugation (213000 g for 16 h). The ribosome pellet was resuspended in 50 μL of buffer A. The ribosome solutions were aliquoted, quick-frozen, and stored at -80 °C.

In vitro transcription of Spinach aptamers

RNA fragments containing various Spinach sequences were prepared by in vitro transcription using T7 RNA polymerase. The template DNAs for transcription were prepared by PCR amplifying pKK3535-h33a-Spinach plasmids using T7-16SrRNA-h33-F and 16SrRNA-h33-R primers (Table 2). Transcripts were purified using Nucleospin RNA spin columns (Macherey-Nagel) with a protocol adapted for short RNAs (Macherey-Nagel).

In vitro fluorescence measurement of Spinach-DFHBI complexes

RNA transcripts were dissolved in water, refolded by heating at 90 °C for 1 min and then placing on ice for 5 min. For refolding using a slow cool step, samples were heated at 90 °C for 1 min, buffer and DFHBI solutions were added, and samples were kept at 65 °C for 5 minutes. The RNA was then refolded by a slow decrease of temperature over a period of 20 minutes (40 cycles comprising a temperature decrease at a rate of 0.3 °C/sec for 3.3 secondes followed by a step of 30 secondes of equilibration) down to 25 °C. Fluorescence measurements were performed in 384-well black microtiter plates at 25 °C with the excitation at 455 nm and emission monitored at 506 nm. The background signal from DFHBI in culture medium or buffer was subtracted for each measurement.

Fluorescence of each Spinach/DFHBI complex was measured as follows: 1 μM Spinach-modified ribosome in buffer A was incubated with 2 μM DFHBI diluted in the same buffer for 15 min at 25 °C. A 10-μL aliquot of the complex solution was introduced into a well of a 384-well microtiter plate, and fluorescence intensity was measured. On the same sample, we plotted excitation spectrum range from 370 nm to 500 nm (emission at 530 nm) and emission spectrum range from 470 nm to 620 nm (excitation at 440 nm). The fluorescence data was collected every 2 nm in the excitation and emission ranges. As for ribosomes with insertion of only Baby spinach, Spinach-mini, Spinach2-mini and Spinach2, the fluorescence was measured again in the similar condition except for supplementation of 125 mM KCl.

Fluorescence from DFHBI bound to Spinach transcripts was measured in samples containing 0.1 μM RNA and 0.2 μM DFHBI or 0.1 μM RNA and 10 μM DFHBI. Fluorescence measurements were performed in ribosome buffer containing KCl [20 mM Tris-HCl (pH 7.5), 100 mM NH4Cl, 10 mM MgCl2, 0.5 mM EDTA, 6 mM 2-mercaptoethanol and 125 mM KCl] or in

HEPES-KOH buffer [20 mM HEPES (pH 7.4), 100 mM KCl and 1 mM MgCl2].

Live cell imaging of Spinach-tagged ribosomes

To measure whole-cell fluorescence in liquid culture, overnight cultures of E. coli strain TA531 harboring pKK3535-h33a-Spinach variants were inoculated into 50 mL of fresh LB containing ampicillin and grown to an OD600 of 0.4. Cells were collected in 1.5-mL aliquots and washed once with the same volume of M9 minimal medium. Washed cells were resuspended in M9 medium to an OD of 1 and incubated with 200 μM DFHBI for 90 min at 37 °C. A 10-μL aliquot was transferred to a 384-well microtiter plate and fluorescence intensity at 25 °C was measured (excitation wavelength, 455 nm; emission wavelength, 506 nm).

Imaging of the *E. coli* cells was performed using am Axio Observer Zeiss microscope (objective 63X, N.A. 1.46, excitation 470 (+/- 13) nm, emission 512 (+/- 15) nm). Fluorescence levels were corrected for the background fluorescence generated by DFHBI alone in the culture medium.

Analysis of RNA degradation

Degradation of Spinach tagged rRNA was investigated by fractionation on urea-PAGE. *E. coli* TA strains harbouring Spinach 16S rRNA plasmids were grown to an OD600 of 0.4 in LB. Total RNA was purified from a 1-mL aliquot of the culture using NucleoSpinRNA columns (Machery-Nagel). Samples of 500 ng of total RNA were loaded on 6% polyacrylamide-7 M urea gels. Gels were washed with water for 5 minutes three times and stained using DFHBI-1T or SYBR Gold as described (14).

Fluorescent primer extension was carried out as described previously (15). Cy5-labelled DNA primer was purchased from MWG Biotech. rRNAs (250 ng) were mixed with the Cy5-labelled primer (10 pmol) in hybridization buffer (25 mM HEPES, pH 7.0, 50 mM KCl), heated to 90 °C (1-2 min), and slowly cooled to 45 °C. Reverse transcription reactions were performed using SuperScript II (Invitrogen) in the supplied reaction buffer at 45 °C for 40 min. The reactions were stopped by ethanol precipitation. cDNA samples were dissolved in 10 μL 7M urea and a small aliquot (1.5 to 3 μL) of each sample was loaded on an 8% polyacrylamide-7 M urea gel. The gel was imaged using Typhoon Trio scanner (GE Healthcare).

Primers used in this Table V-1

Name	Sequence
pkk3535HindApa	TACCGAAGCTTGGGCCCGCACAAGCGGTG
pkk3535EcoXba	CCCGGAATTCTAGACGAAGGGGACACGAAAATTGCTTATC
Mut_PstI_F	GAGATGAGAATGTGCCTGCAGGAACCGTGAGACAGG
Mut_PstI_R	CCTGTCTCACGGTTCCTGCAGGCACATTCTCATCTC
Spinach1_mini_F	AACTGCAGGACGCGACCAGTTACGGAGCTCACACTCTACTCA ACAGTGCCGAAGCAC
Spinach1_mini_R	AACTGCAGGACGCGACCGAAATGGTGAAGGACGGGTCCAGT GCTTCGGCACTGTTGA
Spinach1_F	AGATGAGAATGTGCCTGCAGGACGCAACTGAATGAAATGG
Spinach1_R	CTGTCTCACGGTTCCTGCAGGACGCGACTAGTTACGGAGC
Spinach1.2_F	AGATGAGAATGTGCCTGCAGGACGCGACCGAATGAAAT
Spinach1.2_R	CTGTCTCACGGTTCCTGCAGGACGCGACCAGTTACGGAG
Spinach1.2_tRNA_F	AGATGAGAATGTGCCTGCAGGCCCGGATAGCTCAGTCG
Spinach1.2_tRNA_R	CTGTCTCACGGTTCCTGCAGTGGCGCCCGAACAG
Spinach2_mini_F	GATGAGAATGTGCCTGCAGGATGTAACTGAAATGGTGAAGGA CG
Spinach2_mini_R	CTGTCTCACGGTTCCTGCAGGATGTAACTAGTTACGGAGCTCA CAC
Spinach2_F	GATGTAACTGAATGAAATGGTGAAGGACGGGTCCAGTAGGCT GCTTCGGCAGCCTACT
Spinach2_R	GATGTAACTAGTTACGGAGCTCACACTCTACTCAACAAGTAG GCTGCCGAAGCAGCCT
16S_fusion-Spinach2_ F	AGATGAGAATGTGCCTGCAGGATGTAACTGAATGAAATGGTG A
Baby_Spinach_F	AGATGAGAATGTGCCTGAAGGACGGGTCCAGTAGTTCGCTAC TGTTGAGTAGA
Baby_Spinach_R	CTGTCTCACGGTTCCTGCTCACACTCTACTCAACAGTAGCGAA CTACTGGACC
Micro_Spinac_F	AGATGAGAATGTGCCTGAAGGACGGGTCCGTTCGCGTTGAGT AGA
Micro_Spinac_R	CTGTCTCACGGTTCCTGCTCACACTCTACTCAACGCGAACGGA CC

16S_fusion_ApaI_F	AAATGAATTGACGGGGG
16S_fusion_XbaI_R	TGTCCTGGGCCTCTAGA
pUCpKK-fusion-ApaI	AAATGAATTGACGGGGGCCCGCACAAGC
pUCpKK-fusion-XbaI	GTCCTGGGCCTCTAGACGAAGGGGACACG
pk3302minusseq	CACAAACCAGCAAGTGGC
T7-16SrRNA-h33-F	TAATACGACTCACTATAGATCCACGGAAGTTTTCAG
16SrRNA-h33-R	ACCTGTCTCACGGTTCC

V. 3 Aminoglycoside uptake in bacteria

Neo-cy5 characteristics

Chemical probing of *E. coli* 30S ribosomal subunits

Modification reactions (100 μl) with 30S subunits (10 pmol) were performed in a buffer containing 80 mM potassium cacodylate pH 7.2, 100 mM ammonium chloride, 20 mM magnesium chloride, 1 mM dithiothreitol and 0.5 mM EDTA, as previously described (98). Neomycin was added and modification was performed by addition of DMS (15 μl of a 1/10 dilution in ethanol) followed by incubation at room temperature for 10 min and on ice for 10 min. Reactions were stopped by ethanol precipitation. Sodium borohydride reduction and aniline-induced strand scission was performed as described (165). Modified RNA was resuspended in 10 μl 1 M Tris-HCl pH 8.2. Upon addition of 10 μl of freshly prepared 0.2 M NaBH4, the samples were incubated on ice in the dark for 30 min. The reaction was quenched by addition of 100 μl 0.4 M sodium acetate followed by ethanol precipitation. Pellets were dissolved in 20 μl 1.0 M aniline/acetate, pH 4.5 followed by incubation in the dark for 20 min at 60°C. The reaction was quenched by addition of 100 μl 0.4 M sodium acetate and 100 ml phenol:chloroform:isoamyl alcohol (25:24:1) followed by vigorous mixing and centrifugation. The RNA was concentrated by ethanol precipitation of the aqueous phase and pellets were washed with 100 μl cold 70% ethanol. Samples were resolved on 8% urea-PAGE and scanned on a Typhoon.

MIC measurement

To measure the MIC (minimum inhibitory concentration) of neomycin and Neo-Cy5, the rates of growth were measured in presence of several concentrations of neomycin and Neo-Cy5. Overnight culture of *E. coli* strain MG1655 was diluted with MOPS-G to an OD of 0.2, of which 190 μL were mixed with 10 μL neomycin/Neo-Cy5 stock solution. Growth and measurement of absorbance on these 200 μL samples of cultures were performed in a 96-well microtiter plate with transparent lid using InfiniteM200pro (TECAN). As for the sample with neomycin, absorbance at 600 nm was measured every 15 min, while for the sample with Neo-Cy5, absorbance at 500 nm was measured instead of 600 nm. This is because Neo-Cy5 absorbs light at 600 nm.

Standard condition for observation of cells treated with Neo-cy5

Cell preparation

In this study, *E. coli* wild type strain MG1655 was used unless otherwise stated. MG1655 were plated from the glycerol stock on LB plate, grown overnight and a single colony was picked to

inoculate a liquid medium for overnight culture. For the liquid culture, MOPS minimal medium supplemented with 0.4 % (w/v) glucose as a carbon source (MOPS-G) was generally used. It is notified when other media are used such as M9 minimal medium containing 0.4 % (w/v) glucose (M9-G) or MOPS-G supplemented with something else. Overnight cultures were diluted to OD_{600} = 0.05 with fresh medium and grown until the OD_{600} reached approximately 0.3.

The exposure of cells to Neo-cy5 was performed as follows. Concentration of Neo-Cy5 is estimated from the absorbance at 649 nm. 9μL of cell culture in the exponential phase (OD_{600} = 0.3) was mixed with 1 μM of 4 μM Neo-Cy5 dissolved in milliQ (final concentration of 0.4 μM) and incubated for 2 min on at 37 ˚C (no shaking). After the incubation, the excess of Neo-Cy5 was removed by three-time-wash with 100 μL fresh MOPS-G using centrifugation (8000 g, for 3 min. at room temperature). Cell pellet was finally suspended with 1 μL of MOPS-G and put on 1 % agarose pad, which was formed by pouring MOPS-G containing 1 % agarose melted into a mold (Gene Frame® 25 μL, 10 mm x 10 x mm x 0.25 mm, Thermo) attached on a slide glass. The sample covered with a coverslip was mounted under the microscope for imaging.

Microscopy

Fluorescence images were taken with a EmCCD camera through a 63X oil objective mounted on a inverted microscope Axio Observer Z1 (Zeiss), and image acquisition was done with the Metamorph software.

Cy5 illumination was performed using a 642 nm laser (100 mW) and a filter set (filter for Cy3/Cy5 (TRF59907-EM 532/640nm Laser Dual Band Set: Excitation filter 530/20 and 638/25, Dichroic mirror 585/70 and 650 (long pass), and Emission filter 580/70 and 700/100) (Chroma Technology) in TIRF (Total Internal Reflection Fluorescence) mode. Laser output power was set to 20 %. Unless indicated all image analysis was performed using ImageJ64.

Observation using different parameters

In this study, incubation of cells with Neo-Cy5 was performed with different parameters depending on the aim of each experiment. The detailed conditions used in each observation are described below.

Comparison of different media, MOPS and M9

Cells were grown either in MOPS-G or M9-G. In this experiment, the agarose pad was made using milliQ for both samples.

Comparison of incubation time

The incubation time of cells with Neo-Cy5 was varied. In addition to the standard 2 minutes, periods of 5, 10 and 30 minutes incubation time were tested.

Comparison of Neo-cy5 concentration

A volume of 9 μL of cell culture was mixed with 1 μL of Neo-Cy5 with concentrations of 20, 40 or 80 μM (final 2, 4, or 8 μM).

Testing cell concentration

In this experiment, several parameters were modified: cell concentration, incubation time and wash repeat number. After the standard culture, three cell cultures with different densities were prepared: standard (OD_{600} = 0.3), 10 times dilution in the medium (OD_{600} = 0.03) and 100 times dilution (OD_{600} = 0.003). A volume of 2 μL of 20 μM Neo-Cy5 (final 0.4 μM) was added to 98 μL of 10 times diluted cell culture, and 6 μL was added to 294 μL to 100 times diluted cell culture (final 0.4 μM). All three mixtures were incubated for 15 minutes, then the number of wash was increased to five times to account for the increased Neo-Cy5 amount that results from an increase of the reaction volume due to cell density dilutions.

STORM

1) Cell preparation

For the observation with STORM, 98 μL of ten times diluted cell (OD_{600} = 0.3) were mixed with 2 μM of 0.4 μM Neo-Cy5 (final 0.4 μM) and incubated for 15 min. Cells were washed five times and resuspended with 1 μL MOPS-G for observation.

2) Observation sample preparation

For dSTORM imaging, bacteria were immobilized on coverslips (#1.5 H, Marienfeld) coated with Poly-L-Lysine (0.01% w/v; Sigma P8920) for 10 min and washed once with MOPS-G. The coverslips were then imaged in a cavity slide containing 150 μl of imaging buffer and sealed by twinsil silicone to avoid exchange of oxygen. The imaging buffer contains 50 mM Tris, pH 8, 10 mM NaCl, 10% (w/v) glucose, oxygen scavengers (0.63 mg/mL glucose oxidase and 40 µg/mL catalase), and reducing agent (112 mM mercaptoethylamine).

3) Super resolution microscopy

Super resolution images were acquired with a Nikon N-STORM system mounted on a

Nikon Eclipse Ti E inverted microscope, equipped with a 100X TIRF SR oil-immersion objective (numerical aperture (NA): 1.49) and a perfect focus system to avoid drift along the z axis during long acquisitions.

In dSTORM mode, cells containing Cy5 were photoswitched into dark state using a 647 nm laser (MBP Communication, 300mW) laser and were detected by a quad-band filter block (DM 405/488/561/647, emission filter BP 450/60-525/50-605/50-730/120, Nikon) and using an EMCCD camera (DU-897E iXon3, Andor).

NIS-elements AR software (Nikon, v. 4.30.01) was used to control the system and to perform images reconstruction. 3D localization was performed using a cylindrical lens to introduce astigmatism in the optical path to obtain the z position by analyzing the shape of the PSF. We used an auto-correlation algorithm implemented on the software to correct for lateral and axial drifts.

Live/ Dead check of MG1655 treated with Neo-cy5

To test the viability of cell, we used LIVE/DEAD® BacLight ™ Bacterial Viability Kits (L13152) (Invitrogen™) kindly provided by Christophe Possoz. The two staining reagents were prepared by dissolving the contents in vials, SYTO 9 an**d** Propidium iodide (PI), in a 2.5 mL of milliQ respectively. Then I diluted in water PI 200 times more than recommended in the kit protocol. To prepare 2x stock solution in MOPS, I mixed 200 μL of SYTO 9, 1 μL of PI, 40 μL of 10x MOPS medium and 159 μL of milli Q water. For the cell viability test, I combined the 2x stock solution with an equal volume of the cell culture and incubated at room temperature in the dark for 15 minutes. The final concentration of each dye is 6 µM SYTO 9 and 0.15 µM PI, (200 times lower than recommended in protocol of the kit). After 15 minutes, 9μL of reaction sample were taken and mixed with 1 μL of Neo-Cy5. Subsequent processes until the sample setting under the microscope was the same as standard protocol.

In the observation, five photos were taken for each image field: with BF (50 ms, gain 1), GFP filter set for SYTO 9 signal (50 ms, gain 1), RFP filter set for Propidium iodide signal (50 ms, gain 50) and Cy5 filter set (50 ms, gain 1 and 50) for Cy5 signal detection using laser at 642 nm.

Condition for time-lapse imaging

In this study, several time-lapse imaging were performed in individual condition, which are described in detail as follows.

1) Detecting appearance and disappearance of Neo-Cy5 accumulation at the septum

In this time-lapse, *E. coli* strain SQ171 transformed with a plasmid carrying kanamycin resistant gene was used. Cells in MOPS-G were incubated with a final concentration of 8 μM of Neo-Cy5 for 30 minutes and subsequently washed 5 times with 100 μL of fresh MOPS-G. Cells were finally suspended with 1 μL of MOPS-G and put on 1% agarose pad for observation under the microscope.

During the time-lapse imaging, sequential images of Cy5 signal were taken every five minutes for one hour with the 642 nm laser and Cy5 filter set (200 ms, gain 50). In total, the one-hour-acquisition cycle was repeated four times and ended with an additional 30-minute-acquisition. BF image of the observed field was taken before and after each time-lapse acquisition.

2) Neo-Cy5 leakage experiment

In this experiments, MG1655 grown in M9-G medium was used. Cells were incubated with 8 μM Neo-Cy5 for 50 minutes and subsequently washed 5 times with 100 μL of fresh M9 medium. Cells were finally suspended with 1 μL of M9-G.

Time-lapse was performed for 4 hours as described above

3) Observation of MG1655 with Neo-Cy5 in presence of high concentration of neomycin

To observe the effect of high concentration of neomycin, cells were incubated with Neo-Cy5 in advance as follows. A culture diluted 10 times (OD_{600} = 0.03) was incubated with 0.4 μM Neo-Cy5 for 5 minutes. After cell wash, 1 μL of cell suspension was put on the agarose pad containing 4 μM of neomycin that is enough to kill MG1655, then the observation sample was mounted under the microscope.

Time-lapse was performed for 1 hour as described.

Dye Cy5 uptake and LIVE/DEAD kit

A volume of 9 μL of cell culture was mixed with 1 μL of 4 μM Cy5 and incubated for 30 min at 37°C. After three wash steps, cells were resuspended with 9 μL MOPS-G again. Then 9 μL of 2x stock of Live/Dead kit was added to the cell suspension, and incubated for 30 min at 37°C. For observation, cells were concentrated 9 times by centrifugation (at 8000 g for 1 min), and subsequently 1 μL of the final suspension was put on agarose pad for observation.

Six photos were taken for each field: with BF (50 ms, gain 1), GFP filter set for SYTO 9 signal (50 ms, gain 1), RFP filter set for Propidium iodide signal (50 ms, gain 50) and Cy5 filter set

for (50 ms, gain 1 and 50/ 200 ms, 50 gain) using the 642 nm laser.

Co-detection of Neo-cy5 and Spinach signal

MG1655 was transformed with pGex-Spinach plasmid. Cells were grown in MOPS-G and when an OD_{600} reached 0.25, IPTG (1 mM final concentration) was added to induce the expression of Spinach-ribosomes. After 70 minutes, the culture was stopped at an OD_{600} of 0.42, and then incubated with 200 μM DFHBI for 60 minutes at 37˚C.

A volume of 9 μL of cell culture containing DFHBI was mixed with 1 μL of 4 μM Neo-Cy5 and incubated for 10 minutes at 37˚C. For observation, cells were washed three times and resuspended with 1 μL of MOPS-G containing DFHBI. Subsequently 1 μL of the final suspension was put on agarose pad and imaged.

Three photos were taken: with BF (50 ms, gain 1), GFP filter set for Spinach signal 200 ms, gain 1) and laser at 642 nm /Cy5 filter set (50 ms, gain 1). Data analysis was performed using ImageJ64 including the measurement of values in selected pixel representing fluorescent intensity. Intensities, were plotted with Excel.

Measurement and data analysis on fluorescence images

First, each cell region on the BF image was selected first automatically (command written by Thomas Plenat) and then if necessary by visual inspection. The BF image was converted into thresholded images [Image ◃ Adjust ◃ Threshold] to set lower and upper threshold values, segmenting gray scale images into features of interest, individual cell region, and background. With [Analyze Particle] command, each cell regions in thresholded images were selected individually and recorded as the ROI (Region of Interest) [Analyze ◃ Analyze Particles]. All ROIs defined in one BF image are summarized in “ROI manager”, and overlaid on the corresponding Cy5 image. Using [Measure] function of ROI manager, the average gray values were measured within each ROI. The sum of the gray values of all the pixels in the selection is divided by the number of pixels to calculate the average.

Measurement of background of Cy5 image is as follows. A certain area that does not contain cells is selected on Cy5 image. Then, the average value of the region was measured [Analyze ◃ Measure].

The measured average values of each ROI and background were then transferred into Excel file where all the subsequent analysis process described below was performed. Background value was subtracted from each value of ROI, which is defined as the “cell Cy5 value” representing here the Neo-cy5 amount in individual cells. All Cy5 values in images of the same observation sample are combined and represented with a histogram.

Effect of CCCP on Neo-cy5 uptake by cells

In this experiment, Neo-Cy5 treatment was performed in presence of different concentration (final 40 μM or 100 μM) of CCCP (Carbonyl cyanide *m*-chlorophenyl hydrazone). Stock solutions of CCCP (4 mM or 10 mM) were prepared in DMSO. A volume of 10 μL of each CCCP stock or DMSO for control was added to 990 μL of a cell culture and incubated for 5 min, of which 9 μL were mixed with 1 μM of 4 μM Neo-Cy5 (final 0.4 μM) and incubated for 30 min.

Cell survival test

Cells were incubated with CCCP (dissolved in DMSO and at final concentration of 100 μM) for 5 minutes, while the corresponding volume of DMSO was added to the control cells. To the 8 μL of cell mixture, 1 μL of 40 μM neomycin in MOPS-G and 1 μL of 8 μM Neo-Cy5 were added (final concentration: 4 μM neomycin and 0.8 μM Neo-Cy5). Then, samples were incubated for 10 or 30 min.

Survival assays were performed as follows. After 10 and 30 minutes incubation, 4 μL of mixture were taken from the incubation sample with or without CCCP and several dilutions range from 10^2 to 10^5 times with MOPS-G were made.

Then, four spots we deposited on LB plate by applying 20 μl of every dilution and grown at 37 ˚C over night. As a control, diluted cell culture before the incubation with CCCP and neomycin was put on LB plate in the same way. On the next day, colonies were counted only in spots with 10 to 100 colonies (some spots were having too many colonies to be counted), to estimate the number of surviving cells in the original sample. Finally the survival rate of cells after the treatment with neomycins in presence or absence of 100 μM CCCP was calculated.

Cell observation

Cells were observed in nearly same conditions as survival test.

Here, I reduced the Neo-cy5 concentration in the cell mixture for incubation to a final concentration of 0.4 μM instead of 0.8 μM. Then the incubation was performed for five minutes. The cells were washed three times, and subsequently suspended with 1 μL of MOPS-G for observation. Two images were taken for every sample field: with BF (50 ms, gain 1) and laser at 642 nm /Cy5 filter set (50 ms, gain 50).

Cephalexin test

Here I checked the effect of cephalexin (kindly provided by Christophe Possoz), which is an inhibitor of cell division, on Neo-Cy5 uptake. A volume of 10 μL of 1 mM cephalexin was added to 990 μL of a cell culture and incubated for 30 minutes, of which 9 μL were mixed with 1

μLof 4 μM Neo-Cy5 (final concentration 0.4 μM) and incubated for 5 min.

Neo-cy5 uptake observation in *Bacillus subtilis*

First observation and comparison of cells treated with Neo-Cy5 for 10 min and 30 min

Bacillus subtilis strain wt 168 which is a single tryptophan-requiring auxotroph strain was kindly provided by Etienne Dervyn from INRA (Jouy en Josas).

For experiments, *B. subtilis* was first inoculated on LB plate and cultivated at 37˚C. Then a single colony was picked to inoculate a volume of MOPS-G supplemented with 0.01 % (w/v) tryptophan. Overnight culture was diluted to OD_{600} = 0.05 with fresh medium and cultivated until the OD_{600} reached approximately 0.3. For the treatment with Neo-Cy5, 9μL of cell culture were mixed with 1 μL of 4 μM Neo-cy5 (final 0.4 μM) and incubated for 10 or 30 minutes. Wash process and subsequent observation were performed in the same way as for *E. coli*.

Effect of CCCP on Neo-cy5 uptake of *B. subtilis*

The effect of CCCP on Neo-cy5 uptake was also confirmed or *B. subtilis*. The culture was incubated with 10 μM CCCP for 5 minutes, of which 9μL were mixed with 1 μM of 1 μM Neo-Cy5 (final 0.1 μM) and incubated for 30 minutes.

Chapter VI
Manuscript in revision at NAR

Use of Baby Spinach for imaging of structured cellular RNAs

Maho Okuda[1], Dominique Fourmy[1] and Satoko Yoshizawa[1,*]

[1] Institute for Integrative Biology of the Cell (I2BC), CEA, CNRS UMR9198, Université Paris-Sud, 1 Avenue de la Terrasse, F-91198, Gif-sur-Yvette cedex, France

* To whom correspondence should be addressed. Tel: +33 1 69 82 38 30; Fax: +33 1 69 82 31 60; Email: satoko.yoshizawa@i2bc.paris-saclay.fr

ABSTRACT

The fluorogenic RNA aptamer Spinach provides a powerful tool for study of RNA analogous to green fluorescent protein (GFP) for the study of proteins. Spinach is an RNA selected *in vitro* to bind to an exogenous chromophore that can be genetically inserted into an RNA of interest for live-cell imaging. Since the initial engineering of Spinach, the aptamer has been altered to increase thermal stability and stabilize the desired folding. Here we report a study of the performance of distinct RNA Spinach aptamer sequences in isolation or inserted into the small subunit of the bacterial ribosome. We found that the fluorescence of the most recent versions of Spinach strongly depended on the experimental conditions used. In the context of the 30S subunit of bacterial ribosome the minimized constructs performed best. These trends were even more pronounced *in vivo*. In particular, Baby Spinach, which has specific folding requirements *in vitro*, provides the highest levels of fluorescence in the ribosomal context *in vivo*.

INTRODUCTION

Live-cell imaging of RNA can be performed using aptamer-fluorogen complexes that elicit fluorescence at different wavelengths (1-6). Spinach, a 98-nt RNA aptamer that binds 3,5-difluoro-4-hydroxybenzylidene imidazolinone (DFHBI), was developed as a small-molecule mimic of the GFP fluorophore (1). The original RNA aptamer sequence suffered from thermal instability and a propensity for misfolding that resulted in reduced brightness (7). To address these shortcomings a superfolding Spinach2 sequence was engineered. Spinach2 has fluorescence that is less context-dependent and is brighter in living cells than the original Spinach (7).

Crystal structures of Spinach RNA in complex with DFHBI (8,9) were used to guide miniaturization that led to the generation of "Baby Spinach" (8). In this new version of the aptamer, the length was reduced to 51 nucleotides and fluorescence levels were comparable to that of the parental Spinach. Since illumination of the Spinach-DFHBI complex induces photoconversion with subsequent dissociation of the fluorogen leading fast fluorescence decay, a new illumination scheme was developed to improve Spinach-DFHBI RNA imaging in live cells (10). Despite these numerous improvements a comparative study of Spinach aptamer performance and the delineation of global strategies for tagging cellular RNAs for imaging have yet to be described.

Here we investigated the performance of eight distinct Spinach sequences both as transcripts and as an insertion in 16S rRNA. It was previously reported that Baby Spinach has fluorescence levels comparable to Spinach2 (8). As a transcript, despite use of the recommended folding protocol (8), Baby Spinach behaved poorly. In the context of the ribosomal RNA, however, the shorter Spinach constructs performed best. In particular, Baby Spinach was markedly superior to Spinach and Spinach2 *in vitro* and *in vivo*. Fractionation of total RNA from cells expressing Spinach-tagged 16S rRNA showed that Baby Spinach was more resistant to degradation than other Spinach sequences, which could account for its improved performance in living cells. Our data demonstrate that the

natural scaffold provided by rRNA can drastically influence the folding and stability of RNA aptamers.

MATERIAL AND METHODS

Reagents and equipment

DFHBI and DFHBI-1T were purchased from Lucerna Technologies. Bacterial strains were grown in liquid Luria-Bertani (LB) broth at 37 °C with shaking at 200 rpm or on LB agar plates at 37 °C. In some cases, media contained 100 μg/mL ampicillin and 50 μg/mL kanamycin. Cell imaging experiments were performed using an inverted microscope Zeiss (Axio-observer Z1). Fluorescence excitation, emission spectra and fluorescence intensity measurements were performed using a Tecan Infinite 200 PRO plate reader.

Plasmids construction

Spinach sequences used in this study are summarized in Table 1. Spinach2-mini is a truncated version of Spinach2 designed for this study to harbour the same structural characteristics as Spinach1-mini. The ApaI/XbaI region of rrnB operon was subcloned between HindIII and EcoRI sites of pUC18 in order to facilitate the generation of Spinach ribosome constructs (pUC18-AX). A PstI site was created in the helix 33a region by mutating T1030G and G1032A to facilitate insertion of Spinach sequences (pUC18-AXP). The different Spinach sequences were introduced at the PstI site. Each Spinach sequence was amplified by PCR and cloned into pUC18-AXP using either an In-Fusion HD Cloning Kit (Clontech) or a Quick Ligation Kit (NEB). The ApaI/XbaI fragments harbouring Spinach sequences were then placed into pKK3535, which carries the entire rrnB rRNA

operon under the control of the native constitutive promoter P1P2 (11). These constructs were named pKK3535-h33a-Spinach vectors. All oligonucleotides used are listed in Table 2.

Preparation of *E. coli* TA531 expressing Spinach-modified ribosomes

E. coli strain TA531 from which the seven copies of the chromosomal rRNA operon have been deleted harbours the plasmid pHC-rrnC carrying a single copy of rrnC operon as the sole source of rRNA genes and a kanamycin resistance gene (12). Replacement of pHC-rrnC in TA531 by pKK3535-h33a-Spinach plasmid was achieved by transformation of the *E. coli* followed by growth in liquid LB medium containing ampicillin for at least two days after reaching the stationary phase. The saturated culture was diluted and inoculated onto LB plates containing ampicillin, and single colonies were isolated. Plasmid substitution was tested by evaluating resistance of colonies to ampicillin and sensitivity to kanamycin. Colonies that survived only on ampicillin LB plates were selected.

Growth of *E. coli* expressing Spinach ribosomes

E. coli TA531 harbouring pKK3535-h33a-Spinach series plasmids were inoculated into liquid LB in Erlenmeyer flasks from glycerol stocks. The overnight cultures were diluted with 50 ml of fresh LB medium to an OD of 0.05 – 0.07. ODs at 600 nm were measured every 30 min until cell growth reached early stationary phase.

To confirm that DFHBI was not toxic to *E. coli* that express Spinach-modified ribosomal RNA, cell growth was measured in presence of DFHBI with an Infinite 200 PRO microplate reader. Wells of a 96-well microtiter plate containing 190 μL of LB were inoculated with 5 μL of an overnight culture (OD_{600} = 2) of *E. coli* strain TA531. The growth was followed by measuring the absorbance

at 600 nm every 15 min at 37 °C with constant shaking at 218 rpm except during measurement.

Expression and purification of Spinach ribosomes

LB (1 L) was inoculated with 10 mL of a saturated overnight culture of *E. coli* TA531 harbouring pKK3535-h33a-Spinach plasmid and grown to an OD_{600} of 0.4. Cells were harvested by centrifugation (8000 g, 4 °C for 10 min) and washed with buffer A [20 mM Tris-HCl (pH 7.5), 100 mM NH_4Cl, 10 mM $MgCl_2$, 0.5 mM EDTA, 6 mM 2-mercaptoethanol]. Cells were frozen in liquid nitrogen and stored at -80 °C until use. All subsequent steps were performed at 4 °C or on ice. Cells were resuspended in buffer A and lysed using a bench-top press (Carver). Lysates were diluted with buffer A and centrifuged (15000 g). Crude ribosomes were then prepared by sedimentation (131000 g, 16 h) through sucrose cushions. The resulting ribosome pellet was washed twice with 1 mL of buffer A and resuspended in 250 μL of buffer A. Crude ribosomes were frozen in liquid nitrogen and stored at -80 °C.

Further purification of ribosomes were performed using a cysteine-charged sulfolink resin (13). A 100-μL aliquot of crude ribosome solution was diluted with the same volume of buffer B [20 mM Tris-HCl (pH 7.5), 10 mM $MgCl_2$, 0.5 mM EDTA, 2-mercaptoethanol] to adjust the concentration of NH_4Cl to be 50 mM and was then loaded to 2 mL of charged resin. The column was washed with 10 mL of buffer B containing 60 mM NH_4Cl, and ribosomes were eluted with buffer B containing 500 mM NH_4Cl. Ribosomes in the eluted fractions were collected by ultracentrifugation (213000 g for 16 h). The ribosome pellet was resuspended in 50 μL of buffer A. The ribosome solutions were aliquoted, quick-frozen, and stored at -80 °C.

In vitro transcription of Spinach aptamers

RNA fragments containing various Spinach sequences were prepared by *in vitro* transcription using T7 RNA polymerase. The template DNAs for transcription were prepared by PCR amplifying pKK3535-h33a-Spinach plasmids using T7-16SrRNA-h33-F and 16SrRNA-h33-R primers (Table 2). Transcripts were purified using Nucleospin RNA spin columns (Macherey-Nagel) with a protocol adapted for short RNAs (Macherey-Nagel).

In vitro fluorescence measurement of Spinach-DFHBI complexes

RNA transcripts were dissolved in water, refolded by heating at 90 °C for 1 min and then placing on ice for 5 min. For refolding using a slow cool step, samples were heated at 90 °C for 1 min, buffer and DFHBI solutions were added, and samples were kept at 65 °C for 5 minutes. The RNA was then refolded by a slow decrease of temperature over a period of 20 minutes (40 cycles comprising a temperature decrease at a rate of 0.3 °C/sec for 3.3 secondes followed by a step of 30 secondes of equilibration) down to 25 °C. Fluorescence measurements were performed in 384-well black microtiter plates at 25 °C with the excitation at 455 nm and emission monitored at 506 nm. The background signal from DFHBI in culture medium or buffer was subtracted for each measurement.

Fluorescence of each Spinach/DFHBI complex was measured as follows: 1 μM Spinach-modified ribosome in buffer A was incubated with 2 μM DFHBI diluted in the same buffer for 15 min at 25 °C. A 10-μL aliquot of the complex solution was introduced into a well of a 384-well microtiter plate, and fluorescence intensity was measured. Fluorescence from DFHBI bound to Spinach transcripts was measured in samples containing 0.1 μM RNA and 0.2 μM DFHBI or 0.1 μM RNA and 10 μM DFHBI. Fluorescence measurements were performed in ribosome

buffer containing KCl [20 mM Tris-HCl (pH 7.5), 100 mM NH_4Cl, 10 mM $MgCl_2$, 0.5 mM EDTA, 6 mM 2-mercaptoethanol and 125 mM KCl] or in HEPES-KOH buffer [20 mM HEPES (pH 7.4), 100 mM KCl and 1 mM $MgCl_2$].

Live cell imaging of Spinach-tagged ribosomes

To measure whole-cell fluorescence in liquid culture, overnight cultures of *E. coli* strain TA531 harbouring pKK3535-h33a-Spinach variants were inoculated into 50 mL of fresh LB containing ampicillin and grown to an OD_{600} of 0.4. Cells were collected in 1.5-mL aliquots and washed once with the same volume of M9 minimal medium (47.75 mM Na_2HPO_4, 22.04 mM KH_2PO_4, 8.56 mM NaCl, 18.7 mM NH_4Cl, 2 mM $MgSO_4$, 0.1 mM $CaCl_2$ and 0.4% glucose). Washed cells were resuspended in M9 medium to an OD of 1 and incubated with 200 μM DFHBI for 90 min at 37 °C. A 10-μL aliquot was transferred to a 384-well microtiter plate and fluorescence intensity at 25 °C was measured (excitation wavelength, 455 nm; emission wavelength, 506 nm).

Imaging of the *E. coli* cells was performed using am Axio Observer Zeiss microscope (objective 63X, N.A. 1.46, excitation 470 (+/- 13) nm, emission 512 (+/- 15) nm). Fluorescence levels were corrected for the background fluorescence generated by DFHBI alone in the culture medium.

Analysis of RNA degradation

Degradation of Spinach tagged rRNA was investigated by fractionation on urea-PAGE. *E. coli* TA strains harbouring Spinach 16S rRNA plasmids were grown to an OD_{600} of 0.4 in LB. Total RNA was purified from a 1-mL aliquot of the culture using NucleoSpinRNA columns (Machery-Nagel). Samples of 500 ng of total RNA were loaded on 6% polyacrylamide-7 M urea gels. Gels were washed with water for 5 minutes three times and stained using DFHBI-1T or SYBR Gold as

described (14).

Fluorescent primer extension was carried out as described previously (15). Cy5-labelled DNA primer was purchased from MWG Biotech. rRNAs (250 ng) were mixed with the Cy5-labelled primer (10 pmol) in hybridization buffer (25 mM HEPES, pH 7.0, 50 mM KCl), heated to 90 °C (1-2 min), and slowly cooled to 45 °C. Reverse transcription reactions were performed using SuperScript II (Invitrogen) in the supplied reaction buffer at 45 °C for 40 min. The reactions were stopped by ethanol precipitation. cDNA samples were dissolved in 10 μL 7M urea and a small aliquot (1.5 to 3 μL) of each sample was loaded on an 8% polyacrylamide-7 M urea gel. The gel was imaged using Typhoon Trio scanner (GE Healthcare).

RESULTS AND DISCUSSION

Design of Spinach-tagged ribosomes

Spinach RNA sequences were introduced into helix 33a of 16S rRNA (Figure 1A); the UUCG tetraloop was replaced with Spinach RNAs. In crystal structures of the ribosome (16), helix 33a is not involved in any tertiary interaction and protrudes outside the ribosome structure (Figure 1B). This region of 16S rRNA is not phylogenetically conserved (17), and extension of the helix does not perturb *E. coli* ribosomal function (18). Spinach sequences were inserted at a PstI site, which was introduced in the helix 33a region of 16S rDNA by site-directed mutagenesis (Supplementary Figure 1). Except for Baby and mBaby, Spinach sequences were inserted by conventional ligation resulting in the extension of helix 33a by five base pairs (Supplementary Figure 1). For Baby and mBaby Spinach constructs, we performed cloning by recombination. We took advantage of the natural scaffold provided by helix 33a to shortened helix P2 of the aptamer by two base pairs

(Supplementary Figure 1). In addition to the original Spinach, we tested seven other constructs (Figure 2): minimized Spinach (Spinach-mini) (1), a thermostable variant of Spinach (Spinach1.2), the superfolder Spinach (Spinach2) (7), Spinach1.2 with a tRNA scaffold (tSpinach1.2) (1,19), miniaturized "Baby Spinach" (8), Spinach2-mini (an aptamer we designed by analogy to Spinach-mini), and a deletion mutant of Baby Spinach with the P3 stem shortened by four base pairs (mBabySpinach).

In vitro fluorescence assay of the Spinach constructs

Prior to examining the performance of Spinach sequences in the context of the ribosome, we investigated the level of fluorescence of each aptamer construct in previously used buffers (7,8) and in the ribosome buffer (20 mM Tris-HCl (pH 7.5), 100 mM NH_4Cl, 10 mM $MgCl_2$, 0.5 mM EDTA, 6 mM 2-mercaptoethanol) supplemented with 125 mM KCl. The tested transcripts included helices 33 and 33a of 16S rRNA (Figure 1) and thereby closely resembled the ribosomal context. Transcripts were generated by *in vitro* T7 transcription and purified over Nucleospin columns. The RNAs were folded by heating at 90 °C for 1 min and then placing on ice. The crystal structure of Spinach revealed that K^+ and Mg^{2+} are part of the structure of folded DFHBI-Spinach complex (8,9). For this reason, buffers used for Spinach fluorescence assays contained these cations. The intrinsic fluorescence of most studied aptamers has been characterized (7). Therefore, we focused our effort on the rate of folding using a protocol that included an excess of fluorophore to ensure that the amount of aptamer-DFHBI complex is highly dependent on the amount of RNA that is correctly folded (7).

In the HEPES-KOH buffer previously used in characterization of the Spinach2 construct (7), at a ratio DFHBI to RNA of 2:1, fluorescence of three constructs, Spinach, Spinach-mini, and

Spinach2-mini, was 3-fold higher than that of other constructs (Figure 3A). At a ratio of 100:1 DFHBI to RNA, levels of fluorescence increased, and differences were minimized with the exception of tSpinach1.2 fluorescence, which remained at a low level. In ribosome buffer supplemented with KCl, the same trends were observed (Figure 3B).

Levels of fluorescence in ribosome buffer were almost identical to those measured in the HEPES buffer, indicating that the ribosome buffer is suitable for performing fluorescence assays using Spinach. When the ratios of fluorescence intensities at 100-fold excess vs. 2-fold excess of DFHBI in HEPES-KOH were compared to those in ribosome buffer, ratios were much greater in HEPES-KOH (Figure 3C). This suggests that Spinach constructs fold best in buffer supplemented with KCl.

In the case of Baby Spinach, signals were surprisingly low. Therefore the RNA was folded using slow cooling protocol that was reported previously to improve folding (8). Fluorescence levels were markedly improved using this method and best in the buffers containing Tris-HCl (Figure 4A). When the other constructs were subjected to this folding protocol, the levels of fluorescence increased by at least 30% with the exception of tSpinach1.2 sequence for which a large increase of 4 fold was observed (Figure 4B). The efficiency of Baby Spinach folding remained inferior to that of all other Spinach aptamers.

Expression of 16S rRNA modified with large Spinach sequences adversely impact bacterial cell growth

The plasmid pHC containing the rrnC operon in strain *E. coli* TA531, a strain from which all seven copies of the genomic rRNA operons have been deleted (12), was replaced with plasmid pKK3535 harbouring Spinach sequences within the 16S rDNA. This strain was used because expression of a

homogenous population of ribosomes facilitated evaluation of the effect of Spinach insertion on cell growth and allowed purification of Spinach-tagged ribosomes. As shown in Figure 5, introduction of earlier generation Spinach sequences (Spinach, Spinach 1.2) caused slight defects in *E. coli* growth. Expression of 16S rRNA containing Spinach1.2 with the stabilizing tRNA scaffold (tSpinach1.2) altered the physiology of *E. coli* TA531; aggregates of cells were observed (Supplementary Figure 2). Expression of all other constructs tested here (Spinach, Spinach-mini, Spinach2, Spinach2-mini, Spinach1.2, Baby Spinach, and the deletion mutant, mBabySpinach) did not modify the physiology of cells grown in liquid culture (data not shown) but did reduce growth rate (except for Baby Spinach). The cells that expressed 16S rRNA in which superfolder Spinach2-mini was inserted into helix 33a grew at almost the same rate as wild-type cells. A wild-type level of growth was observed for cells expressing 16S rRNA modified with Baby Spinach, the shortest version of the constructs. These results indicate that the length of the RNA inserted in helix 33a is important. Insertions of around 50 nucleotides were well tolerated. Interestingly, the construct mBaby Spinach, in which 8 nucleotides were removed from the P3 stem of Baby Spinach, was deleterious to cell growth. It is possible that unexpected folding of the RNA *in vivo* altered ribosomal assembly or affected ribosome stability.

Fluorescence of the Spinach constructs in the ribosomal context

We then investigated the fluorescence levels of these Spinach aptamers in the context of the ribosome. Ribosomes were purified from *E. coli* strain TA531 that had a single copy of rrnB operon with the Spinach insertion. This ensured homogeneity of Spinach-tagged ribosomes. DFHBI did not affect the growth rates of cells that expressed any of the constructs (Supplementary Figure 3) indicating that the fluorophore is non-toxic and that it did not affect ribosomal activity.

Fluorescence was examined in samples containing 1 μM RNA and 2 μM DHFBI in ribosome buffer. Spectra were the same for all constructs (Supplementary Figure 4), but intensities were quite different (Figure 6A) and K^+ strongly stimulated the intensity (Figure 6B). Spinach, Spinach1.2, and tSpinach1.2 were not strongly fluorescent in the context of the ribosome. Surprisingly the fluorescence signal measured for the recently developed 'superfolder' Spinach2 construct was only slightly higher than that of Spinach. The three constructs that resulted in the highest fluorescence signal fell into the category of miniaturized Spinach versions: Spinach-mini, Spinach2-mini, and Baby Spinach. Spinach-mini (80 nts) was first described in the original work that introduced the Spinach RNA aptamer (1); Spinach-mini has a deletion in the J1-2 junction and a second deletion in the paired region P3 relative to Spinach. We introduced these same deletions into Spinach-2 to generate Spinach2-mini (80-nts). Finally, Baby Spinach, which is the smallest of all constructs (51-nts), behaved poorly as a RNA transcript but displayed the highest yield of folding and fluorescence in the cellular context. This result demonstrated that ribosomal RNA serves as a scaffold that promotes Baby Spinach folding or prevents its degradation *in vivo*.

Live-cell imaging of Spinach-tagged ribosomes

Spinach-tagged ribosomes were then expressed in strain TA531, and levels of fluorescence were measured in live cells. Values were normalized to the 16S rRNA expression levels determined by RT-PCR of purified total RNA; transcript levels were quite homogenous among the samples. Cells were grown in LB, and the culture media was exchanged for M9-Glucose media before addition of 20 μM DFHBI and incubation at 37 °C. M9 media contains Mg^{2+} and K^+ cations ensuring high levels of fluorescence of Spinach derivatives during measurements. Previously, Spinach2 was found to be more fluorescent than Spinach in eukaryotic cells (7). In *E. coli*, these two aptamers generated

similar signals (Figure 7A). As observed *in vitro*, short Spinach constructs inserted in helix 33a of 16S ribosomal RNA clearly showed highest fluorescence signals. For example, Spinach2-mini generated a signal 6-fold stronger than that observed in cells in which Spinach2 was expressed. Similarly, the fluorescence emitted by the short version of Spinach (Spinach-mini) was 6-fold stronger than its long counterpart. More importantly, cells that expressed Baby Spinach were 7-fold brighter than the 'superfolder' Spinach2. Therefore, the *in vivo* results mirror the *in vitro* data. Imaging of the *E. coli* cells expressing various Spinach-tagged ribosomes confirmed that those expressing Baby Spinach exhibited strong fluorescence (Figure 7B). Fluorescence of Baby Spinach- and Spinach2-mini-expressing cells from the same culture varied (Figure 7B). This might reflect differences, at the single-cell level, in intracellular DFHBI accumulation or differences in the quantity of ribosomes.

RNA degradation *in vivo*

Degradation of ribosomal RNA containing the Spinach insert could account for low fluorescence signals of some of the aptamers in cells. We therefore asked whether the RNA aptamers were subjected to degradation by endo- or exonucleases in *E. coli*. To visualize degradation products, total cellular RNA was extracted from cells expressing Spinach-tagged 16S rRNA. Analysis on 6% polyacrylamide denaturing gel followed by DFHBI-1T (brighter analogue of DFHBI) or SYBR Gold staining revealed the pattern of degradation products (Figure 8A). DFHBI-1T should stain 16S rRNA containing the dye-binding aptamer. mBaby Spinach-modified RNA was undetectable on gels stained with DFHBI-1T. Other constructs showed a major band corresponding to 16S rRNA. Lower molecular weight bands were detected for all constructs but were less intense for the sample in which ribosomal RNA was modified with Baby Spinach (Figure 8A). As expected, a control of

total cellular RNA from a strain expressing non-tagged ribosome had no RNA that generated fluorescence upon staining with DFHBI-1T. The degradation bands observed with other constructs are therefore the results of cleavage of 16S rRNA molecules. Spinach-mini and Spinach 1.2 reproducibly produced a band of higher molecular weight that remains uncharacterized. A similar experiment was performed on purified Spinach-tagged ribosomes (Figure 8B). With the exception of Baby Spinach, which resulted in a single band, all other constructs gave lower molecular weight bands that stained with DFHBI-1T indicating that cleavages within 16S rRNA occurred that generated large fragments of rRNA containing the Spinach tag.

We next identified possible cleavage sites in the vicinity or within the Spinach tags on purified rRNA for three constructs. Purified ribosomes were phenol extracted to obtain rRNA samples that were subjected to fluorescent primer extension as previously described (15). Cleavage by an endonuclease results in a stop of primer extension by reverse transcriptase. In the case of tSpinach1.2, multiple bands were detected in the region of the aptamer and a few bands were detected within the tRNA scaffold (Figure 8C). It was recently reported that endonucleases, which normally process tRNAs *in vivo*, cleave the tRNA-scaffold of tBrocoli and tSpinach sequences followed by a removal of the remaining flanking regions by trimming at the 3' terminus by exonucleases RNase T and RNase PH (20). In the context of the ribosome, the situation seems quite different as we did not observe a strong primer extension stop at the 3' processing site of tRNA within the tSpinach1.2 construct. Instead, multiple stops were observed within the aptamer sequence suggesting that endonucleolytic cleavages occur within this region with only few additional cuts in the tRNA scaffold. The difference may be due to the context of tRNA scaffold. In our study the tRNA scaffold was inserted into helix 33a of the 16S rRNA; thus, 3' and 5' regions of the tRNA are embedded in an RNA stem. In contrast the tRNA was flanked by single-stranded

regions in the construct used by Filonov *et al*. (20). In addition, in the context of the ribosome, steric hindrance may protect the tRNA sequence from RNases. The cleavages that we observed within the aptamer sequence are likely a consequence of accessibility and partial unfolding in the absence of DFHBI *in vivo*. The small size of Baby Spinach aptamer and its enhanced folding propensity likely prevents this non-specific degradation (Figure 8C)

CONCLUSION

Our comparative studies of the performance of different Spinach aptamers when inserted at the same position within a large structured cellular RNA, the 16S rRNA, revealed a strategy that can be used to identify robust aptamers for bacterial live-cell imaging. The site of insertion, helix 33a, was chosen because previous studies showed that this stem-loop protrudes outside the ribosome and is tolerant of extra RNA sequences (18). Here we showed that the number of inserted nucleotides should be kept to less than about 50 nucleotides since, for the larger constructs, the growth rate of cells was altered. Folding properties of the different aptamers were first evaluated *in vitro* in the context of T7 RNA transcripts that included a full domain comprising helices 33 and 33a. Surprisingly, Baby Spinach, which requires a specific folding protocol that includes slow cooling did not bind dye as well as the other Spinach aptamers. In contrast, when the aptamers were expressed *in vivo* and purified in native form as Spinach-tagged ribosomes, the results were drastically different. Clearly, shorter aptamers, Spinach-mini, Spinach2-mini, and Baby Spinach were superior to the other constructs in terms of fluorescence. In isolated ribosomes, Baby Spinach, which is also the shortest of the aptamer with 43 nucleotides inserted into the 16SrRNA, had the highest fluorescence intensity. Similar results were obtained when fluorescence of the aptamers was

assayed directly in live *E. coli* cells expressing the different Spinach-tagged ribosomes. These results indicate that the structured environment of ribosomal RNA helix 33a provides a natural scaffold that promotes folding of Baby Spinach. The small size of Baby Spinach also prevents cleavage of 16S rRNA. Baby Spinach appears to be the Spinach variant that most effectively labels large structured cellular RNAs.

ACKNOWLEDGEMENT

We thank S.C. Blanchard (Weill Medical College, Cornel University) for support and S. Jaffrey (Weill Medical College, Cornel University) for providing the Spinach1 sequence.

FUNDING

This work was supported by the Centre National de la Recherche Scientifique (CNRS) to S.Y. M. O. was supported by JASSO, a fellowship from French embassy in Japan "Bourse du gouvernement français" and a fellowship from FRM (Fondation pour la recherché Médicale-FDT20140931068).

REFERENCES

1. Paige, J.S., Wu, K.Y. and Jaffrey, S.R. (2011) RNA mimics of green fluorescent protein. *Science*, **333**, 642-646.
2. Song, W., Strack, R.L., Svensen, N. and Jaffrey, S.R. (2014) Plug-and-play fluorophores extend the spectral properties of Spinach. *Journal of the American Chemical Society*, **136**, 1198-1201.
3. Dolgosheina, E.V., Jeng, S.C., Panchapakesan, S.S., Cojocaru, R., Chen, P.S., Wilson, P.D., Hawkins, N., Wiggins, P.A. and Unrau, P.J. (2014) RNA mango aptamer-fluorophore: a bright, high-affinity complex for RNA labeling and tracking. *ACS chemical biology*, **9**, 2412-2420.
4. You, M. and Jaffrey, S.R. (2015) Structure and Mechanism of RNA Mimics of Green

Fluorescent Protein. *Annual review of biophysics*, **44**, 187-206.

5. Strack, R.L. and Jaffrey, S.R. (2015) Live-cell imaging of mammalian RNAs with Spinach2. *Methods in enzymology*, **550**, 129-146.
6. You, M., Litke, J.L. and Jaffrey, S.R. (2015) Imaging metabolite dynamics in living cells using a Spinach-based riboswitch. *Proceedings of the National Academy of Sciences of the United States of America*, **112**, E2756-2765.
7. Strack, R.L., Disney, M.D. and Jaffrey, S.R. (2013) A superfolding Spinach2 reveals the dynamic nature of trinucleotide repeat-containing RNA. *Nature methods*, **10**, 1219-1224.
8. Warner, K.D., Chen, M.C., Song, W., Strack, R.L., Thorn, A., Jaffrey, S.R. and Ferre-D'Amare, A.R. (2014) Structural basis for activity of highly efficient RNA mimics of green fluorescent protein. *Nature structural & molecular biology*, **21**, 658-663.
9. Huang, H., Suslov, N.B., Li, N.S., Shelke, S.A., Evans, M.E., Koldobskaya, Y., Rice, P.A. and Piccirilli, J.A. (2014) A G-quadruplex-containing RNA activates fluorescence in a GFP-like fluorophore. *Nature chemical biology*, **10**, 686-691.
10. Han, K.Y., Leslie, B.J., Fei, J., Zhang, J. and Ha, T. (2013) Understanding the photophysics of the spinach-DFHBI RNA aptamer-fluorogen complex to improve live-cell RNA imaging. *Journal of the American Chemical Society*, **135**, 19033-19038.
11. Brosius, J., Ullrich, A., Raker, M.A., Gray, A., Dull, T.J., Gutell, R.R. and Noller, H.F. (1981) Construction and fine mapping of recombinant plasmids containing the rrnB ribosomal RNA operon of E. coli. *Plasmid*, **6**, 112-118.
12. Asai, T., Zaporojets, D., Squires, C. and Squires, C.L. (1999) An Escherichia coli strain with all chromosomal rRNA operons inactivated: complete exchange of rRNA genes between bacteria. *Proceedings of the National Academy of Sciences of the United States of America*, **96**, 1971-1976.
13. Leshin, J.A., Rakauskaite, R., Dinman, J.D. and Meskauskas, A. (2010) Enhanced purity, activity and structural integrity of yeast ribosomes purified using a general chromatographic method. *RNA biology*, **7**, 354-360.
14. Filonov, G.S., Moon, J.D., Svensen, N. and Jaffrey, S.R. (2014) Broccoli: rapid selection of an RNA mimic of green fluorescent protein by fluorescence-based selection and directed evolution. *Journal of the American Chemical Society*, **136**, 16299-16308.
15. Ying, B.W., Fourmy, D. and Yoshizawa, S. (2007) Substitution of the use of radioactivity by fluorescence for biochemical studies of RNA. *RNA*, **13**, 2042-2050.
16. Schuwirth, B.S., Borovinskaya, M.A., Hau, C.W., Zhang, W., Vila-Sanjurjo, A., Holton, J.M. and Cate, J.H. (2005) Structures of the bacterial ribosome at 3.5 A resolution. *Science*, **310**, 827-834.

17. Cannone, J.J., Subramanian, S., Schnare, M.N., Collett, J.R., D'Souza, L.M., Du, Y., Feng, B., Lin, N., Madabusi, L.V., Muller, K.M. *et al*. (2002) The comparative RNA web (CRW) site: an online database of comparative sequence and structure information for ribosomal, intron, and other RNAs. *BMC bioinformatics*, **3**, 2.

18. Dorywalska, M., Blanchard, S.C., Gonzalez, R.L., Kim, H.D., Chu, S. and Puglisi, J.D. (2005) Site-specific labeling of the ribosome for single-molecule spectroscopy. *Nucleic acids research*, **33**, 182-189.

19. Ponchon, L. and Dardel, F. (2007) Recombinant RNA technology: the tRNA scaffold. *Nature methods*, **4**, 571-576.

20. Filonov, G.S., Kam, C.W., Song, W. and Jaffrey, S.R. (2015) In-gel imaging of RNA processing using broccoli reveals optimal aptamer expression strategies. *Chemistry & biology*, **22**, 649-660.

TABLE AND FIGURES LEGENDS

Table 1

Name	Sequence
Spinach (98 nts)	GACGCAACUGAAUGAAAUGGUGAAGGACGGGUCCAGGUGU GGCUGCUUCGGCAGUGCAGCUUGUUGAGUAGAGUGUGAGC UCCGUAACUAGUCGCGUC
Spinach-mini (80 nts)	GACGCGACCGAAAUGGUGAAGGACGGGUCCAGUGCUUCGG CACUGUUGAGUAGAGUGUGAGCUCCGUAACUGGUCGCGUC
Spinach1.2 (95 nts)	GACGCGACCGAAUGAAAUGGUGAAGGACGGGUCCAGCCGG CUGCUUCGGCAGCCGGCUUGUUGAGUAGAGUGUGAGCUCC GUAACUGGUCGCGUC
tSpinach1.2 (153 nts)	GCCCGGAUAGCUCAGUCGGUAGAGCAGGACGCGACCGAAU GAAAUGGUGAAGGACGGGUCCAGCCGGCUGCUUCGGCAGC CGGCUUGUUGAGUAGAGUGUGAGCUCCGUAACUGGUCGCG UCGUCCAGGGUUCAAGUCCCUGUUCGGGCGCCA
Spinach2 (95 nts)	GAUGUAACUGAAUGAAAUGGUGAAGGACGGGUCCAGUAG GCUGCUUCGGCAGCCUACUUGUUGAGUAGAGUGUGAGCUC CGUAACUAGUUACAUC
Spinach2-mini (80 nts)	GAUGUAACUGAAAUGGUGAAGGACGGGUCCAGUGCUUCGG CACUGUUGAGUAGAGUGUGAGCUCCGUAACUAGUUACAUC
mBabySpinach (35 nts)	AAGGACGGGUCCGUUCGCGUUGAGUAGAGUGUGAG
Baby Spinach (43 nts)	AAGGACGGGUCCAGUAGUUCGCUACUGUUGAGUAGAGUGU GAG

Table 2

Name	Sequence
pkk3535HindApa	TACCGAAGCTTGGGCCCGCACAAGCGGTG
pkk3535EcoXba	CCCGGAATTCTAGACGAAGGGGACACGAAAATTGCTTATC
Mut_PstI_F	GAGATGAGAATGTGCCTGCAGGAACCGTGAGACAGG
Mut_PstI_R	CCTGTCTCACGGTTCCTGCAGGCACATTCTCATCTC
Spinach1_mini_F	AACTGCAGGACGCGACCAGTTACGGAGCTCACACTCTACTCAACAGTGCCGAAGCAC
Spinach1_mini_R	AACTGCAGGACGCGACCGAAATGGTGAAGGACGGGTCCAGTGCTTCGGCACTGTTGA
Spinach1_F	AGATGAGAATGTGCCTGCAGGACGCAACTGAATGAAATGG
Spinach1_R	CTGTCTCACGGTTCCTGCAGGACGCGACTAGTTACGGAGC
Spinach1.2_F	AGATGAGAATGTGCCTGCAGGACGCGACCGAATGAAAT
Spinach1.2_R	CTGTCTCACGGTTCCTGCAGGACGCGACCAGTTACGGAG
Spinach1.2_tRNA_F	AGATGAGAATGTGCCTGCAGGCCCGGATAGCTCAGTCG
Spinach1.2_tRNA_R	CTGTCTCACGGTTCCTGCAGTGGCGCCCGAACAG
Spinach2_mini_F	GATGAGAATGTGCCTGCAGGATGTAACTGAAATGGTGAAGGACG
Spinach2_mini_R	CTGTCTCACGGTTCCTGCAGGATGTAACTAGTTACGGAGCTCACAC
Spinach2_F	GATGTAACTGAATGAAATGGTGAAGGACGGGTCCAGTAGGCTGCTTCGGCAGCCTACT
Spinach2_R	GATGTAACTAGTTACGGAGCTCACACTCTACTCAACAAGTAGGCTGCCGAAGCAGCCT
16S_fusion-Spinach2_F	AGATGAGAATGTGCCTGCAGGATGTAACTGAATGAAATGGTGA
Baby_Spinach_F	AGATGAGAATGTGCCTGAAGGACGGGTCCAGTAGTTCG

	CTACTGTTGAGTAGA
Baby_Spinach_R	CTGTCTCACGGTTCCTGCTCACACTCTACTCAACAGTAG CGAACTACTGGACC
Micro_Spinac_F	AGATGAGAATGTGCCTGAAGGACGGGTCCGTTCGCGTT GAGTAGA
Micro_Spinac_R	CTGTCTCACGGTTCCTGCTCACACTCTACTCAACGCGAA CGGACC
16S_fusion_ApaI _F	AAATGAATTGACGGGGG
16S_fusion_XbaI _R	TGTCCTGGGCCTCTAGA
pUCpKK-fusion-ApaI	AAATGAATTGACGGGGGCCCGCACAAGC
pUCpKK-fusion-XbaI	GTCCTGGGCCTCTAGACGAAGGGGACACG
pk3302minusseq	CACAAACCAGCAAGTGGC
T7-16SrRNA-h33 -F	TAATACGACTCACTATAGATCCACGGAAGTTTTCAG
16SrRNA-h33-R	ACCTGTCTCACGGTTCC

Figure 1. Insertion site of Spinach sequences into 16S rRNA. (A) Secondary structure of 16S rRNA. The site of insertion in helix 33a (h33a) is boxed. (B) Side view of 70S *E. coli* ribosome (PDB code 2AW4 (50S) 2AVY (30S) (16)) with the tip of helix 33a highlighted. 16S and 23S rRNA molecules are shown in blue and red, respectively.

Figure 2. Spinach secondary structures: (A) Spinach, (B) Spinach-mini, (C) Spinach1.2, (D) Spinach2, (E) Spinach2-mini, (F) Baby Spinach, and (G) mBaby Spinach. DFHBI is highlighted in green. Grey boxes are the bases deleted in the "mini" versions of Spinach and Spinach2. Red bases are the sites of mutations that transform Spinach into Spinach1.2. Blue base pairs are bases present in Spinach2.

Figure 3. Comparative analysis of the fluorescence of Spinach transcripts. Levels of fluorescence of Spinach-DFHBI complexes were measured at 25 °C in samples containing 0.1 μM RNA and 2-fold molar excess of DFHBI (white bars) or 100-fold molar excess of DFHBI (grey bars) in (A) HEPES buffer or (B) ribosome buffer. (C) Comparison of ratios of fluorescence intensity in 100-fold to 2-fold excess of DFHBI in HEPES buffer (grey bars) or ribosome buffer (black bars). Error bars are s. e. m. for three independent experiments. A large excess of DFHBI ensures that fluorescence is strongly dependent on the amount of RNA that is folded and able to bind the fluorogen.

Figure 4. Fluorescence of Baby Spinach requires slow cooling for efficient folding. (A) The RNA transcript was snap cooled to 65 °C in water and then slow cooled to 25 °C in buffer (65 °C to 25 °C) or snap cooled (25 °C); fluorescence intensities in 2-fold molar excess of DFHBI (white bars) and in 100-fold excess (grey bars) in indicated buffers were determined. (B) Fluorescence

intensities of Spinach sequences in ribosome buffer supplemented with 125 mM KCl at 100-fold DFHBI molar excess snap cooled (light grey bars) or slow cooled (dark grey bars). Error bars are s. e. m. for three independent experiments.

Figure 5. Growth of *E. coli* expressing Spinach-containing 16S rRNA. Rates were measured in liquid culture at 37 °C in LB. Values were normalized to *E. coli* strain TA531, which expresses wild-type 16S rRNA.

Figure 6. Fluorescence of ribosomes that contain Spinach variant 16S rRNAs. (A) Fluorescence of purified 70S ribosomes (1 μM) measured at 25 °C after addition of 2 μM DFHBI. Values are normalized to that of ribosomes with 16S rRNA modified with Spinach. (B) Effects of the addition of 125 mM KCl on the fluorescence of purified 70S ribosomes (1 μM) measured at 25 °C after addition of 2 μM DFHBI. Error bars are s. e. m. for three independent experiments.

Figure 7. *In vivo* fluorescence of cells expressing Spinach variant 16S rRNAs. (A) Fluorescence signal from *E. coli* TA531 cells incubated with 20 μM DFHBI in M9-Glucose (2 mM Mg^{2+}) media at 37 °C for 30 minutes. Samples were excited at 455 nm in a plate reader, and fluorescence was recorded at 506 nm. Values were corrected for DFHBI background and normalized to the level of expression of 16S rRNA. Error bars are s. e. m. for three independent experiments. (B) Imaging of *E. coli* TA531 cells expressing different Spinach-tagged ribosomes. Cells we incubated with 200 μM DFHBI-1T for 90 min at 37 °C, mounted on agar pad, and imaged at room temperature under a microscope. The signal is the sum of 5 cycles of excitation/acquisition (50 ms) spaced by 20 seconds necessary for fluorescence recovery as previously described (10). Brightness of the images

was adjusted based on Baby Spinach signal. Note heterogeneity in the levels of fluorescence at the single-cell level.

Figure 8. Degradation of Spinach-tagged 16S rRNA. (A) Total RNA from *E. coli* TA531 cells expressing Spinach-tagged ribosomes was separated on urea-PAGE and stained with DFHBI-1T (top) and SYBR Gold (bottom). 16S rRNA bands are indicated by arrows. (B) Ribosomes were purified from *E. coli* TA531 cells expressing Spinach-tagged 16S rRNA. RNA was separated on urea-PAGE and stained with DFHBI-1T (top) and SYBR Gold (bottom). (C) Fluorescent primer extension analysis of cleavage sites in Spinach-modified 16S rRNA. Fluorescent primer extension products generated using Cy5-labelled DNA primer were analysed on urea-PAGE. Regions corresponding to helix 33a, tRNA scaffold, Spinach, and Baby Spinach are indicated by arrows.

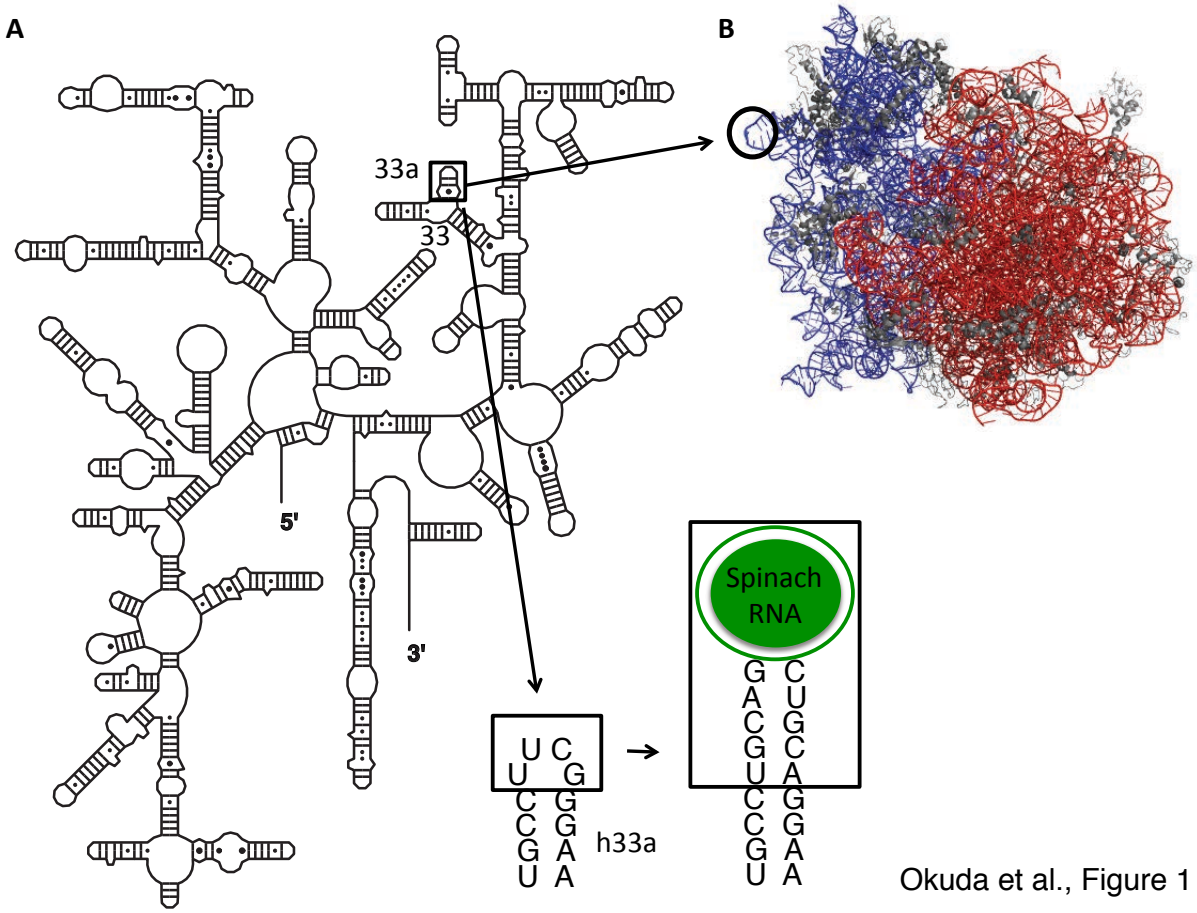

Okuda et al., Figure 1

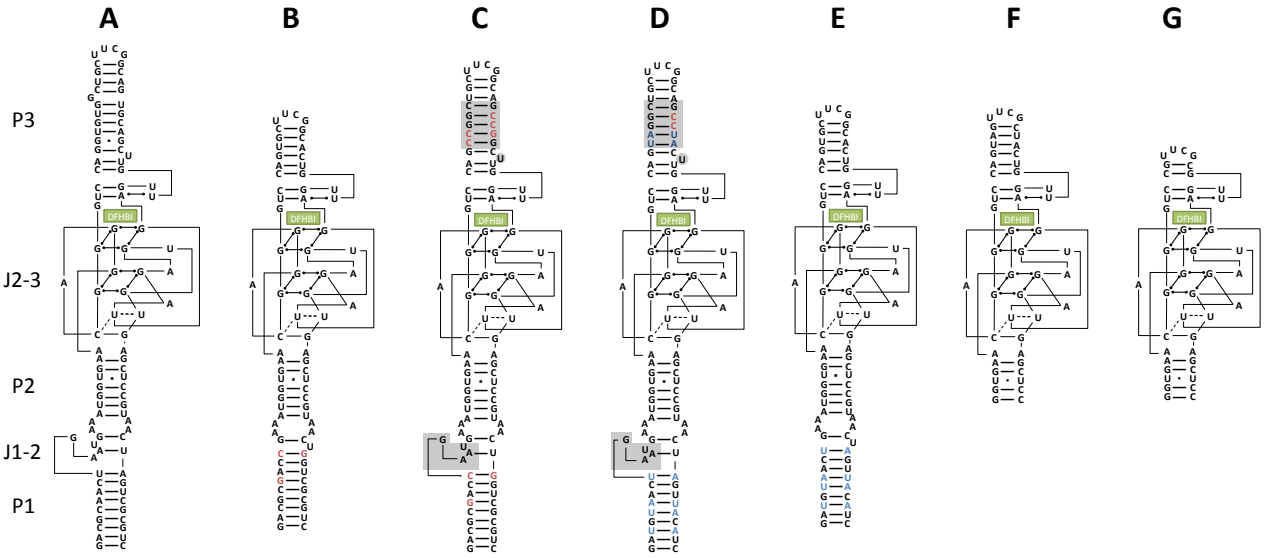

Okuda et al., Figure 2

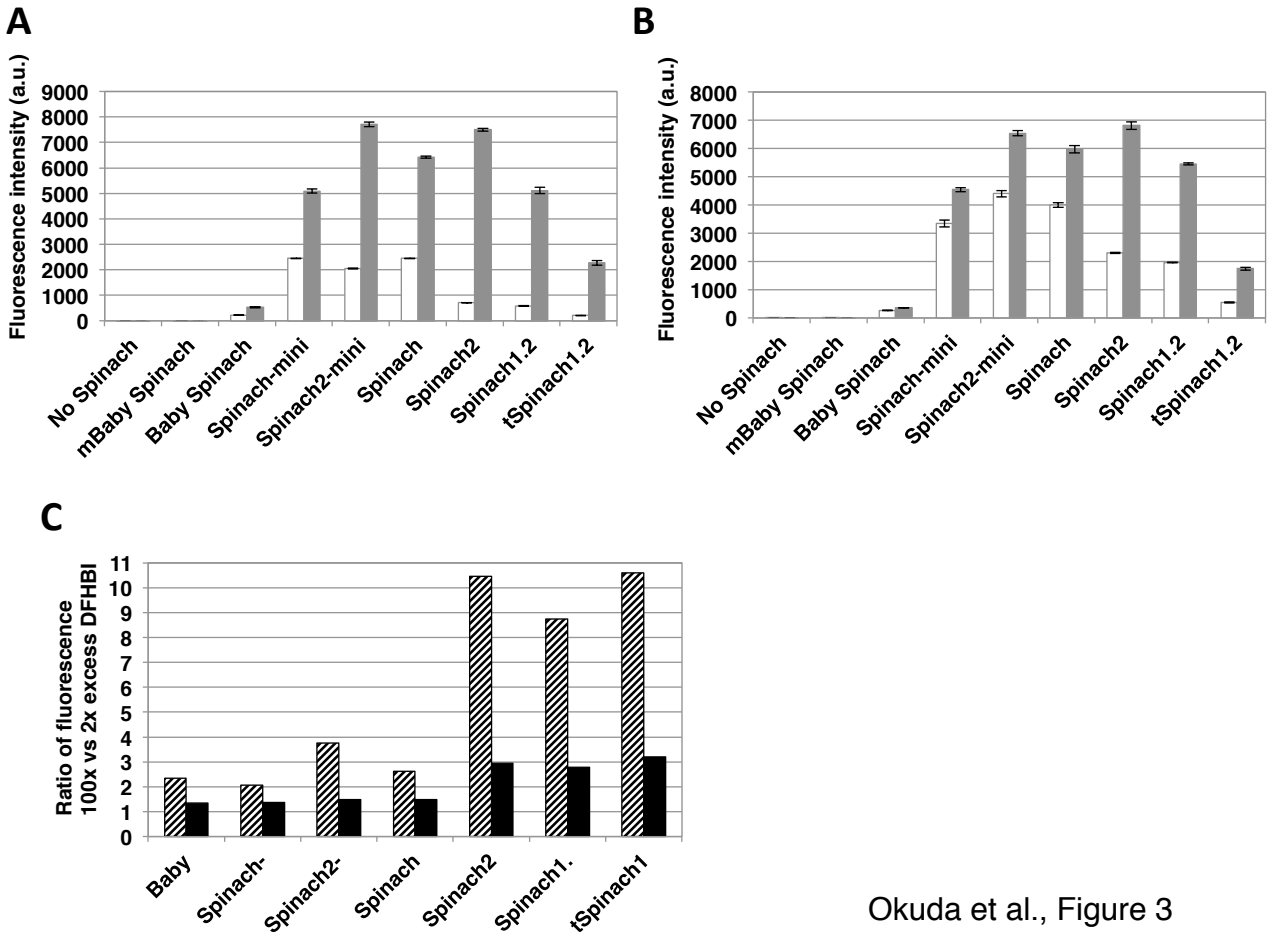

Okuda et al., Figure 3

A

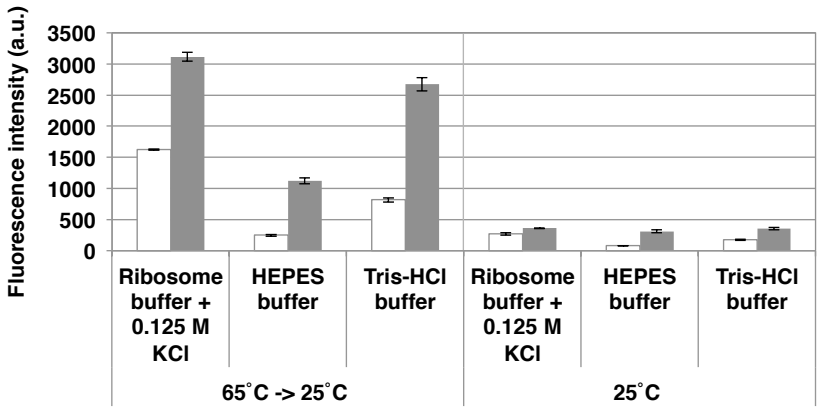

B

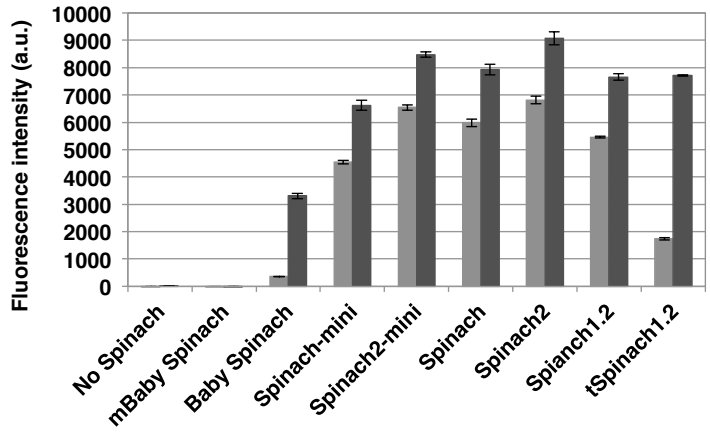

Okuda et al., Figure 4

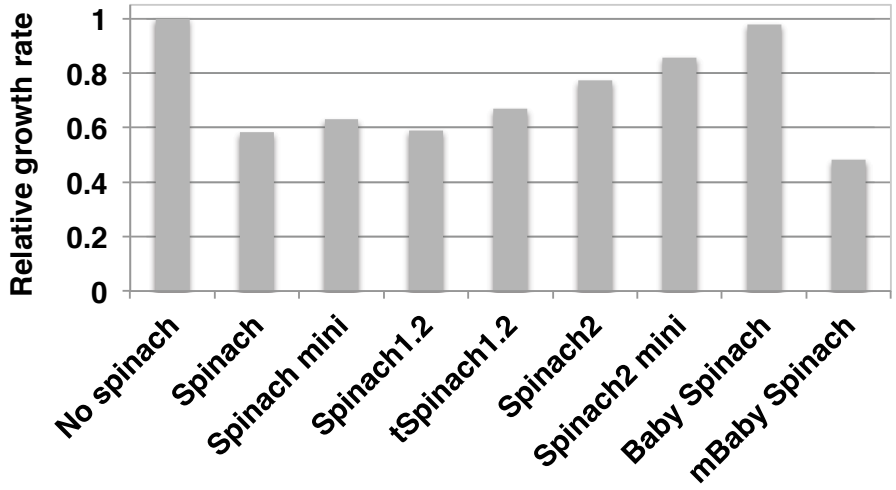

Okuda et al., Figure 5

A

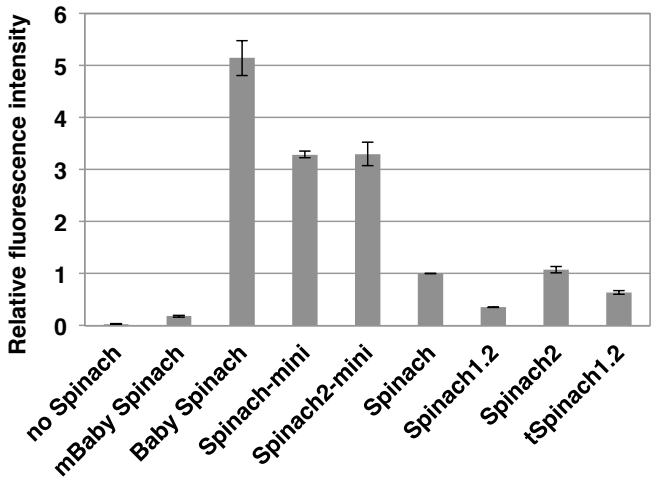

B

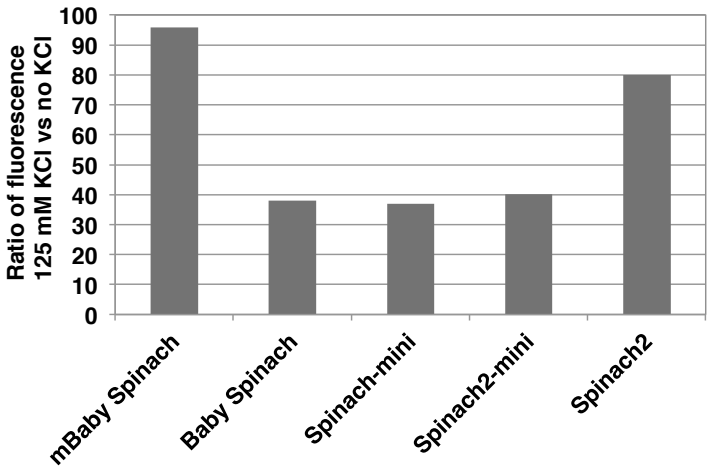

Okuda et al., Figure 6

A

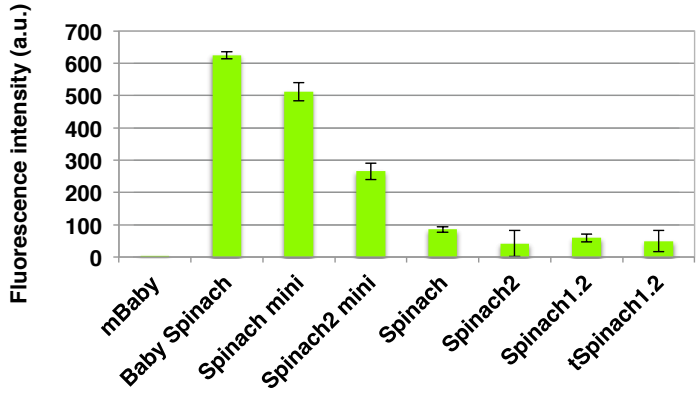

B

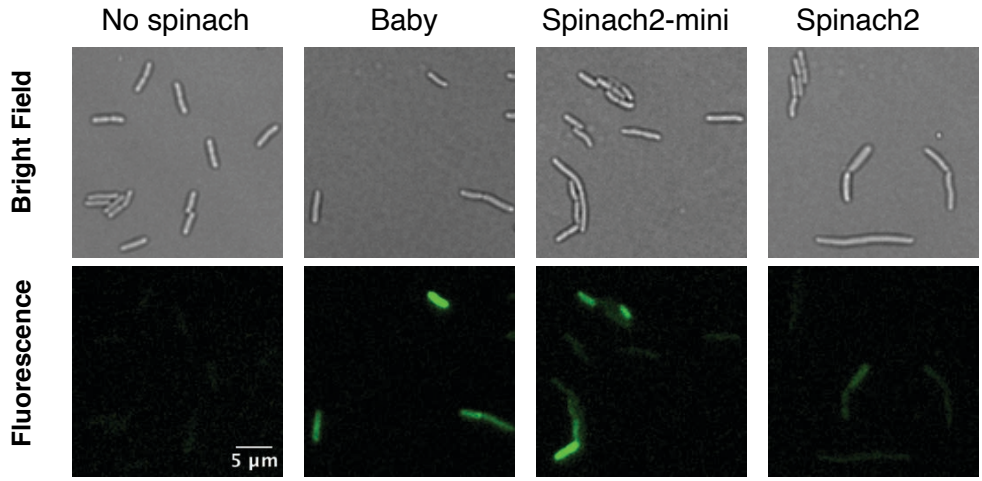

Okuda et al., Figure 7

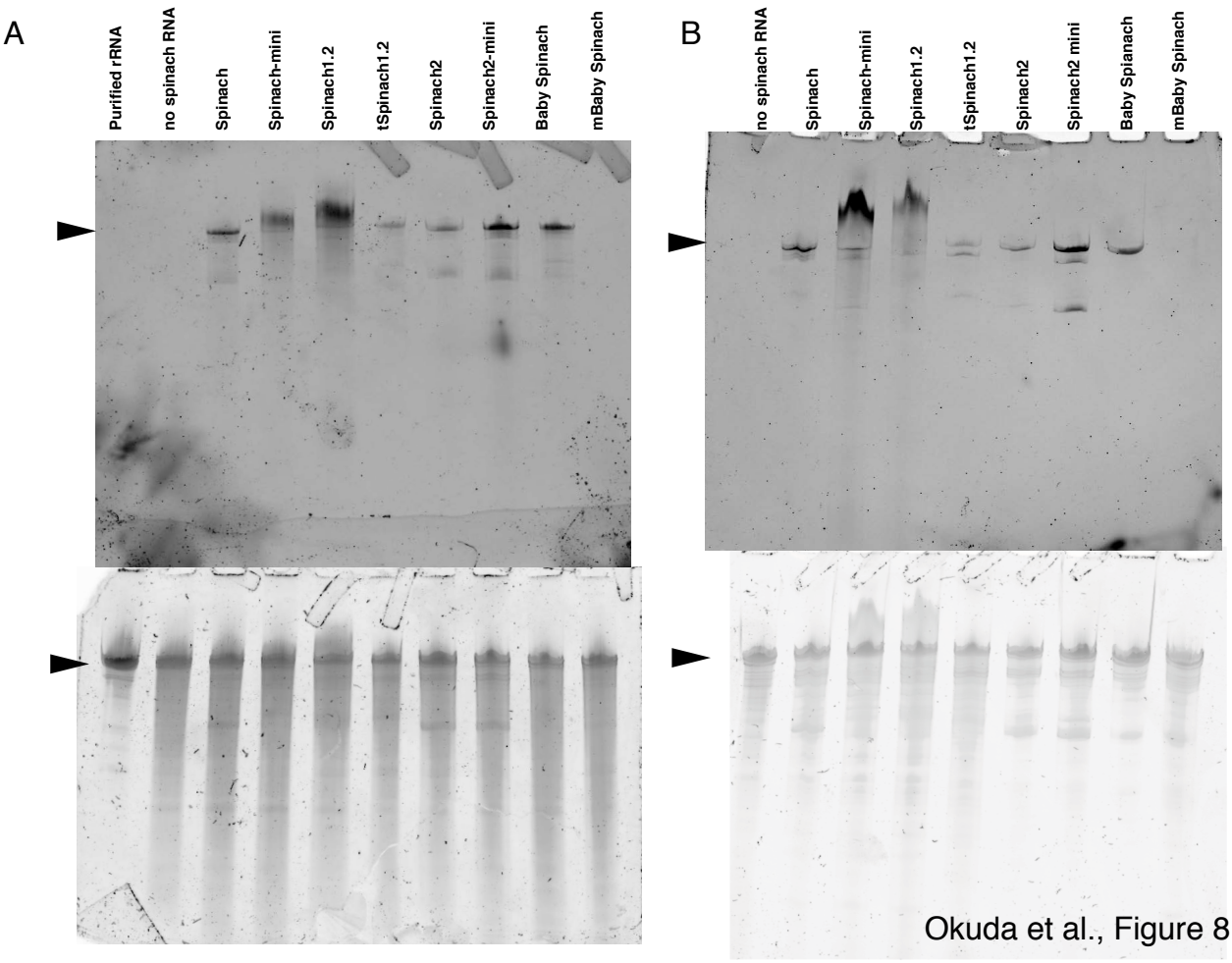

Okuda et al., Figure 8

C

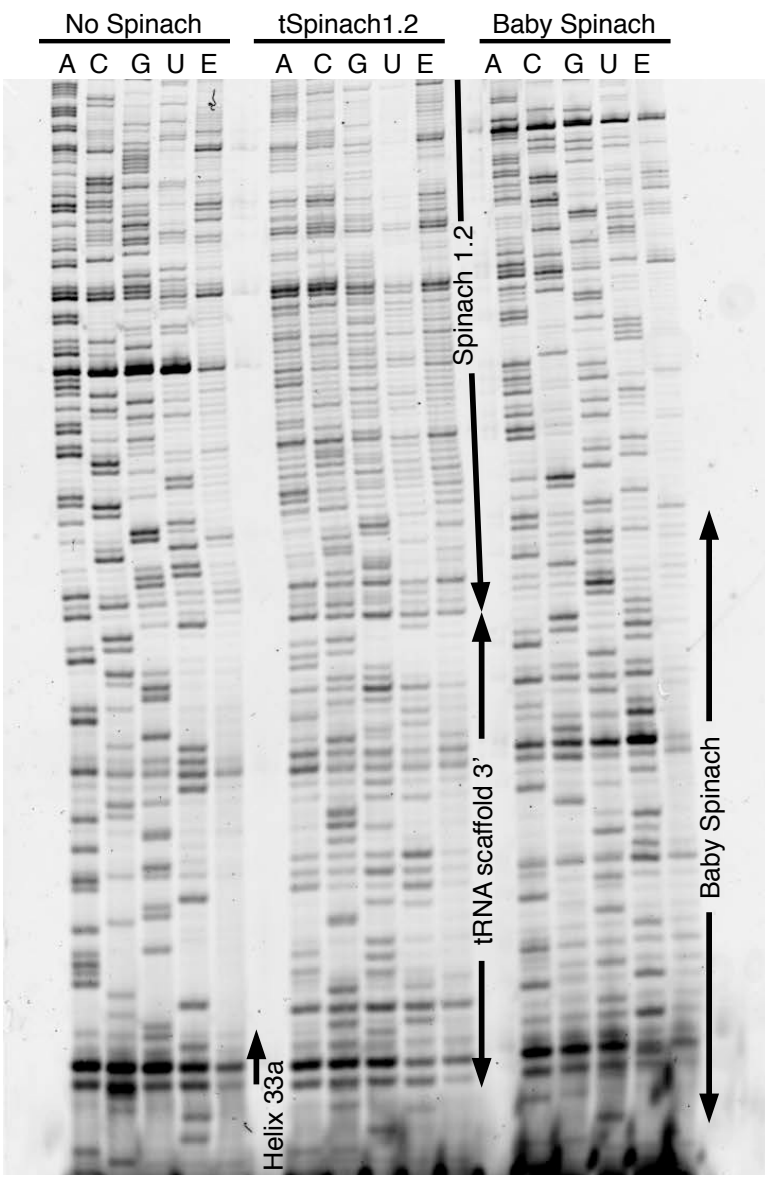

Okuda et al., Figure 8

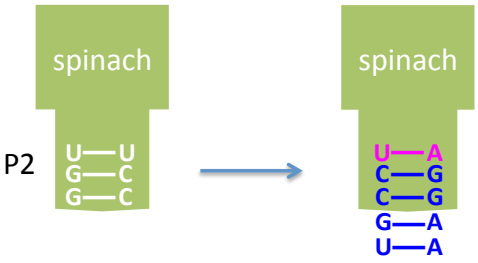

- mBaby Spinach
- Baby Spinach

- Spinach-mini
- Spinach2-mini
- Spinach
- Spinach1.2
- Spinach2

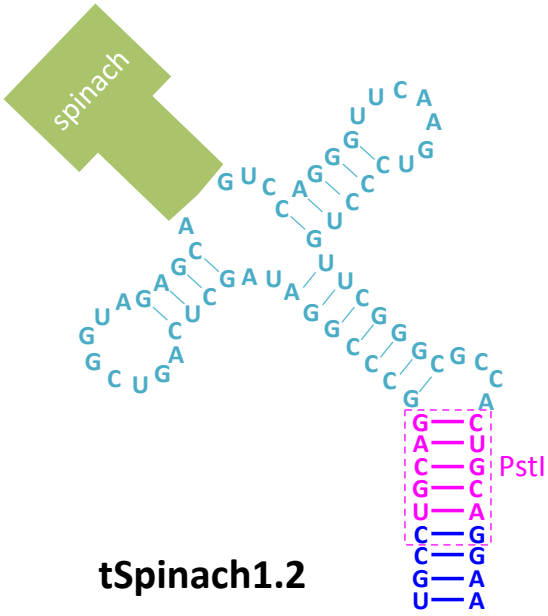

tSpinach1.2

Supplementary Figure 1: Strategy for insertion of Spinach sequences into helix 33a of 16S rRNA; sequences given in Figure 1 are represented as green boxes.

Okuda et al., Supplementary Figure 1

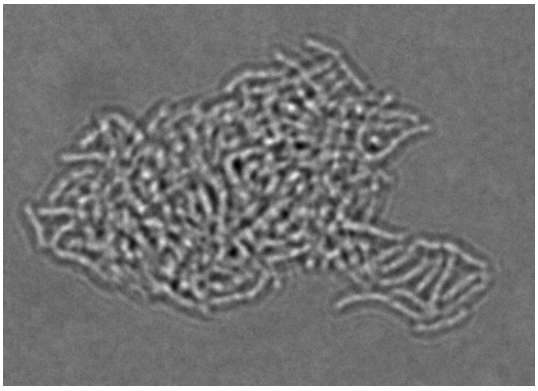

tSpinach1.2

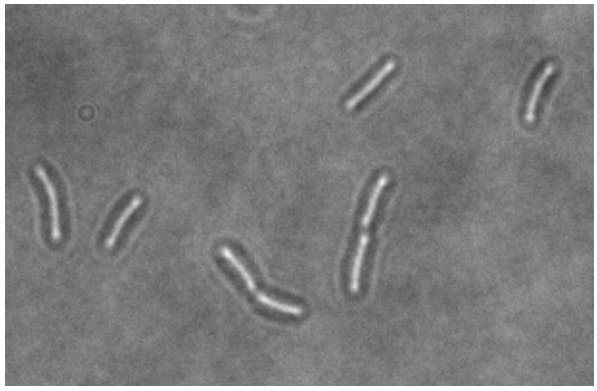

Spinach-mini

Supplementary Figure 2: Brightfield images of *E. coli* TA531 observed from fresh liquid culture in LB. Cells expressing 16S rRNA tagged with tSpinach1.2 formed aggregates.

Okuda et al., Supplementary Figure 2

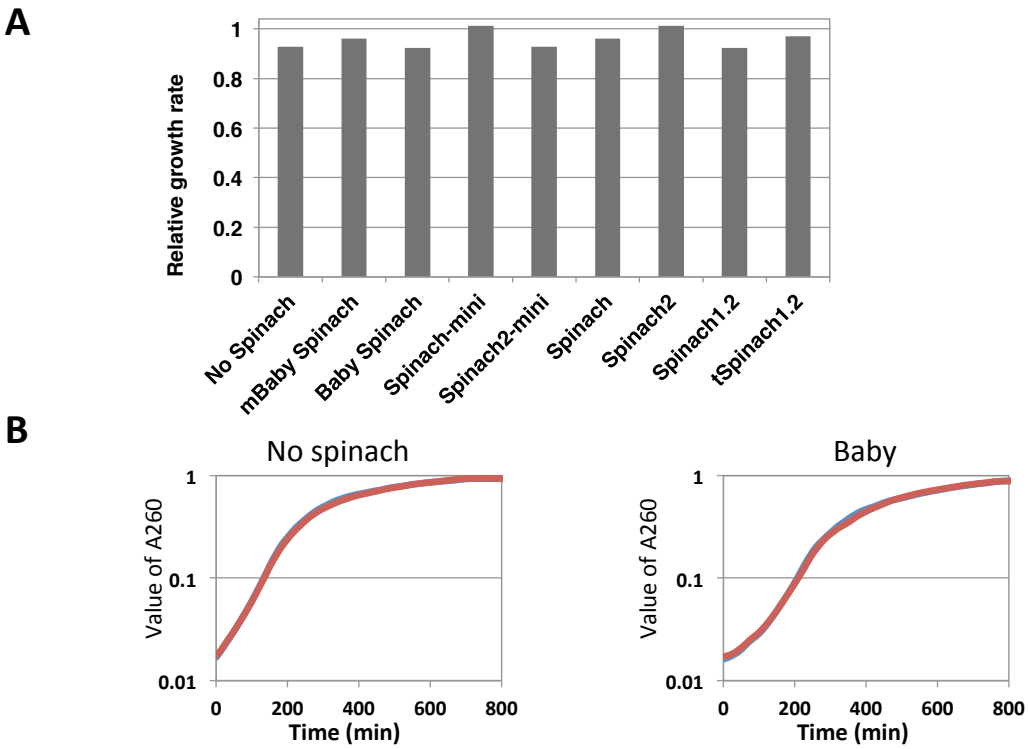

Supplementary Figure 3: (A) Generation time of *E. coli* cells TA531 expressing Spinach-tagged ribosomes is unaffected by the presence of 200 μM DFHBI in culture media (LB). Values are normalized to the growth rate of TA531 in absence of DFHBI (not represented). (B) Representative growth curve for cells expressing native 16S rRNA (left) or Baby Spinach-tagged 16S rRNA (right). Red curves: 200 μM DFHBI; Blue curves: no DFHBI.

Okuda et al., Supplementary Figure 3

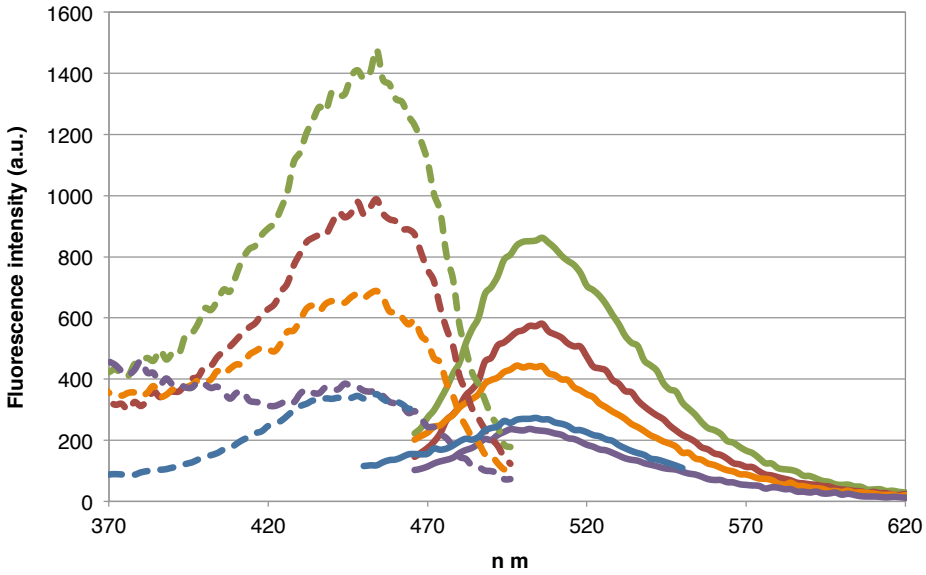

Supplementary Figure 4: Emission spectra of DFHBI in the presence of 16S rRNA tagged with Baby Spinach (green), Spinach-mini (red), Spinach2-mini (orange), Spinach (blue), and Spinach2 (purple). Dotted lines are excitation spectra, solid lines are emission spectra.

Okuda et al., Supplementary Figure 4

Chapter VII
References

1. Russell, J.B. and Cook, G.M. (1995) Energetics of bacterial growth: balance of anabolic and catabolic reactions. Microbiological reviews, 59, 48-62.
2. Yusupov, M.M., Yusupova, G.Z., Baucom, A., Lieberman, K., Earnest, T.N., Cate, J.H. and Noller, H.F. (2001) Crystal structure of the ribosome at 5.5 A resolution. Science, 292, 883-896.
3. Ban, N., Nissen, P., Hansen, J., Moore, P.B. and Steitz, T.A. (2000) The complete atomic structure of the large ribosomal subunit at 2.4 A resolution. Science, 289, 905-920.
4. Yonath, A. (2002) The search and its outcome: high-resolution structures of ribosomal particles from mesophilic, thermophilic, and halophilic bacteria at various functional states. Annual review of biophysics and biomolecular structure, 31, 257-273.
5. Schluenzen, F., Tocilj, A., Zarivach, R., Harms, J., Gluehmann, M., Janell, D., Bashan, A., Bartels, H., Agmon, I., Franceschi, F. et al. (2000) Structure of functionally activated small ribosomal subunit at 3.3 angstroms resolution. Cell, 102, 615-623.
6. Wimberly, B.T., Brodersen, D.E., Clemons, W.M., Jr., Morgan-Warren, R.J., Carter, A.P., Vonrhein, C., Hartsch, T. and Ramakrishnan, V. (2000) Structure of the 30S ribosomal subunit. Nature, 407, 327-339.
7. Carter, A.P., Clemons, W.M., Brodersen, D.E., Morgan-Warren, R.J., Wimberly, B.T. and Ramakrishnan, V. (2000) Functional insights from the structure of the 30S ribosomal subunit and its interactions with antibiotics. Nature, 407, 340-348.
8. Cate, J.H., Yusupov, M.M., Yusupova, G.Z., Earnest, T.N. and Noller, H.F. (1999) X-ray crystal structures of 70S ribosome functional complexes. Science, 285, 2095-2104.
9. Schuwirth, B.S., Borovinskaya, M.A., Hau, C.W., Zhang, W., Vila-Sanjurjo, A., Holton, J.M. and Cate, J.H. (2005) Structures of the bacterial ribosome at 3.5 A resolution. Science, 310, 827-834.

10. Selmer, M., Dunham, C.M., Murphy, F.V.t., Weixlbaumer, A., Petry, S., Kelley, A.C., Weir, J.R. and Ramakrishnan, V. (2006) Structure of the 70S ribosome complexed with mRNA and tRNA. Science, 313, 1935-1942.
11. Lodmell, J.S. and Dahlberg, A.E. (1997) A conformational switch in Escherichia coli 16S ribosomal RNA during decoding of messenger RNA. Science, 277, 1262-1267.
12. Ogle, J.M., Brodersen, D.E., Clemons, W.M., Jr., Tarry, M.J., Carter, A.P. and Ramakrishnan, V. (2001) Recognition of cognate transfer RNA by the 30S ribosomal subunit. Science, 292, 897-902.
13. Ogle, J.M., Murphy, F.V., Tarry, M.J. and Ramakrishnan, V. (2002) Selection of tRNA by the ribosome requires a transition from an open to a closed form. Cell, 111, 721-732.
14. Schmeing, T.M. and Ramakrishnan, V. (2009) What recent ribosome structures have revealed about the mechanism of translation. Nature, 461, 1234-1242.
15. Voorhees, R.M., Weixlbaumer, A., Loakes, D., Kelley, A.C. and Ramakrishnan, V. (2009) Insights into substrate stabilization from snapshots of the peptidyl transferase center of the intact 70S ribosome. Nature structural & molecular biology, 16, 528-533.
16. Leung, E.K., Suslov, N., Tuttle, N., Sengupta, R. and Piccirilli, J.A. (2011) The mechanism of peptidyl transfer catalysis by the ribosome. Annual review of biochemistry, 80, 527-555.
17. Petrelli, D., LaTeana, A., Garofalo, C., Spurio, R., Pon, C.L. and Gualerzi, C.O. (2001) Translation initiation factor IF3: two domains, five functions, one mechanism? The EMBO journal, 20, 4560-4569.
18. Carter, A.P., Clemons, W.M., Jr., Brodersen, D.E., Morgan-Warren, R.J., Hartsch, T., Wimberly, B.T. and Ramakrishnan, V. (2001) Crystal structure of an initiation factor bound to the 30S ribosomal subunit. Science, 291, 498-501.
19. Dahlquist, K.D. and Puglisi, J.D. (2000) Interaction of translation initiation factor IF1 with the E. coli ribosomal A site. Journal of molecular biology, 299, 1-15.
20. Schmeing, T.M., Voorhees, R.M., Kelley, A.C., Gao, Y.G., Murphy, F.V.t., Weir, J.R. and Ramakrishnan, V. (2009) The crystal structure of the ribosome bound to EF-Tu and aminoacyl-tRNA. Science, 326, 688-694.
21. Ramakrishnan, V. and Moore, P.B. (2001) Atomic structures at last: the ribosome in 2000. Current opinion in structural biology, 11, 144-154.

22. Grosjean, H.J., Henau, S. and Crothers, D.M. (1978) On the physical basis for ambiguity in genetic coding interactions. Proc. Natl. Acad. Sci., 75, 610-614.
23. Kurland, C.G. (1992) Translational accuracy and the fitness of bacteria. Annu. Rev. Genet., 26, 29-50.
24. Dunkle, J.A. and Cate, J.H. (2010) Ribosome structure and dynamics during translocation and termination. Annual review of biophysics, 39, 227-244.
25. Youngman, E.M., McDonald, M.E. and Green, R. (2008) Peptide release on the ribosome: mechanism and implications for translational control. Annual review of microbiology, 62, 353-373.
26. Gao, H., Zhou, Z., Rawat, U., Huang, C., Bouakaz, L., Wang, C., Cheng, Z., Liu, Y., Zavialov, A., Gursky, R. et al. (2007) RF3 induces ribosomal conformational changes responsible for dissociation of class I release factors. Cell, 129, 929-941.
27. Klaholz, B.P., Pape, T., Zavialov, A.V., Myasnikov, A.G., Orlova, E.V., Vestergaard, B., Ehrenberg, M. and van Heel, M. (2003) Structure of the Escherichia coli ribosomal termination complex with release factor 2. Nature, 421, 90-94.
28. Hirashima, A. and Kaji, A. (1973) Role of elongation factor G and a protein factor on the release of ribosomes from messenger ribonucleic acid. The Journal of biological chemistry, 248, 7580-7587.
29. Frank, J., Penczek, P., Agrawal, R.K., Grassucci, R.A. and Heagle, A.B. (2000) Three-dimensional cryoelectron microscopy of ribosomes. Methods in enzymology, 317, 276-291.
30. Yokoyama, T., Shaikh, T.R., Iwakura, N., Kaji, H., Kaji, A. and Agrawal, R.K. (2012) Structural insights into initial and intermediate steps of the ribosome-recycling process. The EMBO journal, 31, 1836-1846.
31. Karimi, R., Pavlov, M.Y., Buckingham, R.H. and Ehrenberg, M. (1999) Novel roles for classical factors at the interface between translation termination and initiation. Molecular cell, 3, 601-609.
32. Peske, F., Rodnina, M.V. and Wintermeyer, W. (2005) Sequence of steps in ribosome recycling as defined by kinetic analysis. Molecular cell, 18, 403-412.
33. Hirokawa, G., Nijman, R.M., Raj, V.S., Kaji, H., Igarashi, K. and Kaji, A. (2005) The role of ribosome recycling factor in dissociation of 70S ribosomes into subunits. RNA, 11, 1317-1328.
34. Wilson, D.N. (2014) Ribosome-targeting antibiotics and mechanisms of bacterial resistance. Nature reviews. Microbiology, 12, 35-48.

35. Tsien, R.Y. (1998) The green fluorescent protein. Annual review of biochemistry, 67, 509-544.
36. Shimomura, O., Johnson, F.H. and Saiga, Y. (1962) Extraction, purification and properties of aequorin, a bioluminescent protein from the luminous hydromedusan, Aequorea. Journal of cellular and comparative physiology, 59, 223-239.
37. Cody, C.W., Prasher, D.C., Westler, W.M., Prendergast, F.G. and Ward, W.W. (1993) Chemical structure of the hexapeptide chromophore of the Aequorea green-fluorescent protein. Biochemistry, 32, 1212-1218.
38. Shimomura, O. (1979) Structure of the chromophore of Aequorea green fluorescent protein. FEBS letters, 104, 220-222.
39. Heim, R., Prasher, D.C. and Tsien, R.Y. (1994) Wavelength mutations and posttranslational autoxidation of green fluorescent protein. Proceedings of the National Academy of Sciences of the United States of America, 91, 12501-12504.
40. Cubitt, A.B., Heim, R., Adams, S.R., Boyd, A.E., Gross, L.A. and Tsien, R.Y. (1995) Understanding, improving and using green fluorescent proteins. Trends in biochemical sciences, 20, 448-455.
41. Prasher, D.C., Eckenrode, V.K., Ward, W.W., Prendergast, F.G. and Cormier, M.J. (1992) Primary structure of the Aequorea victoria green-fluorescent protein. Gene, 111, 229-233.
42. Chalfie, M., Tu, Y., Euskirchen, G., Ward, W.W. and Prasher, D.C. (1994) Green fluorescent protein as a marker for gene expression. Science, 263, 802-805.
43. Stearns, T. (1995) Green fluorescent protein. The green revolution. Current biology : CB, 5, 262-264.
44. Wang, S. and Hazelrigg, T. (1994) Implications for bcd mRNA localization from spatial distribution of exu protein in Drosophila oogenesis. Nature, 369, 400-403.
45. Yang, F., Moss, L.G. and Phillips, G.N., Jr. (1996) The molecular structure of green fluorescent protein. Nature biotechnology, 14, 1246-1251.
46. Phillips, G.N., Jr. (1997) Structure and dynamics of green fluorescent protein. Current opinion in structural biology, 7, 821-827.
47. Ward, W.W., Cody, C.W., Hart, R.C. and Cormier, M.J. (1980) Spectrophotometric identity of the energy transfer chromophores in renilla and aequorea green-fluorescent proteins hotochemistry and Photobiology, 31, 611-615.
48. Niwa, H., Inouye, S., Hirano, T., Matsuno, T., Kojima, S., Kubota, M., Ohashi, M.

and Tsuji, F.I. (1996) Chemical nature of the light emitter of the Aequorea green fluorescent protein. Proceedings of the National Academy of Sciences of the United States of America, 93, 13617-13622.

49. McCapra, F., Razavi, Z. and Neary, A.P. (1988) The fluorescence of the chromophore of the green fluorescent protein of Aequorea and Renilla. J. Chem. Soc., Chem. Commun., 790-791.
50. You, Y., He, Y., Burrows, P.E., Forrest, S.R., Petasis, N.A. and Thompson, M.E. (2000) Fluorophores Related to the Green Fluorescent Protein and Their Use in Optoelectronic Devices. Advance Materials, 12, 1678-1680.
51. Kummer, A.D., Kompa, C., Lossau, H., Pöllinger-Dammer, F., Michel-Beyerle, M.E., Silva, C.M., J. Bylina, E.J., Coleman, W.J., Yang, M.M. and Youvan, D.C. (1998) Dramatic reduction in fluorescence quantum yield in mutants of Green Fluorescent Protein due to fast internal conversion. Chemical Physics, 237, 183-193.
52. Webber, N.M., Litvinenko, K.L. and Meech, S.R. (2001) Radiationless relaxation in a synthetic analogue of the green fluorescent protein chromophore. . Journal of Physical Chemistry B, 105, 8036–8039.
53. Cormack, B.P., Valdivia, R.H. and Falkow, S. (1996) FACS-optimized mutants of the green fluorescent protein (GFP). Gene, 173, 33-38.
54. Tyagi, S. and Alsmadi, O. (2004) Imaging native beta-actin mRNA in motile fibroblasts. Biophysical journal, 87, 4153-4162.
55. Chen, A.K., Behlke, M.A. and Tsourkas, A. (2007) Avoiding false-positive signals with nuclease-vulnerable molecular beacons in single living cells. Nucleic acids research, 35, e105.
56. Santangelo, P.J., Nix, B., Tsourkas, A. and Bao, G. (2004) Dual FRET molecular beacons for mRNA detection in living cells. Nucleic acids research, 32, e57.
57. Armitage, B.A. (2011) Imaging of RNA in live cells. Current opinion in chemical biology, 15, 806-812.
58. Brodsky, A.S. and Silver, P.A. (2002) Identifying proteins that affect mRNA localization in living cells. Methods, 26, 151-155.
59. Fusco, D., Accornero, N., Lavoie, B., Shenoy, S.M., Blanchard, J.M., Singer, R.H. and Bertrand, E. (2003) Single mRNA molecules demonstrate probabilistic movement in living mammalian cells. Current biology : CB, 13, 161-167.
60. Urbanek, M.O., Galka-Marciniak, P., Olejniczak, M. and Krzyzosiak, W.J. (2014) RNA imaging in living cells - methods and applications. RNA biology, 11,

1083-1095.

61. Holeman, L.A., Robinson, S.L., Szostak, J.W. and Wilson, C. (1998) Isolation and characterization of fluorophore-binding RNA aptamers. Folding & design, 3, 423-431.
62. Sunbul, M. and Jaschke, A. (2013) Contact-mediated quenching for RNA imaging in bacteria with a fluorophore-binding aptamer. Angewandte Chemie, 52, 13401-13404.
63. Paige, J.S., Wu, K.Y. and Jaffrey, S.R. (2011) RNA mimics of green fluorescent protein. Science, 333, 642-646.
64. Han, K.Y., Leslie, B.J., Fei, J., Zhang, J. and Ha, T. (2013) Understanding the photophysics of the spinach-DFHBI RNA aptamer-fluorogen complex to improve live-cell RNA imaging. Journal of the American Chemical Society, 135, 19033-19038.
65. Strack, R.L., Disney, M.D. and Jaffrey, S.R. (2013) A superfolding Spinach2 reveals the dynamic nature of trinucleotide repeat-containing RNA. Nature methods, 10, 1219-1224.
66. Warner, K.D., Chen, M.C., Song, W., Strack, R.L., Thorn, A., Jaffrey, S.R. and Ferre-D'Amare, A.R. (2014) Structural basis for activity of highly efficient RNA mimics of green fluorescent protein. Nature structural & molecular biology, 21, 658-663.
67. Chen, M.C., Lambert, C.R., Urgitis, J.D. and Zimmer, M. (2001) Photoisomerization of green fluorescent protein and the dimensions of the chromophore cavity. Chemical Physics, 270, 157–164.
68. Huang, H., Suslov, N.B., Li, N.S., Shelke, S.A., Evans, M.E., Koldobskaya, Y., Rice, P.A. and Piccirilli, J.A. (2014) A G-quadruplex-containing RNA activates fluorescence in a GFP-like fluorophore. Nature chemical biology, 10, 686-691.
69. Rust, M.J., Bates, M. and Zhuang, X. (2006) Sub-diffraction-limit imaging by stochastic optical reconstruction microscopy (STORM). Nature methods, 3, 793-795.
70. Betzig, E., Patterson, G.H., Sougrat, R., Lindwasser, O.W., Olenych, S., Bonifacino, J.S., Davidson, M.W., Lippincott-Schwartz, J. and Hess, H.F. (2006) Imaging intracellular fluorescent proteins at nanometer resolution. Science, 313, 1642-1645.
71. Thompson, M.A., Lew, M.D. and Moerner, W.E. (2012) Extending microscopic resolution with single-molecule imaging and active control. Annual review of

biophysics, 41, 321-342.
72. Bobroff, N. (1986) Position measurement with a resolution and noise-limited instrument. Rev. Sci. Instrum., 57, 1152-1157.
73. Sahl, S.J. and Moerner, W.E. (2013) Super-resolution fluorescence imaging with single molecules. Current opinion in structural biology, 23, 778-787.
74. Thompson, R.E., Larson, D.R. and Webb, W.W. (2002) Precise nanometer localization analysis for individual fluorescent probes. Biophysical journal, 82, 2775-2783.
75. Dempsey, G.T., Vaughan, J.C., Chen, K.H., Bates, M. and Zhuang, X. (2011) Evaluation of fluorophores for optimal performance in localization-based super-resolution imaging. Nature methods, 8, 1027-1036.
76. Bates, M., Blosser, T.R. and Zhuang, X. (2005) Short-range spectroscopic ruler based on a single-molecule optical switch. Physical review letters, 94, 108101.
77. Dempsey, G.T., Bates, M., Kowtoniuk, W.E., Liu, D.R., Tsien, R.Y. and Zhuang, X. (2009) Photoswitching mechanism of cyanine dyes. Journal of the American Chemical Society, 131, 18192-18193.
78. Heilemann, M., Margeat, E., Kasper, R., Sauer, M. and Tinnefeld, P. (2005) Carbocyanine dyes as efficient reversible single-molecule optical switch. Journal of the American Chemical Society, 127, 3801-3806.
79. Dempsey, G.T. (2013) Chapter 24: A user's guide to localization-based super-resolution fluorescence imaging. Mehtods in Cell Biology, 114, 561-592.
80. Huang, B., Wang, W., Bates, M. and Zhuang, X. (2008) Three-dimensional super-resolution imaging by stochastic optical reconstruction microscopy. Science, 319, 810-813.
81. Pavani, S.R., Thompson, M.A., Biteen, J.S., Lord, S.J., Liu, N., Twieg, R.J., Piestun, R. and Moerner, W.E. (2009) Three-dimensional, single-molecule fluorescence imaging beyond the diffraction limit by using a double-helix point spread function. Proceedings of the National Academy of Sciences of the United States of America, 106, 2995-2999.
82. Juette, M.F., Gould, T.J., Lessard, M.D., Mlodzianoski, M.J., Nagpure, B.S., Bennett, B.T., Hess, S.T. and Bewersdorf, J. (2008) Three-dimensional sub-100 nm resolution fluorescence microscopy of thick samples. Nature methods, 5, 527-529.
83. Shtengel, G., Galbraith, J.A., Galbraith, C.G., Lippincott-Schwartz, J., Gillette, J.M., Manley, S., Sougrat, R., Waterman, C.M., Kanchanawong, P., Davidson,

M.W. et al. (2009) Interferometric fluorescent super-resolution microscopy resolves 3D cellular ultrastructure. Proceedings of the National Academy of Sciences of the United States of America, 106, 3125-3130.

84. Poehlsgaard, J. and Douthwaite, S. (2005) The bacterial ribosome as a target for antibiotics. Nature reviews. Microbiology, 3, 870-881.
85. Magnet, S. and Blanchard, J.S. (2005) Molecular insights into aminoglycoside action and resistance. Chemical reviews, 105, 477-498.
86. Fosso, M.Y., Li, Y. and Garneau-Tsodikova, S. (2014) New trends in aminoglycosides use. MedChemComm, 5, 1075-1091.
87. Davies, J., Gorini, L. and Davis, B.D. (1965) Misreading of RNA codewords induced by aminoglycoside antibiotics. Molecular pharmacology, 1, 93-106.
88. Cabanas, M.J., Vazquez, D. and Modolell, J. (1978) Inhibition of ribosomal translocation by aminoglycoside antibiotics. Biochemical and biophysical research communications, 83, 991-997.
89. Karimi, R. and Ehrenberg, M. (1994) Dissociation rate of cognate peptidyl-tRNA from the A-site of hyper-accurate and error-prone ribosomes. European journal of biochemistry / FEBS, 226, 355-360.
90. Misumi, M., Nishimura, T., Komai, T. and Tanaka, N. (1978) Interaction of kanamycin and related antibiotics with the large subunit of ribosomes and the inhibition of translocation. Biochemical and biophysical research communications, 84, 358-365.
91. Shoji, S., Walker, S.E. and Fredrick, K. (2006) Reverse translocation of tRNA in the ribosome. Molecular cell, 24, 931-942.
92. Borovinskaya, M.A., Shoji, S., Holton, J.M., Fredrick, K. and Cate, J.H. (2007) A steric block in translation caused by the antibiotic spectinomycin. ACS chemical biology, 2, 545-552.
93. Szaflarski, W., Vesper, O., Teraoka, Y., Plitta, B., Wilson, D.N. and Nierhaus, K.H. (2008) New features of the ribosome and ribosomal inhibitors: non-enzymatic recycling, misreading and back-translocation. Journal of molecular biology, 380, 193-205.
94. Ogle, J.M., Carter, A.P. and Ramakrishnan, V. (2003) Insights into the decoding mechanism from recent ribosome structures. Trends in biochemical sciences, 28, 259-266.
95. Moazed, D. and Noller, H.F. (1987) Interaction of antibiotics with functional sites in 16S ribosomal RNA. Nature, 327, 389-394.

96. Woodcock, J., Moazed, D., Cannon, M., Davies, J. and Noller, H.F. (1991) Interaction of antibiotics with A- and P-site-specific bases in 16S ribosomal RNA. The EMBO journal, 10, 3099-3103.
97. Fourmy, D., Recht, M.I., Blanchard, S.C. and Puglisi, J.D. (1996) Structure of the A site of Escherichia coli 16S ribosomal RNA complexed with an aminoglycoside antibiotic. Science, 274, 1367-1371.
98. Yoshizawa, S., Fourmy, D. and Puglisi, J.D. (1998) Structural origins of gentamicin antibiotic action. The EMBO journal, 17, 6437-6448.
99. Fourmy, D., Yoshizawa, S. and Puglisi, J.D. (1998) Paromomycin binding induces a local conformational change in the A-site of 16 S rRNA. Journal of molecular biology, 277, 333-345.
100. Vicens, Q. and Westhof, E. (2001) Crystal structure of paromomycin docked into the eubacterial ribosomal decoding A site. Structure, 9, 647-658.
101. Lynch, S.R., Gonzalez, R.L. and Puglisi, J.D. (2003) Comparison of X-ray crystal structure of the 30S subunit-antibiotic complex with NMR structure of decoding site oligonucleotide-paromomycin complex. Structure, 11, 43-53.
102. Wimberly, B.T. (2009) The use of ribosomal crystal structures in antibiotic drug design. Current opinion in investigational drugs, 10, 750-765.
103. Ogle, J.M., Murphy, F.V., Tarry, M.J. and Ramakrishnan, V. (2002) Selection of tRNA by the ribosome requires a transition from an open to a closed form. Cell, 111, 721-732.
104. Selmer, M., Dunham, C.M., Murphy, F.V.t., Weixlbaumer, A., Petry, S., Kelley, A.C., Weir, J.R. and Ramakrishnan, V. (2006) Structure of the 70S ribosome complexed with mRNA and tRNA. Science, 313, 1935-1942.
105. Yoshizawa, S., Fourmy, D. and Puglisi, J.D. (1999) Recognition of the codon-anticodon helix by ribosomal RNA. Science, 285, 1722-1725.
106. Borovinskaya, M.A., Pai, R.D., Zhang, W., Schuwirth, B.S., Holton, J.M., Hirokawa, G., Kaji, H., Kaji, A. and Cate, J.H. (2007) Structural basis for aminoglycoside inhibition of bacterial ribosome recycling. Nature structural & molecular biology, 14, 727-732.
107. Wang, L., Pulk, A., Wasserman, M.R., Feldman, M.B., Altman, R.B., Cate, J.H. and Blanchard, S.C. (2012) Allosteric control of the ribosome by small-molecule antibiotics. Nature structural & molecular biology, 19, 957-963.
108. Demeshkina, N., Jenner, L., Westhof, E., Yusupov, M. and Yusupova, G. (2012) A new understanding of the decoding principle on the ribosome. Nature, 484,

256-259.

109. Demeshkina, N., Jenner, L., Westhof, E., Yusupov, M. and Yusupova, G. (2013) New structural insights into the decoding mechanism: translation infidelity via a G.U pair with Watson-Crick geometry. FEBS letters, 587, 1848-1857.
110. Kohanski, M.A., Dwyer, D.J., Wierzbowski, J., Cottarel, G. and Collins, J.J. (2008) Mistranslation of membrane proteins and two-component system activation trigger antibiotic-mediated cell death. Cell, 135, 679-690.
111. Davis, B.D., Chen, L.L. and Tai, P.C. (1986) Misread protein creates membrane channels: an essential step in the bactericidal action of aminoglycosides. Proceedings of the National Academy of Sciences of the United States of America, 83, 6164-6168.
112. Kramer, E.B. and Farabaugh, P.J. (2007) The frequency of translational misreading errors in E. coli is largely determined by tRNA competition. RNA, 13, 87-96.
113. Kohanski, M.A., Dwyer, D.J., Hayete, B., Lawrence, C.A. and Collins, J.J. (2007) A common mechanism of cellular death induced by bactericidal antibiotics. Cell, 130, 797-810.
114. Foti, J.J., Devadoss, B., Winkler, J.A., Collins, J.J. and Walker, G.C. (2012) Oxidation of the guanine nucleotide pool underlies cell death by bactericidal antibiotics. Science, 336, 315-319.
115. Zimmermann, R.A., Rosset, R. and Gorini, L. (1971) Nature of phenotypic masking exhibited by drug-dependent streptomycin A mutants of Escherichia coli. Journal of molecular biology, 57, 403-422.
116. Ezraty, B., Vergnes, A., Banzhaf, M., Duverger, Y., Huguenot, A., Brochado, A.R., Su, S.Y., Espinosa, L., Loiseau, L., Py, B. et al. (2013) Fe-S cluster biosynthesis controls uptake of aminoglycosides in a ROS-less death pathway. Science, 340, 1583-1587.
117. Keren, I., Wu, Y., Inocencio, J., Mulcahy, L.R. and Lewis, K. (2013) Killing by bactericidal antibiotics does not depend on reactive oxygen species. Science, 339, 1213-1216.
118. Dwyer, D.J., Belenky, P.A., Yang, J.H., MacDonald, I.C., Martell, J.D., Takahashi, N., Chan, C.T., Lobritz, M.A., Braff, D., Schwarz, E.G. et al. (2014) Antibiotics induce redox-related physiological alterations as part of their lethality. Proceedings of the National Academy of Sciences of the United States of America, 111, E2100-2109.

119. van Opijnen, T., Bodi, K.L. and Camilli, A. (2009) Tn-seq: high-throughput parallel sequencing for fitness and genetic interaction studies in microorganisms. Nature methods, 6, 767-772.
120. Gallagher, L.A., Shendure, J. and Manoil, C. (2011) Genome-scale identification of resistance functions in Pseudomonas aeruginosa using Tn-seq. mBio, 2, e00315-00310.
121. Lee, S., Hinz, A., Bauerle, E., Angermeyer, A., Juhaszova, K., Kaneko, Y., Singh, P.K. and Manoil, C. (2009) Targeting a bacterial stress response to enhance antibiotic action. Proceedings of the National Academy of Sciences of the United States of America, 106, 14570-14575.
122. Shan, Y., Lazinski, D., Rowe, S., Camilli, A. and Lewis, K. (2015) Genetic Basis of Persister Tolerance to Aminoglycosides in Escherichia coli. mBio, 6.
123. Davis, B.D. (1987) Mechanism of bactericidal action of aminoglycosides. Microbiological reviews, 51, 341-350.
124. Taber, H.W., Mueller, J.P., Miller, P.F. and Arrow, A.S. (1987) Bacterial uptake of aminoglycoside antibiotics. Microbiological reviews, 51, 439-457.
125. Anand, N., Davis, B.D. and Armitage, A.K. (1960) Uptake of streptomycin by Escherichia coli. Nature, 185, 23-24.
126. Rivera, M., Hancock, R.E., Sawyer, J.G., Haug, A. and McGroarty, E.J. (1988) Enhanced binding of polycationic antibiotics to lipopolysaccharide from an aminoglycoside-supersusceptible, tolA mutant strain of Pseudomonas aeruginosa. Antimicrobial agents and chemotherapy, 32, 649-655.
127. Hancock, R.E., Farmer, S.W., Li, Z.S. and Poole, K. (1991) Interaction of aminoglycosides with the outer membranes and purified lipopolysaccharide and OmpF porin of Escherichia coli. Antimicrobial agents and chemotherapy, 35, 1309-1314.
128. Hancock, R.E. and Bell, A. (1988) Antibiotic uptake into gram-negative bacteria. European journal of clinical microbiology & infectious diseases : official publication of the European Society of Clinical Microbiology, 7, 713-720.
129. Muir, M.E., van Heeswyck, R.S. and Wallace, B.J. (1984) Effect of growth rate on streptomycin accumulation by Escherichia coli and Bacillus megaterium. Journal of general microbiology, 130, 2015-2022.
130. Davis, B.D. (1982) Bactericidal synergism between beta-lactams and aminoglycosides: mechanism and possible therapeutic implications. Reviews of infectious diseases, 4, 237-245.

131. Nichols, W.W. and Young, S.N. (1985) Respiration-dependent uptake of dihydrostreptomycin by Escherichia coli. Its irreversible nature and lack of evidence for a uniport process. The Biochemical journal, 228, 505-512.
132. Bryan, L.E. and Van Den Elzen, H.M. (1977) Effects of membrane-energy mutations and cations on streptomycin and gentamicin accumulation by bacteria: a model for entry of streptomycin and gentamicin in susceptible and resistant bacteria. Antimicrobial agents and chemotherapy, 12, 163-177.
133. Anand, N. and Davis, B.D. (1960) Damage by streptomycin to the cell membrane of Escherichia coli. Nature, 185, 22-23.
134. Roth, H., Amos, H. and Davis, B.D. (1960) Purine nucleotide excretion by Escherichia coli in the presence of streptomycin. Biochimica et biophysica acta, 37, 398-405.
135. Dubin, D.T. and Davis, B.D. (1961) The effect of streptomycin on potassium flux in Escherichia coli. Biochimica et biophysica acta, 52, 400-402.
136. Rosano, C.L., Peabody, R.A. and Hurwitz, C. (1960) Studies on the mechanism of action of action of streptomycin. Effect of streptomycin on the excretion of nucleotides by Escherichia coli. Biochimica et biophysica acta, 37, 380-382.
137. Klainer, A.S. and Russell, R.R. (1974) Effect of the inhibition of protein synthesis on the Escherichia coli cell envelope. Antimicrobial agents and chemotherapy, 6, 216-224.
138. Hancock, R. (1962) Uptake of 14C-streptomycin by some microorganisms and its relation to their streptomycin sensitivity. Journal of general microbiology, 28, 493-501.
139. Sandoval, R., Leiser, J. and Molitoris, B.A. (1998) Aminoglycoside antibiotics traffic to the Golgi complex in LLC-PK1 cells. Journal of the American Society of Nephrology : JASN, 9, 167-174.
140. Allison, K.R., Brynildsen, M.P. and Collins, J.J. (2011) Metabolite-enabled eradication of bacterial persisters by aminoglycosides. Nature, 473, 216-220.
141. Montero Llopis, P., Jackson, A.F., Sliusarenko, O., Surovtsev, I., Heinritz, J., Emonet, T. and Jacobs-Wagner, C. (2010) Spatial organization of the flow of genetic information in bacteria. Nature, 466, 77-81.
142. Bakshi, S., Siryaporn, A., Goulian, M. and Weisshaar, J.C. (2012) Superresolution imaging of ribosomes and RNA polymerase in live Escherichia coli cells. Molecular microbiology, 85, 21-38.
143. Moraru, C. and Amann, R. (2012) Crystal ball: fluorescence in situ hybridization

in the age of super-resolution microscopy. Systematic and applied microbiology, 35, 549-552.

144. Rackham, O. and Chin, J.W. (2005) A network of orthogonal ribosome x mRNA pairs. Nature chemical biology, 1, 159-166.

145. You, M. and Jaffrey, S.R. (2015) Structure and Mechanism of RNA Mimics of Green Fluorescent Protein. Annual review of biophysics, 44, 187-206.

146. Cannone, J.J., Subramanian, S., Schnare, M.N., Collett, J.R., D'Souza, L.M., Du, Y., Feng, B., Lin, N., Madabusi, L.V., Muller, K.M. et al. (2002) The comparative RNA web (CRW) site: an online database of comparative sequence and structure information for ribosomal, intron, and other RNAs. BMC bioinformatics, 3, 2.

147. Dorywalska, M., Blanchard, S.C., Gonzalez, R.L., Kim, H.D., Chu, S. and Puglisi, J.D. (2005) Site-specific labeling of the ribosome for single-molecule spectroscopy. Nucleic acids research, 33, 182-189.

148. Brosius, J., Ullrich, A., Raker, M.A., Gray, A., Dull, T.J., Gutell, R.R. and Noller, H.F. (1981) Construction and fine mapping of recombinant plasmids containing the rrnB ribosomal RNA operon of E. coli. Plasmid, 6, 112-118.

149. Ponchon, L. and Dardel, F. (2007) Recombinant RNA technology: the tRNA scaffold. Nature methods, 4, 571-576.

150. Ying, B.W., Fourmy, D. and Yoshizawa, S. (2007) Substitution of the use of radioactivity by fluorescence for biochemical studies of RNA. RNA, 13, 2042-2050.

151. Filonov, G.S., Kam, C.W., Song, W. and Jaffrey, S.R. (2015) In-gel imaging of RNA processing using broccoli reveals optimal aptamer expression strategies. Chemistry & biology, 22, 649-660.

152. Plotz, P.H., Dubin, D.T. and Davis, B.D. (1961) Influence of salts on the uptake of streptomycin by Escherichia coli. Nature, 191, 1324-1325.

153. Baier, J., Maier, M., Engl, R., Landthaler, M. and Baumler, W. (2005) Time-resolved investigations of singlet oxygen luminescence in water, in phosphatidylcholine, and in aqueous suspensions of phosphatidylcholine or HT29 cells. The journal of physical chemistry. B, 109, 3041-3046.

154. Nikaido, H. and Rosenberg, E.Y. (1981) Effect on solute size on diffusion rates through the transmembrane pores of the outer membrane of Escherichia coli. The Journal of general physiology, 77, 121-135.

155. Novo, D., Perlmutter, N.G., Hunt, R.H. and Shapiro, H.M. (1999) Accurate flow cytometric membrane potential measurement in bacteria using

diethyloxacarbocyanine and a ratiometric technique. Cytometry, 35, 55-63.
156. Falconer, S.B., Czarny, T.L. and Brown, E.D. (2011) Antibiotics as probes of biological complexity. Nature chemical biology, 7, 415-423.
157. Arhammer, M., Mardh, P.A., Ripa, T. and Andersson, K.E. (1978) Microcalorimetric study of the effects of cephalexin and cephaloridin on Escherichia coli and Staphylococcus aureus. Acta pathologica et microbiologica Scandinavica. Section B, Microbiology, 86, 59-65.
158. Livermore, D.M. (1990) Antibiotic uptake and transport by bacteria. Scandinavian journal of infectious diseases. Supplementum, 74, 15-22.
159. Matias, V.R. and Beveridge, T.J. (2005) Cryo-electron microscopy reveals native polymeric cell wall structure in Bacillus subtilis 168 and the existence of a periplasmic space. Molecular microbiology, 56, 240-251.
160. Brandt, F., Etchells, S.A., Ortiz, J.O., Elcock, A.H., Hartl, F.U. and Baumeister, W. (2009) The native 3D organization of bacterial polysomes. Cell, 136, 261-271.
161. Chai, Q., Singh, B., Peisker, K., Metzendorf, N., Ge, X., Dasgupta, S. and Sanyal, S. (2014) Organization of ribosomes and nucleoids in Escherichia coli cells during growth and in quiescence. The Journal of biological chemistry, 289, 11342-11352.
162. Kuru, E., Hughes, H.V., Brown, P.J., Hall, E., Tekkam, S., Cava, F., de Pedro, M.A., Brun, Y.V. and VanNieuwenhze, M.S. (2012) In Situ probing of newly synthesized peptidoglycan in live bacteria with fluorescent D-amino acids. Angewandte Chemie, 51, 12519-12523.
163. Asai, T., Zaporojets, D., Squires, C. and Squires, C.L. (1999) An Escherichia coli strain with all chromosomal rRNA operons inactivated: complete exchange of rRNA genes between bacteria. Proceedings of the National Academy of Sciences of the United States of America, 96, 1971-1976.
164. Leshin, J.A., Rakauskaite, R., Dinman, J.D. and Meskauskas, A. (2010) Enhanced purity, activity and structural integrity of yeast ribosomes purified using a general chromatographic method. RNA biology, 7, 354-360.
165. Recht, M.I., Fourmy, D., Blanchard, S.C., Dahlquist, K.D. and Puglisi, J.D. (1996) RNA sequence determinants for aminoglycoside binding to an A-site rRNA model oligonucleotide. J. Mol. Biol., 262, 421-436.